Title 40 CFR Part 191
Subparts B and C
Compliance Recertification
Application
for the
Waste Isolation Pilot Plant

Appendix PA

United States Department of Energy
Waste Isolation Pilot Plant

Carlsbad Field Office
Carlsbad, New Mexico

Appendix PA

Table of Contents

List of Figures

List of Tables

ACRONYMS AND ABBREVIATIONS

AMG	algebraic multi-grid solver
CDF	cumulative distribution function
CCDF	complementary cumulative distribution function
CFR	Code of Federal Regulations
CH-TRU	contact-handled transuranic (waste)
DBR	direct brine release
DOE	United States Department of Energy
DDZ	drilling damaged zone
DRZ	disturbed rock zone
EPA	United States Environmental Protection Agency
FEP	feature, event, or process
LHS	Latin Hypercube Sample
LMG	Link- algebraic multi-grid solver
LWB	Land Withdrawal Boundary
MB	Marker Bed
PA	performance assessment
PAVT	Performance Assessment Verification Test
PCS	panel closure system
PDF	probability density function
PDE	partial differential equations
PRCC	partial rank correlation coefficient
RH-TRU	remote-handled transuranic (waste)
SMC	Salado Mass Concrete
SOR	successive over-relaxation
TRU	transuranic (waste)
TVD	Total Variation Diminishing
WIPP	Waste Isolation Pilot Plan

PA-1.0 INTRODUCTION

This appendix presents the mathematical models used to evaluate performance of the Waste Isolation Pilot Plant (WIPP) and the results of these models for the CRA-2004 Performance Assessment (PA). This appendix supplements information presented in Chapter 6 of this application.

This appendix is organized as follows. Section PA-2.0 describes the overall conceptual structure of the CRA-2004 PA. As described in Section 6.1, the WIPP PA is designed to answer the requirements of Title 40 Code of Federal Regulations (CFR) Part 191, and thus involves three basic entities: (1) A probabilistic characterization of different futures that could occur at the WIPP site over the next 10,000 years, (2) Models for the physical processes that take place at the WIPP site and for the estimation of potential radionuclide releases that may be associated with these processes, and (3) A probabilistic characterization of the uncertainty in the models and parameters that underlie the WIPP PA. Section PA-2.0 is supplemented by Attachment SCR, which documents the results of the screening process for features, events, and processes (FEPs) that are retained in the conceptual models of repository performance.

Section PA-3.0 describes the probabilistic characterization of different futures. This characterization plays an important role in the construction of the complementary cumulative distribution function (CCDF) specified in 40 CFR § 191.13. Regulatory guidance and extensive review of the WIPP site resulted in identification of exploratory drilling for natural resources and the mining of potash as the only significant disruptions at the WIPP site with the potential to affect radionuclide releases to the accessible environment (Section 6.2.5). Section PA-3.0 summarizes the stochastic variables that represent future drilling and mining events in the PA.

Section PA-4.0 presents the mathematical models for the physical processes that take place at the WIPP and for the estimation of potential radionuclide releases. The mathematical models implement the conceptual models described in Section 6.4, and permit the construction of the CCDF specified in 40 CFR § 191.13. Models presented in Section PA-4.0 include: two-phase (i.e., gas and brine) flow in the vicinity of the repository; radionuclide transport in the Salado; releases to the surface at the time of a drilling intrusion due to cuttings, cavings, spallings, and direct releases of brine; brine flow in the Culebra Dolomite Formation; and radionuclide transport in the Culebra Dolomite. Section PA-4.0 is supplemented by Attachments MASS, TFIELD, and PORSURF. Attachment MASS discusses the modeling assumptions used in the WIPP PA. Attachment TFIELD discusses the generation of the transmissivity fields used to model fluid flow in the Culebra. Attachment PORSURF presents results of modeling the effects of excavated region closure, waste consolidation, and gas generation in the repository.

Section PA-5.0 discusses the probabilistic characterization of parameter uncertainty, and summarizes the uncertain variables incorporated into the 2004 PA, the distributions assigned to these variables, and the correlations between variables. Section PA-5.0 is supplemented by Attachments PAR and SOTERM. Attachment PAR catalogs the full set of parameters used in the CRA-2004 PA. Attachment SOTERM describes the actinide source term for the WIPP performance calculations, including calculation of the mobile concentrations of actinides that may be released from the repository in brine.

Section PA-6.0 summarizes the computational procedures used in the CRA-2004 PA, including: sampling techniques (i.e., random and Latin hypercube sampling); sample size; statistical confidence for mean CCDF; generation of Latin hypercube samples (LHSs); generation of individual futures; construction of CCDFs; calculations performed with the models discussed in Section PA-4.0; construction of releases for each future; and the sensitivity analysis techniques in use.

Section PA-7.0 presents the results of the PA for an undisturbed repository. Releases from the undisturbed repository are determined by radionuclide transport in brine flowing from the repository to the land withdrawal boundary (LWB) through the marker beds (MBs) or shafts (Section 6.3.1. Releases in the undisturbed scenario are used to demonstrate compliance with the individual and groundwater protection requirements in 40 CFR Part 191 (Chapter 8).

Section PA-8.0 presents PA results for a disturbed repository. As discussed in Section 6.2.3, the only future events and processes in the analysis of disturbed performance are those associated with mining and deep drilling. Release mechanisms include direct releases at the time of the intrusion via cuttings, cavings, spallings, and direct release of brine; and radionuclide transport up abandoned boreholes to the Culebra and thence to the land withdrawal boundary. Section PA-8.0 presents results for the most significant output variables from the PA models, accompanied by sensitivity analyses to determine which subjectively uncertain parameters are most influential in the uncertainty of PA results.

Section PA-9.0 presents the set of CCDFs resulting from the CRA-2004 PA. This material supplements Section 6.5, which demonstrates compliance with the containment requirements of 40 CFR § 191.13. Section PA.9.0 includes sensitivity analyses that identify which uncertain parameters are most significant in the calculation of releases.

This appendix follows the approach used by Helton et al. (1998) to document the mathematical models used in the CCA PA and the results of that analysis. Much of the content of this appendix derives from Helton et al. (1998); these authors’ contributions are gratefully acknowledged.

PA-2.0 CONCEPTUAL STRUCTURE OF THE PERFORMANCE ASSESSMENT

The conceptual structure of the CRA-2004 PA is unchanged from the CCA PA. Section 6.1 provides a general, less technical overview of the PA conceptual structure. This section of Appendix PA presents the conceptual basis for the CRA-2004 PA in a more formal manner. A corresponding presentation for the CCA PA is provided in Helton et al. (1998).

PA-2.1 Regulatory Requirements

The conceptual structure of the CRA-2004 PA derives from the regulatory requirements imposed on this facility. The primary regulation determining this structure is the Environmental Protection Agency’s (EPA’s) standard for the geologic disposal of radioactive waste, Environmental Radiation Protection Standards for the Management and Disposal of Spent Nuclear Fuel, High-Level and Transuranic Radioactive Wastes (40 CFR Part 191) (EPA 1985, 1993), which is divided into three subparts. Subpart A applies to a disposal facility prior to decommissioning and limits the annual radiation doses members of the public can be exposed to from waste management and storage operations. Subpart B applies after decommissioning and sets probabilistic limits on cumulative releases of radionuclides to the accessible environment for 10,000 years (40 CFR § 191.13) and assurance requirements to provide confidence that 40 CFR Section 191.13 will be met (40 CFR Section 191.14). Subpart B also sets limits on radiation doses to members of the public in the accessible environment for 10,000 years of undisturbed performance (40 CFR § 191.15). Subpart C limits radioactive contamination of groundwater for 10,000 years after disposal (40 CFR § 191.24). The Department of Energy (DOE) must demonstrate a reasonable expectation that the WIPP will continue to comply with the requirements of Subparts B and C of 40 CFR Part 191.

The following is the central requirement in 40 CFR Part 191, Subpart B, and the primary determinant of the conceptual structure of the CRA-2004 PA (p. 38086, EPA 1985):

> § 191.13 Containment requirements:
>
> (a) Disposal systems for spent nuclear fuel or high-level or transuranic radioactive wastes shall be designed to provide a reasonable expectation, based upon performance assessments, that cumulative releases of radionuclides to the accessible environment for 10,000 years after disposal from all significant processes and events that may affect the disposal system shall:
>
> > (1) Have a likelihood of less than one chance in 10 of exceeding the quantities calculated according to Table 1 (Appendix A); and
> >
> > (2) Have a likelihood of less than one chance in 1,000 of exceeding ten times the quantities calculated according to Table 1 (Appendix A).
>
> (b) Performance assessments need not provide complete assurance that the requirements of 191.13(a) will be met. Because of the long time period involved and the nature of the events and processes of interest, there will inevitably be substantial uncertainties in projecting disposal system performance. Proof of the future performance of a disposal system is not to be had in the ordinary sense of the word in situations that deal with much shorter time frames. Instead, what is required is a reasonable expectation, on the basis of the record before the implementing agency, that compliance with 191.13(a) will be achieved.

Section 191.13(a) refers to "quantities calculated according to Table 1 (Appendix A)," which means a normalized radionuclide release to the accessible environment based on the type of waste being disposed of, the initial waste inventory, and the size of release that may occur (EPA 1985, Appendix A). Table 1 of Appendix A specifies allowable releases (i.e., release limits) for individual radionuclides and is reproduced as Table PA-1 of this appendix. The WIPP is a repository to transuranic (TRU) waste, which is defined as "waste containing more than 100 nanocuries of alpha-emitting transuranic isotopes, with half-lives greater than twenty years, per gram of waste" (p. 38084, EPA 1985). The normalized release R for transuranic waste is defined by

$$R = \sum_i \left(\frac{Q_i}{L_i} \right) \left(1 \times 10^6 \ Ci / C \right) \tag{1}$$

where Q_i is the cumulative release of radionuclide i to the accessible environment during the 10,000-year period following closure of the repository (curies), L_i is the release limit for radionuclide i given in Table PA-1 (curies), and C is the amount of TRU waste emplaced in the repository (curies). In the CRA-2004 PA, $C = 2.48 \times 10^6$ curies (Appendix TRU WASTE, Section TRU WASTE-2.3.1). Further, accessible environment means (1) the atmosphere, (2) land surfaces, (3) surface waters, (4) oceans, and (5) all of the lithosphere that is beyond the controlled area; and controlled area means (1) a surface location, to be identified by passive institutional controls, that encompasses no more than 100 square kilometers and extends horizontally no more than five kilometers in any direction from the outer boundary of the original location of the radioactive wastes in a disposal system and (2) the subsurface underlying such a surface location (40 CFR § 191.13).

To help clarify the intent of 40 CFR Part 191, the EPA promulgated 40 CFR Part 194, Criteria for the Certification and Re-Certification of the Waste Isolation Pilot Plant's Compliance With the 40 CFR Part 191 Disposal Regulations. There, the following elaboration on the intent of 40 CFR § 191.13 set out.

> § 194.34 Results of performance assessments.
>
> > (a) The results of performance assessments shall be assembled into "complementary, cumulative distributions functions" (CCDFs) that represent the probability of exceeding various levels of cumulative release caused by all significant processes and events.
> >
> > (b) Probability distributions for uncertain disposal system parameter values used in performance assessments shall be developed and documented in any compliance application.
> >
> > (c) Computational techniques, which draw random samples from across the entire range of the probability distributions developed pursuant to paragraph (b) of this section, shall be used in generating CCDFs and shall be documented in any compliance application.
> >
> > (d) The number of CCDFs generated shall be large enough such that, at cumulative releases of 1 and 10, the maximum CCDF generated exceeds the 99th percentile of the population of CCDFs with at least a 0.95 probability.

Table PA-1. Release Limits for the Containment Requirements (EPA 1985, Appendix A, Table 1)

Radionuclide	Release Limit L_i per 1000 MTHM[1] or other unit of waste[2]
Americium (Am)-241 or –243	100
Carbon 14	100
Cesium-135 or -137	1,000
Iodine-129	100
Neptunium-237	100
Plutonium (Pu)-238, -239, -240, or -242	100
Radium-226	100
Strontium-90	1,000
Technetium-99	10,000
Thorium (Th)-230 or -232	10
Tin-126	1,000
Uranium (U)-233, -234, -235, -236, or -238	100
Any other alpha-emitting radionuclide with a half-life greater than 20 years	100
Any other radionuclide with a half-life greater than 20 years that does not emit alpha particles	1,000

[1] Metric tons of heavy metal exposed to a burnup between 25,000 megawatt-days per metric ton of heavy metal (MWd/MTHM) and 40,000 MWd/MTHM

[2] An amount of transuranic wastes containing one million curies of alpha-emitting transuranic radionuclides with half-lives greater than 20 years

> (e) Any compliance application shall display the full range of CCDFs generated.
>
> (f) Any compliance application shall provide information which demonstrates that there is at least a 95 percent level of statistical confidence that the mean of the population of CCDFs meets the containment requirements of § 191.13 of this chapter.

Three basic entities (EN1, EN2, EN3) underlie the results required by Sections 191.13 and § 194.34 and ultimately determine the conceptual and computational structure of the CRA-2004 PA:

EN1 - a probabilistic characterization of the likelihood of different futures occurring at the WIPP site over the next 10,000 years,

EN2 - a procedure for estimating the radionuclide releases to the accessible environment associated with each of the possible futures that could occur at the WIPP site over the next 10,000 years,

EN3 - a probabilistic characterization of the uncertainty in the parameters used in the definition of EN1 and EN2.

The preceding entities arise from an attempt to answer three questions about the WIPP:

Q1 - What events could occur at the WIPP site over the next 10,000 years?

Q2 - How likely are the different futures that could take place at the WIPP site over the next 10,000 years?

Q3 - What are the consequences of the different occurrences that could take place at the WIPP site over the next 10,000 years?

and one question about the PA:

Q4 - How much confidence can be placed in answers to these questions?

In the WIPP PA, EN1 provides answers to Q1 and Q2, EN2 provides an answer to Q3, and EN3 provides an answer to Q4. Together, EN1 and EN2 give rise to the CCDF specified in Section 191.13(a), and EN3 corresponds to the distributions specified by Section 194.34(b). The nature of EN1, EN2 and EN3, the role that they play in the CRA-2004 PA, and the method for constructing CCDFs are elaborated on in the next three sections.

PA-2.2 EN1: Probabilistic Characterization of Different Futures

The entity EN1 results from the scenario development process for the WIPP outlined in Section 6.3. The EN1 entity provides a probabilistic characterization of the likelihood of different futures that could occur at the WIPP site over the 10,000-year period specified in 40 CFR Part 191. Formally, EN1 is defined by a probability space $\left(\boldsymbol{X_{st}}, \boldsymbol{S_{st}}, \boldsymbol{p_{st}}\right)$, with the sample space X_{st} given by Equation (2).

$$\boldsymbol{X_{st}} = \left\{\boldsymbol{x_{st}} : \boldsymbol{x_{st}} \textbf{\textit{ is a possible 10,000-year sequence of occurrences at the WIPP}}\right\} \tag{2}$$

The subscript st refers to stochastic (i.e., aleatory) uncertainty and is used because $\left(\boldsymbol{X_{st}}, \boldsymbol{S_{st}}, \boldsymbol{p_{st}}\right)$ is providing a probabilistic characterization of occurrences that may take place in the future (Helton 1997). Incorporation of stochastic uncertainty is fundamental to the DOE's methodology for performance assessment Section 6.1.2. It is this stochastic uncertainty that gives rise to the distribution of releases evident in a CCDF.

A probability space $\left(\boldsymbol{X}, \boldsymbol{S}, \boldsymbol{p}\right)$ consists of three components: a set X that contains everything that could occur for the particular "universe" under consideration, a suitably restricted set S of subsets of X and a function p defined for elements of S that actually defines probability (Feller 1971). In the terminology of probability theory, X is the sample space, the elements of X are elementary events, the subsets of X contained in S are events, and p is a probability measure. In most applied problems, the function p defined on S is replaced by a probability density function (PDF) d (e.g., d_{st} in Figure PA-1).

In the CCA PA, the scenario development process for the WIPP identified exploratory drilling for natural resources as the only disruption with sufficient likelihood and consequence for inclusion in the definition of EN1 (CCA Appendix SCR [DOE 1996]). Reexamination of the FEPs and the scenario development process for the CRA-2004 PA did not change this conclusion (Section 6.2.6). In addition, 40 CFR Part 194 specifies that the occurrence of mining within the land withdrawal boundary must be included in the PA. As a result, the elements $\boldsymbol{x}_{st}$ of X_{st} are vectors of the form

$$\boldsymbol{x}_{st} = [\underbrace{t_1, e_1, l_1, b_1, p_1, \mathbf{a}_1}_{1^{st}\ intrusion}, \underbrace{t_2, e_2, l_2, b_2, p_2, \mathbf{a}_2}_{2^{nd}\ intrusion}, \ldots, \underbrace{t_n, e_n, l_n, b_n, p_n, \mathbf{a}_n}_{n^{th}\ intrusion}, t_{min}], \tag{3}$$

where n is the number of drilling intrusions, t_i is the time (year) of the i^{th} $_{intrusion}$, l_i designates the location of the i^{th} intrusion, e_i designates the penetration of an excavated or nonexcavated area by the i^{th} intrusion, b_i designates whether or not the i^{th} intrusion penetrates pressurized brine in the Castile Formation, p_i designates the plugging procedure used with the i^{th} intrusion (i.e., continuous plug, two discrete plugs, three discrete plugs), $\mathbf{a}_i$ designates the type of waste penetrated by the i^{th} intrusion (i.e., no waste, contact-handled (CH-TRU) waste, remote-handled (RH-TRU) waste), and t_{min} is the time at which potash mining occurs within the land withdrawal boundary.

In the development of $\left(X_{st}, S_{st}, p_{st}\right)$, the probabilistic characterization of n, t_i, l_i and e_i is based on the assumption that drilling intrusions will occur randomly in time and space (i.e., follow a Poisson process), the probabilistic characterization of b_i derives from assessed properties of brine pockets, the probabilistic characterization of $\mathbf{a}_i$ derives from the properties of the waste emplaced in the WIPP, and the probabilistic characterization of p_i derives from current drilling practices in the sedimentary basin (i.e., the Delaware Basin) in which the WIPP is located. A vector notation is used for $\mathbf{a}_i$ because it is possible for a given drilling intrusion to penetrate several different types of waste. Further, the probabilistic characterization for t_{min} follows from the guidance in 40 CFR Part 194 that the occurrence of potash mining within the land withdrawal boundary should be assumed to occur randomly in time (i.e., follow a Poisson process with a rate constant of $\lambda_m = 10^{-4}$ yr^{-1}), with all commercially viable potash reserves within the land withdrawal boundary being extracted at time t_{min}.

With respect to the three fundamental questions discussed about, X_{st} provides an answer to Q1, while S_{st} and p_{st} provide an answer to Q2. In practice, Q2 will be answered by specifying distributions for n , t_i , e_i , l_i , b_i , p_i , $\mathbf{a}_i$, and t_{min} , which in turn lead to definitions for S_{st} and p_{st} . The CCDF in 40 CFR Part 191 will be obtained by evaluating an integral involving $\left(X_{st}, S_{st}, p_{st}\right)$ (Figure PA-1). The definition of $\left(X_{st}, S_{st}, p_{st}\right)$ is discussed in more detail in Section PA-3.0.

PA-2.3 EN2: Estimation of Releases

The entity EN2 is the outcome of the model development process for the WIPP and provides a way to estimate radionuclide releases to the accessible environment for the different futures (i.e., elements $\mathbf{x}_{st}$ of X_{st}) that could occur at the WIPP. Estimation of environmental releases corresponds to evaluation of the function f in Figure PA-1. Release mechanisms associated with f include direct transport of material to the surface at the time of a drilling intrusion (i.e., cuttings, spallings, brine flow) and release subsequent to a drilling intrusion due to brine flow up a borehole with a degraded plug (i.e., groundwater transport).

The function f in Figure PA-1 is evaluated by a series of computational models shown in Figure PA-2. These computational models implement the conceptual models representing the repository system as described in Section 6.4, and the mathematical models for physical processes that are presented in Section PA-4.0. Most of the computational models involve the numerical solution of partial differential equations used to represent processes such as material deformation, fluid flow and radionuclide transport.

The models in Figure PA-2 are too complex to permit a closed form evaluation of the integral in Figure PA-1 that defines the CCDF specified in 40 CFR Part 191. Rather, a Monte Carlo procedure is used in the CRA-2004 PA. Specifically, elements $\mathbf{x}_{st,i}$, i = 1, 2, …, nS are randomly sampled from X_{st} in consistency with the definition of (X_{st}, S_{st}, p_{st}). Then, the integral in Figure PA-1, and hence the associated CCDF, is approximated by

$$prob(Rel > R) = \int_{S_{st}} \delta_R\left[f(\mathbf{x}_{st})\right] d_{st}(\mathbf{x}_{st})\, dV_{st} = \sum_{i=1}^{nS} \delta_R\left[f(\mathbf{x}_{st,i})\right] / nS\,, \tag{4}$$

where $\delta_R\left[f(\mathbf{x}_{st})\right] = 1$ if $f(\mathbf{x}_{st}) > R$ and $\delta_R\left[f(\mathbf{x}_{st})\right] = 0$ if $f(\mathbf{x}_{st}) \le R$ (Helton and Shiver 1996). However, the models in Figure PA-2 are also too computationally intensive to permit their evaluation for every element $\mathbf{x}_{st,i}$ of X_{st} in Equation (4). Due to this constraint, the models in Figure PA-2 are evaluated for representative elements of X_{st} and the results of these evaluations are used to construct values of f for the large number of $\mathbf{x}_{st,i}$ (e.g., nS = 10,000) in Equation (4). The representative elements are the scenarios E0, E1, E2, and E1E2 defined in Section PA-3.9; the procedure for constructing a CCDF from these scenarios is described in Section PA-6.0.

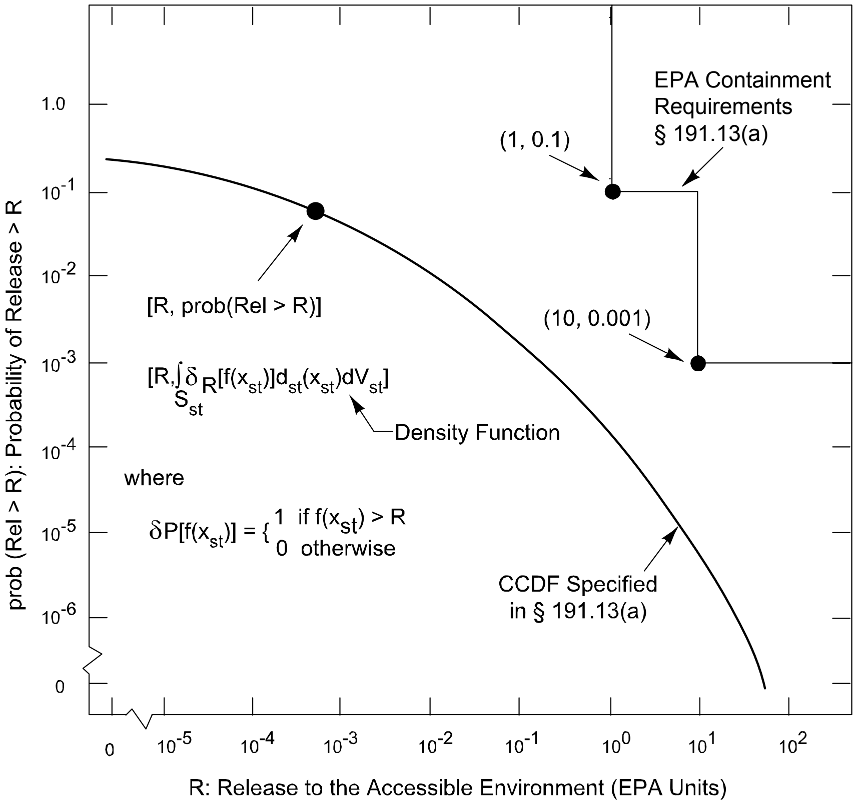

Figure PA-1. Construction of the CCDF Specified in 40 CFR Part 191, Subpart B.

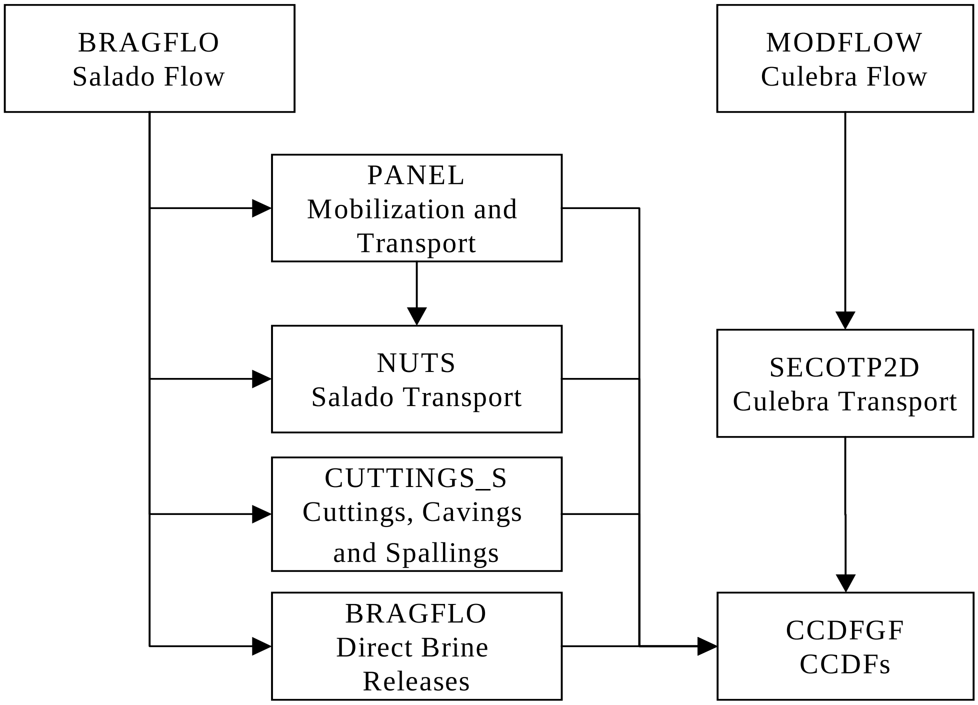

Figure PA-2. Computational Models Used in the CRA-2004 PA.

PA-2.4 EN3: Probabilistic Characterization of Parameter Uncertainty

The entity EN3 is the outcome of the data development effort for the WIPP (summarized in Chapter 2) and provides a probabilistic characterization of the uncertainty in the parameters that underlie the CRA-2004 PA. When viewed formally, EN3 is defined by a probability space $\left(X_{su}, S_{su}, p_{su}\right)$, with the sample space X_{su} given by Equation (5).

$$X_{su} = \left\{ \mathbf{x}_{su} : \mathbf{x}_{su} \textit{ is a possible vector of parameter values for the WIPP PA models} \right\} \tag{5}$$

The subscript su refers to subjective (i.e., epistemic) uncertainty and is used because $\left(X_{su}, S_{su}, p_{su}\right)$ is providing a probabilistic characterization of the possible inputs to the WIPP PA (Helton 1997). In practice, some elements of $\mathbf{x}_{su}$ could affect the definition of $\left(X_{st}, S_{st}, p_{st}\right)$ (e.g., the rate constant λ used to define the Poisson process for drilling intrusions) and other elements could relate to the models in Figure PA-2 that determine the function f in Figure PA-1 (e.g., radionuclide solubilities in Castile brine). Incorporation of subjective uncertainty is fundamental to the DOE's methodology for PA (Section 6.1.2).

If the value for $\mathbf{x}_{su}$ was precisely known, the CCDF in Figure PA-1 could be determined with certainty and compared with the boundary line specified in 40 CFR Part 191. However, given the complexity of the WIPP site and the 10,000-year time period under consideration, $\mathbf{x}_{su}$ can never be known with certainty. Rather, uncertainty in $\mathbf{x}_{su}$ as characterized by $\left(X_{su}, S_{su}, p_{su}\right)$ will lead to a distribution of CCDFs (Figure PA-3), with a different CCDF resulting for each possible value that $\mathbf{x}_{su}$ can take on. The proximity of this distribution to the boundary line in Figure PA-1 provides an indication of the confidence with which 40 CFR Part 191 will be met.

The distribution of CCDFs in Figure PA-3 can be summarized by distributions of exceedance probabilities conditional on individual release values (Figure PA-4). For a given release value R, this distribution is defined by a double integral over X_{su} and X_{st} (Helton 1996, 1997). In practice, this integral is too complex to permit a closed-form evaluation. Instead, the WIPP PA uses Latin hypercube sampling (McKay et al. 1979) to evaluate the integral over S_{su} and, as indicated in Equation (4), simple random sampling to evaluate the integral over X_{st}.

Specifically, a LHS $\mathbf{x}_{su,k}$, k = 1, 2, …, nLHS, is generated from S_{su} in consistency with the definition of $\left(X_{su}, S_{su}, p_{su}\right)$ and a random sample $\mathbf{x}_{st,i}$, i = 1, 2, …, nS, is generated from X_{st} in consistency with the definition of $\left(X_{st}, S_{st}, p_{st}\right)$. The probability $\mathbf{prob}\left(p \le P \middle| R\right)$ is approximated by

$$\mathbf{prob}\left(p \le P \mid R\right) \cong 1 - \sum_{k=1}^{nLHS} \delta_P \left[\sum_{i=1}^{nS} \delta_R \left[f\left(\mathbf{x}_{st,i}, \mathbf{x}_{su,k}\right) \right] / nS \right] / nLHS \tag{6}$$

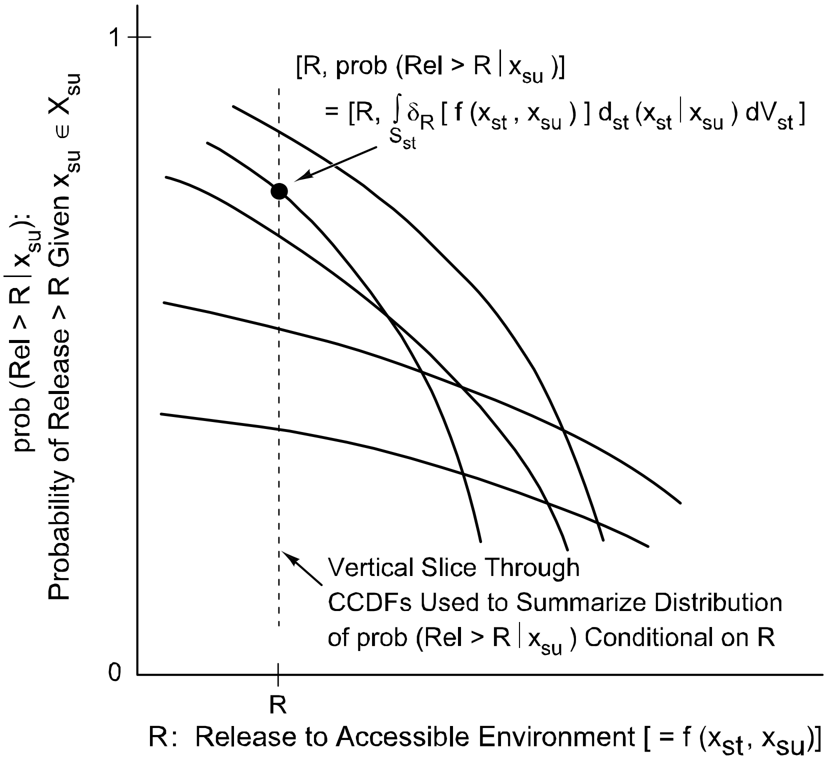

Figure PA-3. Distribution of CCDFs Resulting from Possible Values for $x_{su} \in X_{su}$.

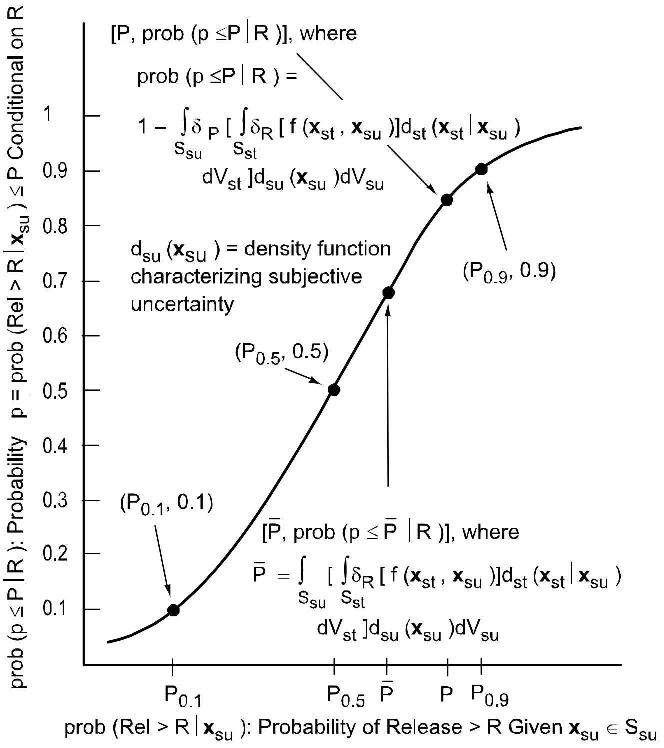

Figure PA-4. Distribution of Exceedance Probabilities Due to Subjective Uncertainty.

The result of the preceding calculation is typically displayed by plotting percentile values (e.g., $P_{0.1}$, $P_{0.5}$, $P_{0.9}$ in Figure PA-4) and also mean values for exceedance probabilities above the corresponding release values (i.e., R) and then connecting these points to form continuous curves (Figure PA-5). The proximity of these curves to the indicated boundary line provides an indication of the confidence with which 40 CFR Part 191 will be met.

With respect to the previously indicated questions, $\left(\boldsymbol{X}_{su}, \boldsymbol{S}_{su}, \boldsymbol{p}_{su}\right)$ and results derived from $\left(\boldsymbol{X}_{su}, \boldsymbol{S}_{su}, \boldsymbol{p}_{su}\right)$ (e.g., the distributions in Figure PA-3 and Figure PA-5) provide an answer to Q4. The definition of $\left(\boldsymbol{X}_{su}, \boldsymbol{S}_{su}, \boldsymbol{p}_{su}\right)$ is discussed in more detail in Section PA-5.0.

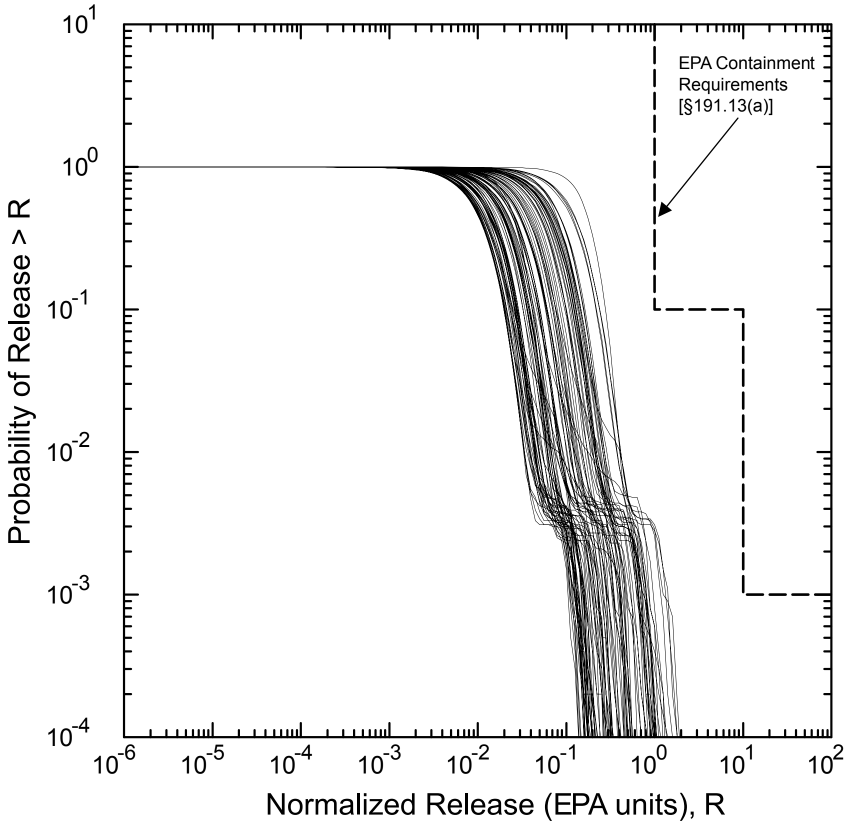

Figure PA-5. Example CCDF Distribution From CRA-2004 PA.

PA-3.0 PROBABILISTIC CHARACTERIZATION OF FUTURES

This section describes how stochastic uncertainty is implemented in PA. Screening analyses of possible future events concluded that the only significant events with potential to affect radionuclide releases to the accessible environment are drilling and mining within the land withdrawal boundary (Section 6.2.6). Consequently, modeling the future states of the repository focuses on representing the occurrences and effects of these two events.

PA-3.1 Probability Space

The first entity that underlies the CRA-2004 PA is a probabilistic characterization of the likelihood of different futures occurring at the WIPP site over the next 10,000 years. As discussed in Section PA-2.2, this entity is defined by a probability space $\left(\boldsymbol{X_{st}}, \boldsymbol{S_{st}}, \boldsymbol{p_{st}}\right)$ that characterizes stochastic uncertainty. The individual elements $\boldsymbol{x_{st}}$ of X_{st} are vectors of the form shown in Equation (3). Sections PA-3.2 through PA-3.8 describe the individual components t_i, e_i, l_i, b_i, p_i, a_i, and t_{min} of $\boldsymbol{x_{st}}$, and their associated probability distributions. These components and their associated distributions give rise to the probability space $\left(\boldsymbol{X_{st}}, \boldsymbol{S_{st}}, \boldsymbol{p_{st}}\right)$ for stochastic uncertainty. The concept of a scenario as a subset of the sample space X_{st} for stochastic uncertainty is discussed in Section PA-3.9. Further, the procedure used to sample the individual elements $\boldsymbol{x_{st,i}}$ of X_{st} indicated in Equation (4) is described in Section PA-6.5.

PA-3.2 Drilling Intrusion

As described in Section 6.3.2, drilling intrusions in the CRA-2004 PA are assumed to occur randomly in time and space (i.e., follow a Poisson process). Specifically, the drilling rate considered within the area marked by a berm as part of the system for passive institutional controls (Figure PA-6) is 5.25×10^{-3} intrusions per km $^{-2}$ yr $^{-1}$ (Section 6.4.12.2). Active institutional controls are assumed to prevent any drilling intrusions for the first 100 years after the decommissioning of the WIPP (Section 7.1). Unlike in the CCA PA, passive institutional controls are not assumed to reduce the drilling rate after decommissioning (Section 7.3).

For the computational implementation of the CRA-2004 PA, it is convenient to represent the Poisson process for drilling intrusions by its corresponding rate term $\lambda_d\left(t\right)$ for intrusions into the area marked by the berm. Specifically,

$$\lambda_d\left(t\right) = \begin{cases} 0 & 0 \le t \le 100\,yr \\ (0.6285\ km^2)(52.5\ km^{-2}\,10^{-4}\ yr) = 3.3 \times 10^{-3}\ yr^{-1} & 100 \le t \le 10{,}000\,yr \end{cases} \qquad (7)$$

where 0.6285 km^2 is the area of the berm Attachment PAR, Table PAR-45 and t is elapsed time since decommissioning of the WIPP.

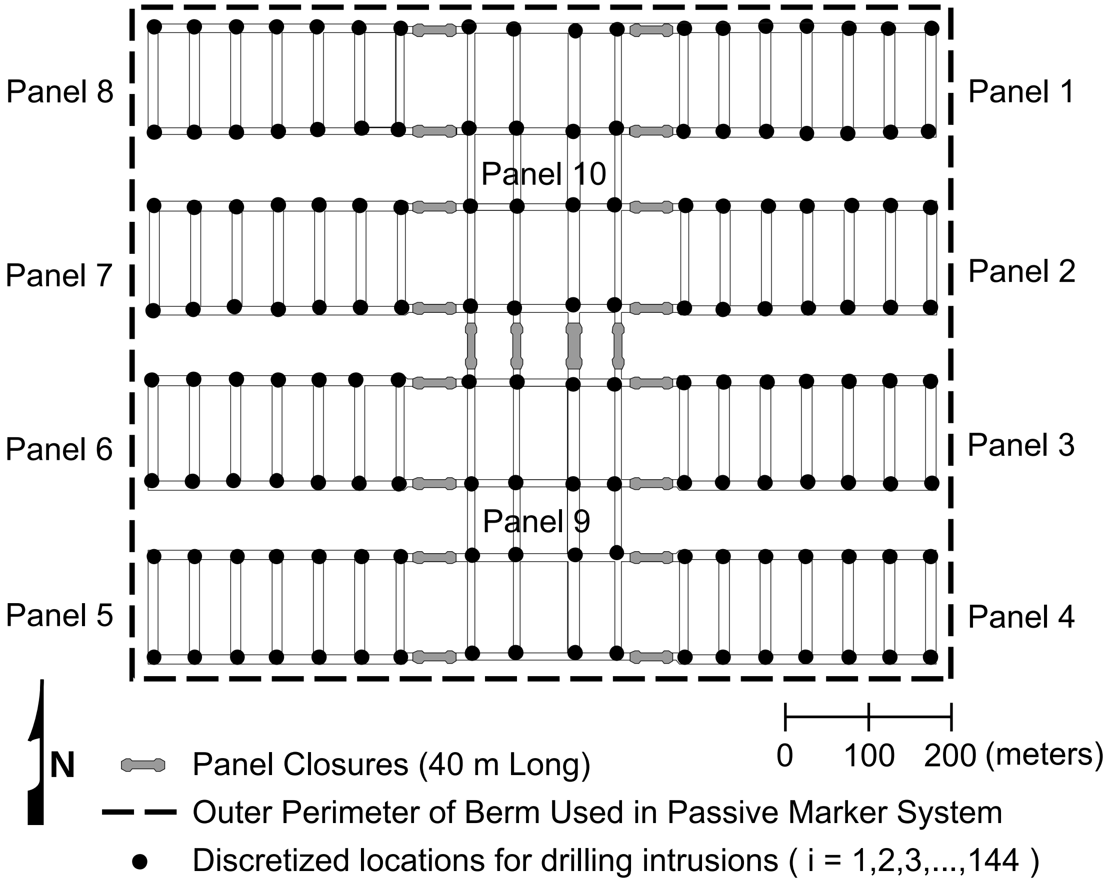

Figure PA-6. Location of Berm Used in Passive Marker System.

The function $\lambda_d(t)$ defines the part of the probability space (X_{st}, S_{st}, p_{st}) in Section PA-2.2 that corresponds to t_i . In the computational implementation of the analysis, $\lambda_d(t)$ is used to define the distribution of time between drilling intrusions (Figure PA-7). As a reminder, the occurrence of one event in a Poisson process has no effect on the occurrence of the next event. Thus, the cumulative distributions in Figure PA-7 can be used to define the time from one drilling event to the next (Section PA-6.5). Due to the 10,000-year regulatory period specified in 40 CFR § 191.13, t_i is assumed to be bounded above by 10,000 years in the definition of X_{st}. Further, t_i is bounded below by 100 years as defined in Equation (7).

The function $\lambda_d(t)$ also determines the probability $prob(nBH = n|[a,b])$ that a future will have exactly n drilling intrusions in the time interval [a, b] (Helton 1993), where

$$prob(nBH = n \mid [a,b]) = \left[\left(\int_a^b \lambda_d(t)dt\right)^n / n!\right] \exp\left(-\int_a^b \lambda_d(t)dt\right). \tag{8}$$

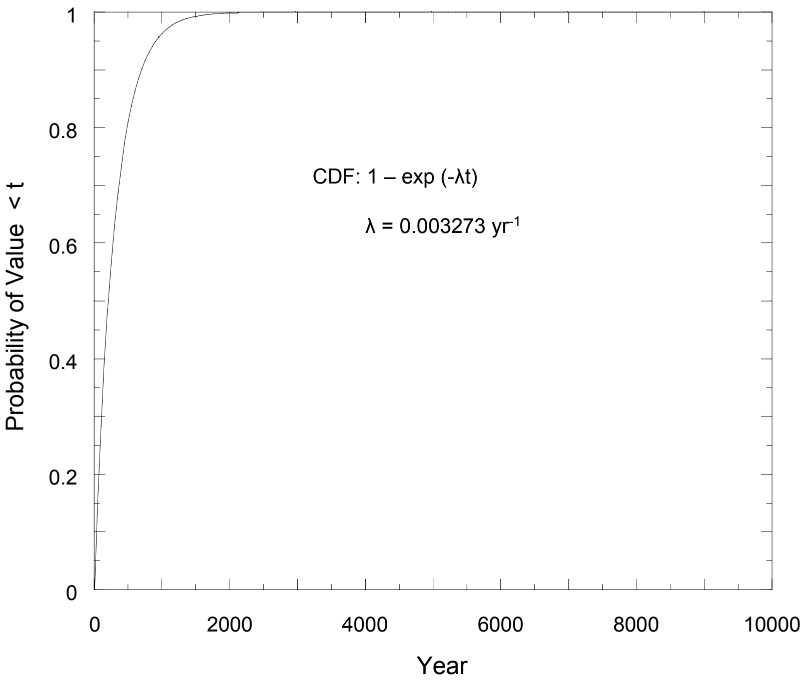

Figure PA-7. Cumulative Distribution Function (CDF) for Time Between Drilling Intrusions.

Further, the probability $prob\left(nBH \geq n \middle| [a,b]\right)$ that a future will have greater than or equal to n drilling intrusions in the time interval [a, b] is given by

$$prob(nBH \geq n \,|\, [a,b]) = \begin{cases} 1 & n = 0 \\ 1 - \sum_{m=0}^{n-1} prob(nBH = m \,|\, [a,b]) & n > 0 \end{cases} \tag{9}$$

PA-3.3 Penetration of Excavated/Nonexcavated Area

The variable e_i is a designator for whether or not the i^{th} drilling intrusion penetrates an excavated, waste-filled area of the repository (i.e., $e_i = 0, 1$ implies penetration of nonexcavated, excavated area, respectively). The corresponding probabilities pE_0 and pE_1 for $e_i = 0$ and $e_i = 1$ are

$$pE_1 = 0.1273 \text{ km}^2 / 0.6285 \text{ km}^2 = 0.203 \tag{10}$$

$$pE_0 = 1 - pE_1 = 0.797 \,, \tag{11}$$

where 0.1273 km^2 and 0.6285 km^2 are the excavated area of the repository filled with waste and the area of the berm, respectively (Attachment PAR, Table PAR-45). The probabilities pE_0 and pE_1 define the part of $\left(X_{st}, S_{st}, p_{st}\right)$ in Section PA.2.2 associated with e_i.

PA-3.4 Drilling Location

Locations of drilling intrusions through the excavated, waste-filled area of the repository are discretized to the 144 locations in Figure PA-6. Assuming that a drilling intrusion occurs within the excavated area, it is assumed to be equally likely to occur at each of these 144 locations. Thus, the (conditional) probability pL_j that drilling intrusion i will occur at location L_j, j = 1, 2, …, 144, in Figure PA-6 is

$$pL_j = 1/144 = 6.94 \times 10^{-3}. \tag{12}$$

The probabilities pL_j define the part of $\left(\boldsymbol{X}_{st}, \boldsymbol{S}_{st}, \boldsymbol{p}_{st}\right)$ in Section PA.2.2 associated with l_i.

PA-3.5 Penetration of Pressurized Brine

The conceptual models for the Castile Formation include the possibility that pressurized brine reservoirs underlie the repository (Section 6.4.8). The variable b_i is a designator for whether or not the i^{th} drilling intrusion penetrates pressurized brine, where $b_i = 0$ signifies nonpenetration and $b_i = 1$ signifies penetration of pressurized brine. In the CCA PA, the probabilities pB_0 and pB_1 for $b_i = 0$ and $b_i = 1$ were 0.92 and 0.08, respectively (see CCA Section 6.4.12.6). In the CRA-2004 PA, the probability pB_1 is sampled from a uniform distribution ranging from 0.01 to 0.60 (Section 6.4.12.6; see also PBRINE in Table PA-17). The probabilities pB_0 and pB_1 define the part of $\left(\boldsymbol{X}_{st}, \boldsymbol{S}_{st}, \boldsymbol{p}_{st}\right)$ in Section PA-2.2 that corresponds to b_i.

PA-3.6 Plugging Pattern

As presented in Section 6.4.7.2, three borehole plugging patterns are considered in the 2004 PA: (1) p_1 , a full concrete plug through Salado Formation to the Bell Canyon Formation, (2) p_2 , a two plug configuration with concrete plugs at Rustler/Salado interface and Castile/Bell Canyon interface, and (3) p_3 , a three plug configuration with concrete plugs at the Rustler/Salado, Salado/Castile and Castile/Bell Canyon interfaces. The probability that a given drilling intrusion will be sealed with plugging pattern p_j, j = 1, 2, 3, is given by pPL_j , where $pPL_1 = 0.015$, $pPL_2 = 0.696$ and $pPL_3 = 0.289$ (Section 6.4.12.7). The probabilities pPL_j define the part of $\left(\boldsymbol{X}_{st}, \boldsymbol{S}_{st}, \boldsymbol{p}_{st}\right)$ in Section PA-2.2 that corresponds to p_i.

PA-3.7 Activity Level

The waste intended for disposal at the WIPP is represented by 779 distinct waste streams with 693 of these waste streams designated as CH-TRU waste and 86 designated as RH-TRU waste. For the CRA-2004 PA, the 86 separate RH-TRU waste streams are represented by a single, combined RH-TRU waste stream. The activity levels for the waste streams are given in Attachment PAR, Table PAR-50. Each waste container emplaced in the repository contains waste from a single CH-TRU waste stream. Waste packaged in 55-gallon drums is stacked three drums high within the repository. Although waste in other packages (e.g., standard waste boxes, 10 drum overpacks, etc.) may not be stacked three high, the CRA-2004 PA assumes that each drilling intrusion into CH-TRU waste might intersect three different waste streams. In contrast, all RH-TRU waste is represented by a single waste stream, and so each drilling intrusion through RH-TRU waste is assumed to intersect this single waste stream. Attachment MASS (Section MASS.21) examines the sensitivity of PA results to the assumption that three waste streams are intersected by each drilling intrusion into CH-TRU waste.

The vector $\boldsymbol{a}_i$ characterizes the type of waste penetrated by the i$^{\text{th}}$ drilling intrusion. Specifically,

$$\boldsymbol{a}_i = 0 \text{ if } e_i = 0 \tag{13}$$

(i.e., if the i$^{\text{th}}$ drilling intrusion does not penetrate an excavated area of the repository);

$$\boldsymbol{a}_i = 1 \text{ if } e_i = 1 \text{ and RH-TRU is penetrated;} \tag{14}$$

and

$$\boldsymbol{a}_i = [iCH_{i1}, CH_{i2}, iCH_{i3}] \text{ if } e_i = 1 \text{ and CH-TRU is penetrated ,} \tag{15}$$

where iCH_{i1}, iCH_{i2} and iCH_{i3} are integer designators for the CH-TRU waste streams intersected by the i$^{\text{th}}$ drilling intrusion (i.e., each of iCH_{i1}, iCH_{i2} and iCH_{i3} is an integer between 1 and 693).

Whether the i$^{\text{th}}$ intrusion penetrates a nonexcavated or excavated area is determined by the probabilities pE_0 and pE_1 discussed in Section PA-3.4. The type of waste penetrated is determined by the probabilities pCH and pRH. The excavated area used for disposal of CH-TRU waste is 1.115 × 105 m^2 and the area used for disposal of RH-TRU waste is 1.576×10^4 m^2 (Attachment PAR, Table PAR-43), for a total disposal area of aEX = aCH + aRH = 1.273×10^5 m^2. Given that the i$^{\text{th}}$ intrusion penetrates an excavated area, the probabilities pCH and pRH of penetrating CH- and RH-TRU waste are given by

$$pCH = aCH / aEX = \left(1.115 \times 10^5 \ m^2\right) / \left(1.273 \times 10^5 \ m^2\right) = 0.876 \tag{16}$$

$$pCH = aCH / aEX = \left(1.576 \times 10^4 \ m^2\right) / \left(1.273 \times 10^5 \ m^2\right) = 0.124 \,. \tag{17}$$

As indicated in this section, the probabilistic characterization of $\boldsymbol{a}_i$ in $\left(X_{st}, S_{st}, p_{st}\right)$ depends on a number of individual probabilities. Specifically, pE_0 and pE_1 determine whether a nonexcavated or excavated area is penetrated (Section PA-3.4); pCH and pRH determine whether CH- or RH-TRU waste is encountered given penetration of an excavated area; and the individual waste stream probabilities in Attachment PAR, Table PAR-50 determine the specific waste streams iCH_{i1} , iCH_{i2} , and iCH_{i3} encountered given a penetration of CH-TRU waste.

PA-3.8 Mining Time

As presented in Section 6.2.5.2, full mining of known potash reserves within the land withdrawal boundary is assumed to occur at time t_{min}. The occurrence of mining within the land withdrawal boundary in the absence of institutional controls is specified as following a Poisson process with a rate of $\lambda_m = 1 \times 10^{-4}$ yr^{-1}. However, this rate can be reduced by active and passive institutional controls. Specifically, active institutional controls are assumed to result in no possibility of mining for the first 100 years after decommissioning of the WIPP (Section 7.1.4). In the CCA PA, passive institutional controls were assumed to reduce the base mining rate by two orders of magnitude between 100 and 700 years after decommissioning (CCA Section 7.3.4). In the CRA-2004 PA, passive institutional controls do not affect the mining rate (Section 7.3.4). Thus, the mining rate $\lambda_m(t)$ is:

$$\lambda_m(t) = 0 \; yr^{-1} \quad for \; 0 \le t \le 100 \; yrs \tag{18}$$

$$\lambda_m(t) = 1 \times 10^{-4} \; yr^{-1} \quad for \; 100 \le t \le 10{,}000 \; yrs \, , \tag{19}$$

where t is elapsed time since decommissioning of the WIPP. The function $\lambda_m(t)$ defines the part of $(\boldsymbol{X}_{st}, \boldsymbol{S}_{st}, \boldsymbol{p}_{st})$ that corresponds to t_{min}.

In the computational implementation of the analysis, $\lambda_m(t)$ is used to define the distribution of time to mining. The use of $\lambda_m(t)$ to characterize t_{min} is analogous to the use of λ_d to characterize the t_i except that only one mining event is assumed to occur (i.e., $\boldsymbol{x}_{st}$ contains only one value for t_{min}) in consistency with guidance given in 40 CFR Part 194 that mining within the land withdrawal boundary should be assumed to remove all economically viable potash reserves. Due to the 10,000-year regulatory period specified in 40 CFR § 191.13, t_{min} is assumed to be bounded above by 10,000 years in the definition of X_{st}.

PA-3.9 Scenarios and Scenario Probabilities

A scenario is a subset $\mathcal{S}$ of the sample space X_{st} for stochastic uncertainty. More specifically, a scenario is an element $\mathcal{S}$ of the set S_{st} in the probability space $(\boldsymbol{X}_{st}, \boldsymbol{S}_{st}, \boldsymbol{p}_{st})$ for stochastic uncertainty, and the probability of $\mathcal{S}$ is given by $p_{st}(\mathcal{S})$. Thus, a scenario is what is called an event in the usual terminology of probability theory.

Given the complexity of the elements $\boldsymbol{x}_{st}$ of X_{st} (see Equation (3)), many different scenarios can be defined. The computational complexity of the function f in Figure PA-1 limits evaluation to only a few scenarios. As presented in Section 6.3, the CRA-2004 PA considers four fundamental scenarios:

E0 = { $\boldsymbol{x}_{st} : \boldsymbol{x}_{st}$ involves no drilling intrusion through an excavated area of the repository (i.e., n = 0 or $e_i = 0$ in Equation (3) for i = 1, 2, …, n > 0)};

E1 = { $\boldsymbol{x}_{st} : \boldsymbol{x}_{st}$ involves one drilling intrusion through an excavated area of the repository with this intrusion penetrating pressurized brine in the Castile Formation (i.e., $n > 0$ in Equation (3) and there exists exactly one integer i such that $1 \le i \le n$, $e_i = 1$, $b_i = 1$, and $e_j = 0$ for $j \ne i$ and $1 \le j \le n$)};

E2 = { $\boldsymbol{x}_{st} : \boldsymbol{x}_{st}$ involves one drilling intrusion through an excavated area of the repository, with this intrusion not penetrating pressurized brine in the Castile Formation (i.e., $n > 0$ in Equation (3) and there exists exactly one integer i such that $1 \le i \le n$, $e_i = 1$, $b_i = 0$, and $e_j = 0$ for $j \ne i$ and $1 \le j \le n$)};

E1E2 = { $\boldsymbol{x}_{st} : \boldsymbol{x}_{st}$ involves two drilling intrusions through excavated areas of the repository, with the first intrusion not penetrating pressurized brine and the second intrusion penetrating pressurized brine (i.e., $n \ge 2$ in Equation (3) and there exist two integers i, j such that $1 \le i < j \le n$, $e_i = 1$, $b_i = 0$, $e_j = 1$, $b_j = 1$, and $e_k = 0$ for $k \ne i$, j and $1 \le k \le n$)}.

The definitions of the preceding four scenarios are quite simple. In general, scenarios can be defined on the basis of any possible characterization of the properties of the individual elements of $\boldsymbol{x}_{st}$, which can lead to very complex scenario definitions.

The scenarios E0, E1, E2, and E1E2 are elements of S_{st}, and their probabilities are formally represented by $p_{st}(E0)$, $p_{st}(E1)$, $p_{st}(E2)$, and $p_{st}(E1E2)$, with these probabilities deriving from the probability distributions assigned to the individual elements of $\boldsymbol{x}_{st}$. For example, assume that pB_1 takes on its mean value of 0.305 (see Section PA-3.5), the probabilities of the first three scenarios can be calculated exactly:

$$p_{st}(E0) = \exp\left(-\int_a^b pE_1 \lambda_d(t)\,dt\right) = 1.3 \times 10^{-3} \tag{20}$$

$$p_{st}(E1) = \left[\left(\int_a^b pE_1 \lambda_d(t)\,dt\right)^1 \Big/ 1!\right]\left[\exp\left(-\int_a^b pE_1 \lambda_d(t)\,dt\right)\right]\left[pB_1\right] = 2.6 \times 10^{-3} \tag{21}$$

$$p_{st}(E2) = \left[\left(\int_a^b pE_1 \lambda_d(t)\,dt\right)^1 \Big/ 1!\right]\left[\exp\left(-\int_a^b pE_1 \lambda_d(t)\,dt\right)\right]\left[pB_0\right] = 6.0 \times 10^{-3}, \tag{22}$$

where $[a,b] = [100,\ 10{,}000\ yrs]$, $pE_1 = 0.203$ (see Section PA-3.4), $\lambda_d(t)$ is defined in Equation (7), and the probabilities in Equation (21) and Equation (22) are based on the relationship in Equation (8).

The expressions defining $p_{st}(E0)$, $p_{st}(E1)$, and $p_{st}(E2)$ are relatively simple because the scenarios E0, E1, and E2 are relatively simple. The scenario E1E2 is more complex and, as a result, $p_{st}\left(E1E2\right)$ is also more complex. Closed-form formulas for the probabilities of quite complex scenarios can be derived but they are very complicated and involve large numbers of iterated integrals (Helton 1993). Thus, p_{st} can be defined in concept but does not have a simple form that can be easily displayed.

The fundamental scenarios E0, E1, E2, and E1E2 have infinitely many elements because the drilling intrusions and mining events can occur throughout the regulatory period. However, scenarios involving drilling intrusions that occur at specific times will have a probability of zero. For example, the scenario

$$\mathcal{S}=\left\{\mathbf{x}_{st}:\mathbf{x}_{st}=\left[t_1=350\,yr,\ e_1=1,\ l_1,\ b_1=1,\ p_1=2,\ \mathbf{a}_1,\ t_{min}\right]\right\}, \tag{23}$$

where e_1, $\mathbf{a}_1$ and t_{min} are arbitrary, contains infinitely many futures (i.e., infinitely many $\mathbf{x}_{st}$ meet the criteria to belong to $\mathcal{S}$ due to the infinite number of values that l_1, $\mathbf{a}_1$, and t_{min} can assume) and also has a probability of zero (i.e., $p_{st}\left(\mathcal{S}\right)=0$) because t_1 is restricted to a single value. Sets that contain single elements of X_{st} are also scenarios, but such scenarios will typically have a probability of zero; the only single element scenario that has a nonzero probability contains the future that has no drilling intrusions and no mining.

Releases from the repository are calculated (i.e. the function f in Figure PA-1 is evaluated) for a small number of elements belonging to each of the four fundamental scenarios (Sections PA-6.7 and PA-6.8). Releases for an arbitrary element $\mathbf{x}_{st}$ of X_{st} are estimated from the results of the fundamental scenarios (Section PA-6.8); these releases are used to construct CCDFs by Equation (4).

PA-3.10 Historical Review of CCDF Construction

The 1991 and 1992 WIPP PAs used an approach to the construction of the CCDF specified in 40 CFR § 191.13 based on the exhaustive division of X_{st} into a collection of mutually exclusive scenarios $S_{st,i}$, i = 1, 2, …, nS (Helton and Iuzzolino 1993). A probability $p_{st}\left(S_{st,i}\right)$ and a normalized release R_i were then calculated for each scenario $S_{st,i}$ and used to construct the CCDF specified in 40 CFR § 191.13. Due to the complexity of the elements $\mathbf{x}_{st}$ of X_{st} (see Equation (3)), this approach was not used in the CCA PA. In particular, the decomposition of X_{st} into a suitable and defensible collection of scenarios $S_{st,i}$, i = 1, 2, …, nS, is quite difficult. Further, once these scenarios are defined, it is necessary to calculate their probabilities $p_{st}\left(S_{st,i}\right)$, which is also not easy. Although the calculation of the probabilities $p_{st}\left(S_{st,i}\right)$ is difficult, the development of an appropriate and acceptable decomposition of X_{st} into the scenarios $S_{st,i}$ posed a great challenge. Accordingly, the CCA PA used the Monte Carlo approach to CCDF construction indicated in Equation (4), thus avoiding the difficulties associated with decomposing X_{st} into a collection of mutually exclusive scenarios and then calculating the probabilities of these scenarios. The CRA-2004 PA uses the same approach as used in the CCA PA.

PA-4.0 ESTIMATION OF RELEASES

This section describes how releases to the accessible environment are estimated for a particular future in the CRA-2004 PA.

PA-4.1 Results for Specific Futures

The function $f\left(\mathbf{x}_{st}\right)$ (Figure PA-1) estimates the radionuclide releases to the accessible environment associated with each of the possible futures $\mathbf{x}_{st}$ that could occur at the WIPP site over the next 10,000 years. In practice, f is quite complex and is constructed by the models implemented in computer programs used to simulate important processes and releases at the WIPP. In the context of these models, f has the form

$$\begin{aligned} f\left(\mathbf{x}_{st}\right) = {} & f_C\left(\mathbf{x}_{st}\right) + f_{SP}\left[\mathbf{x}_{st}, f_B\left(\mathbf{x}_{st}\right)\right] + f_{DBR}\left[\mathbf{x}_{st}, f_B\left(\mathbf{x}_{st}\right)\right] \\ & + f_{MB}\left[\mathbf{x}_{st}, f_B\left(\mathbf{x}_{st}\right)\right] + f_{DL}\left[\mathbf{x}_{st}, f_B\left(\mathbf{x}_{st}\right)\right] + f_S\left[\mathbf{x}_{st}, f_B\left(\mathbf{x}_{st}\right)\right], \\ & + f_{ST}\left[\mathbf{x}_{st,0}, f_{MF}\left(\mathbf{x}_{st}\right), f_{NP}\left[\mathbf{x}_{st}, f_B\left(\mathbf{x}_{st}\right)\right]\right] \end{aligned} \qquad (24)$$

where

$\mathbf{x}_{st}$ ~ particular future under consideration,

$\mathbf{x}_{st,0}$ ~ future involving no drilling intrusions but a mining event at the same time $t_{\min}$ as in $\mathbf{x}_{st}$,

$f_C\left(\mathbf{x}_{st}\right)$ ~ cuttings and cavings release to accessible environment for $\mathbf{x}_{st}$ calculated with CUTTINGS_S,

$f_B\left(\mathbf{x}_{st}\right)$ ~ two-phase flow in and around the repository calculated for $\mathbf{x}_{st}$ with BRAGFLO; in practice, $f_B\left(\mathbf{x}_{st}\right)$ is a vector containing a large amount of information, including pressure and brine saturation in various geologic members,

$f_{SP}\left[\mathbf{x}_{st}, f_B\left(\mathbf{x}_{st}\right)\right]$ ~ spallings release to accessible environment for $\mathbf{x}_{st}$ calculated with the spallings model contained in CUTTINGS_S; this calculation requires repository conditions calculated by $f_B\left(\mathbf{x}_{st}\right)$ as input,

$f_{DBR}\left[\mathbf{x}_{st}, f_B\left(\mathbf{x}_{st}\right)\right]$ ~ direct brine release to accessible environment for $\mathbf{x}_{st}$ also calculated with BRAGFLO; this calculation requires repository conditions calculated by $f_B\left(\mathbf{x}_{st}\right)$ as input,

$f_{MB}\left[\mathbf{x}_{st}, f_B\left(\mathbf{x}_{st}\right)\right]$ ~ release through anhydrite marker beds to accessible environment for $\mathbf{x}_{st}$ calculated with NUTS; this calculation requires flows in and around the repository calculated by $f_B\left(\mathbf{x}_{st}\right)$ as input,

$f_{DL}\left[\mathbf{x}_{st}, f_B\left(\mathbf{x}_{st}\right)\right]$ ~ release through Dewey Lake Red Beds to accessible environment for $\mathbf{x}_{st}$ calculated with NUTS; this calculation requires flows in and around the repository calculated by $f_B\left(\mathbf{x}_{st}\right)$ as input,

$f_S\left[\mathbf{x}_{st}, f_B\left(\mathbf{x}_{st}\right)\right]$ ~ release to land surface due to brine flow up a plugged borehole for $\mathbf{x}_{st}$ calculated with NUTS or PANEL; this calculation requires flows in and around the repository calculated by $f_B\left(\mathbf{x}_{st}\right)$ as input,

$f_{MF}\left(\mathbf{x}_{st,0}\right)$ ~ flow field in the Culebra calculated for $\mathbf{x}_{st,0}$ with MODFLOW,

$f_{NP}\left[\mathbf{x}_{st}, f_B\left(\mathbf{x}_{st}\right)\right]$ ~ release to Culebra for $\mathbf{x}_{st}$ calculated with NUTS or PANEL as appropriate; this calculation requires flows in and around the repository calculated by $f_B\left(\mathbf{x}_{st}\right)$ as input, and

$f_{ST}\left[\mathbf{x}_{st,0}, f_{MF}\left(\mathbf{x}_{st,0}\right), f_{NP}\left[\mathbf{x}_{st}, f_B\left(\mathbf{x}_{st}\right)\right]\right]$ ~ groundwater transport release through Culebra to accessible environment calculated with SECOTP2D.This calculation requires MODFLOW results (i.e., $f_{MF}\left(\mathbf{x}_{st,0}\right)$) and NUTS or PANEL results (i.e., $f_{NP}\left[\mathbf{x}_{st}, f_B\left(\mathbf{x}_{st}\right)\right]$ as input; $\mathbf{x}_{st,0}$ is used as an argument to f_{ST} because drilling intrusions are assumed to cause no perturbations to the flow field in the Culebra.

The remainder of this section describes the mathematical structure of the mechanistic models that underlie the component functions of f in Equation (24).

The Monte Carlo CCDF construction procedure, implemented in the code CCDFGF (WIPP PA 2003a), uses a sample of size nS = 10,000 in the CRA-2004 PA. The individual programs that estimate releases do not run fast enough to allow this number of evaluations of f. As a result, a two-step procedure is being used to evaluate f in the calculation of the integral in Equation (4). First, f and its component functions are evaluated with the procedures (i.e., models) described in this section for a group of preselected futures. Second, values of $f\left(\mathbf{x}_{st,i}\right)$ for the randomly selected futures $\mathbf{x}_{st,i}$ used in the numerical evaluation of the integral in Equation (4) are then constructed from results obtained in the first step. These constructions are described in Sections PA-6.7 and PA-6.8, and produce the evaluations of f that are actually used in Equation (4).

For notational simplicity, the functions on the right hand side of Equation (24) will typically be written with only $\mathbf{x}_{st}$ as an argument (e.g., $f_{SP}\left(\mathbf{x}_{st}\right)$ will be used instead of $f_{SP}\left[\mathbf{x}_{st}, f_B\left(\mathbf{x}_{st}\right)\right]$). However, the underlying dependency on the other arguments will still be present.

The major topics considered in this chapter are two-phase flow in the vicinity of the repository as modeled by BRAGFLO (i.e., f_B) (Section PA-4.2), radionuclide transport in the vicinity of the repository as modeled by NUTS (i.e., f_{MB}, f_{DL}, f_S, f_{NP}) (Section PA-4.3), radionuclide transport in the vicinity of the repository as modeled by PANEL (i.e., f_S, f_{NP}) (Section PA-4.4), cuttings and cavings releases to the surface as modeled by CUTTINGS_S (i.e., f_C) (Section PA-4.5), spallings releases to the surface as modeled by DRSPALL and CUTTINGS_S (i.e., f_{SP}) (Section PA-4.6), direct brine releases to the surface as modeled by BRAGFLO (i.e., f_{DBR}) (Section PA-4.7), brine flow in the Culebra as modeled by MODFLOW (i.e., f_{MF}) (Section PA-4.8), and radionuclide transport in the Culebra as modeled by SECOTP2D (i.e., f_{ST}) (Section PA-4.9).

PA-4.2 Two-Phase Flow: BRAGFLO

Quantification of the effects of gas and brine flow on radionuclide transport from the repository requires use of a two-phase (brine and gas) flow code. For the CRA-2004 PA, the DOE uses the two-phase flow code BRAGFLO to simulate gas and brine flow in and around the repository (WIPP PA 2003b). Additionally, the BRAGFLO code incorporates the effects of disposal room consolidation and closure, gas generation, and rock fracturing in response to gas pressure. This section describes the mathematical models on which BRAGFLO is based, the representation of the repository in the model, and the numerical techniques employed in the solution.

PA-4.2.1 Mathematical Description

Two-phase flow in the vicinity of the repository is represented by the following system of two conservation equations, two constraint equations, and three equations of state:

Gas Conservation

$$\nabla \bullet \left[\frac{\alpha \rho_g \mathbf{K}_g k_{rg}}{\mu_g}\left(\nabla p_g + \rho_g g \nabla h\right)\right] + \alpha q_{wg} + \alpha q_{rg} = \alpha \frac{\partial\left(\phi \rho_g S_g\right)}{\partial t}, \tag{25a}$$

Brine Conservation

$$\nabla \bullet \left[\frac{\alpha \rho_b \mathbf{K}_b k_{rb}}{\mu_b}\left(\nabla p_b + \rho_b g \nabla h\right)\right] + \alpha q_{wb} + \alpha q_{rb} = \alpha \frac{\partial\left(\phi \rho_b S_b\right)}{\partial t}, \tag{25b}$$

Saturation Constraint

$$S_g + S_b = 1, \tag{25c}$$

Capillary Pressure Constraint

$$p_C = p_g - p_b = f\left(S_b\right), \tag{25d}$$

Gas Density

ρ_g (determined by Redlich-Kwong-Soave equation of state; see Equation (46)), (25e)

Brine Density

$$\rho_b = \rho_0 \exp\left[\beta_b\left(\rho_b - \rho_{b0}\right)\right], \text{ and} \tag{25f}$$

Formation Porosity

$$\phi_b = \phi_0 \exp\left[\beta_f\left(\rho_b - \rho_{b0}\right)\right], \tag{25g}$$

where

g = acceleration due to gravity (m/s^2)

h = vertical distance from a reference location (m)

K_l = permeability tensor (m^2) for fluid l (l = g ~ gas, l = b ~ brine)

k_{rl} = relative permeability (dimensionless) to fluid l

p_C = capillary pressure (Pa)

p_l = pressure of fluid l (Pa)

q_{rl} = rate of production (or consumption, if negative) of fluid l due to chemical reaction (kg/m^3 s)

q_{wl} = rate of injection (or removal, if negative) of fluid l (kg/m^3 s)

S_l = saturation of fluid l (dimensionless)

t = time (s)

α = geometry factor (m)

ρ_l = density of fluid l (kg/m^3)

μ_l = viscosity of fluid l (Pa s)

ϕ = porosity (dimensionless)

ϕ_0 = reference (i.e., initial) porosity (dimensionless)

p_{b0} = reference (i.e., initial) brine pressure (Pa), constant in Equation (25f) and spatially variable in Equation (25g)

ρ_0 = reference (i.e., initial) brine density (kg/m^3)

β_f = pore compressibility (Pa^{-1})

β_b = brine compressibility (Pa^{-1}).

The conservation equations are valid in one (i.e., $\nabla = [\partial/\partial \boldsymbol{x}]$), two (i.e., $\nabla = [\partial/\partial \boldsymbol{x}, \partial/\partial \boldsymbol{y}]$) and three (i.e., $\nabla = [\partial/\partial \boldsymbol{x}, \partial/\partial \boldsymbol{y}, \partial/\partial \boldsymbol{z}]$) dimensions. In the CRA-2004 PA, the preceding system of equations is used to model two-phase fluid flow within the two-dimensional region shown in Figure PA-8. The details of this system are now discussed.

The α term in Equation (25a) and Equation (25b) is a dimension-dependent geometry factor and is specified by

α = area normal to flow direction in one-dimensional flow (i.e., $\Delta y \Delta z$; units = m^2),

= thickness normal to flow plane in two-dimensional flow (i.e., Δz; units = m),

= 1 in three-dimensional flow (dimensionless). (26)

The CRA-2004 PA uses a two-dimensional geometry for computation of two-phase flow in the vicinity of the repository, and as a result, α is the thickness of the modeled region (i.e., Δz) normal to the flow plane (Figure PA-8). Due to the use of the two-dimensional grid in Figure PA-8, α is spatially dependent, with the values used for α defined in the column labeled “Δz .” Specifically, α increases with distance away from the repository edge in both directions to incorporate the increasing pore volume through which fluid flow occurs. The method used in the CRA-2004 PA, called rectangular flaring, is illustrated in Figure PA-9 and ensures that the total volume surrounding the repository is conserved in the numerical grid. The equations and method used to determine α for the grid shown in Figure PA-8 are described in detail by Stein (2002a).

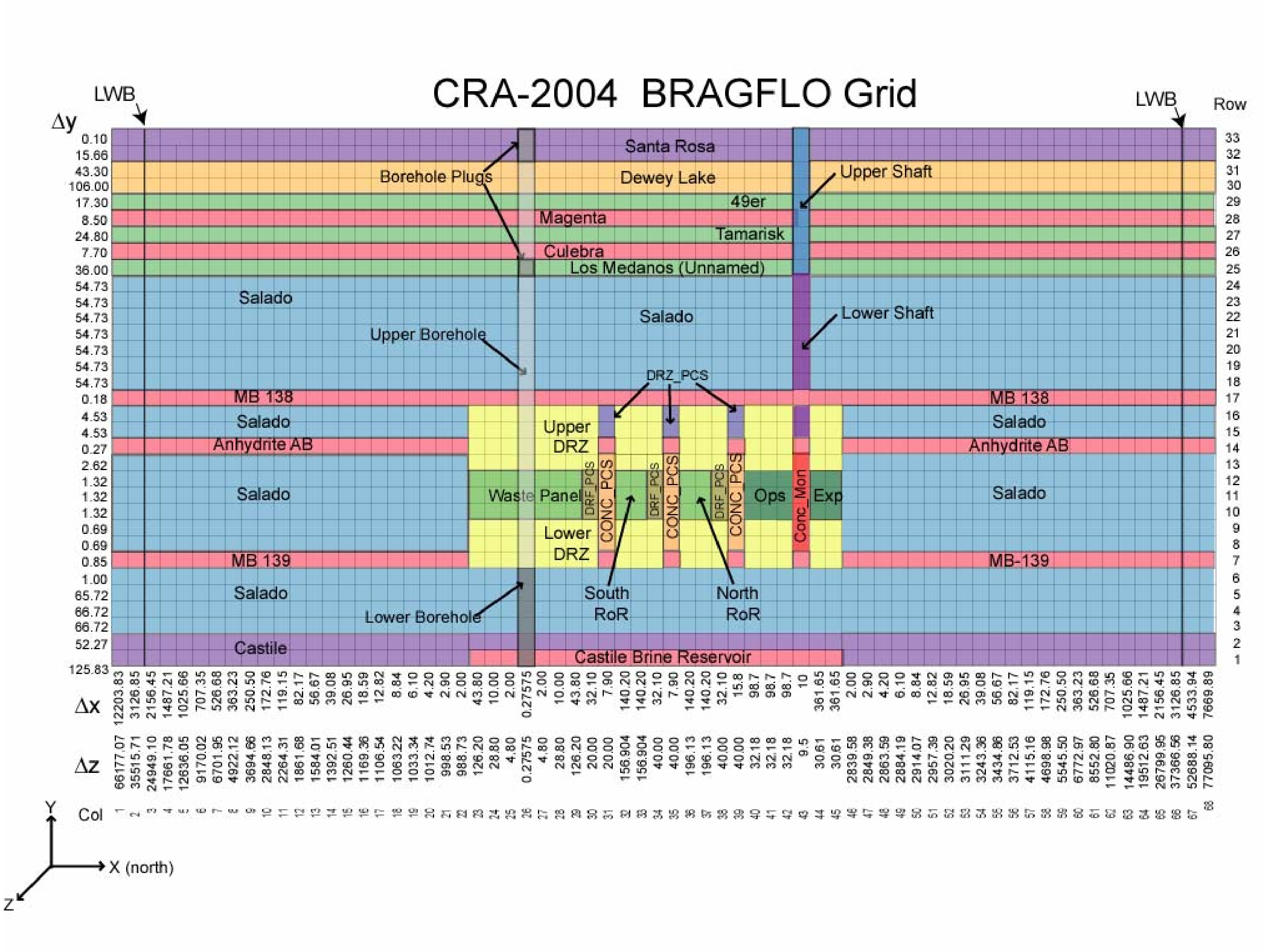

Figure PA-8. Computational Grid Used in BRAGFLO in the CRA-2004 PA.

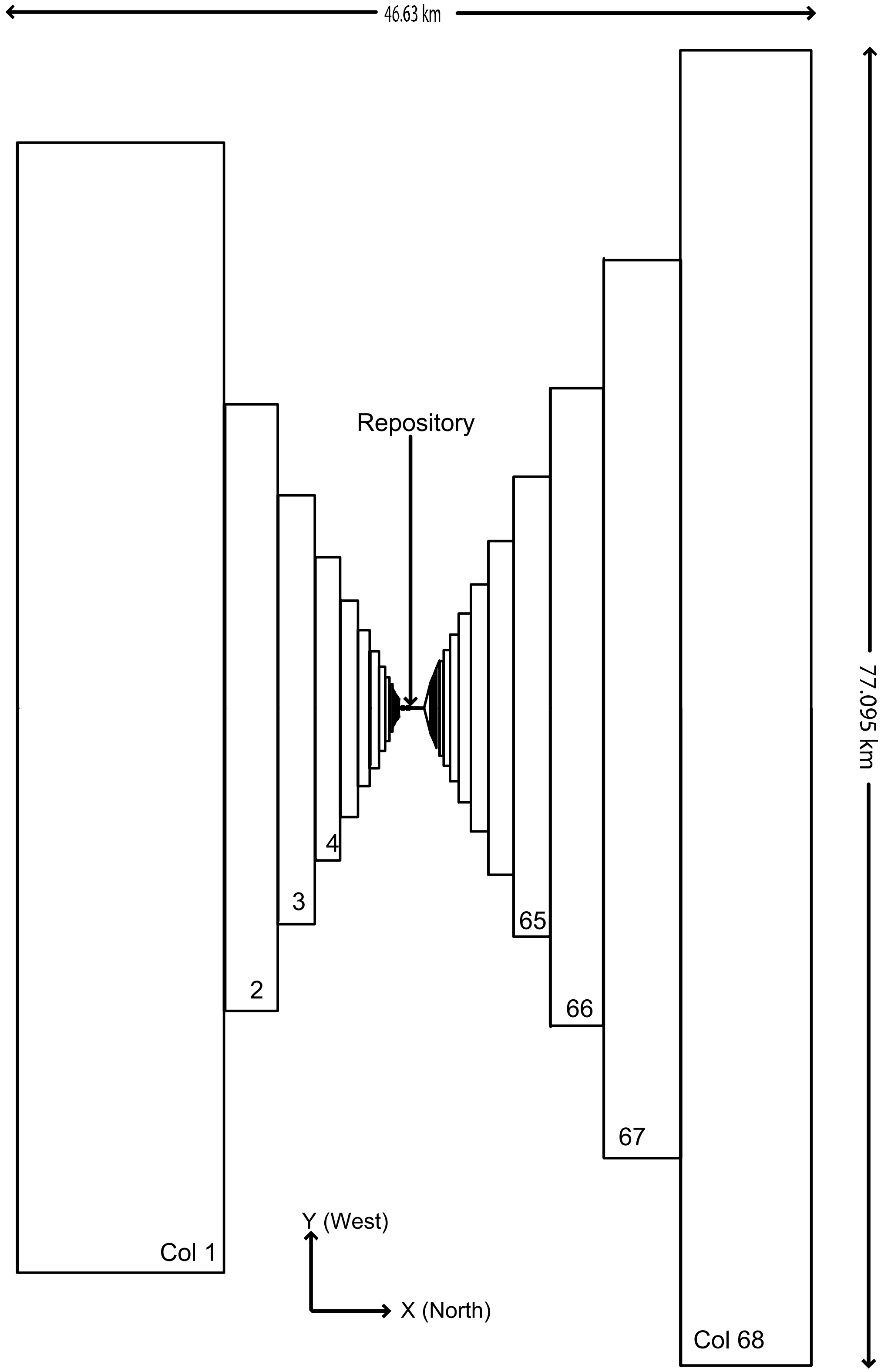

Figure PA-9. Definition of Element Depth in BRAGFLO Grid in the CRA-2004 PA.

The h term in Equation (25a) and Equation (25b) defines vertical distance from a reference point. In the CRA-2004 PA, this reference point is taken to be the center of MB 139 at the location of the shaft (i.e., $\left(x_{ref}, y_{ref}\right) = \left(23664.9\ m,\ 378.685\ m\right)$, which is the center of cell 1266 in Figure PA-10). Specifically, h is defined by

$$h\left(x, y\right) = \left(x - x_{ref}\right)\sin\theta + \left(y - y_{ref}\right)\cos\theta, \tag{27}$$

where θ is the inclination of the formation in which the point $\left(x, y\right)$ is located. In the CRA-2004 PA, the Salado Formation is modeled as having an inclination of 1° from north to south, and all other formations are modeled as being horizontal. Thus, $\theta = 1°$ for points within the Salado, and $\theta = 0°$ otherwise. Treating the Salado as an inclined formation and treating the Castile Formation, Castile brine reservoir, Rustler Formation, and overlying units as horizontal creates discontinuities in the grid at the lower and upper boundaries of the Salado. However, this treatment does not create a computational problem, since the Salado is isolated from vertical flow; its upper boundary adjoins the impermeable Los Medaños Member (formerly referred to as the Unnamed Member) at the base of the Rustler Formation, and its lower boundary adjoins the impermeable Castile Formation.

In the solution of Equation (25), S_b and S_g are functions of location and time. Thus, p_C, k_{rb} and k_{rg} are functions of the form $p_C\left(x, y, t\right)$, $k_{rb}\left(x, y, t\right)$, and $k_{rg}\left(x, y, t\right)$. In the computational implementation of the solution of the preceding equations, flow of phase l out of a computational cell (Figure PA-10) cannot occur when $S_l\left(x, y, t\right) \le S_{lr}\left(x, y, t\right)$, where S_{lr} denotes the residual saturation for phase l. The values used for S_{lr} , l = b, g are summarized in Table PA-2.

Values for ϕ_0 and β_f (Equation (25g)) are also given in Table PA-2. Initial porosity ϕ_0 for the DRZ is a function of the uncertain parameter for initial halite porosity ϕ_{0H} (HALPOR; see Table PA-17) and is given by Martell (1996a, Chapter 4; Bean et al. 1996)

$$\phi_0 = \phi_{0H} + 0.0029\ . \tag{28}$$

This representation is used because the DRZ and halite porosities are correlated, with the high, low, and median porosity values for the DRZ being 0.0029 higher than the corresponding undisturbed halite values. Initial porosity ϕ_0 of the Castile brine reservoir is correlated to the uncertain sampled parameter for bulk compressibility (BPCOMP; see Table PA-17), according to the following relationship:

$$\phi_0 = \frac{BPCOMP}{1.0823 \times 10^{-10}}, \tag{29}$$

where 1.0860×10^{-10} is a scaling constant that ensures that the productivity ratio, PR, remains constant at 2.0×10^{-3} m^3/Pa. The productivity ratio PR is computed by

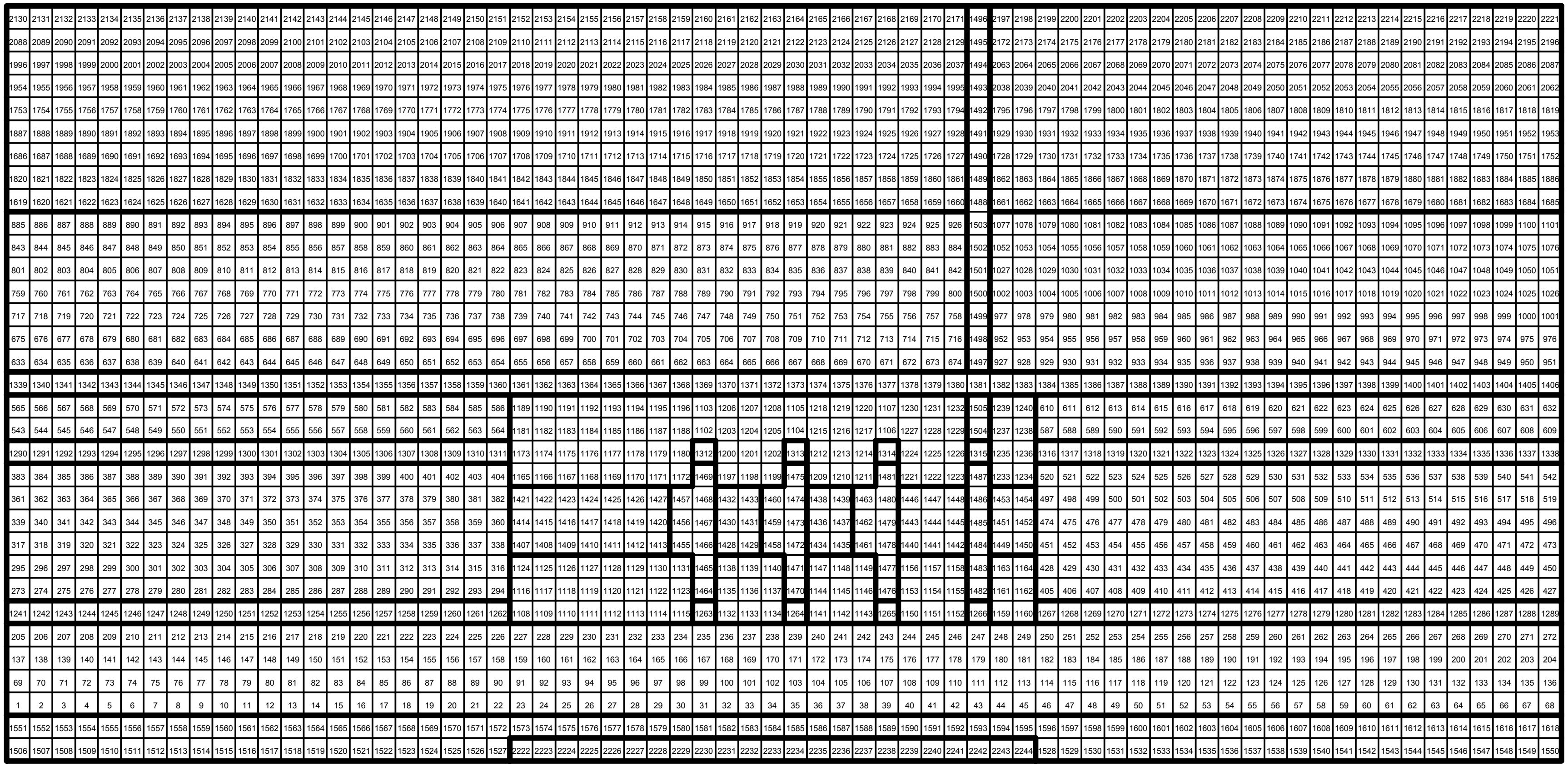

2130	2131	2132	2133	2134	2135	2136	2137	2138	2139	2140	2141	2142	2143	2144	2145	2146	2147	2148	2149	2150	2151	2152	2153	2154	2155	2156	2157	2158	2159	2160	2161	2162	2163	2164	2165	2166	2167	2168	2169	2170	2171	1496	2197	2198	2199	2200	2201	2202	2203	2204	2205	2206	2207	2208	2209	2210	2211	2212	2213	2214	2215	2216	2217	2218	2219	2220	2221
2088	2089	2090	2091	2092	2093	2094	2095	2096	2097	2098	2099	2100	2101	2102	2103	2104	2105	2106	2107	2108	2109	2110	2111	2112	2113	2114	2115	2116	2117	2118	2119	2120	2121	2122	2123	2124	2125	2126	2127	2128	2129	1495	2172	2173	2174	2175	2176	2177	2178	2179	2180	2181	2182	2183	2184	2185	2186	2187	2188	2189	2190	2191	2192	2193	2194	2195	2196
1996	1997	1998	1999	2000	2001	2002	2003	2004	2005	2006	2007	2008	2009	2010	2011	2012	2013	2014	2015	2016	2017	2018	2019	2020	2021	2022	2023	2024	2025	2026	2027	2028	2029	2030	2031	2032	2033	2034	2035	2036	2037	1494	2063	2064	2065	2066	2067	2068	2069	2070	2071	2072	2073	2074	2075	2076	2077	2078	2079	2080	2081	2082	2083	2084	2085	2086	2087
1954	1955	1956	1957	1958	1959	1960	1961	1962	1963	1964	1965	1966	1967	1968	1969	1970	1971	1972	1973	1974	1975	1976	1977	1978	1979	1980	1981	1982	1983	1984	1985	1986	1987	1988	1989	1990	1991	1992	1993	1994	1995	1493	2038	2039	2040	2041	2042	2043	2044	2045	2046	2047	2048	2049	2050	2051	2052	2053	2054	2055	2056	2057	2058	2059	2060	2061	2062
1753	1754	1755	1756	1757	1758	1759	1760	1761	1762	1763	1764	1765	1766	1767	1768	1769	1770	1771	1772	1773	1774	1775	1776	1777	1778	1779	1780	1781	1782	1783	1784	1785	1786	1787	1788	1789	1790	1791	1792	1793	1794	1492	1795	1796	1797	1798	1799	1800	1801	1802	1803	1804	1805	1806	1807	1808	1809	1810	1811	1812	1813	1814	1815	1816	1817	1818	1819
1887	1888	1889	1890	1891	1892	1893	1894	1895	1896	1897	1898	1899	1900	1901	1902	1903	1904	1905	1906	1907	1908	1909	1910	1911	1912	1913	1914	1915	1916	1917	1918	1919	1920	1921	1922	1923	1924	1925	1926	1927	1928	1491	1929	1930	1931	1932	1933	1934	1935	1936	1937	1938	1939	1940	1941	1942	1943	1944	1945	1946	1947	1948	1949	1950	1951	1952	1953
1686	1687	1688	1689	1690	1691	1692	1693	1694	1695	1696	1697	1698	1699	1700	1701	1702	1703	1704	1705	1706	1707	1708	1709	1710	1711	1712	1713	1714	1715	1716	1717	1718	1719	1720	1721	1722	1723	1724	1725	1726	1727	1490	1728	1729	1730	1731	1732	1733	1734	1735	1736	1737	1738	1739	1740	1741	1742	1743	1744	1745	1746	1747	1748	1749	1750	1751	1752
1820	1821	1822	1823	1824	1825	1826	1827	1828	1829	1830	1831	1832	1833	1834	1835	1836	1837	1838	1839	1840	1841	1842	1843	1844	1845	1846	1847	1848	1849	1850	1851	1852	1853	1854	1855	1856	1857	1858	1859	1860	1861	1489	1862	1863	1864	1865	1866	1867	1868	1869	1870	1871	1872	1873	1874	1875	1876	1877	1878	1879	1880	1881	1882	1883	1884	1885	1886
1619	1620	1621	1622	1623	1624	1625	1626	1627	1628	1629	1630	1631	1632	1633	1634	1635	1636	1637	1638	1639	1640	1641	1642	1643	1644	1645	1646	1647	1648	1649	1650	1651	1652	1653	1654	1655	1656	1657	1658	1659	1660	1488	1661	1662	1663	1664	1665	1666	1667	1668	1669	1670	1671	1672	1673	1674	1675	1676	1677	1678	1679	1680	1681	1682	1683	1684	1685
885	886	887	888	889	890	891	892	893	894	895	896	897	898	899	900	901	902	903	904	905	906	907	908	909	910	911	912	913	914	915	916	917	918	919	920	921	922	923	924	925	926	1503	1077	1078	1079	1080	1081	1082	1083	1084	1085	1086	1087	1088	1089	1090	1091	1092	1093	1094	1095	1096	1097	1098	1099	1100	1101
843	844	845	846	847	848	849	850	851	852	853	854	855	856	857	858	859	860	861	862	863	864	865	866	867	868	869	870	871	872	873	874	875	876	877	878	879	880	881	882	883	884	1502	1052	1053	1054	1055	1056	1057	1058	1059	1060	1061	1062	1063	1064	1065	1066	1067	1068	1069	1070	1071	1072	1073	1074	1075	1076
801	802	803	804	805	806	807	808	809	810	811	812	813	814	815	816	817	818	819	820	821	822	823	824	825	826	827	828	829	830	831	832	833	834	835	836	837	838	839	840	841	842	1501	1027	1028	1029	1030	1031	1032	1033	1034	1035	1036	1037	1038	1039	1040	1041	1042	1043	1044	1045	1046	1047	1048	1049	1050	1051
759	760	761	762	763	764	765	766	767	768	769	770	771	772	773	774	775	776	777	778	779	780	781	782	783	784	785	786	787	788	789	790	791	792	793	794	795	796	797	798	799	800	1500	1002	1003	1004	1005	1006	1007	1008	1009	1010	1011	1012	1013	1014	1015	1016	1017	1018	1019	1020	1021	1022	1023	1024	1025	1026
717	718	719	720	721	722	723	724	725	726	727	728	729	730	731	732	733	734	735	736	737	738	739	740	741	742	743	744	745	746	747	748	749	750	751	752	753	754	755	756	757	758	1499	977	978	979	980	981	982	983	984	985	986	987	988	989	990	991	992	993	994	995	996	997	998	999	1000	1001
675	676	677	678	679	680	681	682	683	684	685	686	687	688	689	690	691	692	693	694	695	696	697	698	699	700	701	702	703	704	705	706	707	708	709	710	711	712	713	714	715	716	1498	952	953	954	955	956	957	958	959	960	961	962	963	964	965	966	967	968	969	970	971	972	973	974	975	976
633	634	635	636	637	638	639	640	641	642	643	644	645	646	647	648	649	650	651	652	653	654	655	656	657	658	659	660	661	662	663	664	665	666	667	668	669	670	671	672	673	674	1497	927	928	929	930	931	932	933	934	935	936	937	938	939	940	941	942	943	944	945	946	947	948	949	950	951
1339	1340	1341	1342	1343	1344	1345	1346	1347	1348	1349	1350	1351	1352	1353	1354	1355	1356	1357	1358	1359	1360	1361	1362	1363	1364	1365	1366	1367	1368	1369	1370	1371	1372	1373	1374	1375	1376	1377	1378	1379	1380	1381	1382	1383	1384	1385	1386	1387	1388	1389	1390	1391	1392	1393	1394	1395	1396	1397	1398	1399	1400	1401	1402	1403	1404	1405	1406
565	566	567	568	569	570	571	572	573	574	575	576	577	578	579	580	581	582	583	584	585	586	1189	1190	1191	1192	1193	1194	1195	1196	1103	1206	1207	1208	1105	1218	1219	1220	1107	1230	1231	1232	1505	1239	1240	610	611	612	613	614	615	616	617	618	619	620	621	622	623	624	625	626	627	628	629	630	631	632
543	544	545	546	547	548	549	550	551	552	553	554	555	556	557	558	559	560	561	562	563	564	1181	1182	1183	1184	1185	1186	1187	1188	1102	1203	1204	1205	1104	1215	1216	1217	1106	1227	1228	1229	1504	1237	1238	587	588	589	590	591	592	593	594	595	596	597	598	599	600	601	602	603	604	605	606	607	608	609
1290	1291	1292	1293	1294	1295	1296	1297	1298	1299	1300	1301	1302	1303	1304	1305	1306	1307	1308	1309	1310	1311	1173	1174	1175	1176	1177	1178	1179	1180	1312	1200	1201	1202	1313	1212	1213	1214	1314	1224	1225	1226	1315	1235	1236	1316	1317	1318	1319	1320	1321	1322	1323	1324	1325	1326	1327	1328	1329	1330	1331	1332	1333	1334	1335	1336	1337	1338
383	384	385	386	387	388	389	390	391	392	393	394	395	396	397	398	399	400	401	402	403	404	1165	1166	1167	1168	1169	1170	1171	1172	1469	1197	1198	1199	1475	1209	1210	1211	1481	1221	1222	1223	1487	1233	1234	520	521	522	523	524	525	526	527	528	529	530	531	532	533	534	535	536	537	538	539	540	541	542
361	362	363	364	365	366	367	368	369	370	371	372	373	374	375	376	377	378	379	380	381	382	1421	1422	1423	1424	1425	1426	1427	1457	1468	1432	1433	1460	1474	1438	1439	1463	1480	1446	1447	1448	1486	1453	1454	497	498	499	500	501	502	503	504	505	506	507	508	509	510	511	512	513	514	515	516	517	518	519
339	340	341	342	343	344	345	346	347	348	349	350	351	352	353	354	355	356	357	358	359	360	1414	1415	1416	1417	1418	1419	1420	1456	1467	1430	1431	1459	1473	1436	1437	1462	1479	1443	1444	1445	1485	1451	1452	474	475	476	477	478	479	480	481	482	483	484	485	486	487	488	489	490	491	492	493	494	495	496
317	318	319	320	321	322	323	324	325	326	327	328	329	330	331	332	333	334	335	336	337	338	1407	1408	1409	1410	1411	1412	1413	1455	1466	1428	1429	1458	1472	1434	1435	1461	1478	1440	1441	1442	1484	1449	1450	451	452	453	454	455	456	457	458	459	460	461	462	463	464	465	466	467	468	469	470	471	472	473
295	296	297	298	299	300	301	302	303	304	305	306	307	308	309	310	311	312	313	314	315	316	1124	1125	1126	1127	1128	1129	1130	1131	1465	1138	1139	1140	1471	1147	1148	1149	1477	1156	1157	1158	1483	1163	1164	428	429	430	431	432	433	434	435	436	437	438	439	440	441	442	443	444	445	446	447	448	449	450
273	274	275	276	277	278	279	280	281	282	283	284	285	286	287	288	289	290	291	292	293	294	1116	1117	1118	1119	1120	1121	1122	1123	1464	1135	1136	1137	1470	1144	1145	1146	1476	1153	1154	1155	1482	1161	1162	405	406	407	408	409	410	411	412	413	414	415	416	417	418	419	420	421	422	423	424	425	426	427
1241	1242	1243	1244	1245	1246	1247	1248	1249	1250	1251	1252	1253	1254	1255	1256	1257	1258	1259	1260	1261	1262	1108	1109	1110	1111	1112	1113	1114	1115	1263	1132	1133	1134	1264	1141	1142	1143	1265	1150	1151	1152	1266	1159	1160	1267	1268	1269	1270	1271	1272	1273	1274	1275	1276	1277	1278	1279	1280	1281	1282	1283	1284	1285	1286	1287	1288	1289
205	206	207	208	209	210	211	212	213	214	215	216	217	218	219	220	221	222	223	224	225	226	227	228	229	230	231	232	233	234	235	236	237	238	239	240	241	242	243	244	245	246	247	248	249	250	251	252	253	254	255	256	257	258	259	260	261	262	263	264	265	266	267	268	269	270	271	272
137	138	139	140	141	142	143	144	145	146	147	148	149	150	151	152	153	154	155	156	157	158	159	160	161	162	163	164	165	166	167	168	169	170	171	172	173	174	175	176	177	178	179	180	181	182	183	184	185	186	187	188	189	190	191	192	193	194	195	196	197	198	199	200	201	202	203	204
69	70	71	72	73	74	75	76	77	78	79	80	81	82	83	84	85	86	87	88	89	90	91	92	93	94	95	96	97	98	99	100	101	102	103	104	105	106	107	108	109	110	111	112	113	114	115	116	117	118	119	120	121	122	123	124	125	126	127	128	129	130	131	132	133	134	135	136
1	2	3	4	5	6	7	8	9	10	11	12	13	14	15	16	17	18	19	20	21	22	23	24	25	26	27	28	29	30	31	32	33	34	35	36	37	38	39	40	41	42	43	44	45	46	47	48	49	50	51	52	53	54	55	56	57	58	59	60	61	62	63	64	65	66	67	68
1551	1552	1553	1554	1555	1556	1557	1558	1559	1560	1561	1562	1563	1564	1565	1566	1567	1568	1569	1570	1571	1572	1573	1574	1575	1576	1577	1578	1579	1580	1581	1582	1583	1584	1585	1586	1587	1588	1589	1590	1591	1592	1593	1594	1595	1596	1597	1598	1599	1600	1601	1602	1603	1604	1605	1606	1607	1608	1609	1610	1611	1612	1613	1614	1615	1616	1617	1618
1506	1507	1508	1509	1510	1511	1512	1513	1514	1515	1516	1517	1518	1519	1520	1521	1522	1523	1524	1525	1526	1527	2222	2223	2224	2225	2226	2227	2228	2229	2230	2231	2232	2233	2234	2235	2236	2237	2238	2239	2240	2241	2242	2243	2244	1528	1529	1530	1531	1532	1533	1534	1535	1536	1537	1538	1539	1540	1541	1542	1543	1544	1545	1546	1547	1548	1549	1550

Figure PA-10. Identification of Individual Cells in BRAGFLO Grid in the CRA-2004 PA.

Table PA-2. Parameter Values Used in Representation of Two Phase Flow

Region	Material	Material Description	Brooks-Corey Pore Distribution λ	Threshold Pressure Linear Parameter a	Threshold Pressure Exponential Parameter η	Residual Brine Saturation S_{br}	Residual Gas Saturation S_{gr}	Porosity ϕ_0	Pore Compressibility β_f	Intrinsic Permeability k, m2
Salado	S_HALITE	Undisturbed halite	0.7	0.56	–0.346	0.3	0.2	HALPOR1	f(HALCOMP1)3	10x, x = HALPRM1
Upper DRZ	DRZ_0	Disturbed rock zone, –5 to 0 years	0.7	0.0	0.0	0.0	0.0	f(HALPOR1)2	f(HALCOMP1)3	9.999999 × 10–18
	DRZ_1	Disturbed rock zone, 0 to 10,000 years	0.7	0.0	0.0	0.0	0.0	f(HALPOR1)2	f(HALCOMP1)3	10x, x = DRZPRM1
Lower DRZ	DRZ_0	Disturbed rock zone, –5 to 0 years	0.7	0.0	0.0	0.0	0.0	f(HALPOR1)2	f(HALCOMP1)3	9.999999 × 10–18
	DRZ_1	Disturbed rock zone, 0 to 10,000 years	0.7	0.0	0.0	0.0	0.0	f(HALPOR1)2	f(HALCOMP1)3	10x, x = DRZPRM1
MB 138	S_MB138	Anhydrite marker bed in Salado Formation	ANHBCEXP1	0.26	–0.348	ANRBSAT1	ANRGSSAT1	0.011	f(ANHCOMP1)3	10x, x = ANHPRM1
Anhydrite AB	S_ANH_AB	Anhydrite layers a and b in Salado Formation	ANHBCEXP1	0.26	–0.348	ANRBSAT1	ANRGSSAT1	0.011	f(ANHCOMP1)3	10x, x = ANHPRM1
MB 139	S_MB139	Anhydrite marker bed in Salado Formation	ANHBCEXP1	0.26	–0.348	ANRBSAT1	ANRGSSAT1	0.011	f(ANHCOMP1)3	10x, x = ANHPRM1
Waste Panel	CAVITY_1	Single waste panel, –5 to 0 years	0.7	0.0	0.0	0.0	0.0	1.0	0.0	1.0 × 10–10
	WAS_AREA	Single waste panel, 0 to 10,000 years	2.89	0.0	0.0	WRBRNSAT1	WRGSSAT1	0.8485	0.0	2.4 × 10–13
South RoR	CAVITY_2	Rest of repository, –5 to 0 years	0.7	0.0	0.0	0.0	0.0	1.0	0.0	1.0 × 10–10
	REPOSIT	Rest of repository, 0 to 10,000 years	2.89	0.0	0.0	WRBRNSAT1	WRGSSAT1	0.848 5	0.0	2.4 × 10–13
North RoR	CAVITY_2	Rest of repository, –5 to 0 years	0.7	0.0	0.0	0.0	0.0	1.0	0.0	1.0 × 10–10
	REPOSIT	Rest of repository, 0 to 10,000 years	2.89	0.0	0.0	WRBRNSAT1	WRGSSAT1	0.848 5	0.0	2.4 × 10–13
Ops	CAVITY_3	Operations area, –5 to 0 years	0.7	0.0	0.0	0.0	0.0	1.0	0.0	1.0 × 10–10
	OPS_AREA	Operations area, 0 to 10,000 years	0.7	0.0	0.0	0.0	0.0	0.18	0.0	1.0 × 10–11

Table PA-2. Parameter Values Used in Representation of Two Phase Flow — Continued

Region	Material	Material Description	Brooks-Corey Pore Distribution λ	Threshold Pressure Linear Parameter a	Threshold Pressure Exponential Parameter η	Residual Brine Saturation S_{br}	Residual Gas Saturation S_{gr}	Porosity ϕ_0	Pore Compressibility β_f	Intrinsic Permeability k, m2
Exp	CAVITY_3	Experimental area, –5 to 0 years	0.7	0.0	0.0	0.0	0.0	1.0	0.0	1.0 × 10–10
	EXP_AREA	Experimental area, 0 to 10,000 years	0.7	0.0	0.0	0.0	0.0	0.18	0.0	1.0 × 10–11
Castile	IMPERM_Z	Castile Formation	0.7	0.0	0.0	0.0	0.0	0.005	0.0	9.999999 × 10–36
Castile Brine Reservoir	CASTILER	Brine Reservoir in Castile Formation	0.7	0.56	–0.346	0.2	0.2	f(BPCOMP 1)4	f(BPCOMP 1)3	10x, x = BPPRM1
Culebra	CULEBRA	Culebra Member of Rustler Formation	0.6436	0.26	–0.348	0.08363	0.07711	0.151	6.622517 × 10–10	2.098938 × 10–14
Magenta	MAGENTA	Magenta Member of Rustler Formation	0.6436	0.26	–0.348	0.08363	0.07711	0.138	1.915942 × 10–9	6.309576 × 10–16
Dewey Lake	DEWYLAKE	Dewey Lake Redbeds	0.6436	0.0	0.0	0.08363	0.07711	0.143	6.993007 × 10–8	5.011881 × 10–17
Santa Rosa	SANTAROS	Santa Rosa Formation	0.6436	0.0	0.0	0.08363	0.07711	0.175	5.714286 × 10–8	1.0 × 10–10
Los Medanos	UNNAMED	Los Medaños Member of Rustler Formation	0.7	0.0	0.0	0.2	0.2	0.181	0.0	9.999999 × 10–36
Tamarisk	TAMARISK	Tamarisk Member of Rustler Formation	0.7	0.0	0.0	0.2	0.2	0.064	0.0	9.999999 × 10–36
49er	FORTYNIN	Fortyniner Member of Rustler Formation	0.7	0.0	0.0	0.2	0.2	0.082	0.0	9.999999 × 10–36
DRZ_PCS	DRZ_0	Disturbed rock zone, -5 to 0 years	0.7	0.0	0.0	0.0	0.0	f(HALPOR1)2	f(HALCOMP1)3	9.999999 × 10–18
DRZ_PCS	DRZ_PCS	DRZ above the panel closures, 0 to 10,000 years	0.7	0.0	0.0	0.0	0.0	f(HALPOR1)2	f(HALCOMPa)c	10x, x = DRZPCPRM1
CONC_PCS	CAVITY_4	Concrete portion of panel closures, –5 to 0 years	0.7	0.0	0.0	0.0	0.0	1.0	0.0	1.0 × 10–10
	CONC_PCS	Concrete portion of panel closures, 0 to 10,000 years	0.9193	0.0	0.0	CONBRSAT1	CONGSSAT1	0.005	1.2 × 10–9	10x, x = CONPRM1
DRF_PCS	CAVITY_4	Drift adjacent to panel closures, –5 to 0 years	0.7	0.0	0.0	0.0	0.0	1.0	0.0	1.0 × 10–10

Table PA-2. Parameter Values Used in Representation of Two Phase Flow — Continued

Region	Material	Material Description	Brooks-Corey Pore Distribution λ	Threshold Pressure Linear Parameter a	Threshold Pressure Exponential Parameter η	Residual Brine Saturation S_{br}	Residual Gas Saturation S_{gr}	Porosity ϕ_0	Pore Compressibility β_f	Intrinsic Permeability k, m2
	DRF_PCS	Drift adjacent to panel closures, 0 to 10,000 years	2.89	0.0	0.0	WRBRNSAT1	WRGSSAT1	0.848	0.0	2.4 × 10–13
CONC_MON	CAVITY_4	Concrete monolith portion of shaft seals, –5 to 0 years	0.7	0.0	0.0	0.0	0.0	1.0	0.0	1.0 × 10–10
	CONC_MON	Concrete monolith portion of shaft seals, 0 to 10,000 years	0.94	0.0	0.0	SHURBRN1	SHURGAS1	0.05	1.2 × 10–9	1.0 × 10–14
Upper Shaft	CAVITY_4	Upper portion of shaft seals, –5 to 0 years	0.7	0.0	0.0	0.0	0.0	1.0	0.0	1.0 × 10–10
	SHFTU	Upper portion of shaft seals, 0 to 10,000 years	0.9193	0.0	0.0	SHURBRN1	SHURGAS1	0.005	2.05 × 10–8	10x, x = SHUPRM 1
Lower Shaft	CAVITY_4	Lower portion of shaft seals, –5 to 0 years	0.7	0.0	0.0	0.0	0.0	1.0	0.0	1.0 × 10–10
	SHFTL_T1	Lower portion of shaft seals, 0 - 200 years	0.9193	0.0	0.0	SHURBRN1	SHURGAS1	0.005	4.28 × 10–9	10x, x = SHLPRM11
	SHFTL_T2	Lower portion of shaft seals, 200 - 10,000 years	0.9193	0.0	0.0	SHURBRN1	SHURGAS1	0.005	4.28 × 10–9	10x, x = SHLPRM21
Borehole plugs	CONC_PLG	Concrete borehole plug, before plug degradation	0.94	0.0	0.0	0.0	0.0	0.32	0.0	10x, x = PLGPRM1
	BH_SAND	Borehole after plug degradation, 200 years after intrusion	0.94	0.0	0.0	0.0	0.0	0.32	0.0	10x, x = BHPRM1
Upper Borehole	BH_OPEN	Borehole above repository before plug degradation	0.7	0.0	0.0	0.0	0.0	0.32	0.0	1.0 × 10–9
	BH_SAND	Borehole after plug degradation, 200 years after intrusion	0.94	0.0	0.0	0.0	0.0	0.32	0.0	10x, x = BHPRM1
Lower Borehole	BH_OPEN	Borehole below repository before creep closure	0.7	0.0	0.0	0.0	0.0	0.32	0.0	1.0 × 10–9

Table PA-2. Parameter Values Used in Representation of Two Phase Flow — Continued

Region	Material	Material Description	Brooks-Corey Pore Distribution λ	Threshold Pressure Linear Parameter a	Threshold Pressure Exponential Parameter η	Residual Brine Saturation S_{br}	Residual Gas Saturation S_{gr}	Porosity ϕ_0	Pore Compressibility β_f	Intrinsic Permeability k, m2
	BH_CREEP	Borehole below repository after creep closure, 1,000 years after intrusion	0.94	0.0	0.0	0.0	0.0	0.32	0.0	10x/10, x = BHPRM1

[1] Uncertain variable, see Table PA-17.

[2] See Equation (28).

[3] See Equation (31); ϕ_0 can also be defined by an uncertain variable.

[4] See Equation (29).

[5] Initial value of porosity ϕ_0; porosity changes dynamically to account for creep closure (see Section PA-4.2.3).

$$PR = V\frac{BPCOMP}{\phi_0}, \tag{30}$$

where V is the volume of the grid block representing the Castile brine reservoir in Figure PA-8. The effect of this relationship is that the initial porosity of the brine reservoir ranges from 0.1842 to 0.9208. This range of porosity is not meant to represent an actual reservoir, but rather allows a reservoir to supply a volume of brine to the repository in the event of an E1 intrusion consistent with observed brine flows in the Delaware Basin.

The compressibility β_f in Equation (25f) and Table PA-2 is pore compressibility. Compressibility is treated as uncertain for Salado anhydrite, Salado halite, and regions of pressurized brine in the Castile Formation. However, the sampled value for each of these variables corresponds to bulk compressibility rather than to the pore compressibility actually used in the calculation. The conversion from bulk compressibility β_{fB} to pore compressibility β_f is approximated by

$$\beta_f = \beta_{fB} / \phi_0 , \tag{31}$$

where ϕ_0 is the initial porosity in the region under consideration.

The primary model used in the CRA-2004 PA for capillary pressure p_C and relative permeability k_{rl} is a modification of the Brooks-Corey model (Brooks and Corey 1964). In this model, p_C, k_{rb} and k_{rg} are defined by

$$p_C = p_t(k) / S_{e2}^{1/\lambda} \tag{32a}$$

$$k_{rb} = S_{e1}^{(2+3\lambda)/\lambda} \tag{32b}$$

$$k_{rg} = \left(1 - S_{e2}\right)^2 \left(1 - S_{e2}^{(2+\lambda)/\lambda}\right), \tag{32c}$$

where

λ = pore distribution parameter (dimensionless)

$p_t(k)$ = capillary threshold pressure (Pa) as a function of intrinsic permeability k (Webb 1992)

$$= ak^{\eta} \tag{33}$$

S_{e1} = effective brine saturation (dimensionless) without correction for residual gas saturation

$$= \left(S_b - S_{br}\right) / \left(1 - S_{br}\right) \tag{34}$$

S_{e2} = effective brine saturation (dimensionless) with correction for residual gas saturation

$$= \left(S_b - S_{br}\right) \Big/ \left(1 - S_{gr} - S_{br}\right) \; . \qquad (35)$$

The values used for λ, a, η, S_{br}, S_{gr}, and k are summarized in Table PA-2. The statement that the Brooks-Corey model is in use means that p_C , k_{rb}, and k_{rg} are defined by Equation (32). The Brooks-Corey model is used for all materials with the two exceptions, as identified in Table PA-3. In the anhydrite MBs, either the Brooks-Corey model or the van Genuchten-Parker model is used as determined by the subjectively uncertain parameter ANHBCVGP (see Table PA-17). A linear model is used in the representation of two-phase flow in an open borehole (i.e., for the first 200 years after a drilling intrusion for boreholes with two-plug or three-plug configurations (Section 6.4.7.2)). Each of these alternatives to the Brooks-Corey model is now discussed.

Table PA-3. Models for Relative Permeability and Capillary Pressure for Two-Phase Flow

Material	Relative Permeability[1]	Capillary Pressure[2]	Material	Relative Permeability[1]	Capillary Pressure[2]
S_HALITE	4	2	WAS_AREA	4	1
DRZ_0	4	1	DRZ_1	4	1
S_MB139	ANHBCVGP[3]	2	DRZ_PCS	4	1
S_ANH_AB	ANHBCVGP[3]	2	CONC_PCS	4	1
S_MB138	ANHBCVGP[3]	2	UNNAMED	4	1
CAVITY_1	4	1	TAMARISK	4	1
CAVITY_2	4	1	FORTYNIN	4	1
CAVITY_3	4	1	DRF_PCS	4	1
CAVITY_4	4	1	REPOSIT	4	1
IMPERM_Z	4	1	CONC_MON	4	1
CASTILER	4	2	SHFTU	4	1
OPS_AREA	4	1	SHFTL_T1	4	1
EXP_AREA	4	1	SHFTL_T2	4	1
CULEBRA	4	2	CONC_PLG	4	1
MAGENTA	4	2	BH_OPEN	5	1
DEWYLAKE	4	1	BH_SAND	4	1
SANTAROS	4	1	BH_CREEP	4	1

[1] Relative permeability model, where 4 ~ Brooks-Corey model (Equation (32)), 5 ~ linear model (Equation (37)), and ANHBCVGP ~ use of Brooks-Corey or van Genuchten-Parker model treated as a subjective uncertainty.

[2] Capillary pressure model, where 1 ~ $p_C = 0$ Pa, 2 ~ p_C bounded above by 1×10^8 Pa as S_b approaches S_{br}.

[3] See ANHBCVGP in Table PA-17.

In the van Genuchten-Parker model, p_C, k_{rb}, and k_{rg} are defined by (van Genuchten 1978):

$$p_C = p_{VGP}\left(S_{e2}^{-1/m} - 1\right)^{1-m} \qquad (36a)$$

$$k_{rb} = S_{e1}^{1/2}\left[1-\left(1-S_{e1}^{1/m}\right)^{m}\right]^{2} \tag{36b}$$

$$k_{rg} = \left(1-S_{e2}\right)^{1/2}\left(1-S_{e2}^{1/m}\right)^{2m}, \tag{36c}$$

where $m = \lambda/(1+\lambda)$ and the capillary pressure parameter p_{VGP} is determined by requiring that the capillary pressures defined in Equation (32a) and Equation (36a) are equal at an effective brine saturation of $S_{e2} = 0.5$ (Webb 1992). The van Genuchten-Parker model is only used for the anhydrite MBs in the Salado and uses the same values for λ, S_{br}, and S_{gr} as the Brooks-Corey model (Table PA-2).

In the linear model, p_C, k_{rb}, and k_{rg} are defined by:

$$p_C = 0,\ k_{rb} = S_{e1},\ k_{rg} = 1 - S_{e1}. \tag{37}$$

Capillary pressure p_C for both the van Genuchten-Parker and Brooks-Corey models becomes unbounded as brine saturation S_b approaches the residual brine saturation, S_{br}. To avoid unbounded values, p_C is capped at 1×10^8 Pa in selected regions (Table PA-3).

The saturation and capillary pressure constraints (i.e., Equation (25c) and Equation (25d)) permit a reduction of the number of equations to be solved from four to two. In particular, the constraint equations are used to reformulate Equation (25a) and Equation (25b) so that the unknown functions are gas saturation S_g and brine pressure p_b. Specifically, the saturation constraint in Equation (25c) allows S_b to be expressed as

$$S_b = 1 - S_g, \tag{38}$$

and thus allows S_{e1} and S_{e2} in Equation (34) and Equation (35) to be reformulated as

$$S_{e1} = \left(1 - S_g - S_{br}\right)/\left(1 - S_{br}\right) \tag{39}$$

$$S_{e1} = \left(1 - S_g - S_{br}\right)/\left(1 - S_{gr} - S_{br}\right). \tag{40}$$

Further, the capillary pressure constraint in Equation (25d) allows p_g to be expressed as

$$\begin{aligned} p_g &= p_b + p_C \\ &= p_b + p_t(k)/S_{e2}^{1/2} \quad \text{for Brooks-Corey model, Equation (32a)} && \text{(41a)} \\ &= p_b + p_{VGP}\left(S_{e2}^{-1/m} - 1\right)^{1-m} && \text{(41b)} \end{aligned}$$

for van Genuchten-Parker model, Equation (36a)
= p_b for linear model, Equation (37). (41c)

The equalities in Equation (39), Equation (40), and Equation (41) allow the transformation of Equation (25a) and Equation (25b) into two equations whose unknown functions are S_g and p_b, which are the equations that are actually solved in BRAGFLO:

$$\nabla \bullet \left[\frac{\alpha \rho_g \boldsymbol{K}_g k_{rg}}{\mu_g} \left(\nabla p_g + \rho_g g \nabla h \right) \right] + \alpha q_{wg} + \alpha q_{rg} = \alpha \frac{\partial \left(\phi \rho_g S_g \right)}{\partial t} \tag{42a}$$

$$\nabla \bullet \left[\frac{\alpha \rho_b \boldsymbol{K}_b k_{rb}}{\mu_b} \left(\nabla p_b + \rho_b g \nabla h \right) \right] + \alpha q_{wb} + \alpha q_{rb} = \alpha \frac{\partial \left(\phi \rho_b S_b \right)}{\partial t}. \tag{42b}$$

Once S_g and p_b are known, S_b and p_g can be obtained from Equation (38) and from Equation (41), respectively.

All materials are assumed to be isotropic (Howarth and Christian-Frear 1997). Thus, the tensor K_l in Equation (25) has the form

$$\mathbf{K}_l = \begin{bmatrix} k_l & 0 \\ 0 & k_l \end{bmatrix}, \tag{43}$$

where k_l is the permeability to fluid l for the particular material under consideration. For brine (i.e., fluid l = b), the permeability k_b is the same as the intrinsic permeability k in Table PA-2. For gas (i.e., fluid l = g), the permeability k_g is obtained by modifying the intrinsic permeability k to account for the Klinkenberg effect (Klinkenberg 1941). Specifically,

$$k_g = k \left(\frac{1 + b k^a}{p_g} \right), \tag{44}$$

where $a = a_{klink}$ and $b = b_{klink}$ are gas- and formation-dependent constants. Values of $a_{klink} = -0.3410$ and $b_{klink} = 0.2710$ were determined from data obtained for MB 139 (Christian-Frear 1996), with these values used for all regions in Figure PA-8. A pressure-dependent modification of k is used in the anhydrite MBs and in the DRZ in the presence of pressure-induced fracturing (see Section PA-4.2.4).

Gas density is computed using the Redlich-Kwong-Soave (RKS) equation of state, with the gas assumed to be pure hydrogen. For a pure gas, the RKS equation of state has the form (pp. 43-54, Walas 1985)

$$p_g = \frac{RT}{V - b} - \frac{a\alpha}{V(V + b)}, \tag{45}$$

where

R = gas constant = 8.31451 J mol^{-1} K^{-1},

T = temperature (K) = 300.15 K (= 30° C),

V = molar volume (m^3 mol^{-1}),

a = 0.42747 $R^2T_c^2 / P_c$,

b = 0.08664 RT_c / P_c,

$$\alpha = \left[1+\left(0.48508+1.55171\omega-0.15613\omega^2\right)\left(1-T_r^{0.5}\right)\right]^2$$
$$\approx 1.202\exp\left(-0.30288T_r\right) \quad \text{for hydrogen (Graboski and Daubert 1979),}$$

T_c = critical temperature (K),

P_c = critical pressure (Pa),

T_r = T / T_c = reduced temperature,

ω = acentric factor
= 0 for hydrogen (Graboski and Daubert 1979).

For hydrogen, pseudo-critical temperature and pressure values of T_c = 43.6 °K and $P_c = 2.047 \times 10^6$ Pa are used instead of the true values of these properties (Prausnitz 1969). Equation (45) is solved for molar volume V. The gas density ρ_g then is given by

$$\rho_g = \frac{M_{w,H_2}}{V}, \tag{46}$$

where M_{w,H_2} is the molecular weight of hydrogen (i.e., 2.01588×10^{-3} kg/mol; see p. B-26, Weast 1969).

Brine density ρ_b is defined by Equation (25f), with $\rho_0 = 1230.0$ kg/m^3 at a pressure of p_{b0} = 1.0132×10^5 Pa and $\beta_b = 2.5 \times 10^{-10}$ Pa^{-1} (Roberts 1996). Porosity, ϕ, is used as defined by Equation (25g) with two exceptions: in the repository (see Section PA-4.2.3) and in the MBs subsequent to fracturing (see Section PA-4.2.4). The values of ϕ_0 and β_f used in conjunction with Equation (25g) are listed in Table PA-2. The reference pressure p_{b0} in Equation (25g) is spatially-variable and corresponds to the initial pressures $p_b\left(x, y, -5\right)$ (see Section PA-4.2.2).

The gas and brine viscosities μ_l, l = g, b in Equation (25a) and Equation (25b) were assumed to have values of $\mu_g = 8.92 \times 10^{-6}$ Pa s (Vargaftik 1975) and $\mu_b = 2.1 \times 10^{-3}$ Pa s (McTigue 1993).

The terms q_{wg}, q_{rg}, q_{wb}, and q_{rb} in Equation (25a) and Equation (25b) relate to well injection or removal (i.e., q_{wg} , q_{wb}) and reaction production or consumption (i.e., q_{rg} , q_{rb}) of gas and brine, with positive signs corresponding to injection or production and negative signs corresponding to removal or consumption. No injection or removal of gas or brine is assumed to take place within the region in Figure PA-8. Thus, q_{wg} and q_{wb} are equal to zero. Further, no gas consumption occurs (see below), and gas production has the potential to occur (due to corrosion of steel or microbial degradation of cellulosic, plastic, or rubber (CPR) materials) only in the waste disposal regions of the repository (i.e., Waste Panel, South RoR, and North RoR in Figure PA-8). Thus,

$$\begin{aligned} q_{rg} &\geq 0 \quad \text{in waste disposal regions of Figure PA-8} \\ &= 0 \quad \text{elsewhere.} \end{aligned} \tag{47}$$

In actuality, some gas consumption does occur due to the reaction of CO_2 with the MgO in the waste panels. This gas consumption is not modeled explicitly and is accounted for by reducing the gas generation rate q_{rg}, as discussed in Section PA-4.2.5. Finally, no brine production occurs, and brine consumption has the potential to occur (due to the consumption of brine during the corrosion of steel) only in the waste disposal regions of the repository. Thus,

$$\begin{aligned} q_{rb} &\leq 0 \quad \text{in waste disposal regions of Figure PA-8} \\ &= 0 \quad \text{elsewhere.} \end{aligned} \tag{48}$$

More detail on the definition of q_{rg} and q_{rb} is provided in Section PA-4.2.5.

PA-4.2.2 Initial Conditions

In each two-phase flow simulation, a short period of time representing disposal operations is simulated. This period of time is called the start-up period and covers five years from t = –5 years to 0 years, corresponding to the amount of time a typical panel is expected to be open during disposal operations. All grid locations require initial brine pressure and gas saturation at the beginning of the simulation (t = –5 years).

The Rustler Formation and overlying units (except in the shaft) are modeled as horizontal with spatially constant initial pressure in each layer (see Figure PA-8). Table PA-4 lists the initial brine pressure p_b and gas saturation S_g for the Rustler Formation.

Table PA-4. Initial Conditions in the Rustler Formation

Name	Mesh Row (Figure PA-8)	$p_b(x, y, -5)$, Pa	$S_g(x, y, -5)$
Santa Rosa Formation	33	1.013250×10^5	1 – Sbr = 0.916

Santa Rosa Formation	32	1.013250×10^5	1 – Sbr = 0.916
Dewey Lake	31	1.013250×10^5	1 – Sbr = 0.916
Dewey Lake	30	7.355092×10^5	1 – Sbr = 0.916
49er	29	1.473284×10^6	0
Magenta	28	9.170000×10^5	0
Tamarisk	27	1.827087×10^6	0
Culebra	26	8.220000×10^5	0
Los Medaños Unnamed	25	2.274809×10^6	0

The Salado Formation (mesh rows 3 – 24 in Figure PA-8) is assumed to dip uniformly $\theta = 1°$ downward from north to south (right to left in Figure PA-8). Except in the repository excavations and in the shaft, brine is assumed initially (i.e., at –5 years) to be in hydrostatic equilibrium relative to an uncertain initial pressure $p_{b,ref}$ (SALPRES, see Table PA-17) at a reference point located at center of shaft at the elevation of the midpoint of MB139, which is the center of cell 1266 in Figure PA-10). This gives rise to the condition

$$p_b\left(x,y,-5\right) = p_{b0} + \left(\frac{1}{\beta_b}\right)\ln\left[\frac{\rho_b\left(x,y,-5\right)}{\rho_{b0}}\right], \qquad (49)$$

where

$$\rho_b\left(x,y,-5\right) = \frac{1}{g\,\beta_b\left[y_e - \Phi\left(x_{ref}, y_{ref}, -5\right) + \dfrac{1}{g\,\beta_b\,\rho_{b0}}\right]}$$

$$\Phi\left(x_{ref}, y_{ref}, -5\right) = y_{ref} + \frac{1}{g\,\beta_b}\left[\frac{1}{\rho_{b0}} - \frac{1}{\rho_b\left(x_{ref}, y_{ref}, -5\right)}\right]$$

$$\rho_b\left(x_{ref}, y_{ref}, -5\right) = \rho_{b0}\exp\left[-\beta_b\left(p_{b,ref} - p_{b0}\right)\right]$$

$$y_e = y_{ref} + h(x,y) = y_{ref} + \left(x - x_{ref}\right)\sin\theta + \left(y - y_{ref}\right)\cos\theta \quad \text{(see Equation (27))}$$

and $\rho_{b0} = 1220$ kg/m^3, $\beta_b = 3.1 \times 10^{-10}$ Pa^{-1}, $g = 9.80665$ m/s^2, and $p_{b0} = 1.01325 \times 10^5$ Pa. In the Salado Formation, initial gas saturation $S_g\left(x,y,-5\right) = 0$.

The Castile Formation (mesh rows 1 and 2) is modeled as horizontal, and initial brine pressure is spatially constant within each layer, except that the brine reservoir is treated as a different material from rest of Castile and has a different initial pressure. Specifically, outside the brine reservoir,

$$p_b(x, y, -5) = \begin{cases} 1.54445 \times 10^7 \ Pa \quad \text{in mesh row 2} \\ 1.65151 \times 10^7 \ Pa \quad \text{in mesh row 1} \end{cases}. \tag{50}$$

Within the reservoir, $p_b\left(x, y, -5\right) = BPINTPRS$, the uncertain initial pressure in the reservoir (see Table PA-17). Initial gas saturation $S_g\left(x, y, -5\right) = 0$.

Within the shaft (areas Upper Shaft, Lower Shaft, and CONC_MON) and panel closures (areas CONC_PCS and DRF_PCS), $p_b\left(x, y, -5\right) = 1.01325 \times 10^5$ Pa and $S_g\left(x, y, -5\right) = 1 \times 10^{-7}$. Within the excavated areas (Waste Panel, South RoR, and North RoR, Ops and Exp), $p_b\left(x, y, -5\right) = 1.01325 \times 10^5$ Pa and $S_g\left(x, y, -5\right) = 0$.

At the end of the initial five-year start-up period and the beginning of the regulatory period (t = 0 years), brine pressure and gas saturation are reset in the shaft, panel closures, and excavated areas. In the shaft (areas Upper Shaft, Lower Shaft, and CONC_MON) and panel closures (areas CONC_PCS and DRF_PCS), $p_b\left(x, y, 0\right) = 1.01325 \times 10^5$ Pa and $S_g\left(x, y, 0\right) = 1 \times 10^{-7}$. In the waste disposal regions (areas Waste Panel, South RoR, and North RoR), $p_b\left(x, y, 0\right) = 1.01325 \times 10^5$ Pa and $S_g\left(x, y, 0\right) = 0.985$. In the other excavated areas, $p_b\left(x, y, 0\right) = 1.01325 \times 10^5$ Pa and $S_g\left(x, y, 0\right) = 1.0$.

PA-4.2.3 Creep Closure of Repository

The porosity of the waste disposal regions and neighboring access drifts (i.e., Waste Panel, South RoR, North RoR, and DRF_PCS in Figure PA-8) is assumed to change through time due to creep closure of the halite surrounding the excavations. The equations on which BRAGFLO is based do not incorporate this type of deformation. Therefore, the changes in repository porosity due to halite deformation are modeled in a separate analysis with the geomechanical program SANTOS, which implements a quasi-static, large-deformation, finite-element procedure (Stone 1997). Interpolation procedures are then used with the SANTOS results to define ϕ within the repository as a function of time, pressure, and gas generation rate.

For more information on the generation of the porosity surface for BRAGFLO for the CRA-2004 PA, see Appendix PA, Attachment PORSURF.

PA-4.2.4 Fracturing of Marker Beds and Disturbed Rock Zone

Fracturing within the anhydrite MBs (i.e., regions MB 138, Anhydrite AB, and MB 139 in Figure PA-8) and in the DRZ (region DRZ in Figure PA-8) is assumed to occur at pressures slightly below lithostatic pressure and is implemented through a pressure-dependent compressibility $\beta_f\left(p_b\right)$ (Mendenhall and Gerstle 1995). Specifically, fracturing of the MBs begins at a brine pressure of

$$p_{bi} = p_{b0} + \Delta p_i \ , \tag{51}$$

where p_{bi} and p_{b0} are spatially dependent (i.e., $p_{b0} = p_b\left(x, y, 0\right)$ as in Section PA-4.2.2) and $\Delta p_i = 2 \times 10^5$ Pa.

Fracturing ceases at a pressure of

$$p_{ba} = p_{b0} + \Delta p_a \tag{52}$$

and a fully-fractured porosity of

$$\phi\left(p_{ba}\right) = \phi_a = \phi_0 + \Delta\phi_a \ , \tag{53}$$

where $\Delta p_a = 3.8 \times 10^6$ Pa, ϕ_0 is spatially dependent (Table PA-2), and $\Delta\phi_a = 0.04$, 0.24, and 0.04 for anhydrite materials S_MB138, S_ANH_AB and S_MB139, respectively.

Compressibility β_f is a linear function

$$\beta_f\left(p_b\right) = \beta_f + \left(\frac{p_b - p_{bi}}{p_{ba} - p_{bi}}\right)\left(\beta_{fa} - \beta_f\right) \tag{54}$$

of brine pressure for $p_{bi} \le p_b \le p_{ba}$, with β_{fa} defined so that the solution ϕ of

$$\frac{d\phi}{dp_b} = \beta_{fa}(p_b)\phi, \quad where \ \ \phi(p_{bi}) = \phi_0 \exp\left[\beta_f(p_{bi} - p_{b0})\right] \tag{55}$$

satisfies $\phi\left(p_{ba}\right) = \phi_a$; specifically, β_{fa} is given by

$$\beta_{fa} = \beta_f\left[1 - \frac{2\left(p_{ba} - p_{b0}\right)}{p_{ba} - p_{bi}}\right] + \left[\frac{2}{p_{ba} - p_{bi}}\right]\ln\left(\frac{\phi_a}{\phi_0}\right) . \tag{56}$$

The permeability $k_f\left(p_b\right)$ of fractured material at brine pressure p_b is related to the permeability of unfractured material at brine pressure p_{bi} by

$$k_f(p_b) = \left[\frac{\phi(p_b)}{\phi(p_{bi})}\right]^n k \ , \tag{57}$$

where k is the permeability of unfractured material (i.e., at p_{bi}) and n is defined so that $k_f\left(p_b\right) = 1 \times 10^{-9}\ m^2$ (i.e., n is a function of k, which is an uncertain input to the analysis; see ANHPRM in Table PA-17). When fracturing occurs, $k_f\left(p_b\right)$ is used instead of k in the definition of the permeability tensor K_l in Equation (43) for the fractured areas of the anhydrite MBs.

Fracturing is also modeled in the DRZ. The implementation of the fracture model is the same as for the anhydrite materials. In this case, fracturing would be in halite rather than anhydrite, but because of the limited extent of the DRZ and the proximity of the nearby interbeds, this representation was deemed acceptable by the Salado Flow Peer Review panel (Caporuscio et al. 2003).

PA-4.2.5 Gas Generation

Gas production is assumed to result from anoxic corrosion of steel and microbial degradation of CPR materials. Thus, the gas generation rate q_{rg} in Equation (25a) is of the form

$$q_{rg} = q_{rgc} + q_{rgm}, \tag{58}$$

where q_{rgc} is the rate of gas production per unit volume of waste (kg/m^3/s) due to anoxic corrosion of Fe-base metals and q_{rgm} is the rate of gas production per unit volume of waste (kg/m^3/s) due to microbial degradation of CPR materials. Furthermore, q_{rb} in Equation (25b) is used to describe the consumption of brine during the corrosion process.

Gas generation takes place only within the waste disposal regions (i.e., Waste Panel, South RoR, and North RoR in Figure PA-8) and all the generated gas is assumed to have the same properties as H_2 (see discussion in Attachment MASS, Section MASS-3.2). In the CCA PA and the CRA-2004 PA, the consumable materials are assumed to be homogeneously distributed throughout the waste disposal regions (i.e., the concentration of Fe-base metals and of CPR materials in the waste is a constant; see Appendix TRU WASTE, Table TRU WASTE-1). A separate analysis examined the potential effects on PA results of spatially-varying concentrations of Fe-base metals and CPR materials, and concluded that PA results are not affected by representing these materials with spatially-varying concentrations (see Attachment MASS, Section MASS.21).

The rates q_{rgc}, q_{rb} and q_{rgm} are defined by

$$q_{rgc} = \left(R_{ci} S_{b,eff} + R_{ch} S_g^*\right) D_s \rho_{Fe} X_c\left(H_2 \middle| Fe\right) M_{H_2} \tag{59}$$

$$q_{rb} = \left(q_{rgc} / M_{H_2}\right) X_c\left(H_2O \middle| H_2\right) M_{H_2O} \tag{60}$$

$$q_{rgm} = \left(R_{mi} S_{b,eff} + R_{mh} S_g^*\right) D_c y\left(H_2 \middle| C\right) M_{H_2}, \tag{61}$$

where

D_s = surface area concentration of steel in the repository ((m^2 surface area steel)/ (m^3 disposal volume)),

D_c = mass concentration of cellulosics in the repository ((kg biodegradable material)/(m^3 of disposal volume)),

M_{H_2} = molecular weight of H_2 (kg H_2/mol H_2),

M_{H_2O} = molecular weight of H_2O (kg H_2O/mol H_2O),

R_{ci} = corrosion rate under inundated conditions (m/s),

R_{ch} = corrosion rate under humid conditions (m/s),

R_{mi} = rate of cellulose biodegradation under inundated conditions (mol $C_6H_{10}O_5$/kg $C_6H_{10}O_5$/s),

R_{mh} = rate of cellulose biodegradation under humid conditions (mol $C_6H_{10}O_5$/kg $C_6H_{10}O_5$/s),

$S_{b,eff}$ = effective brine saturation due to capillary action in the waste materials (see Equation (78) in Section PA-4.2.6),

$$S_g^* = \begin{cases} 1 - S_{b,eff} & \text{if } S_{b,eff} > 0 \\ 0 & \text{if } S_{b,eff} = 0 \end{cases},$$

$X_c\left(H_2 \middle| Fe\right)$ = stoichiometric coefficient for gas generation due to corrosion of steel, i.e., moles of H_2 produced by the corrosion of 1 mole of Fe (mol H_2 / mol Fe),

$X_c\left(H_2O \middle| H_2\right)$ = stoichiometric coefficient for brine consumption due to corrosion of steel, i.e., moles of H_2O consumed per mole of H_2 generated by corrosion (mol H_2O / mol H_2),

$y\left(H_2 \middle| C\right)$ = average stoichiometric factor for microbial degradation of cellulose, i.e., the moles of H_2 generated per mole of carbon consumed by microbial action (mol H_2 / mol $C_6H_{10}O_5$), and

ρ_{Fe} = molar density of steel (mol/m^3).

The products $R_{ci}\,D_s\,\rho_{Fe}\,X_c$, $R_{ch}\,D_s\,\rho_{Fe}\,X_c$, $R_{mi}\,D_c\,y$, and $R_{mh}\,D_c\,y$ in Equation (59) and Equation (61) define constant rates of gas generation (mol/m^3/s) that continue until the associated substrate (i.e. steel or cellulose) is exhausted (i.e., zero order kinetics). The terms $S_{b,eff}$ and S_g^* in Equation (59) and Equation (61), which are functions of location and time, correct for the amount of substrate that is exposed to inundated and humid conditions, respectively. All the corrosion and microbial action is assumed to cease when no brine is present, which is the reason that 0 replaces $S_g = 1$ in the definition of S_g^*. In the CRA-2004 PA, $R_{ch} = 0$ and R_{ci}, R_{mh}, and R_{mi} are defined by uncertain variables (see WGRCOR, WGRMICH, WGRMICI in Table PA-17). Further, $M_{H_2} = 2.02 \times 10^{-3}$ kg/mol (pp. 1-7, 1-8, Lide 1991), $M_{H_2O} = 1.80 \times 10^{-2}$ kg/mol (pp. 1-7, 1-8, Lide 1991), $\rho_{Fe} = 1.41 \times 10^5$ mol/m^3 (Telander and Westerman 1993), and D_s , D_c , $X_c\left(H_2O\middle|H_2\right)$, $X_c\left(H_2\middle|Fe\right)$ and $y\left(H_2\middle|C\right)$ are discussed below.

The concentration D_s in Equation (59) is defined by

$$D_s = A_d n_d / V_R, \tag{62}$$

where

A_d = surface area of steel associated with a waste disposal drum (m^2/drum),

V_R = initial volume of the repository (m^3), and

n_d = number of waste drums required to hold all the waste emplaced in the repository (drums).

In the CRA-2004 PA, $A_d = 6$ m^2/drum (Vol. 3, WIPP PA 1991-1992), $V_R = 438{,}406$ m^3 (Stein 2002b), and $n_d = 818{,}498$ drums ($n_d = V_R \times$ DROOM / VROOM, where DROOM is the number of drums per room {6804 drums} and VROOM is the volume of each room {3644 m^3}).

The biodegradable materials to be disposed of at the WIPP consist of cellulosic materials, rubbers, and both waste plastics and container plastics. Cellulosics have been demonstrated experimentally to be the most biodegradable among these materials (Francis et al. 1997). The occurrence of significant microbial gas generation in the repository will depend on: (1) whether microbes capable of consuming the emplaced organic materials will be present and active; (2) whether sufficient electron acceptors will be present and available; and (3) whether enough nutrients will be present and available. Given the uncertainties in these factors, a probability of 0.5 is assigned to the occurrence of microbial gas generation (see WMICDFLG in Table PA-17). Furthermore, two factors may increase the biodegradability of plastics and rubbers: long time scale and cometabolism. Over a time scale of 10,000 years, the chemical properties of plastics and rubbers may change, increasing their biodegradability. Cometabolism means that microbes may degrade organic compounds, but do not use them as a source of energy, which is derived from other substrates. Both of these factors are highly uncertain and therefore a probability of 0.5 is assigned to biodegradation of plastics and rubbers conditional on the occurrence of biodegradation of cellulosic materials(see WMICDFLG in Table PA-17). In cases where biodegradation of rubbers and plastics occur, rubbers and plastics are converted to an equivalent quantity of cellulosics based on their carbon equivalence (Wang and Brush 1996a). This produces the density calculation

$$D_c = \begin{cases} m_{cel} / V_R & \text{for biodegradation of cellulosics only} \\ \left(m_{cel} + m_r + 1.7 m_p\right) / V_R & \text{for biodegradation of CPR materials,} \end{cases} \qquad (63)$$

where m_{cel} is mass of cellulosics (kg), m_r is the mass of rubbers (kg), and m_p is the mass of plastics (kg). The factor of 1.7 converts all plastics to an equivalent quantity of cellulosics based on carbon equivalence. In the CRA-2004 PA,

$$m_{cel} = [(58.0 \text{ kg/ m}^3 \times 168{,}485 \text{ m}^3) + (4.5 \text{ kg/ m}^3 \times 7{,}079 \text{ m}^3)] = 9.8 \times 10^6 \text{ kg},$$

$$m_r = [(14.0 \text{ kg/ m}^3 \times 168{,}485 \text{ m}^3) + (3.1 \text{ kg/m3} \times 7{,}079 \text{ m}^3)] = 2.4 \times 10^6 \text{ kg}$$

$$m_p = [(58.0 \text{ kg/m3} \times 168{,}485 \text{ m}^3) + (6.3 \text{ kg/m3} \times 7{,}079 \text{ m}^3)] = 9.8 \times 10^6 \text{ kg}.$$

Values for the density for CPR materials can be found in Appendix DATA, Attachment F.

The most plausible corrosion reactions after closure of the WIPP are believed to be (Wang and Brush 1996a)

$$Fe + 2H_2O = Fe(OH)_2 + H_2 \qquad (64)$$

and

$$3Fe + 4H_2O = Fe_3O_4 + 4H_2. \qquad (65)$$

When linearly weighted by the factors x and $1 - x$ $(0 \le x \le 1)$, the two preceding reactions become

$$Fe + \left(\frac{4+2x}{3}\right) H_2O = \left(\frac{4-x}{3}\right) H_2 + xFe(OH)_2 + \left(\frac{1-x}{3}\right) Fe_3O_4 , \qquad (66)$$

where x and $1 - x$ are the fractions of iron consumed in the reactions in Reaction (64) and Reaction (65), respectively. Although magnetite (Fe_3O_4) has been observed to form on iron as a corrosion product in low-Mg anoxic brines at elevated temperatures (Telander and Westerman 1997) and in oxic brine (Haberman and Frydrych 1988), there is no evidence that it will form at WIPP repository temperatures. If Fe_3O_4 were to form, H_2 would be produced (on a molar basis) in excess of the amount of Fe consumed. However, anoxic corrosion experiments (Telander and Westerman 1993) did not indicate the production of H_2 in excess of the amount of Fe consumed. Therefore, the stoichiometric factor x in Reaction (66) is set to 1.0 (i.e., x = 1), which implies that Reaction (64) represents corrosion. Thus, the stoichiometric factor for corrosion is

$$X_c\left(H_2 \middle| Fe\right) = \left(4 - x\right)/3 = 1\ mol/mol\ , \qquad (67)$$

which implies that one mole of H_2 is produced for each mole of iron consumed, and the stoichiometric factor for brine consumption is

$$X_c\left(H_2O \middle| H_2\right) = \left(4 + 2x\right)/3 = 2\ mol/mol\ , \qquad (68)$$

which implies that two moles of H_2O are consumed for each mole of H_2 produced.

The most plausible biodegradation reactions after closure of the WIPP are believed to be (Wang and Brush 1996a)

Denitrification: $$C_6H_{10}O_5 + 4.8H^+ + 4.8NO_3^- = 7.4H_2O + 6CO_2 + 2.4N_2\ , \qquad (69a)$$

Sulfate reduction: $$C_6H_{10}O_5 + 6H^+ + 3SO_4^{2-} = 5H_2O + 6CO_2 + 3H_2S\ , \qquad (69b)$$

Methanogenesis: $$C_6H_{10}O_5 + H_2O = 3CH_4 + 3CO_2\ . \qquad (69c)$$

Accumulation of CO_2 produced by the above reactions could decrease pH and thus increase actinide solubility in the repository (Wang and Brush 1996b). To improve WIPP performance, a sufficient amount of MgO will be added to the repository to remove CO_2 (Bynum et al. 1997). The consumption of CO_2 by MgO in the repository takes place by the reactions outlined in Section 6.4.3.4. The removal of CO_2 by MgO is not explicitly represented in the BRAGFLO code. Rather, the effect of CO_2 consumption is accounted for by modifying the stoichiometry of Reaction (69) to remove the CO_2 from the mass of gas produced by microbial action.

The average stoichiometry of Reaction (69), is

$$C_6H_{10}O_5 + unknowns = 6\,y\ (mol)\ gas + \ unknowns\ , \qquad (70)$$

where the average stoichiometric factor y in Reaction (70) represents the number of moles of gas produced and retained in the repository from each mole of carbon consumed. This factor y depends on the extent of the individual biodegradation pathways in Reaction (69), and the consumption of CO_2 by MgO. An range of values for y is estimated by considering the maximum mass of gas that can be produced from consumption of cellulosics (M_{cel}) and Fe-base metals (M_{Fe}), and is derived as follows (Wang and Brush 1996b).

Estimates of the maximum quantities M_{cel} and M_{Fe} (mol) of cellulosics (i.e., $C_6H_{10}O_5$) and steels that can be potentially consumed in 10,000 years are given by

$$M_{cel} = \min\left\{\frac{6000 m_{cel}}{162},\ 3.2 \times 10^{11} R_m m_{cel}\right\} \qquad (71)$$

$$M_{Fe} = \min\left\{\frac{1000 m_{Fe}}{56},\ 4.4 \times 10^{16} R_{ci} A_d n_d\right\}, \qquad (72)$$

where m_{cel} and m_{Fe} are the masses (kg) of cellulosics (see Equation (63) for definition) and steels initially present in the repository. The mass of cellulosics that can be consumed is determined by the uncertain parameter WMICDFLG (see Table PA-17). The mass of steels, $m_{Fe} = 5.15 \times 10^7$ kg; this value is calculated as:

$$V_{CH}\left(\rho_{WCH} + \rho_{CCH}\right) + V_{RH}\left(\rho_{WRH} + \rho_{CRH}\right), \qquad (73)$$

where V_{CH} and V_{RH} are the volumes of CH- and RH-TRU waste, ρ_{WCH} and ρ_{WRH} are the iron densities in CH- and RH-TRU waste, and ρ_{CCH} and ρ_{CRH} are the iron densities of the containers of CH- and RH-TRU waste (Appendix DATA, Attachment F). The terms $6000\ m_{cel}/162$ and $1000\ m_{Fe}/56$ in Equation (71) and Equation (72) equal the inventories in moles of cellulosics and steel, respectively. The terms $3.2 \times 10^{11}\ R_m m_{cel}$ and $4.4 \times 10^{16}\ R_{ci} A_d n_d$ equal the maximum amounts of cellulosics and steel that could be consumed over 10,000 years. In Equation (71), $R_m = \max\left\{R_{mh}, R_{mi}\right\}$, where R_{mh} and R_{mi} are defined by uncertain variables (see WGRMICH and WGRMICI in Table PA-17, respectively), and $3.2 \times 10^{11} = (3.15569 \times 10^7\ \text{s/yr})\ (10^4\ \text{yr})$. In Equation (72), $A_d n_d$ is the total surface area of all drums (m^2) and the factor $4.4 \times 10^{16} = (3.15569 \times 10^7\ \text{s/yr})\ (10^4\ \text{yr})\ (1.41 \times 10^5\ \text{mol/ m}^3)$, where $\rho_{Fe} = 1.41 \times 10^5\ \text{mol/m}^3$ (see Equation (59)) (Telander and Westerman 1993), converts the corrosion rate from m/s to mol/m^2/s.

A range of possible values for the average stoichiometric factor y in Reaction (70) can be obtained by considering individual biodegradation pathways involving M_{cel} and accounting for the removal of CO_2 by the MgO. Two extreme cases corresponding to the maximum and minimum values of y exist: (1) there is no reaction of microbially produced H_2S with ferrous metals and metal corrosion products, and (2) there is a complete reaction of microbially produced H_2S with ferrous metals and metal corrosion products. If no H_2S is consumed by reactions with Fe and Fe-corrosion products, the maximum quantity of microbial gas will be retained in the repository and therefore the maximum value for y results. Thus, the maximum value of y can be estimated by averaging the gas yields for all reaction pathways to produce

$$y_{max} = \frac{\dfrac{2.4 M_{NO_3}}{4.8} + \dfrac{3 M_{SO_4}}{3} + 0.5\left(M_{cel} - \dfrac{6 M_{NO_3}}{4.8} - \dfrac{6 M_{SO_4}}{3}\right)}{M_{cel}}, \qquad (74)$$

where M_{NO_3} and M_{SO_4} are the quantities of NO_3^- and SO_4^{2-} (in moles) initially present in the repository. Specifically, M_{NO_3} = 2.51 × 10^7 mol and M_{SO_4} = 4.21 × 10^5 mol (Appendix DATA, Attachment F, Table DATA-F-35).

If H_2S reacts with Fe and Fe- corrosion products, a significant quantity or perhaps all of the microbially produced H_2S would be consumed to produce FeS, which would result in the minimum value of y. Specifically,

$$y_{min} = \frac{\frac{2.4M_{NO_3}}{4.8} + \frac{3M_{SO_4}}{3} + 0.5\left(M_{cel} - \frac{6M_{NO_3}}{4.8} - \frac{6M_{SO_4}}{3}\right) - G}{M_{cel}} = y_{max} - \frac{G}{M_{cel}}, \qquad (75)$$

where

$$G = \min\left\{\frac{3M_{SO_4}}{3},\ M_{Fe}\right\}. \qquad (76)$$

The stoichiometric factor y value is believed to be located within the interval $\left[y_{min}, y_{max}\right]$. That is,

$$y = y_{min} + \beta\left(y_{max} - y_{min}\right),\ \ 0 \le \beta \le 1. \qquad (77)$$

The variable β in the preceding equation is treated as an uncertain quantity in the CRA-2004 PA (see WFBETCEL in Table PA-17).

PA-4.2.6 Capillary Action in the Waste

Capillary action (wicking) refers to the ability of a material to carry a fluid by capillary forces above the level it would normally seek in response to gravity. In the current analysis, this phenomena is accounted for by defining an effective saturation given by

$$S_{b,eff} = \begin{cases} S_b + S_{wick} & \text{if } 0 < S_b < 1 - S_{wick} \\ 0 & \text{if } S_b = 0 \\ 1 & \text{if } S_b > 1 - S_{wick} \end{cases}, \qquad (78)$$

where

$S_{b,eff}$ = effective brine saturation,

S_b = brine saturation,

S_{wick} = wicking saturation.

The effective saturation is used on a grid block basis within all waste regions (Waste Panel, South RoR, and North RoR in Figure PA-8). The wicking saturation, S_{wick}, is treated as an uncertain variable (see WASTWICK in Table PA-17). The effective brine saturation $S_{b,eff}$ is only used in the calculation of the corrosion of steel (Equation (59)) and the microbial degradation of cellulose (Equation (61)) and does not directly affect the two-phase flow calculations indicated.

PA-4.2.7 Shaft Treatment

The WIPP excavation includes four shafts that connect the repository region to the surface: the air intake shaft, salt handing shaft, waste handling shaft, and exhaust shaft. In both the CCA PA and the CRA-2004 PA, these four shafts are modeled as a single shaft. The rationale for this modeling treatment is set forth in WIPP PA 1992-1993 (Section 2.3, Vol. 5).

A shaft seal model is included in the CRA-2004 grid (column 43 in Figure PA-8), but it is implemented in a simpler fashion than for the CCA PA. A detailed description of the new implementation and its parameters are discussed in AP-094 (James and Stein 2002) and the resulting analysis report (James and Stein 2003). The final version of the shaft seal model used in the CRA-2004 PA is described by Stein and Zelinski (2003a); this model was approved by the Salado Flow Peer Review panel (Caporuscio et al. 2003).

The planned design of the shaft seals involves numerous materials including earth, crushed salt, clay, asphalt, and Salado Mass Concrete (SMC) (CCA Appendix SEAL). The design is intended to control both short-term and long-term fluid flow through the Salado portion of the shafts. For the CCA PA, each material in the shaft seal was represented in the BRAGFLO grid. Analysis of the flow results from the CCA PA and subsequent 1997 Performance Assessment Verification Test (PAVT) (SNL 1997) indicated that no significant flows of brine or gas occurred in the shaft during the 10,000-year regulatory period. As a result of these analyses, a simplified shaft seal model was developed for the CRA-2004 PA.

A conceptual representation of the simplified shaft seal system used in CRA-2004 PA is shown in Figure PA-11. The simplified model divides the shaft into three sections: an upper section (shaft seal above the Salado), a lower section (within the Salado), and a concrete monolith section within the repository horizon. A detailed discussion on how the material properties were assigned for the simplified shaft seal model is included in James and Stein (2003). The permeability value used to represent the upper and lower sections is defined as the harmonic mean of the permeability of the component materials in the detailed shaft seal model (including permeability adjustments made for the DRZ assumed to surround the lower shaft seal section within the Salado). Porosity is defined as the thickness-weighted mean porosity of the component materials. Other material properties are described in James and Stein (2003).

The lower section of the shaft experiences a change in material properties at 200 years. This change simulates the consolidation of the seal materials within the Salado and results in a significant decrease in permeability. This time was chosen as a conservative overestimate of the amount of time expected for this section of the shaft to become consolidated. The concrete monolith section of the shaft is unchanged from the CCA PA and is represented as being highly permeable for 10,000 years to ensure that fluids can access the north end (operations and experimental areas) in the model. In three thin regions at the stratigraphic position of the anhydrite MBs, the shaft seal is modeled as MB material (Figure PA-11). This model feature is included so that fluids flowing in the DRZ and MB fractures can access the interbeds to the north of the repository "around" the shaft seals. Because these layers are so thin, they have virtually no effect on the effective permeability of the shaft seal itself.

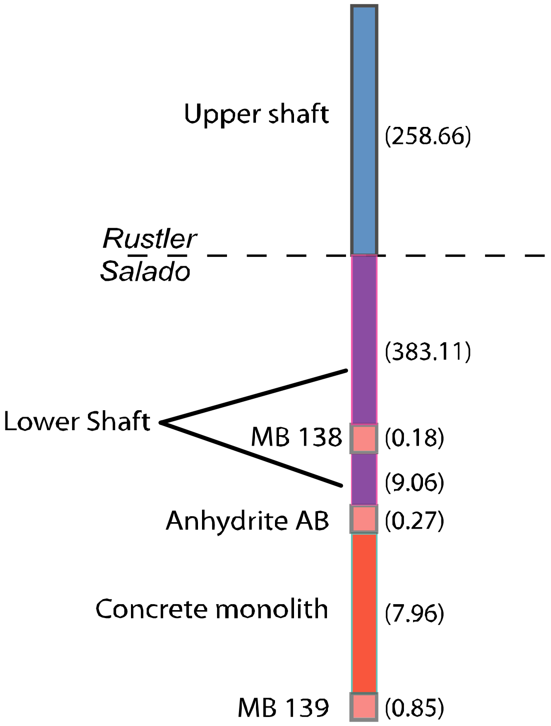

Figure PA-11. Schematic View of the Simplified Shaft Model.

The simplified shaft model was tested in the AP-106 analysis (Stein and Zelinski 2003a), which supported the Salado Flow Peer Review. The results of the AP-106 analysis demonstrated that vertical brine flow through the simplified shaft model was comparable to brine flows seen through the detailed shaft model used in the CCA PA and subsequent PAVT calculations.

PA-4.2.8 Option D Panel Closures

The CRA-2004 PA includes panel closures models that represent the Option D panel closure design (Section 6.4.3). Option D closures (Figure PA-12) are designed to allow minimal fluid flow between panels. The CRA-2004 PA explicitly represents selected Option D panel closures in the computational grid using a model that was approved by the Salado Flow Peer Review Panel (Caporuscio et al. 2003). The Option D panel closure design has several components: an SMC monolith, which extends into the DRZ in all directions, an empty drift section, and a block and mortar explosion wall (Figure PA-13). Each set of panel closures are represented in the BRAGFLO grid by four materials in 13 grid cells:

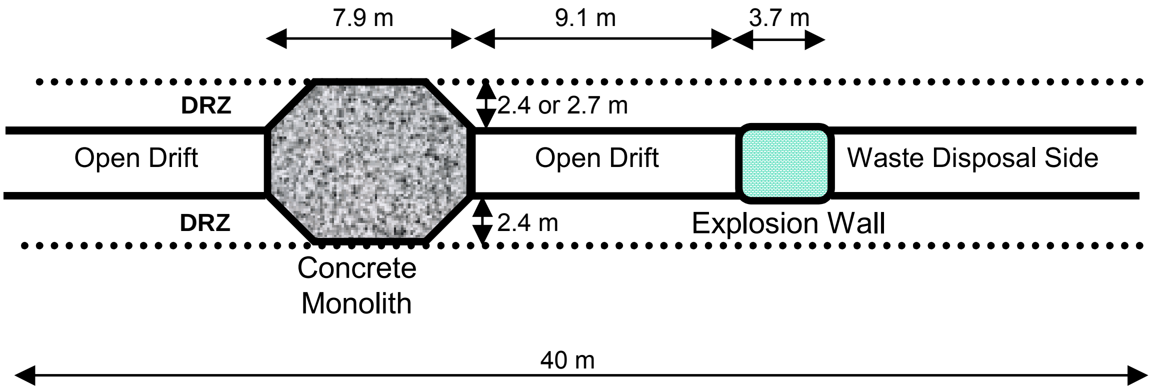

Figure PA-12. Schematic Side View of Option D Panel Closure.

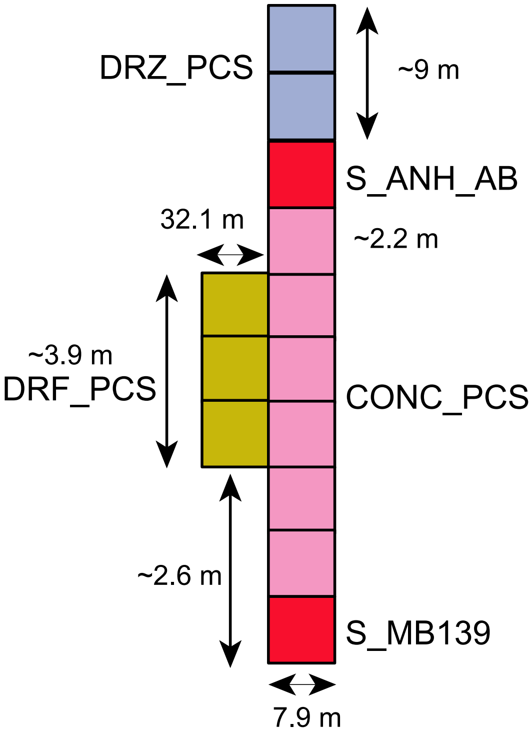

Figure PA-13. Representation of Option D Panel Closures in the BRAGFLO Grid.

- Six cells of panel closure concrete (area CONC_PCS, material CONC_PCS),
- One cell above and one cell below the concrete material consisting of MB anhydrite (areas MB 139 and Anhydrite AB, materials S_MB139 and S_ANH_AB, respectively),
- Two cells of healed DRZ above Anhydrite AB above the panel closure system (PCS) (area DRZ_PCS, material DRZ_PCS), and
- Three cells of empty drift and explosion wall (area DRF_PCS, material DRF_PCS).

Properties for the materials comprising the panel closure system are listed in Table PA-2.

PA-4.2.8.1 Panel Closure Concrete

The Option D panel closure design requires the use of a salt-saturated concrete, identified as SMC, as specified for the shaft seal system. The design of the shaft seal system and the properties of SMC are described in Hurtado et al. (1997). The BRAGFLO grid incorporates the material, CONC_PCS, which is assigned the material properties of undegraded SMC and is used to represent the concrete portion of the Option D panel closure system (Figure PA-8). A double-thick concrete segment is used to represent the northernmost set of panel closures (between the north rest of repository and the operations area). This feature is meant to represent the two sets of panel closures in series that will be emplaced between the waste filled repository and the shaft.

PA-4.2.8.2 Panel Closure Abutment with Marker Beds

In the BRAGFLO grid, regions where the Option D panel closures intersect the MBs are represented as blocks of MB material (Figure PA-8). This representation is warranted for two reasons:

1. The MB material has a very similar permeability distribution (10^{-21} to $10^{-17.1}$ m^2) as the concrete portion of the Option D panel closures ($10^{-20.699}$ to 10^{-17} m^2), and thus, assigning this material as anhydrite MB in the model has essentially the same effect as calling it concrete, as long as pressures are below the fracture initiation pressure.

2. In the case of high pressures, it is expected that fracturing may occur in the anhydrite MBs and flow could go “around” the panel closures out of the two-dimensional plane considered in the model grid. In this case, the flow would be through the MB material, which incorporates a fracture model, as described above.

PA-4.2.8.3 Disturbed Rock Zone Above the Panel Closure

After construction of the concrete portion of the panel closure, the salt surrounding the monolith will be subjected to compressive stresses, which will facilitate the rapid healing of disturbed halite. The rounded configuration of the monolith creates a situation very favorable for concrete durability: high compressive stresses and low stress differences. In turn, the compressive stresses developed within the salt will quickly heal any damage caused by construction excavation, thereby eliminating the DRZ along the length of this portion of the panel closure. The permeability of the salt immediately above and below the rigid concrete monolith component of Option D will approach the intrinsic permeability of the undisturbed Salado halite.

To represent the DRZ above the monoliths, the CRA-2004 PA uses the material, DRZ_PCS, in the BRAGFLO grid (Figure PA-8). The values assigned to DRZ_PCS are the same as those values used for the DRZ above the excavated areas (material DRZ_1, see Table PA-2), except for the properties PRMX_LOG, PRMY_LOG, and PRMZ_LOG, the logarithm of permeability in the x, y, and z directions, respectively. These permeability values are assigned the same distributions used for the material CONC_PCS. In this instance, the values are based on the nature of the model set-up, and not directly on experimental data (although the general range of the distribution agrees with experimental observations of healed salt). The use of these permeabilities ensures that any fluid flow is equally probable through or around the Option D panel closures and represents the range of uncertainty that exists in the performance of the panel closure system.

PA-4.2.8.4 Empty Drift and Explosion Wall Materials

The DRF_PCS is the material representing the empty drift and explosion wall. For simplicity, this material is assumed to have hydrologic properties equivalent to the material representing the waste panel and is used for the three sets of panel closures represented in the grid (Figure PA-8). The creep closure model is applied to this material to be consistent with the neighboring materials. The assignment of a high permeability to this region containing the explosion wall is justified because the explosion wall is not designed to withstand the stresses imposed by creep closure and will be highly permeable following rapid room closure.

PA-4.2.9 Borehole Model

The major disruptive event in the CRA-2004 PA is the penetration of the repository by a drilling intrusion. In the undisturbed scenario (scenario S1; see Section PA-6.7.1), these blocks have the material properties of the neighboring stratigraphic or excavated modeling unit, and there is no designation in the grid of a borehole except for the reduced lateral dimensions of this particular column of grid blocks.

In the scenarios simulating drilling disturbance, these cells start out with the same material properties as in the undisturbed scenario, but at the time of intrusion the borehole grid blocks are reassigned to borehole material properties. The drilling intrusion is modeled by modifying the permeability of the grid blocks in column 26 of Figure PA-8 (values listed in Table PA-5). Further, the drilling intrusion is assumed to produce a borehole with a diameter of 12.25 in. (0.31 m) (Vaughn 1996; Howard 1996); borehole fill is assumed to be incompressible; capillary effects are ignored; residual gas and brine saturations are set to zero; and porosity is set to 0.32 (see materials CONC_PLG, BH_OPEN, BH_SAND and BH_CREEP in Table PA-2). When a borehole that penetrates pressurized brine in the Castile Formation is simulated (i.e., an E1 intrusion), the permeability modifications indicated in Table PA-5 extend from the land surface (i.e., grid cell 2155 in Figure PA-10) to the base of the pressurized brine (i.e., grid cell 2225 in Figure PA-10). When a borehole that does not penetrate pressurized brine in the Castile Formation is under consideration (i.e., an E2 intrusion), the permeability modifications indicated in Table PA-5 stop at the bottom of the lower DRZ (i.e., grid cell 1111 in Figure PA-10).

Table PA-5. Permeabilities for Drilling Intrusions Through the Repository

Time After Intrusion	Assigned Permeabilities
0 - 200 years	Concrete plugs are assumed to be emplaced at the Santa Rosa Formation (i.e., a surface plug with a length of 15.76 m; corresponds to grid cells 2113, 2155 in Figure PA-10) and the Los Medanõs Member of the Rustler Formation (i.e., a plug at top of Salado with a length of 36 m; corresponds to grid cell 1644 in Figure PA-10). Concrete plugs are assumed to have a permeability of $k = 5 \times 10^{-17}$ m^2; open potions of the borehole are assumed to have a permeability of 1×10^{-9} m^2. See material CONC_PLG in Table PA-3.
200 - 1200 years	Concrete plugs are assumed to fail after 200 years (DOE 1995) an entire borehole is assigned a permeability typical of silty sand, i.e., $k = 10^x$ m^2, x = BHPRM, where BHPRM is an uncertain input to the analysis (see Table PA-17). See material BH_SAND in Table PA-3.
> 1200 years	Permeability reduced by one order of magnitude in Salado Formation beneath repository due to creep closure of borehole (Thompson et al. 1996) (i.e., $k = 10^x/10$, x = BHPRM, in grid cells 2225, 1576, 26, 94, 162, 230, 1111, 1119, 1127 of Figure PA-10). No changes are made within and above the lower DRZ. See material BH_CREEP in Table PA-3.

PA-4.2.10 Numerical Solution

Determination of gas and brine flow in the vicinity of the repository requires the numerical solution of the two nonlinear partial differential equations in Equation (42) on the computational domain in Figure PA-8 together with evaluation of appropriate auxiliary conditions (Equation (25f), Equation (25g), and Equation (41)). The actual unknown functions in this solution are p_b and S_g, although the constraint conditions also give rise to values for p_g and S_b. As two dimensions in space and one dimension in time are in use, p_b, p_g, S_b and S_g are functions of the form $p_b(x,y,t)$, $p_g(x,y,t)$, $S_b(x,y,t)$ and $S_g(x,y,t)$.

The solution of Equation (42) requires both initial value and boundary value conditions for p_b and S_g . The initial value conditions for p_b and S_g are given in Section PA.4.2.2. As indicated there, the calculation starts at time t = –5 years, with a possible resetting of values at t = 0 years, which corresponds to final waste emplacement and sealing of the repository. The boundary conditions are such that no brine or gas moves across the exterior grid boundary (Table PA-6). This Neumann-type boundary condition is maintained for all time. Further, BRAGFLO allows the user to specify pressure and/or saturation at any grid block. This feature is used to specify Dirichlet-type conditions at the surface grid blocks (i = 1, 2, …, 68, j = 33, Figure PA-8) and at the far field locations in the Culebra and Magenta Formations (i = 1, 68, j = 26 and i = 1, 68, j = 28, Figure PA-8). These auxiliary conditions are summarized in Table PA-7).

Table PA-6. Boundary Value Conditions for p_g and p_b

Boundaries below (y = 0 m) and above (y = 1039 m) system for 0 ≤ x ≤ 46630 m and –5 yr ≤ t	
$\left(\nabla p_g + \rho_g g \nabla h\right)\Big\vert_{(x,y,t)} \cdot \boldsymbol{j} = 0 \ Pa/m$	no gas flow condition
$\left(\nabla p_b + \rho_b g \nabla h\right)\Big\vert_{(x,y,t)} \cdot \boldsymbol{j} = 0 \ Pa/m$	no brine flow condition
Boundaries at left (x = 0 m) and right (x = 46630 m) of system for 0 ≤ y ≤ 1039 m and –5 yr ≤ t	
$\left(\nabla p_g + \rho_g g \nabla h\right)\Big\vert_{(x,y,t)} \cdot \boldsymbol{i} = 0 \ Pa/m$	no gas flow condition
$\left(\nabla p_b + \rho_b g \nabla h\right)\Big\vert_{(x,y,t)} \cdot \boldsymbol{i} = 0 \ Pa/m$	no brine flow condition

Table PA-7. Auxiliary Dirichlet Conditions for p_b and S_g

Surface Grid Blocks	
$S_g\left(i, j, t\right) = 0.08363$	i = 1, 2, …, 68, j = 33, –5 yr ≤ t
$p_b\left(i, j, t\right) = 1.01 \times 10^5$ Pa	i = 1, 2, …, 68, j = 33, –5 yr ≤ t
Culebra and Magenta Far Field	
$p_b\left(i, 26, t\right) = 8.22 \times 10^5$ Pa	i = 1 and 68, j = 26, –5 yr ≤ t (Culebra)
$p_b\left(i, 28, t\right) = 9.17 \times 10^5$ Pa	i = 1 and 68, j = 28, –5 yr ≤ t (Magenta)

A fully implicit finite difference procedure is used to solve Equation (42). The associated discretization of the gas mass balance equation is given by

$$
\begin{aligned}
&\frac{1}{\Delta x_i}\left\{\frac{1}{x_{i+1}-x_i}\left[\frac{\alpha\rho_g k_x k_{rg}}{\mu_g}\right]_{i+1/2,j}^{n+1}\left(\Phi_{g_{i+1,j}}^{x-}-\Phi_{g_{i,j}}^{x+}\right)^{n+1}\right.\\
&\left.-\frac{1}{x_i-x_{i-1}}\left[\frac{\alpha\rho_g k_x k_{rg}}{\mu_g}\right]_{i-1/2,j}^{n+1}\left(\Phi_{g_{i,j}}^{x-}-\Phi_{g_{i-1,j}}^{x+}\right)^{n+1}\right\}\\
&+\frac{1}{\Delta y_j}\left\{\frac{1}{y_{j+1}-y_j}\left[\frac{\alpha\rho_g k_y k_{rg}}{\mu_g}\right]_{i,j+1/2}^{n+1}\left(\Phi_{g_{i,j+1}}^{y-}-\Phi_{g_{i,j}}^{y+}\right)^{n+1}\right.
\end{aligned}
$$

$$-\frac{1}{y_j - y_{j-1}}\left[\frac{\alpha\rho_g k_y k_{rg}}{\mu_g}\right]_{i,j-1/2}^{n+1}\left(\Phi_{g_{i,j}}^{y-} - \Phi_{g_{i,j-1}}^{y+}\right)^{n+1}\Bigg\}$$

$$+\alpha_{i,j} q_{wg_{i,j}}^{n+1} + \alpha_{i,j} q_{rg_{i,j}}^{n+1} - \frac{\left(\alpha\phi\rho_g S_g\right)_{i,j}^{n+1} - \left(\alpha\phi\rho_g S_g\right)_{i,j}^{n}}{\Delta t} = 0\,, \qquad (79)$$

where Φ represents the phase potentials given by

$$\Phi_{gi,j}^{x+} = p_{gi,j} + \rho_{gi+1/2,j}\, g h_{i,j}, \quad \Phi_{gi,j}^{x-} = p_{gi,j} + \rho_{gi-1/2\,j}\, g h_{i,j}$$

and

$$\Phi_{gi,j}^{y+} = p_{gi,j} + \rho_{gi,j+1/2}\, g h_{i,j}, \quad \Phi_{gi,j}^{y-} = p_{gi,j} + \rho_{gi,j-1/2}\, g h_{i,j}\,,$$

and the subscripts are defined by

i = x-direction grid index

j = y-direction grid index

$i \pm 1/2$ = x-direction grid block interface

$j \pm 1/2$ = y-direction grid block interface

x_i = grid block center in the x-coordinate direction (m)

y_j = grid block center in the y-coordinate direction (m)

Δx_i = grid block length in the x-coordinate direction (m)

Δy_j = grid block length in the y-coordinate direction (m),

the superscripts are defined by

n= index in the time discretization, known solution time level

n+1= index in the time discretization, unknown solution time level,

and the interblock densities are defined by

$$\rho_{gi+1/2,j} = \frac{\Delta x_{i+1,j}}{\Delta x_{i,j} + \Delta x_{i+1,j}}\rho_{gi,j} + \frac{\Delta x_{i,j}}{\Delta x_{i,j} + \Delta x_{i+1,j}}\rho_{gi+1,j}\,,$$

$$\rho_{gi-1/2,j} = \frac{\Delta x_{i,j}}{\Delta x_{i-1,j} + \Delta x_{i,j}} \rho_{g,i-1,j} + \frac{\Delta x_{i-1,j}}{\Delta x_{i-1,j} + \Delta x_{i,j}} \rho_{gi,j},$$

$$\rho_{gi,j+1/2} = \frac{\Delta y_{i,j+1}}{\Delta y_{i,j} + \Delta y_{i,j+1}} \rho_{gi,j} + \frac{\Delta y_{i,j}}{\Delta y_{i,j} + \Delta y_{i,j+1}} \rho_{gi,j+1},$$

$$\rho_{gi,j-1/2} = \frac{\Delta y_{i,j}}{\Delta y_{i,j-1} + \Delta y_{i,j}} \rho_{gi,j-1} + \frac{\Delta y_{i,j-1}}{\Delta y_{i,j-1} + \Delta y_{i,j}} \rho_{gi,j}.$$

The interface values of k_{rg} in Equation (79) are evaluated using upstream weighted values (i.e., the relative permeabilities at each grid block interface are defined to be the relative permeabilities at the center of the adjacent grid block that has the highest potential). Further, interface values for $\alpha\rho_g k_x / \mu_g$ and $\alpha\rho_g k_y / \mu_g$ are obtained by harmonic averaging of adjacent grid block values for these expressions.

The discretization of the brine mass balance equation is obtained by replacing the subscript for gas, g, by the subscript for brine, b. As a reminder, p_g and S_b are replaced in the numerical implementation with the substitutions indicated by Equation (25d) and Equation (25c), respectively. For the CRA-2004 PA, wells are not used in the conceptual model. Thus, the terms q_{wg} and q_{wb} are zero. For this analysis, the wellbore is not treated by a well model, but rather is explicitly modeled within the grid as a distinct material region (i.e., Upper Borehole and Lower Borehole in Figure PA-8).

The resultant coupled system of nonlinear brine and gas mass balance equations is integrated in time using the Newton-Raphson method with upstream weighting of the relative permeabilities as previously indicated. The primary unknowns at each computational cell center are brine pressure and gas saturation.

PA-4.2.11 Gas and Brine Flow across Specified Boundaries

The Darcy velocity vectors $\mathbf{v}_g(x, y, t)$ and $\mathbf{v}_b(x, y, t)$ for gas and brine flow ($(m^3/m^2)/s = m/s$) are defined by the expressions

$$\mathbf{v}_g(x,y,t) = \mathbf{K}_g k_{rg} \left(\nabla p_g + \rho_g g \nabla h\right) / \mu_g \tag{80}$$

and

$$\mathbf{v}_b(x,y,t) = \mathbf{K}_b k_{rb} \left(\nabla p_b + \rho_b g \nabla h\right) / \mu_b . \tag{81}$$

Values for $\mathbf{v}_g$ and $\mathbf{v}_b$ are obtained and saved as the numerical solution of Equation (42) is carried out. Cumulative flows of gas, $C_g(t,\mathcal{B})$, and brine, $C_b(t,\mathcal{B})$, from time 0 to time t across an arbitrary boundary $\mathcal{B}$ in the domain of (Figure PA-8) is then given by

$$C_l(t,\mathcal{B}) = \int_0^t \left[\int_{\mathcal{B}} \alpha(x,y) \mathbf{v}_l(x,y,t) \cdot \mathbf{n}(x,y)\, ds \right] dt \tag{82}$$

for l = g, b, where $\alpha(x,y)$ is the geometry factor defined in Figure PA-9, $\mathbf{n}(x,y)$ is an outward pointing unit normal vector, and $\int_{\mathcal{B}} ds$ denotes a line integral. As an example, $\mathcal{B}$ could correspond to the boundary of the waste disposal regions in Figure PA-8. The integrals defining $C_g(t,\mathcal{B})$ and $C_b(t,\mathcal{B})$ are evaluated using the Darcy velocities defined by Equation (80) and Equation (81). Due to the dependence of gas volume on pressure, $C_g(t,\mathcal{B})$ is typically calculated in moles or in m^3 at standard temperature and pressure, which requires an appropriate change of units for $\mathbf{v}_g$ in Equation (82).

PA-4.2.12 Additional Information

Additional information on BRAGFLO and its use in the CRA-2004 PA can be found in the BRAGFLO User's Manual (WIPP PA 2003c) and in the analysis package for the Salado flow calculations for the CRA-2004 PA (Stein and Zelinski 2003b).

PA-4.3 Radionuclide Transport in the Salado: NUTS

This section describes the model used to compute transport of radionuclides in the Salado for E0, E1 and E2 scenarios (defined in Section 6.3). The model for transport in the E1E2 scenario is described in Section PA-4.4.

PA-4.3.1 Mathematical Description

The following system of partial differential equations is used to model radionuclide transport in the Salado:

$$-\nabla \cdot \alpha \mathbf{v}_b C_{bl} + \alpha S_l = \alpha \frac{\partial}{\partial t}\left(\phi S_b C_{bl}\right) + \left(\alpha \phi S_b C_{bl}\right)\lambda_l - \alpha \phi S_b \sum_{p \in P(l)} C_{bp} \lambda_p \tag{83a}$$

$$-S_l = \frac{\partial}{\partial t}\left(C_{sl}\right) + C_{sl}\lambda_l - \sum_{p \in P(l)} C_{sp} \lambda_p \tag{83b}$$

for l = 1, 2, …, nR, where

$\mathbf{v}_b$ = Darcy velocity vector ((m^3/m^2)/s = m/s) for brine (supplied by BRAGFLO from solution of Equation (81)),

C_{bl} = concentration (kg/m^3) of radionuclide l in brine,

C_{sl} = concentration (kg/m^3) of radionuclide l in solid phase (i.e., not in brine), with concentration defined with respect to total (i.e., bulk) formation volume (only used in repository; see Figure PA-8),

S_l = linkage term ((kg/m^3)/s) due to dissolution/precipitation between radionuclide l in brine and in solid phase (see Equation (84)),

ϕ = porosity (supplied by BRAGFLO from solution of Equation (25)),

S_b = brine saturation (supplied by BRAGFLO from solution of Equations (25)),

λ_l = decay constant (s^{-1}) for radionuclide l,

$\boldsymbol{P}(\boldsymbol{l})$ = {p: radionuclide p is a parent of radionuclide l},

nR = number of radionuclides,

and α is the dimension dependent geometry factor in Equation (26). The CRA-2004 PA uses a two-dimensional representation for fluid flow and radionuclide transport in the vicinity of the repository with α defined by the element depths in Figure PA-8 . Although omitted from the notation for brevity, the terms α, $\boldsymbol{v_b}$, C_{bl}, C_{sl}, S_l, ϕ and S_b are functions $\boldsymbol{\alpha(x,y)}$, $\boldsymbol{v_b(x,y,t)}$, $\boldsymbol{C_{bl}(x,y,t)}$, $\boldsymbol{C_{sl}(x,y,t)}$, $\boldsymbol{S_l(x,y,t)}$, $\boldsymbol{\phi(x,y,t)}$, and $\boldsymbol{S_b(x,y,t)}$ of time t and the spatial variables x, y. Equation (83) is defined and solved on the same computational grid used with BRAGFLO for the solution of Equation (25) (Figure PA-8).

Radionuclides are assumed to be present in both brine (Equation (83a)) and in an immobile solid phase (Equation (83b)). Radionuclide transport takes place only by brine flow (Equation (83a)). A maximum radionuclide concentration in brine is assumed for each element (Section PA-4.3.2). Then, each individual radionuclide equilibrates between the brine and solid phases on the basis of the maximum concentration of its associated element and the mole fractions of other isotopes of this element that are included in the calculation. The linkage between the brine and solid phases in Equation (83) accomplished by the term S_l, where

$$\boldsymbol{S_l} = \begin{cases} \boldsymbol{\delta(\tau - t)\, Dif\left(S_T, C_{b,El(l)}\right) MF_{sl}} & \boldsymbol{if\ \ 0 \le Dif\left(S_T, C_{b,El(l)}\right) \le C_{s,El(l)} / \left(\phi S_b\right),\ 0 < S_b} \\ \boldsymbol{\delta(\tau - t)\left[C_{s,El(l)} / \left(\phi S_b\right)\right] MF_{sl}} & \boldsymbol{if\ \ 0 \le C_{s,El(l)} / \left(\phi S_b\right) < Dif\left(S_T, C_{b,El(l)}\right),\ 0 < S_b} \\ \boldsymbol{\delta(\tau - t)\, Dif\left(S_T, C_{b,El(l)}\right) MF_{bl}} & \boldsymbol{if\ \ Dif\left(S_T, C_{b,El(l)}\right) < 0,\ 0 < S_b} \\ \boldsymbol{0} & \boldsymbol{otherwise} \end{cases} ,\tag{84}$$

with

$S_T\left[Br(t), Ox(l), Mi, El(l)\right]$ = maximum concentration (kg/m^3) of element $El(l)$ in oxidation state $Ox(l)$ in brine type $Br(t)$, where $El(l)$ denotes the element of which radionuclide l is an isotope, $Ox(l)$ denotes the oxidation state in which element $El(l)$ is present, Mi indicates whether microbial activity is present, and $Br(t)$ denotes the type of brine present in the repository at time t (see Section PA-4.3.2 for definition of $S_T(Br, Ox, Mi, El)$.

$C_{p,El(l)}$ = concentration (kg/m^3) of element $El(l)$ in brine (p = b) or solid (p = s) (i.e., sum of concentrations of radionuclides that are isotopes of same element as radionuclide l, where $k \in El(l)$ only if k is an isotope of element $El(l)$)

$$= \sum_{k \in El(l)} C_{pk} \tag{85}$$

$Dif\left(S_T, C_{b,El(l)}\right)$ = difference (kg/m^3) between maximum concentration of element $El(l)$ in brine and existing concentration of element $El(l)$ in brine

$$= S_T\left[Br(t), Ox(l), Mi, El(l)\right] - C_{b,El(l)} \tag{86}$$

MF_{pl} = mole fraction of radionuclide l in phase p, where p = b ~ brine and p = s ~ solids

$$= C_{pl} CM_l \Big/ \sum_{k \in El(l)} C_{pk} CM_k \tag{87}$$

CM_l = conversion factor (mole/kg) from kilograms to moles for radionuclide l

$\delta(\tau - t)$ = Dirac delta function (s^{-1})(i.e., $\delta(\tau - t) = 0 \;\; if \;\; \tau \neq t \;\; and \;\; \int_{-\infty}^{\infty} \delta(\tau - t)\, d\tau = 1$).

Although omitted for brevity, the terms S_l, $C_{p,El(l)}$, MF_{pl}, ϕ and S_b are functions of time t and spatial variables x, y. The Dirac delta function, $\delta(t - \tau)$, appears in Equation (84) to indicate that the adjustments to concentration are implemented instantaneously within the numerical solution of Equation (83) whenever a concentration imbalance is observed.

The velocity vector $\mathbf{v}_b$ in Equation (83) is defined in Equation (81) and is obtained from the numerical solution of Equation (25). If $\mathcal{B}$ denotes an arbitrary boundary (e.g., the land withdrawal boundary) in the domain of Equation (83) (i.e., Figure PA-8), then the cumulative transport of $C_l(t, \mathcal{B})$ of radionuclide l from time 0 to time t across $\mathcal{B}$ is given by

$$C_l\left(t,\mathcal{B}\right)=\int_0^t\left[\int_{\mathcal{B}} \mathbf{v}_b\left(x,y,t\right)C_l\left(x,y,t\right)\alpha\left(x,y\right)\cdot\mathbf{n}\left(x,y\right)ds\right]dt\ , \tag{88}$$

where $\mathbf{n}\left(x,y\right)$ is an outward pointing unit normal vector and $\int_{\mathcal{B}} ds$ denotes a line integral over $\mathcal{B}$.

Equation (83) models advective radionuclide transport due to the velocity vector $\mathbf{v}_b$. Although the effects of solubility limits are considered, no chemical or physical retardation is included in the model. Also, molecular diffusion is not included in the model, with this omission having little effect as the radionuclides under consideration have molecular diffusion coefficients on the order of 10^{-10} m^2/s and thus can be expected to move approximately 10 m over 10,000 years due to molecular diffusion. Mechanical dispersion is also not included, with this omission having little effect on the final results due to the uniform initial radionuclide concentrations assumed within the repository and the use of time-integrated releases in assessing compliance with 40 CFR § 191.13.

PA-4.3.2 Calculation of Maximum Concentration $S_T\left(Br,Ox,Mi,El\right)$

A maximum concentration $S_T\left(Br,Ox,Mi,El\right)$ S_T(Br, Ox, Mi, El) (mol/l) is calculated for each brine type (Br ~ Salado, Castile), oxidation state (Ox ~ +3, +4, +5, +6), presence of microbial action (present or not) and element (El ~ Am, Pu, U, and Th). The maximum concentration is given by

$$S_T\left(Br,Ox,Mi,El\right)=S_D\left(Br,Ox,Mi,El\right)+S_C\left(Br,Ox,Mi,El\right), \tag{89}$$

where $S_D\left(Br,Ox,Mi,El\right)$ is the dissolved solubility (mol/l) and $S_C\left(Br,Ox,Mi,El\right)$ is the concentration (mol/l) of the element sorbed to colloids.

The dissolved solubility $S_D\left(Br,Ox,Mi,El\right)$ is given by

$$S_D\left(Br,Ox,Mi,El\right)=S_{FMT}\left(Br,Ox,Mi\right)\times 10^{UF\left(Br,Ox,El\right)} \tag{90}$$

where

$S_{FMT}\left(Br,Ox,Mi\right)$ = dissolved solubility (mol/l) calculated by FMT model (WIPP PA 1998a) for brine type Br, oxidation state Ox, and presence of microbial action Mi,

$UF\left(Br,Ox,El\right)$ = logarithm (base 10) of uncertainty factor for solubilities calculated by FMT expressed as a function of brine type Br, oxidation state Ox and element El.

Table PA-8 lists the calculated values of $S_{FMT}\left(Br,Ox,Mi\right)$; details of the calculation are provided in Attachment SOTERM. The values of Mi are determined by the uncertain parameter

WMICDFLG; see Table PA-17. The uncertainty factors $\boldsymbol{UF}\left(\boldsymbol{Br},\boldsymbol{Ox},\boldsymbol{El}\right)$ are determined by the uncertain parameters listed in Table PA-9; definition of each uncertain parameter is provided in Table PA-17.

Table PA-8. Calculated Values for Dissolved Solubility

Brine/Microbial action	Oxidation State			
	+3	+4	+5	+6
Salado/No microbial gas generation	3.07×10^{-7}	1.24×10^{-8}	9.72×10^{-7}	8.7×10^{-6}
Castile/No microbial gas generation	1.77×10^{-7}	5.84×10^{-9}	2.13×10^{-5}	8.8×10^{-6}
Salado/With microbial gas generation	3.07×10^{-7}	1.19×10^{-8}	1.02×10^{-6}	8.7×10^{-6}
Castile/With microbial gas generation	1.69×10^{-7}	2.47×10^{-8}	5.08×10^{-6}	8.8×10^{-6}

Table PA-9. Uncertainty Factors for Dissolved Solubility

Brine	Oxidation State, Element					
	+3, Am	+3, Pu	+4, Pu	+4, U	+6, U	+4, Th
Salado	WSOLAM3S	WSOLPU3S	WSOLPU4S	WSOLU4S	WSOLU6S	WSOLTH4S
Castile	WSOLAM3C	WSOLPU3C	WSOLPU4C	WSOLU4C	WSOLU6C	WSOLTH4C

The concentration (mol/l) of the element sorbed to colloids $\boldsymbol{S_C}\left(\boldsymbol{Br},\boldsymbol{Ox},\boldsymbol{Mi},\boldsymbol{El}\right)$ is given by

$$\boldsymbol{S_C}\left(\boldsymbol{Br},\boldsymbol{Ox},\boldsymbol{Mi},\boldsymbol{El}\right) = \boldsymbol{S_{Hum}}\left(\boldsymbol{Br},\boldsymbol{Ox},\boldsymbol{Mi},\boldsymbol{El}\right) + \boldsymbol{S_{Mic}}\left(\boldsymbol{Br},\boldsymbol{Ox},\boldsymbol{Mi},\boldsymbol{El}\right) + \boldsymbol{S_{Act}}\left(\boldsymbol{El}\right) + \boldsymbol{S_{Mn}}, \quad (91)$$

where

$\boldsymbol{S_{Hum}}\left(\boldsymbol{Br},\boldsymbol{Ox},\boldsymbol{Mi},\boldsymbol{El}\right)$ = solubility (i.e., concentration expressed in mol/l) in brine type Br of element El in oxidation state Ox with or without microbial action (Mi) resulting from formation of humic colloids

$$= \min\left\{\boldsymbol{SF_{Hum}}\left(\boldsymbol{Br},\boldsymbol{Ox},\boldsymbol{El}\right) \times \boldsymbol{S_D}\left(\boldsymbol{Br},\boldsymbol{Ox},\boldsymbol{Mi},\boldsymbol{El}\right), \boldsymbol{UB_{Hum}}\right\}$$

$\boldsymbol{SF_{Hum}}\left(\boldsymbol{Br},\boldsymbol{Ox},\boldsymbol{El}\right)$ = scale factor used as a multiplier on $\boldsymbol{S_D}\left(\boldsymbol{Br},\boldsymbol{Ox},\boldsymbol{Mi},\boldsymbol{El}\right)$ in definition of $\boldsymbol{S_{Hum}}\left(\boldsymbol{Br},\boldsymbol{Ox},\boldsymbol{Mi},\boldsymbol{El}\right)$ (see Table PA-10),

Table PA-10. Scale Factor $SF_{Hum}(Br, Ox, El)$ Used in Definition of $S_{Hum}(Br, Ox, Mi, El)$

Brine	Oxidation state, Element					
	+3, Am	+3, Pu	+4, Pu	+4, U	+6, U	+4, Th
Salado	0.19	0.19	6.3	6.3	0.12	6.3
Castile	WPHUMOX3[1]	WPHUMOX3[1]	6.3	6.3	0.51	6.3

[1] See Table PA-17.

UB_{Hum} = upper bound on solubility (i.e., concentration expressed in mol/l) of individual actinide elements resulting from formation of humic colloids

= 1.1×10^{-5} mol/l,

$S_{Mic}(Br, Ox, Mi, El)$ = solubility (i.e., concentration expressed in mol/l) in brine type Br of element El in oxidation state Ox with or without microbial action (Mi) resulting from formation of microbial colloids

= $\min\left\{SF_{Mic}(Ox, Mi, El) \times S_D(Br, Ox, Mi, El), UB_{Mic}(Ox, El)\right\}$,

$SF_{Mic}(Ox, Mi, El)$ = scale factor used as multiplier on $S_D(Br, Ox, Mi, El)$ in definition of $S_{Mic}(Br, Ox, Mi, El)$ (see Table PA-11),

$UB_{Mic}(Ox, El)$ = upper bound on solubility (i.e., concentration expressed in mol/l) of element El in oxidation state Ox resulting from formation of microbial colloids (see Table PA-11),

Table PA-11. Scale Factor $SF_{Mic}(Ox, Mi, El)$ and Upper Bound $UB_{Mic}(Ox, Mi, El)$ (mol/l) Used in Definition of $S_{Mic}(Br, Ox, Mi, El)$

Oxidation state, Element						
	+3, Am	+3, Pu	+4, Pu	+4, U	+6, U	+4, Th
No Microbial Action						
$SF_{Mic}(Ox, Mi, El)$	0.0	0.0	0.0	0.0	0.0	0.0
$UB_{Mic}(Ox, Mi, El)$	0.0	0.0	0.0	0.0	0.0	0.0
Microbial Action						
$SF_{Mic}(Ox, Mi, El)$	3.6	0.3	0.3	2.1×10^{-3}	2.1×10^{-3}	3.1
$UB_{Mic}(Ox, Mi, El)$	1	6.8×10^{-5}	6.8×10^{-5}	2.1×10^{-3}	2.1×10^{-3}	1.9×10^{-3}

$S_{Act}(El)$ = solubility (i.e., concentration expressed in mol/l) of element El resulting from formation of actinide intrinsic colloids

$$= \begin{Bmatrix} 1 \times 10^{-9}\ mol/l & if\ El = plutonium \\ 0\ \ mol/l & otherwise \end{Bmatrix},$$

S_{Mn} = solubility (i.e., concentration expressed in mol/l) of individual actinide element resulting from formation of mineral fragment colloids

= 2.6 × 10–8 mol/l.

PA-4.3.3 Radionuclides Transported

Appendix TRU WASTE (Table TRU WASTE-9) lists the radionuclides included in the transport calculations. With the exceptions of ^{137}Cs, ^{147}Pm, and ^{90}Sr, the radionuclides in Table TRU WASTE-9 belong to the following decay chains:

$$\begin{tikzcd} & {}^{238}Pu \arrow[d] \\ {}^{242}U \arrow[r] & {}^{238}U \arrow[r] & {}^{234}U \arrow[r] & {}^{230}Th \arrow[r] & {}^{226}Ra \arrow[r] & {}^{210}Pb \end{tikzcd} \tag{92a}$$

$$\begin{tikzcd} {}^{243}Cm \arrow[d] \\ {}^{243}Am \arrow[r] & {}^{239}Pu \arrow[r] & {}^{235}U \arrow[r] & {}^{231}Pa \end{tikzcd} \tag{92b}$$

$$^{252}Cf \rightarrow {}^{248}Cm \rightarrow {}^{244}Pu \rightarrow {}^{240}Pu \rightarrow {}^{236}U \rightarrow {}^{232}Th \rightarrow {}^{228}Ra \tag{92c}$$

$$^{245}Cm \rightarrow {}^{241}Pu \rightarrow {}^{241}Am \rightarrow {}^{237}Np \rightarrow {}^{233}U \rightarrow {}^{229}Th\,. \tag{92d}$$

Since the solution of Equation (83) for this many radionuclides and decay chains would be very time-consuming, the number of radionuclides for direct inclusion in the analysis was reduced using the algorithm shown in Appendix TRU WASTE (Figure TRU WASTE-5); the rationale for each radionuclide excluded from transport is presented in Table TRU WASTE-10. The CRA-2004 PA uses the same reduction algorithm as was used in the CCA PA (see CCA Appendix WCA); the algorithm was found to be acceptable in the review of the CCA (EPA 1998, Section 4.6.1.1).

After the reduction of radionuclides summarized in Table TRU WASTE-10, the following 10 radionuclides remained from the decay chains shown above:

$$^{242}Pu\ \ and\ \ {}^{238}U \rightarrow {}^{234}U \rightarrow {}^{230}Th \tag{93a}$$

$$^{239}Pu \tag{93b}$$

$$^{240}Pu \tag{93b}$$

$$^{241}Pu \rightarrow {}^{241}Am \rightarrow {}^{233}U \rightarrow {}^{229}Th\,. \tag{93d}$$

Next, ^{238}Pu was eliminated from transport calculations due to its short half-life (87.8 years). The remaining nine radionuclides were then further reduced by combining radionuclides that have similar decay and transport properties. In particular, ^{234}U, ^{230}Th, and ^{239}Pu were used as surrogates for the groups {^{234}U, ^{233}U}, {^{230}Th, ^{229}Th}, and {^{242}Pu, ^{239}Pu, ^{240}Pu}, with the initial inventories of ^{234}U, ^{230}Th and ^{239}Pu being redefined to account for the additional radionuclide(s) in each group. In redefining the initial inventories, the individual radionuclides were combined on either a mole or curie basis (i.e., moles added and then converted back to curies or curies added directly). In each case, the method that maximized the combined inventory was used, i.e.: ^{233}U was added to ^{234}U by curies; ^{240}Pu was added to ^{239}Pu by curies; ^{242}Pu was added to ^{239}Pu by moles; and ^{229}Th was added to ^{230}Th by curies. In addition, ^{241}Pu was added to ^{241}Am by moles because ^{241}Pu has a half life of 14 years and will quickly decay to ^{241}Am, and neglect of this ingrowth would underestimate the ^{241}Am inventory by about four percent (Table PA-12). The outcome of this process was the following five radionuclides and three simplified decay chains:

$$^{241}Am, \quad ^{238}Pu \rightarrow {}^{234}U \rightarrow {}^{230}Th, \quad ^{239}Pu, \tag{94}$$

which were then used with Equation (83) for transport in the vicinity of the repository and also for transport in the Culebra Dolomite (Section PA-4.9). These radionuclides account for 99 percent of the EPA units in the waste after 2,000 years (Appendix TRU WASTE, Table TRU WASTE-9), and hence will dominate any releases by transport.

Table PA-12. Combination of Radionuclides for Transport

Combination	Isotope Initial Values	Combination Procedure	Combined Inventory
$^{233}U \rightarrow {}^{234}U$	1.27 × 10^3 Ci ^{233}U 3.19 × 10^2 Ci ^{234}U	1.27 × 10^3 Ci ^{233}U → 1.27 × 10^3 Ci ^{234}U	1.59 × 10^3 Ci ^{234}U
$^{242}Pu \rightarrow {}^{239}Pu$	2.71 × 10^1 Ci ^{242}Pu	2.71 × 10^1 Ci ^{242}Pu = 2.82 × 10^1 moles ^{242}Pu → 2.82 × 10^1 moles ^{239}Pu = 4.24 × 10^2 Ci ^{239}Pu	7.73 × 10^5 Ci ^{239}Pu
$^{240}Pu \rightarrow {}^{239}Pu$	1.08 × 10^5 Ci ^{240}Pu 6.65 × 10^5 Ci ^{239}Pu	1.08 × 10^5 Ci ^{240}Pu → 1.08 × 10^5 Ci ^{239}Pu	
$^{229}Th \rightarrow {}^{230}Th$	5.39 × 10^0 Ci ^{229}Th 1.76 × 10^{-1} Ci ^{230}Th	5.39 × 10^0 Ci ^{229}Th → 5.39 × 10^0 Ci ^{230}Th	5.57 × 10^0 Ci ^{230}Th
$^{241}Pu \rightarrow {}^{241}Am$	5.38 × 10^5 Ci ^{241}Pu 4.58 × 10^5 Ci ^{241}Am	5.38 × 10^5 Ci ^{241}Pu = 2.15 × 10^1 moles ^{241}Pu → 2.15 × 10^1 moles ^{241}Am = 1.80 × 10^4 Ci ^{241}Am	4.60 × 10^5 Ci ^{241}Am

PA-4.3.4 Numerical Solution

Equation (83) is numerically solved by the NUTS program (WIPP PA 1997a) on the same computational grid (Figure PA-8) used by BRAGFLO in the solution of Equation (25). In the solution procedure, Equation (83a) is numerically solved with $S_l = 0$ for each time step, with the instantaneous updating of concentrations indicated in Equation (84) and the appropriate modification to C_{sl} in Equation (83b) taking place after the time step. The solution is carried out for the five radionuclides indicated in Equation (94).

The initial value and boundary value conditions used with Equation (83) are given in Table PA-13. At time t = 0 (i.e., year 2033), the total inventory of each radionuclide is assumed to be in brine; the solubility constraints associated with Equation (84) then immediately adjust the values for $C_{bl}(x, y, t)$ and $C_{sl}(x, y, t)$ for consistency with the constraints imposed by $S_T\,[Br(t), Ox(l), Mi, El(l)]$ and available radionuclide inventory.

Table PA-13. Initial and Boundary Conditions for $C_{bl}(x, y, t)$ and $C_{sl}(x, y, t)$

Initial Conditions for $C_{bl}(x, y, t)$ and $C_{sl}(x, y, t)$		
$C_{bl}(x,y,t)$	=	$A_l(0)/V_b(0)$ if x, y is a point in the repository (i.e., areas Waste Panel, South RoR and North RoR, in Figure PA-8), where $A_l(0)$ is the amount (kg) of radionuclide l present at time t = 0 (Table PA-12) and $V_b(0)$ is the amount (m^3) of brine in repository at time t = 0 (from solution of Equation (25) with BRAGFLO) for all x, y.
	=	0 otherwise.
$C_{sl}(x,y,t)$	=	0 if x, y is a point in the repository.
Boundary Conditions for $C_{bl}(x, y, t)$		
$f_l(\mathcal{B},t)$	=	$\int_{\mathcal{B}} \mathbf{v}_b(x,y,t)\, C_{bl}(x,y,t)\, \alpha(x,y) \cdot \mathbf{n}(x,y)\, ds$, where $\mathcal{B}$ is any subset of the outer boundary of the computational grid in Figure PA-8, $f_l(\mathcal{B},t)$ is the flux (kg/s) at time t of radionuclide l across $\mathcal{B}$, $\mathbf{v}_b(x,y,t)$ is the Darcy velocity ((m^3/m^2)/s) of brine at (x,y) on $\mathcal{B}$ and is obtained from the solution of Equation (25) by BRAGFLO, $\mathbf{n}(x,y)$ denotes an outward-pointing unit normal vector, and $\int_{\mathcal{B}} ds$ denotes a line integral along $\mathcal{B}$.

The nR partial differential equations in Equation (83a) are discretized in two dimensions and then developed into a linear system of algebraic equations for numerical implementation. The following conventions are used in the representation of each discretized equation:

- the subscript b is dropped from C_{bl}, with the result that the unknown function is represented by C_l,

- a superscript n denotes time (t_n), with the assumption that the solution C_l is known at time t_n and is to be advanced (i.e., computed) at time t_{n+1},

- the grid indices are i in the x-direction, j in the y-direction, and are identical with the BRAGFLO grid indices; fractional indices refer to quantities evaluated at grid block interfaces, and

- each time step by NUTS is equal to 20 BRAGFLO time steps, which results because BRAGFLO reported (i.e., stored) results (i.e., $\boldsymbol{v_b}$, ϕ, S_b) every 20 time steps.

The following finite difference discretization is used for the lth equation in each grid block i, j:

$$
\begin{aligned}
& q_{b,i+1/2,j}^{n+1} C_{l,i+1/2,j}^{n+1} - q_{b,i-1/2,j}^{n+1} C_{l,i-1/2,j}^{n+1} + q_{b,i,j+1/2}^{n+1} C_{l,i,j+1/2}^{n+1} - q_{b,i,j-1/2}^{n+1} C_{l,i,j-1/2}^{n+1} = \\
& \frac{V_{R,i,j}}{\Delta t}\left[\left\{\phi_{i,j} S_{b_{i,j}} C_{l,i,j}\right\}^{n+1} - \left\{\phi_{i,j} S_{b_{i,j}} C_{l,i,j}\right\}^{n}\right] \\
& + V_{R,i,j}\left\{\phi_{i,j} S_{b_{i,j}} C_{l,i,j}\right\}^{n+1} \lambda_l - V_{R,i,j}\left(\phi_{i,j} S_{b_{i,j}}\right)^{n+1} \sum_{p \in P(l)} C_{p,i,j}^{n+1} \lambda_p
\end{aligned}
\quad , (95)
$$

where q_b is the grid block interfacial brine flow rate (m^3/s) and V_R is the grid block volume (m^3). The quantity q_b is based on $\boldsymbol{v_b}$ and α in Equation (83a), and the quantity V_R is based on grid block dimensions (Figure PA-8) and α .

The interfacial values of concentration in Equation (95) are discretized using the one-point upstream weighting method (Aziz and Settari 1979), which results in

$$
\begin{aligned}
& q_{b,i+1/2,j}^{n+1}\left(\omega_{i+1} C_{l,i,j}^{n+1} + \left(1-\omega_{i+1}\right) C_{l,i+1,j}^{n+1}\right) - q_{b,i-1/2,j}^{n+1}\left(\omega_i C_{l,i-1,j}^{n+1} + \left(1-\omega_i\right) C_{l,i,j}^{n+1}\right) \\
& + q_{b,i,j+1/2}^{n+1}\left(\omega_{j+1} C_{l,i,j}^{n+1} + \left(1-\omega_{j+1}\right) C_{l,i,j+1}^{n+1}\right) - q_{b,i,j-1/2}^{n+1}\left(\omega_j C_{b,i,j-1}^{n+1} + \left(1-\omega_j\right) C_{l,i,j}^{n+1}\right) = \\
& \frac{V_{R,i,j}}{\Delta t}\left[\left\{\phi_{i,j} S_{b_{i,j}} C_{l,i,j}\right\}^{n+1} - \left\{\phi_{i,j} S_{b_{i,j}} C_{l,i,j}\right\}^{n}\right] + V_{R,i,j}\left\{\phi_{i,j} S_{b_{i,j}} C_{l,i,j}\right\}^{n+1} \lambda_l \\
& - V_{R,i,j}\left(\phi_{i,j} S_{b_{i,j}}\right)^{n+1} \sum_{p \in P(l)} C_{p,i,j}^{n+1} \lambda_p
\end{aligned}
\quad , (96)
$$

where ω derives from the upstream weighting for flow between adjacent grid blocks and is defined by

$$\omega_i = \begin{cases} 1 & \text{if flow is from grid block } i-1, j \text{ to grid block } i, j \\ 0 & \text{otherwise} \end{cases}$$

$$\omega_j = \begin{cases} 1 & \text{if flow is from grid block } i, j-1 \text{ to grid block } i, j \\ 0 & \text{otherwise.} \end{cases}$$

By collecting similar terms, Equation (96) can be represented by the linear equation

$$AC^{n+1}_{l,i,j-1} + BC^{n+1}_{l,i-1,j} - j + DC^{n+1}_{l,i,j} + EC^{n+1}_{l,i+1,j} + FC^{n+1}_{l,i,j+1} = R_{l,i,j}, \tag{97}$$

where

$$A = -\omega_j q^{n+1}_{b,i,j-1/2} \qquad B = -\omega_j q^{n+1}_{b,i-1/2,j}$$
$$E = \left(1-\omega_{i+1}\right) q^{n+1}_{b,i+1/2,j} \qquad F = \left(1-\omega_{j+1}\right) q^{n+1}_{b,i,j+1/2}$$

$$\begin{aligned} D = &-\left(1-\omega_j\right) q^{n+1}_{b,i,j-1/2} - \left(1-\omega_i\right) q^{n+1}_{b,i-1/2,j} + \omega_{j+1} q^{n+1}_{b,i,j+1/2} + \omega_{i+1} q^{n+1}_{b,i+1/2,j} \\ &-\left(\frac{V_{R,i,j}}{\Delta t} - V_{R,i,j}\lambda_l\right)\left\{\phi_{i,j} S_{b_{i,j}}\right\}^{n+1} \end{aligned}$$

$$R_{l,i,j} = -\frac{V_{R,i,j}}{\Delta t}\left\{\phi_{i,j} S_{b_{i,j}} C_{l,i,j}\right\}^{n} - V_{R,i,j}\left(\phi_{i,j} S_{b_{i,j}}\right)^{n+1} \sum_{p \in P(l)} C^{n+1}_{p,i,j}\lambda_p .$$

Given the form of Equation (97), the solution of Equation (83a) has now been reduced to the solution of nR × nG linear algebraic equations in nR × nG unknowns, where nR is the number of equations for each grid block (i.e., the number of radionuclides) and nG is the number of grid blocks into which the spatial domain is discretized (Figure PA-8).

The system of partial differential equations in Equation (83a) is strongly coupled because of the contribution from parental decay to the equation governing the immediate daughter. Consequently, a sequential method is used to solve the system in which radionuclide concentrations are solved for by starting at the top of a decay chain and working down from parent to daughter. This implies that when solving Equation (97) for the l^{th} isotope concentration, all parent concentrations occurring in the right hand side term R are known. The resulting system of equations is then linear in the concentrations of the l^{th} isotope. As a result, solution of Equation (83a) is reduced from the solution of one algebraic equation at each time step with nR × nG unknowns to the solution of nR algebraic equations each with nG unknowns at each time step, which can result in a significant computational savings.

The matrix resulting from one-point upstream weighting has the following structural form for a 3 × 3 system of grid blocks and a similar structure for a larger number of grid blocks:

	1	2	3	4	5	6	7	8	9
1	X	X	0	X					
2	X	X	X	0	X				
3	0	X	X	0	0	X			
4	X	0	0	X	X	0	X		
5		X	0	X	X	X	0	X	
6			X	0	X	X	0	0	X
7				X	0	0	X	X	0
8					X	0	X	X	X
9						X	0	X	X

,

where X designates possible nonzero matrix entries, and 0 designates zero entries. Entries outside of the banded structure are zero. Because of this structure, a banded direct elimination solver (Aziz and Settari 1979, Section 8.2.1) is used to solve the linear system for each radionuclide. The bandwidth is minimized by indexing equations first in the coordinate direction having the minimum number of grid blocks. The coefficient matrix is stored in this banded structure and all infill coefficients calculated during the elimination procedure are contained within the band structure. Therefore, for the matrix system in two dimensions, a pentadiagonal matrix of dimension IBW × nG is inverted instead of a full nG × nG matrix, where IBW is the band width.

The numerical implementation of Equation (83b) enters the solution process through an updating of the radionuclide concentrations in Equation (96) between each time step as indicated in Equation (84). The numerical solution of Equation (83) also generates the concentrations required for the numerical evaluation of the integral that defines $C_l(t,B)$ in Equation (88).

PA-4.3.5 Additional Information

Additional information on NUTS and its use in WIPP PA can be found in the NUTS users manual (WIPP PA 1997a) and in the analysis package for Salado transport calculations for the CRA-2004 PA (Lowry 2003). Furthermore, additional information on dissolved and colloidal actinides is given in Attachment SOTERM.

PA-4.4 Radionuclide Transport in the Salado: PANEL

This section describes the model used to compute transport of radionuclides in the Salado for E1E2 scenario. The model for transport in E0, E1, and E2 scenarios is described in Section PA-4.3.

PA-4.4.1 Mathematical Description

A relatively simple mixed-cell model is used for radionuclide transport in the vicinity of the repository when connecting flow between two drilling intrusions into the same waste panel is assumed to take place (i.e., an E1E2 intrusion). With this model, the amount of radionuclide l contained in a waste panel is represented by

$$\frac{dA_l}{dt} = -r_b C_{bl} - \lambda_l A_l + \sum_{p \in P(l)} \lambda_p A_p \,, \tag{98}$$

where

$A_l(t)$ = amount (mol) of radionuclide l in waste panel at time t,

$C_{bl}(t)$ = concentration (mol/m^3) of radionuclide l in brine in waste panel at time t (Equation (99)),

$r_b(t)$ = rate (m^3/s) at which brine flows out of the repository at time t (supplied by BRAGFLO from solution of Equation (81), and λ_l and ***P(l)*** are defined in conjunction with Equation (84).

The brine concentration C_{bl} in Equation (98) is defined by

$$C_{bl}(t) = S_T\left[Br(t), Ox(l), Mi, El(l)\right] MF_l(t) \quad \text{if} \quad S_T\left[Br(t), Ox(l), Mi, El(l)\right] \le \sum_{k \in El(l)} A_k(t)/V_b(t) \tag{99a}$$

$$= A_l(t)/V_b(t) \quad \text{if} \quad \sum_{k \in El(l)} A_k(t)/V_b(t) < S_T\left[Br(l), Ox(l), Mi, El(l)\right], \tag{99b}$$

where

$MF_l(t)$ = mole fraction of radionuclide l in waste panel at time t

$$= \frac{A_l(t)}{\sum_{k \in El(l)} A_k(t)} \tag{100}$$

$V_b(t)$ = volume (m^3) of brine in waste panel at time t (supplied by BRAGFLO from solution of Equation (25)), and $S_T\left[Br(l), Ox(l), Mi, El(l)\right]$ and ***E(l)*** are by Equation (89).

For use in Equation (99), $S_T\left[Br(l), Ox(l), Mi, El(l)\right]$ must be expressed in units of mol/l. In words, $C_{bl}(t)$ is defined to be the maximum concentration (S_T in Equation (89)) if there is sufficient radionuclide inventory in the waste panel to generate this concentration (Equation (99a)); otherwise, $C_{bl}(t)$ is defined by the concentration that results when all the relevant element in the waste panel is placed in solution (Equation (99b)).

Given r_b and C_{bl}, evaluation of the integral

$$\mathbf{v}_i(x,y) = \left[u_i(x,y), v_i(x,y)\right] = SFC\left[\mathbf{K}_i(x,y)\nabla h_i(x,y)\right]^T \qquad (101)$$

provides the cumulative release $R_l(t)$ of radionuclide l from the waste panel through time t.

PA-4.4.2 Numerical Solution

Equation (98) is numerically evaluated by the PANEL model (WIPP PA 1998b).

A discretization based on 50-year or smaller time steps is used by PANEL. Specifically, Equation (98) is evaluated with the approximation

$$A_l\left(t_{n+1}\right) = A_l\left(t_n\right) - \left[\int_{t_n}^{t_{n+1}} r_b(\tau)\,d\tau\right] C_{bl}\left(t_n\right) - A_l\left(t_n\right)\exp\left(-\lambda_l \Delta t\right) + G_l\left(t_n, t_{n+1}\right), \qquad (102)$$

where

$G_l\left(t_n, t_{n+1}\right)$ = gain in radionuclide l due to the decay of precursor radionuclides between t_n and t_{n+1} (see Equation (103)),

Δt = $t_{n+1} - t_n = 50\ yr$.

As the solution progresses, values for $C_{bl}\left(t_n\right)$ are updated in consistency with Equation (99) and the products $r_b\left(t_n\right)C_{bl}\left(t_n\right)$ are accumulated to provide an approximation to R_l in Equation (101).

The term $G_l\left(t_n, t_{n+1}\right)$ in Equation (102) is evaluated with the Bateman equations (Bateman 1910), with PANEL programmed to handle up to four succeeding generations of a given radionuclide (i.e., decay chains of length 5). As a single example, if radionuclide l is the third radionuclide in a decay chain (i.e., l = 3) and the two preceding radionuclides in the decay chain are designated by l = 1 and l = 2, then

$$\begin{aligned} G_3\left(t_n, t_{n+1}\right) = {} & \lambda_2 A_2\left(t_n\right)\left[\exp\left(-\lambda_2 \Delta t\right) - \exp\left(-\lambda_3 \Delta t\right)\right] / \left(\lambda_3 - \lambda_2\right) \\ & + \lambda_1 \lambda_2 A_2\left(t_n\right)\Big\{\left[\exp\left(-\lambda_1 \Delta t\right)\right] / \left[\left(\lambda_2 \lambda_1\right)\left(\lambda_3 \lambda_1\right)\right] \\ & \qquad + \left[\exp\left(-\lambda_2 \Delta t\right)\right] / \left[\left(\lambda_3 - \lambda_2\right)\left(\lambda_1 - \lambda_2\right)\right] \\ & \qquad + \left[\exp\left(-\lambda_3 \Delta t\right)\right] / \left[\left(\lambda_1 - \lambda_3\right)\left(\lambda_2 - \lambda_3\right)\right]\Big\} \end{aligned} \tag{103}$$

in Equation (102).

PA-4.4.3 Implementation in Performance Assessment

The preceding model was used in two ways in the CRA-2004 PA. First, Equation (101) was used to estimate releases to the Culebra associated with E1E2 intrusions (scenario S6; see Section PA-6.7). Second, with r_b set to a very small number and V_b set to a fixed value, Equation (98) and Equation (99) were used to estimate radionuclide concentrations in brine for use in the estimation of direct brine releases (see Section PA-6.8.5).

For E1E2 intrusions, the initial amount A_l of radionuclide l is the inventory of the isotope decayed to at the time of the E1 intrusion. Isotopes considered in the PANEL calculations for release to the Culebra are listed in Appendix TRU WASTE (Table TRU WASTE-9). PANEL calculates the inventory of each radionuclide throughout the regulatory period. The initial concentration C_{bl} of radionuclide l is computed by Equation (98) and Equation (99). For use as part of the direct brine release calculations, the initial amount Al of radionuclide l is the inventory of the isotope at the time of repository closure; isotopes considered in the PANEL calculations for direct brine releases are listed in Appendix TRU WASTE (Table TRU WASTE-9).

PA-4.4.4 Additional Information

Additional information on PANEL and its use in the CRA-2004 PA calculations can be found in the PANEL user's manual (WIPP PA 2003d) and the analysis package for PANEL calculations (Garner 2003).

PA-4.5 Cuttings and Cavings to Surface: CUTTINGS_S

Cuttings are waste solids contained in the cylindrical volume created by the cutting action of the drill bit passing through the waste. Cavings are additional waste solids eroded from the borehole by the upward-flowing drilling fluid within the borehole. The releases associated with these processes are computed within the CUTTINGS_S code (WIPP PA 2003e). The mathematical representations used for the first two processes, cuttings and cavings, are described in this section.

PA-4.5.1 Cuttings

The uncompacted volume of cuttings removed and transported to the surface in the drilling mud, V_{cut}, is given by

$$V_{cut} = AH_i = \pi D^2 H_i / 4 , \tag{104}$$

where H_i is the initial (i.e., uncompacted) repository height (m), A is the drill bit area (m^2), and D is the drill-bit diameter (m). In the CRA-2004 PA, D = 12.25 in. = 0.31115 m and H_i = 3.96 m (Attachment PAR, Table PAR-13). For drilling intrusions through RH-TRU waste, H_i = 0.509 m is used (Attachment PAR, Table PAR-45).

PA-4.5.2 Cavings

The cavings component of the direct surface release is caused by the shearing action of the drilling fluid (mud) on the waste as the mud flows up the borehole annulus. As for the cuttings release, the cavings release is assumed to be independent of the conditions that exist in the repository at the time of a drilling intrusion.

The final diameter of the borehole will depend on the diameter of the drillbit and on the extent to which the actual borehole diameter exceeds the drill-bit diameter. Although a number of factors affect erosion within a borehole (Broc 1982), the most important factor is believed to be the fluid shear stress on the borehole wall (i.e., the shearing force per unit area, (kg $m/s^2/m^2$)) resulting from circulating drilling fluids (Darley 1969; Walker and Holman 1971). As a result, the CRA-2004 PA estimates cavings removal with a model based on the effect of shear stress on the borehole diameter. In particular, the borehole diameter is assumed to grow until the shear stress on the borehole wall is equal to the shear strength of the waste (i.e., the limiting shear stress below which the erosion of the waste ceases).

The final eroded diameter D_f (m) of the borehole through the waste determines the volume V (m^3) of uncompacted waste that will be removed to the surface by circulating drilling fluid. Specifically,

$$V = V_{cut} + V_{cav} = \pi D_f^2 H_i / 4 , \tag{105}$$

where V_{cav} is the volume (m^3) of waste removed as cavings.

Most borehole erosion is believed to occur in the vicinity of the drill collar (Figure PA-14) because of decreased flow area and consequent increased mud velocity (Rechard et al. 1990, Letters 1a and 1b, App. A). An important determinant of the extent of this erosion is whether the flow of the drilling fluid in the vicinity of the collar is laminar or turbulent. The CRA-2004 PA uses Reynolds numbers to distinguish between the occurrence of laminar flow and turbulent flow. The Reynolds number is the ratio between inertial and viscous (i.e., shear) forces in a fluid and can be expressed as (Fox and McDonald 1985):

$$R_e = \frac{\rho_f \|\mathbf{v}\| D_e}{\eta} , \tag{106}$$

where R_e is the Reynolds number (dimensionless), ρ_f is the fluid density (kg m^{-3}), D_e is the equivalent diameter (m), v is the fluid velocity (m s^{-1}), and η is the fluid viscosity (kg m^{-1} s^{-1}).

Typically, ρ, v and η are averages over a control volume with an equivalent diameter of D_e. In the CRA-2004 PA, $\rho f = 1.21 \times 10^3$ kg m^{-3} (Attachment PAR, Table PAR-13), $\|\boldsymbol{v}\| = 0.7089$ m s^{-1} (based on 40 gallons/min per inch of drill diameter) (Berglund 1992), and $D_e = 2\,(R - R_i)$, as shown in Figure PA-14. The diameter of the drill collar (i.e., $2R_i$ in Figure PA-14) is 8.0 in = 0.2032 m (Dunagan 2003b). The determination of η is discussed below. Reynolds numbers less than 2100 are assumed to be associated with laminar flow, while Reynolds numbers greater than 2100 are assumed to be associated with turbulent flow (Walker 1976).

Drilling fluids are modeled as non-Newtonian, which means that the viscosity η is a function of the shear rate within the fluid (i.e., the rate at which the fluid velocity changes normal to the flow direction, ((m/s)/m). The CRA-2004 PA uses a model proposed by Oldroyd (1958) to estimate the viscosity of drilling fluids. As discussed by Broc (1982), the Oldroyd model leads to the following expression for the Reynolds number associated with the helical flow of a drilling fluid within an annulus:

$$R_e = \frac{0.8165 \rho_f \|\boldsymbol{v}\| D_e}{\eta_\infty}, \tag{107}$$

where ρ_f, $\|\boldsymbol{v}\|$ and D_e are defined as in Equation (106), and η_∞ is the asymptotic value for the derivative of the shear stress (τ, kg m^{-1} s^{-2}) with respect to the shear rate (Γ, s^{-1}) obtained as the shear rate increases (i.e., $\eta_\infty = d\tau/d\Gamma$ *as* $\Gamma \to \infty$). The CRA-2004 PA uses Equation (107) to obtain the Reynolds numbers that are used to determine whether drilling fluids in the area of the drill collar are undergoing laminar or turbulent flow.

The Oldroyd model assumes that the shear stress τ is related to the shear rate Γ by the relationship

$$\tau = \eta_0 \left(\frac{1 + \sigma_2 \Gamma^2}{1 + \sigma_1 \Gamma^2} \right) \Gamma, \tag{108}$$

where η_0 is the asymptotic value of the viscosity (kg m^{-1} s^{-1}) that results as the shear rate Γ approaches zero, and σ_1, σ_2 are constants (s^2). The expression leads to

$$\eta_\infty = \eta_0 \left(\frac{\sigma_2}{\sigma_1} \right). \tag{109}$$

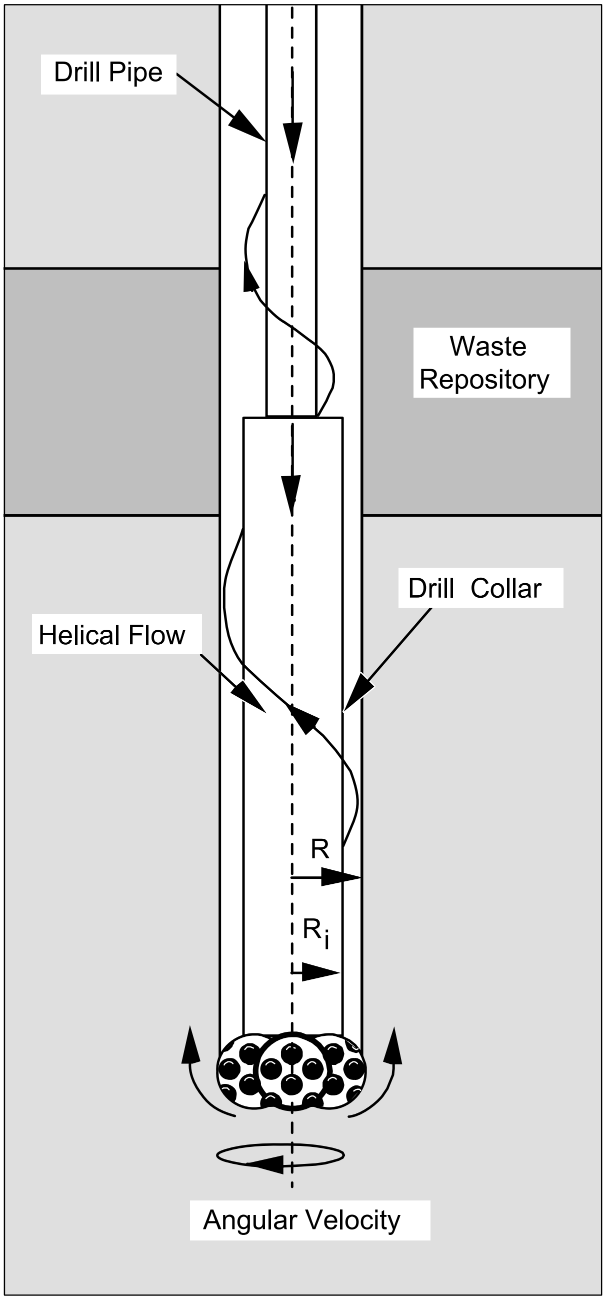

Figure PA-14. Detail of Rotary Drill String Adjacent to Drill Bit.

The CRA-2004 PA uses values of $\eta_0 = 1.834 \times 10^{-2}$ kg m^{-1} s^{-1}, $\sigma_1 = 1.082 \times 10^{-6}$ s^2 and $\sigma_2 = 5.410 \times 10^{-7}$ s^2 (Berglund 1996), and a resultant value of $\eta_\infty = 9.17 \times 10^{-3}$ kg m^{-1} s^{-1}. The quantity η_∞ is comparable to the plastic viscosity of the fluid (Broc 1982).

As previously indicated, different models are used to determine the eroded diameter D_f of a borehole depending on whether flow in the vicinity of the drill collar is laminar or turbulent. The model for borehole erosion in the presence of laminar flow is described next, and is then followed by a description of the model for borehole erosion in the presence of turbulent flow.

PA-4.5.2.1 Laminar Flow Model

As shown by Savins and Wallick (1966), the shear stresses associated with the laminar helical flow of a non-Newtonian fluid can be expressed as

$$\tau(R,r) = \left\{ \left[\frac{C}{r^2} \right]^2 + \left[\frac{RJ}{2} \left(\frac{r^2 - \lambda^2}{r} \right) \right]^2 \right\}^{1/2} \tag{110}$$

for $R_i / R \le r \le 1$, where R_i and R are the inner and outer radii within which the flow occurs as indicated in Figure PA-14; $\tau(R,\rho)$ is the shear stress (kg m^{-1} s^{-2}) at a radial distance ΔR beyond the inner boundary (i.e., at $r = (R_i + \Delta R)/R$); and the quantities C, J, and λ are functions of R that satisfy conditions indicated below. The shear stress at the outer boundary (i.e., R) is given by

$$\tau(R,1) = \left\{ C^2 + \left[\frac{RJ}{2} \left(1 - \lambda^2 \right) \right]^2 \right\}^{1/2}. \tag{111}$$

As previously indicated, the borehole radius R is assumed to increase as a result of erosional processes until a value of R is reached at which $\tau(R,1)$ is equal to the shear strength of the waste. In the CRA-2004 PA, the shear strength of the waste is treated as an uncertain parameter (see WTAUFAIL in Table PA-17). Computationally, determination of the eroded borehole diameter R associated with a particular value for waste shear strength requires repeated evaluation of $\tau(R,1)$, as indicated in Equation (111), until a value of R is determined for which $\tau(R,1)$ equals that shear strength.

The quantities C, J, and λ must satisfy the following three conditions (Savins and Wallick 1966) for the expression in Equation (111) to be valid:

$$0 = \int_{R_i/R}^{1} \left(\frac{\rho^2 - \lambda^2}{\rho\eta} \right) d\rho \tag{112a}$$

$$0 = C \int_{R_i / R}^{1} \left(\frac{1}{\rho^3 \eta} \right) d\rho - \Delta\Omega \tag{112b}$$

and

$$0 = \frac{4Q}{\pi R^3} + 2RJ \int_{R_i / R}^{1} \left(\frac{(R_i / R)^2 - \rho^2}{\rho\eta} \right) \left(\frac{\rho^2 - \lambda^2}{\rho\eta} \right) d\rho , \tag{112c}$$

where η is the drilling fluid viscosity (kg m^{-1} s^{-1}) and is a function of R and ρ, $\Delta\Omega$ is the drill string angular velocity (rad s^{-1}), and Q is the drilling fluid flow rate (m^3 s^{-1}).

The viscosity η in Equation (112) is introduced into the analysis through the assumption that the drilling fluid follows the Oldroyd model for shear stress in Equation (108). In particular, because

$$\tau = \eta\Gamma \tag{113}$$

as a result of the definition of the viscosity η and

$$\Gamma^2 = \frac{(\eta - \eta_0)}{(\eta_0\sigma_2 - \eta\sigma_1)} \tag{114}$$

from Equation (108), the expression in Equation (110) can be reformulated as

$$\frac{\eta^2 (\eta - \eta_0)^2}{(\eta_0\sigma_2 - \eta\sigma_1)^2} = \left[\frac{C}{\rho^2} \right]^2 + \left[\frac{RJ}{2} \left(\frac{\rho^2 - \lambda^2}{\rho} \right) \right]^2 . \tag{115}$$

As discussed by Savins and Wallick (1966) and also by Berglund (1992), the expressions in Equation (112) and Equation (114) can be numerically evaluated to obtain C, J, and λ for use in Equation (110) and Equation (111). In the CRA-2004 PA, the drill string angular velocity $\Delta\Omega$ is treated as an uncertain parameter (see DOMEGA in Table PA-17), and

$$Q = \|\boldsymbol{v}\| \left(\pi R^2 - \pi R_i^2 \right) , \tag{116}$$

where $\|\boldsymbol{v}\|$ = 0.7089 m s^{-1} as used in Equation (106), and η_0, σ_1, and σ_2 are defined by Equation (109).

PA-4.5.2.2 Turbulent Flow Model

The model for borehole erosion in the presence of turbulent flow is now described. Unlike the theoretically derived relationship for erosion in the presence of laminar flow, the model for borehole erosion in the presence of turbulent flow is empirically based. In particular, pressure loss for axial flow in an annulus under turbulent flow conditions can be approximated by (Broc 1982)

$$\Delta P = \frac{2\, f L \rho_f \left\| \mathbf{v} \right\|^2}{0.8165 D_e} \tag{117}$$

where ΔP is the pressure change (Pa), L is distance (m) over which pressure change ΔP occurs, f is the Fanning friction factor (dimensionless), and ρ_f, $\left\| \mathbf{v} \right\|$ and D_e are defined in Equation (106).

For pipe flow, f is empirically related to the Reynolds number R_e and a roughness term ε by (Whittaker 1985)

$$\frac{1}{\sqrt{f}} = -4 \log_{10}\left(\frac{\varepsilon}{3.72 D} + \frac{1.255}{R_e \sqrt{f}} \right), \tag{118}$$

where D is the inside diameter (m) of the pipe and ε is the average depth (m) of pipe wall irregularities. In the absence of a similar equation for flow in an annulus, Equation (118) is used in the CRA-2004 PA to define f for use in Equation (117), with D replaced by the effective diameter $D_e = 2\left(R - R_i\right)$ and ε equal to the average depth of irregularities in the waste-borehole interface. In the present analysis, ε = 0.025 m (Attachment PAR, Table PAR-34), which exceeds the value often chosen for use in calculations involving very rough concrete or riveted steel piping (Streeter 1958). Further, the Reynolds number R_e is defined in Equation (107).

The pressure change ΔP in Equation (117) and the corresponding shear stress τ at the walls of the annulus are approximately related by

$$\Delta P \left[\pi \left(R^2 - R_i^2 \right) \right] = \tau \left[2\pi L \left(R + R_i \right) \right] \tag{119}$$

where $\pi\left(R^2 - R_i^2\right)$ is the cross-sectional area of the annulus (see Figure PA-14) and $2\pi L\left(R + R_i\right)$ is the total (i.e., interior and exterior) surface area of the annulus. Rearrangement of Equation (117) and use of the relationship in Equation (113) yields

$$\tau = \frac{f \rho_f \left\| \mathbf{v} \right\|^2}{2(0.8165)}, \tag{120}$$

which was used in the 1991 and 1992 WIPP PAs to define the shear stress at the surface of a borehole of radius R. As a reminder, R enters into Equation (112a) through the use of $D = 2\left(R - R_i\right)$ in the definition of f in Equation (118). As in the case for laminar flow, the borehole radius R is assumed to increase until a value of τ (actually, $\tau\left(R\right)$) is reached that equals the sample value for the shear strength of the waste (i.e., the uncertain parameter WTAUFAIL in Table PA-17). Computationally, the eroded borehole diameter is determined by solving Equation (120) for R under the assumption that τ equals the assumed shear strength of the waste.

In the CRA-2004 PA, a slight modification to the definition of τ in Equation (120) was made to account for drill string rotation when fluid flow in the vicinity of the drill collars is turbulent (Abdul Khader and Rao 1974; Bilgen et al. 1973). Specifically, an axial flow velocity correction factor (i.e., a rotation factor), F_r, was introduced into the definition of τ. The correction factor F_r is defined by

$$F_r = \left\|\mathbf{v}_{2100}\right\| / \left\|\mathbf{v}\right\|, \tag{121}$$

where $\left\|\mathbf{v}_{2100}\right\|$ is the norm of the flow velocity required for the eroded diameters to be the same for turbulent and laminar flow at a Reynolds number of $R_e = 2100$ and is obtained by solving

$$\tau_{fail} = \frac{f \rho_f \left\|\mathbf{v}_{2100}\right\|^2}{2(0.8165)} \tag{122}$$

for $\left\|\mathbf{v}_{2100}\right\|$ with D in the definition of f in Equation (118) assigned the final diameter value that results for laminar flow at a Reynolds number of $R_e = 2100$ (i.e., the D in $D_e = 2\left(R - R_i\right) = D - 2R_i$ obtained from Equation (107) with $R_e = 2100$). The modified definition of τ is

$$\tau = \frac{f \rho_f \left(F_r \left\|\mathbf{v}\right\|\right)^2}{2(0.8165)}, \tag{123}$$

and results in turbulent and laminar flow having the same eroded diameter at a Reynolds number of 2100, which is the Reynolds number at which a transition between turbulent and laminar flow is assumed to take place.

PA-4.5.2.3 Calculation of R_f

The following algorithm was used to determine the final eroded radius R_f of a borehole and incorporates the possible occurrence of a transition from turbulent to laminar fluid flow within a borehole.

Step 1. Use Equation (107) to determine an initial Reynolds number R_e, with R set to the drill-bit radius, R_0 = 12.25 in (Attachment PAR, Table PAR-13).

Step 2. If $R_e < 2100$, the flow is laminar and the procedure in Section PA-4.5.2.1 is used to determine R_f. Because any increase in the borehole diameter will cause the Reynolds number to decrease, the flow will remain laminar and there is no need to consider the possibility of turbulent flow as the borehole diameter increases, with the result that R_f determined in this step is the final eroded radius of the borehole.

Step 3. If $R_e \geq 2100$, then the flow is turbulent and the procedure discussed in Section PA-4.5.2.2 is used to determine R_f. Once R_f is determined, the associated Reynolds number R_e is calculated with Equation (107) and $R = R_f$. If $R_e > 2100$, then a transition from turbulent to laminar flow cannot take place, and the final eroded radius is R_f determined in this step.

Step 4. If the Reynolds number R_e determined in Step 3 satisfies the inequality $R_e \leq 2100$, then a transition from turbulent to laminar flow is assumed to have taken place. In this case, the calculation of R_f is redone for laminar flow, with the outer borehole radius R initially defined to be the radius at which the transition from turbulent to laminar flow occurs (i.e., the radius associated with $R_e = 2100$). In particular, the initial value for R is given by

$$R = R_i + \frac{2100\eta_\infty}{2(0.8165)\|\mathbf{V}\|\rho}, \tag{124}$$

which is obtained from Equation (107) by solving for R with $R_e = 2100$. A new value for R_f is then calculated with the procedure discussed in Section PA-4.5.2.1 for laminar flow, with this value of R_f replacing the value from Step 3 as the final eroded diameter of the borehole.

Step 5. Once R_f is known, the amount of waste removed to the surface is determined by Equation (105) with $D_f = 2R_f$.

PA-4.5.3 Additional Information

Additional information on CUTTINGS_S and its use in the CRA-2004 PA to determine cuttings and cavings releases can be found in the CUTTINGS_S user’s manual (WIPP PA 2003e) and in the analysis package for cuttings and cavings releases (Dunagan 2003a).

PA-4.6 Spallings to Surface: DRSPALL and CUTTINGS_S

Spallings are waste solids introduced into a borehole by the movement of waste-generated gas towards the lower-pressure borehole. In engineering literature, the term “spalling” is used to describe the phenomenon of dynamic fracture of a solid material such as rock or metal (Antoun et al. 2003). In WIPP PA, the model for spallings describes a series of processes including tensile failure of solid waste, fluidization of failed material, entrainment into the wellbore flow, and transport up the wellbore to the land surface. Spallings releases could occur when pressure differences between the repository and the wellbore are sufficient to cause solid stresses in the waste exceeding the waste material strength and gas velocities sufficient to mobilize failed waste material.

The spallings model is described in the following sections. Presented first are the primary modeling assumptions used to build the conceptual model. Next, the mathematical model and its numerical implementation in the FORTRAN code DRSPALL (for Direct Release Spall) are described. Finally, implementation of the spallings model in WIPP PA by means of the code CUTTINGS_S.

PA-4.6.1 Summary of Assumptions

Assumptions underlying the spallings model include the future state of the waste, specifications of drilling equipment, and the driller's actions at the time of intrusion. Consistent with the other PA models, the spallings model assumes massive degradation of the emplaced waste through mechanical compaction, corrosion, and biodegradation. Waste is modeled as a homogeneous, isotropic, weakly-consolidated material with uniform particle size and shape. The rationale for selection of the spallings model material properties is addressed in detail in reports by Hansen et al. (1997, 2003).

Drilling equipment specifications, such as bit diameter and drilling mud density, are based on surveys of drillers in the Delaware Basin (Hansen et al. 2003). Assumptions about the driller's actions during the intrusion are conservative. Typically, the drilling mud density is controlled to maintain a slightly "overbalanced" condition so that the mud pressure is always slightly higher that the fluid pressures in the formation. If the borehole suddenly passes through a high-pressure zone, the well can quickly become "underbalanced," with a resulting fluid pressure gradient driving formation fluids into the wellbore. This situation is known as a "kick," and is of great concern to drillers because a violent kick can lead to a blowout of mud, gas, and oil from the wellbore, leading to equipment damage and worker injury. Standard drilling practice is to watch diligently for kicks. The first indicator of a kick is typically an increase in mud return rate leading to an increase in mud pit volume (Frigaard and Humphries 1997). Down-hole monitors detect whether the kick is air, H_2S, or brine. If the kick fluid is air, the standard procedure is to stop drilling and continue pumping mud in order to circulate the air pocket out. If the mud return rate continues to grow after drilling has stopped and the driller believes that the kick is sufficiently large to cause damage, the well may be shut in by closing the blowout preventer. Once shut in, the well pressure may be bled off slowly and mud weight eventually increased and circulated to offset the higher formation pressure before drilling continues. The spallings model simulates an underbalanced system in which a gas kick is assured, and the kick proceeds with no intervention from the drill operation. Therefore, drilling and pumping continue during the entire blowout event.

PA-4.6.2 Conceptual Model

The spallings model calculates transient repository and wellbore fluid flow before, during, and after the drilling intrusion. To simplify the calculations, both the wellbore and the repository are modeled by one-dimensional geometries. The wellbore assumes a compressible Newtonian fluid consisting of a mixture of mud, gas, salt and waste solids; viscosity of the mixture varies with the fraction of waste solids in the flow. In the repository, flow is viscous, isothermal, compressible single-phase (gas) flow in a porous medium.

The wellbore and repository flows are coupled by a cylinder of porous media before penetration, and by a cavity representing the bottom of the borehole after penetration. Schematic diagrams of the flow geometry prior to and after penetration are shown in Figure PA-15 and Figure PA-16, respectively. The drill bit moves downward as a function of time, removing salt or waste material. After penetration, waste solids freed by drilling, tensile failure, and associated fluidization may enter the wellbore flow stream at the cavity forming the repository-wellbore boundary.

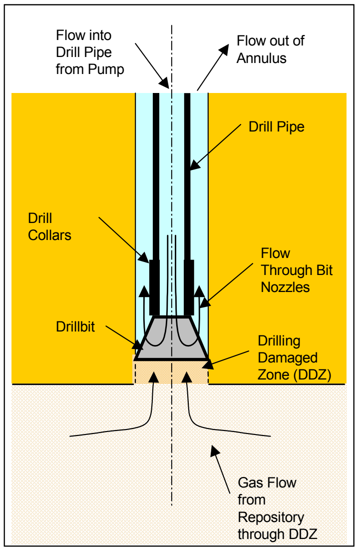

Figure PA-15. Schematic Diagram of the Flow Geometry Prior to Repository Penetration.

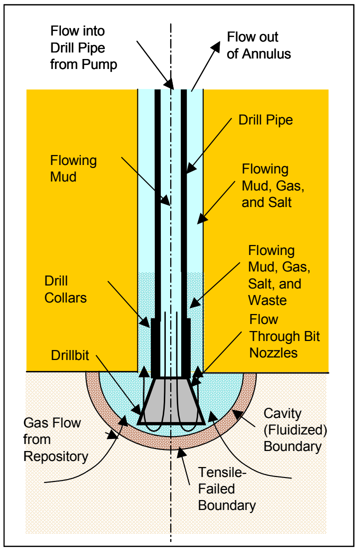

Figure PA-16. Schematic Diagram of the Flow Geometry After Repository Penetration.

PA-4.6.2.1 Wellbore Flow Model

Flow in the well is modeled as one-dimensional pipe flow with cross-sectional areas corresponding to the appropriate flow area at a given position in the well, as shown in Figure PA-17 and Figure PA-18. In concept, this model is similar to that proposed by Podio and Yang (1986) and now in use in the oil and gas industry. Drilling mud is added at the wellbore entrance by the pump. Flow through the drill bit is treated as a choke with cross-sectional area appropriate for the bit nozzle area. At the annulus output to the surface, mixture ejection is to a constant atmospheric pressure. The gravitational body force acts in its appropriate direction based on position before or after the bit.

Prior to drill bit penetration into the repository, gas from the repository can flow through drilling-damaged salt into the well. After penetration, the cavity at the bottom of the wellbore couples the wellbore flow and the repository flow models; gas and waste material can exit the repository domain into the cavity. The cavity radius increases as waste materials are moved into the wellbore.

The system of equations representing flow in the wellbore includes: four equations for mass conservation, one for each phase (salt, waste, mud and gas); one equation for conservation of total momentum; two equations relating gas and mud density to pressure; the definition of density for the fluid mixture; and one constraint imposed by the fixed volume of the wellbore. The conservation of mass and momentum are described by:

$$\frac{\partial}{\partial t}\left(\rho_q V_q\right)+\frac{\partial}{\partial z}\left(\rho_q V_q u\right)=S_q \tag{125a}$$

$$\frac{\partial}{\partial t}\left(\rho V u\right)+\frac{\partial}{\partial z}\left(\rho V u^2\right)=-V\left(\frac{\partial P}{\partial z}-\rho g+F\right)+S_{mom}\,, \tag{125b}$$

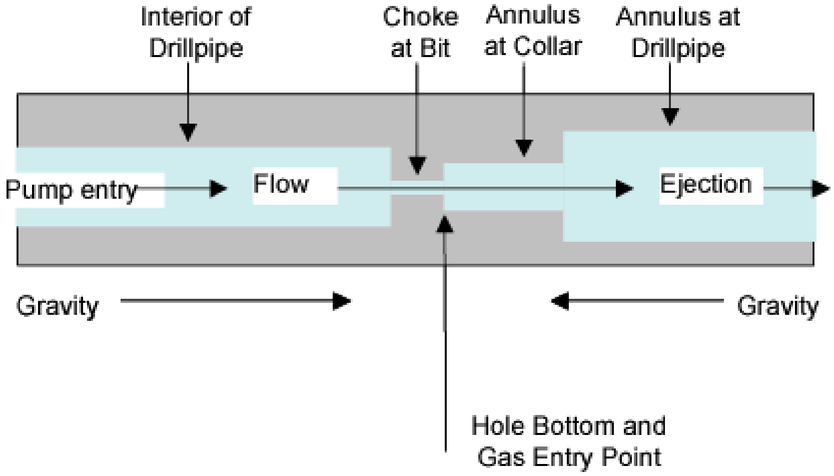

Figure PA-17. Effective Wellbore Flow Geometry Before Bit Penetration.

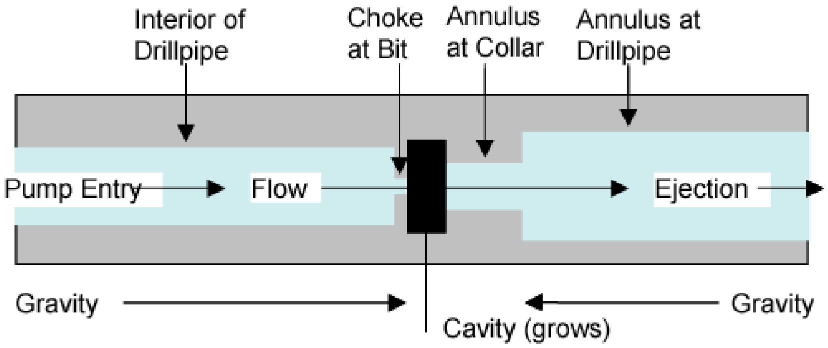

Figure PA-18. Effective Wellbore Flow Geometry After Bit Penetration.

where

q = phase (w for waste, s for salt, m for mud, and g for gas),

V_q = volume (m^3) of phase q,

V = total volume (m^3) ,

ρ_q = density (kg/m^3) of phase q, constant for salt and waste (2180 and 2650 kg/m^3, respectively) and pressure-dependent for gas and mud (see Equation (126) and Equation (127)),

ρ = density of fluid mixture (kg/m^3) determined by Equation (128),

u = velocity (m/s) of fluid mixture in wellbore ,

t = time (s),

z = distance (m) from inlet at top of well ,

S_q = rate of mass (kg/s) of phase q entering and exiting wellbore domain at position z (Equation (138)),

S_{mom} = rate of momentum ($kg\ m / s^2$) entering and exiting wellbore domain at position z (Equation (141)),

P = pressure (Pa) at position z ,

g = gravity constant (9.8067 $kg/m\ s^2$),

F = friction loss using pipe flow model ($kg/m^2\ s^2$) determined by Equation (130).

Gas is treated as isothermal and ideal, so

$$\frac{\rho}{\rho_{g,0}} = \frac{P}{P_{atm}}, \tag{126}$$

where $\rho_{g,0}$ is the density of the gas at atmospheric pressure (8.24182×10^{-2} kg/m^3 in the CRA-2004 PA).

The mud is assumed to be a compressible liquid, so

$$\rho_m = \rho_{m,0}\left[1 + c_m\left(P - P_{atm}\right)\right], \tag{127}$$

where $\rho_{m,0}$ is the density of the mud at atmospheric pressure (1210 kg/m^3 in the CRA-2004 PA) and c_m is the compressibility of the mud (3.1×10^{-10} Pa^{-1} in the CRA-2004 PA).

The density of the fluid mixture is determined from the densities and volumes occupied by the phases:

$$\rho = \frac{\rho_g V_g + \rho_m V_m + \rho_s V_s + \rho_w V_w}{V}. \tag{128}$$

The volume of each phase is constrained by the fixed volume of the wellbore:

$$V = V_g + V_m + V_s + V_w. \tag{129}$$

The friction loss is a standard formulation for pipe flow (Fox and McDonald 1985), where the head loss per unit length is given as:

$$F = f\frac{\rho}{d_h}\frac{u^2}{2}. \tag{130}$$

The hydraulic diameter d_h is given by

$$d_h = \frac{4A}{\pi\left(D_i + D_o\right)}. \tag{131}$$

In the CRA-2004 PA, $D_o = 0.31115$ m throughout the domain. From the bit to the top of the collar, $D_i = 0.2032$ m; above the collar, $D_i = 0.1143$ m. The area A is calculated as the area of the annulus between the outer and inner radii. Thus, $d_h = 0.108$ m from the bit to the top of the collar, and $d_h = 0.197$ m above the collar.

The friction factor f is determined by method of Colebrook (Fox and MacDonald 1985). In the laminar regime (Re < 2100)

$$f = \frac{64}{\mathrm{Re}}, \tag{132}$$

and in the turbulent regime (Re > 2100)

$$\frac{1}{\sqrt{f}} = 1.0 \log\left(\frac{\varepsilon/d_h}{3.7} + \frac{2.51}{\mathrm{Re}\sqrt{f}}\right), \tag{133}$$

where $\mathrm{Re} = \frac{u\rho d_h}{\eta}$ is the Reynolds number of the mixture, and η is the viscosity calculated by Equation (134). As the wellbore mixture becomes particle-laden, the viscosity of the mixture is determined from an empirical relationship developed for proppant slurry flows in channels for the oil and gas industry (Barree and Conway 1995). Viscosity is computed by an approximate slurry formula based on the volume fraction of waste solids:

$$\eta = \eta_0 \left(1 - \frac{w}{w_{max}}\right)^s, \tag{134}$$

where η_0 is a base mixture viscosity (9.17×10^{-3} Pa sec in the CRA-2004 PA), $w = V_w / V$ is the current volume fraction of waste solids, w_{max} is an empirically determined maximal volume fraction above which flow is choked (0.615 in the CRA-2004 PA), and s is an empirically determined constant (−1.5 in the CRA-2004 PA) (Hansen et al. 2003).

PA.-4.6.2.1.1 Wellbore initial conditions

Initial conditions in the wellbore approximate mixture flow conditions just prior to penetration into the waste. The wellbore is assumed to contain only mud and salt. Initial conditions for the pressure, fluid density, volume fractions of mud and salt, and the mixture velocity are set by the following algorithm.

Step 1. Set pressure in the wellbore to hydrostatic: $P(z) = P_{atm} + \rho_{m,0} g z$.

Step 2. Set mud density using Equation (127).

Step 3. Set mixture velocity: $u(z) = \frac{R_m}{A(z)}$, where R_m is the volume flow rate of the pump (0.0202 m^3/s in the CRA-2004 PA), and $A(z)$ is the cross-sectional area of the wellbore.

Step 4. Set volume of salt in each cell: $V_{s,i} = R_{drill} A_{bit} \frac{\Delta z_i}{u_i}$, where R_{drill} is the rate of drilling (0.004445 m/s in the CRA-2004 PA), $A_{bit} = \frac{\pi d_{bit}^2}{4}$ is the area of the bottom of the wellbore and d_{bit} is the diameter of the bit (0.31115 m in the CRA-2004 PA).

Step 5. Set volume fraction of mud in each cell: $V_{m,i} = V_i - V_{s,i}$.

Step 6. Recalculate mixture density using Equation (128), assuming no waste or gas in the wellbore.

The initial conditions set by this algorithm approximate a solution to the wellbore flow (Equation (125)) for constant flow of mud and salt in the well. The approximation rapidly converges to a solution for wellbore flow if steady-state conditions are maintained (WIPP PA 2003f).

PA-4.6.2.1.2 Wellbore boundary conditions

For simplicity, the CRA-2004 PA does not model flow of mud down the pipe to the bit. Mass can enter the wellbore below the drill bit, and can exit at the wellbore outlet. Below the bit, mud, salt, gas, and waste can enter the wellbore. The CRA-2004 PA assumes a constant volume of mud flow down the drilling pipe; therefore, the source term for mud, $S_{m,\,in}$, is set by the volume flow rate of the pump R_m (0.0202 m^3/s in the CRA-2004 PA) and the density of the mud at the bottom of the wellbore:

$$S_{m,in} = \rho_m R_m . \tag{135}$$

Until the drill bit penetrates the repository, salt enters the wellbore at a constant rate:

$$S_{s,in} = \rho_s R_{drill} A_{bit} . \tag{136}$$

Additional mass enters the wellbore by gas flow from the repository ($S_{gas,in}$) or by drilling or spalling of waste material ($S_{w,in}$); these mass sources are discussed in Section PA-4.6.2.3. The outlet of the wellbore is set to atmospheric pressure. Mass exiting the wellbore is determined from the mixture velocity, the area of the outlet A_{out} (0.066 m^2 in the CRA-2004 PA), and the density and volume fraction of each phase at the outlet of the wellbore:

$$S_{q,out} = \rho u_{out} A_{out} \frac{V_q}{V} . \tag{137}$$

Finally, the net change in mass for phase q is

$$S_q = S_{q,in} - S_{q,out} . \tag{138}$$

$$S_{mom,in} = \frac{\rho_{0,m}}{A_p} R_{mudpump} . \tag{139}$$

The outlet of the wellbore is set to atmospheric pressure. Momentum exiting the wellbore is determined from the fluid velocity and the area of the outlet A_{out} (0.066 m^2 in the CRA-2004 PA):

$$S_{mom,out} = -\rho A_{out} u_{out}^2 . \tag{140}$$

No momentum is added by mass flow into the wellbore from the repository, thus:

$$S_{mom} = S_{mom,in} - S_{mom,out} . \tag{141}$$

PA-4.6.2.2 Repository Flow Model

The repository is modeled as a radially-symmetric domain. A spherical coordinate system is used for this presentation and for most DRSPALL calculations in the CRA-2004 PA. In a few circumstances, cylindrical coordinates are used in CRA-2004 PA calculations, where spall volumes are large enough that spherical coordinates are not representative of the physical process (Lord et al. 2003). Cylindrical coordinates are also available; the Design Document for DRSPALL (WIPP PA 2003g) provides details on the implementation of the repository flow model in cylindrical coordinates.

Flow in the repository is transient, compressible, viscous, and single phase (gas) flow in a porous medium. Gas is treated as isothermal and ideal. The equations governing flow in the repository are the equation of state for gas, conservation of mass, and Darcy’s law with the Forchheimer correction (Aronson 1986; Whitaker 1996):

$$\frac{\rho_g}{\rho_{g,0}} = \frac{P}{P_{atm}} , \tag{142a}$$

$$\phi \frac{\partial \rho_g}{\partial t} + \nabla \cdot \left(\rho_g u \right) = 0 , \tag{142b}$$

$$\nabla P = -\frac{\eta_g}{k} \left(1 + F \right) u , \tag{142c}$$

where

P = pressure in pore space (Pa),

ρ_g = density of gas (kg/m^3),

u = velocity of gas in pore space (m/s),

ϕ = porosity of the solid (unitless),

η_g = gas viscosity (8.934×10^{-6} Pa s),

k = permeability of waste solid (m^2),

F = Forchheimer coefficient (unitless).

The Forchheimer correction is included to account for inertia in the flowing gas, which becomes important at high gas velocities (Ruth and Ma 1992). When the Forchheimer coefficient is zero, Equation (142c) reduces to Darcy's Law. A derivation of Equation (142c) from the Navier-Stokes equations is given by Whitaker (1996); the derivation suggests that F is a linear function of gas velocity for a wide range of Reynolds numbers.

In the CRA-2004 PA, the Forchheimer coefficient takes the form

$$F = \beta_{nd} \rho u, \tag{143}$$

where β_{nd} is the non-Darcy coefficient, which depends on material properties such as the tortuosity and area of internal flow channels, and is empirically determined (Belhaj et al. 2003). The CRA-2004 PA uses a value from a study by Li et al. (2001) that measured high-velocity nitrogen flow through porous sandstone wafers, giving the result

$$\beta_{nd} = \frac{1.15 \times 10^{-6}}{k\phi}. \tag{144}$$

Equation (142) combines into a single equation for pressure in the porous solid:

$$\frac{\partial P}{\partial t} = \frac{k'}{2\phi\eta_g} \nabla^2 P^2 + \frac{1}{2\phi\eta_g} \nabla P^2 \cdot \nabla k', \tag{145}$$

where

$$k' = \frac{k}{1+F} = \frac{k}{1+\beta_{nd}\rho u}, \tag{146}$$

and the operator in a radially-symmetric coordinate system is given by

$$\nabla^2 = \frac{1}{r^{n-1}} \frac{\partial}{\partial r}\left(r^{n-1} \frac{\partial}{\partial r} \right), \tag{147}$$

where n = 2 and n = 3 for cylindrical and spherical coordinates, respectively.

In the CRA-2004 PA, the permeability of the waste solid is a subjectively uncertain parameter that is constant for waste material that has not failed and fluidized. In a region of waste that has failed, the permeability increases as the waste fluidizes by a factor of $1 + F_f$, where F_f is the fraction of failed material that has fluidized and is based on the fluidization relaxation time. This approximately accounts for the bulking of material as it fluidizes.

Initial pressure in the repository is set to a constant value P_{ff}. A no-flow boundary condition is imposed at the outer boundary (r = R):

$$\nabla \boldsymbol{P}\left(\boldsymbol{R}\right) = \boldsymbol{0}. \tag{148}$$

At the inner boundary ($r = r_{cav}$), the pressure is specified as $\boldsymbol{P}\left(\boldsymbol{r_{cav}}, \boldsymbol{t}\right) = \boldsymbol{P_{cav}}\left(\boldsymbol{t}\right)$, where $\boldsymbol{P_{cav}}\left(\boldsymbol{t}\right)$ is defined in the next section. The cavity radius r_{cav} increases as drilling progresses and as waste material fails and moves into the wellbore; calculation of r_{cav} is described in Section PA-4.6.2.3.3.

PA-4.6.2.3 Wellbore to Repository Coupling

Prior to penetration, a cylinder of altered-permeability salt material with diameter equal to the drill bit is assumed to connect the bottom of the wellbore to the repository. At the junction of the repository and this cylinder of salt, a small, artificial cavity is used to determine the boundary pressure for repository flow. After penetration, the cavity merges with the bottom of the wellbore to connect the wellbore to the repository.

PA-4.6.2.3.1 Flow Prior to Penetration

The cylinder of salt connecting the wellbore to the repository is referred to as the Drilling Damaged Zone (DDZ) in Figure PA-15. The permeability of the DDZ, k_{DDZ}, is 1×10^{-14} (m^2) in the CRA-2004 PA. The spall model starts with the bit 0.15 m above the repository; the bit advances at a rate of $R_{drill} = 0.004445$ (m/s).

To couple the repository to the DDZ, the model uses an artificial pseudo-cavity in the small hemispherical region of the repository below the wellbore, with the same surface area as the bottom of the wellbore (Figure PA-18). The pseudo-cavity is a numerical device that smoothes the discontinuities in pressure and flow that would otherwise occur upon bit penetration of the repository. The pseudo-cavity contains only gas and is initially at repository pressure. The mass of gas in the cavity m_{cav} is given by:

$$\frac{\boldsymbol{dm_{cav}}}{\boldsymbol{dt}} = \boldsymbol{S_{rep}} - \boldsymbol{S_{g,in}}, \tag{149}$$

where

S_{rep} = gas flow from repository into pseudo-cavity (kg/s); see Equation (150),

$S_{g,\,in}$ = gas flow from pseudo-cavity through DDZ into wellbore (kg/s); see Equation (151).

Flow from the repository into the pseudo-cavity is given by

$$S_{rep} = \rho_{g,rep} u_{rep} \phi A_{cav}, \tag{150}$$

where

$\rho_{g,rep}$ = gas density in repository at cavity surface (kg/m^3) = $\rho_g\left(r_{cav}\right)$,

u_{rep} = gas velocity (m/s) in repository at cavity surface = $u\left(r_{cav}\right)$,

ϕ = porosity of waste (unitless),

A_{cav} = surface area of hemispherical part of the cavity (m^2),

= $\frac{\pi}{4} d_{bit}^2$, where d_{bit} is the diameter of the bit (m).

Flow out of the pseudo-cavity through the DDZ and into the wellbore is modeled as steady-state using Darcy's Law:

$$S_{g,in} = \frac{k_{DDZ}\pi\left(\frac{d_{bit}}{2}\right)^2}{2\eta_g R_0 T L}\left(P_{cav}^2 - P_{BH}^2\right), \tag{151}$$

where

η_g = gas viscosity (8.934×10^{-6} Pa s),

R_0 = ideal gas constant for hydrogen (4116 J / kg °K),

T = repository temperature (constant at 300 °K),

L = length (m) of DDZ (from bottom of borehole to top of repository)

P_{cav} = pressure in pseudo-cavity (Pa),

P_{BH} = pressure at bottom of wellbore (Pa).

A justification for the use of this steady-state equation is provided in the Design Document for DRSPALL (WIPP PA 2003g). The pseudo-cavity is initially filled with gas at a pressure of P_{ff}. The boundary pressure on the well side (P_{BH}) is the pressure immediately below the bit, determined by Equation (125). The pressure in the pseudo-cavity (P_{cav}) is determined by the ideal gas law:

$$P_{cav} = \frac{m_{cav} R_0 T}{V_{cav}}, \tag{152}$$

where the volume of the cavity V_{cav} is given by

$$V_{cav} = \left(\frac{\pi}{24\sqrt{2}} \right) d_{bit}^3 . \tag{153}$$

In the CRA-2004 PA the drilling rate is constant at 0.004445 (m/s) thus $L = L_i - 0.004445t$ until $L = 0$, at which time the bit penetrates the waste. The term L_i is the distance from the bit to the waste at the start of calculation (0.15 m in the CRA-2004 PA).

PA-4.6.2.3.2 Flow After Penetration

After penetration of the waste, the bottom of the wellbore is modeled as a hemispherical cavity in the repository, the radius of which grows as drilling progresses and as material fails and moves into the cavity. Gas, drilling mud, and waste are assumed to thoroughly mix in this cavity; the resulting mixture flows around the drill collars and then up the annulus between the wellbore and the drill string. Gas flow from the repository into the cavity is given by Equation (150); however, A_{cav} is now dependent on the increasing radius of the cavity (see Section PA-4.6.2.3.3). Mudflow into the cavity from the wellbore is given by Equation (135). Waste flow into the cavity is possible if the waste fails and fluidizes; these mechanisms are discussed in Sections PA-4.6.2.3.4 and PA-4.6.2.3.5. Pressure in the cavity is equal to the pressure at the bottom of the wellbore and is computed by Equation (152).

PA-4.6.2.3.3 Cavity Volume After Penetration

The cylindrical cavity of increasing depth created by drilling is mapped to a hemispherical volume at the bottom of the wellbore to form the cavity. This mapping maintains equal surface areas in order to preserve the gas flux from the repository to the wellbore. The cavity radius from drilling is thus

$$r_{drill} = \sqrt{\frac{d_{bit}^2 + 4 d_{bit} \Delta H}{8}}, \tag{154}$$

where ΔH is the depth of the drilled cylinder. In the CRA-2004 PA, the drilling rate is constant at 0.004445 (m/s) thus $\Delta H = 0.004445t$ until $\Delta H = H$, the height of compacted waste (m). Since the initial height of the repository is 3.96 m, H is computed from the porosity ϕ by $H = 3.96 \times \frac{1 - \phi_0}{1 - \phi}$, where ϕ is the initial porosity of a waste-filled room.

The cavity radius r_{cav} is increased by the radius of failed and fluidized material r_{fluid}, which is the depth to which fluidization has occurred beyond the drilled radius. That is,

$$r_{cav} = r_{drill} + r_{fluid} \,. \tag{155}$$

PA-4.6.2.3.4 Waste Failure

Gas flow from the waste creates a pressure gradient within the waste, which induces elastic stresses in addition to the far-field confining stress. These stresses may lead to tensile failure of the waste material, assumed to be prerequisite to spallings releases. While the fluid calculations using Equation (142) are fully transient, the elastic stress calculations are assumed to be quasi-static (i.e., sound-speed phenomena in the solid are ignored). Elastic effective stresses are (Timoshenko and Goodier 1970):

$$\sigma_r(r) = \sigma_{sr}(r) + \sigma_{ff}\left(1 - \left(\frac{r_{cav}}{r}\right)^3\right) + P(r_{cav})\left(\frac{r_{cav}}{r}\right)^3 - \beta P(r), \tag{156}$$

$$\sigma_\theta(r) = \sigma_{s\theta}(r) + \sigma_{ff}\left[1 + \frac{1}{2}\left(\frac{r_{cav}}{r}\right)^2\right] - \frac{P(r_{cav})}{2}\left(\frac{r_{cav}}{r}\right)^3 - \beta P(r), \tag{157}$$

where β is Biot's constant (1.0 in the CRA-2004 PA) and σ_{ff} is the confining far-field stress (assumed constant at 14.9 MPa in the CRA-2004 PA).

The flow-related radial and tangential stresses (σ_{sr} and $\sigma_{s\theta}$, respectively) are computed by equations analogous to differential thermal expansion (Timoshenko and Goodier 1970):

$$\sigma_{sr}(r) = 2\beta\left(\frac{1-2\upsilon}{1-\upsilon}\right)\frac{1}{r^3}\int_{r_{cav}}^{r}\left(P(s) - P_{ff}\right)s^2 ds, \tag{158}$$

$$\sigma_{s\theta}(r) = -\beta\left(\frac{1-2\upsilon}{1-\upsilon}\right)\left(\frac{1}{r^3}\int_{r_{cav}}^{r}\left(P(s) - P_{ff}\right)s^2 ds - \left(P(r) - P_{ff}\right)\right), \tag{159}$$

where P_{ff} is the initial repository pressure and υ is Poisson's ratio (0.38 in the CRA-2004 PA).

Since stresses are calculated as quasi-static, an initial stress reduction caused by an instantaneous pressure drop at the cavity face propagates instantaneously through the waste. The result of calculating Equation (156) can be an instantaneous early-time tensile failure of the entire repository if the boundary pressure is allowed to change suddenly. This is non-physical and merely a result of the quasi-static stress assumption combined with the true transient pore pressure and flow-related stress equations. To prevent this non-physical behavior, tensile failure propagation is limited by a tensile failure velocity (1000 m/s in the CRA-2004 PA; see Hansen et al. 1997). This limit has no quantitative effect on results other than to prevent non-physical tensile failure.

At the cavity face, Equation (156) and Equation (158) evaluate to zero, consistent with the quasi-static stress assumption. This implies that the waste immediately at the cavity face cannot experience tensile failure; however, tensile failure may occur at some distance into the waste material. Consequently, the radial effective stress σ_r is averaged from the cavity boundary into the waste over a characteristic length L_t (0.02 m in the CRA-2004 PA). If this average radial stress $\bar{\sigma}_r$ is tensile and its magnitude exceeds the material tensile strength ($|\bar{\sigma}_r| > \mathit{TENSLSTR}$), the waste is no longer capable of supporting radial stress and fails, permitting fluidization. The waste tensile strength is an uncertain parameter in the analysis (see TENSLSTR in Table PA-14).

Equation (157) and (159) evaluate shear stresses in the waste. The CRA-2004 PA does not use the shear stresses in the waste in the calculation of waste failure for spall releases. These stresses are included in this discussion for completeness.

PA-4.6.2.3.5 Waste Fluidization

Failed waste material is assumed to be disaggregated, but not in motion; it remains as a porous, bedded material lining the cavity face, and is treated as a continuous part of the repository from the perspective of the porous flow calculations. The bedded material may be mobilized and may enter the wellbore if the gas velocity in the failed material (see Equation (142c)) exceeds a minimum fluidization velocity, U_f. The minimum fluidization velocity is determined by solving the following quadratic equation (Cherimisinoff and Cherimisinoff 1984; Ergun 1952):

$$\frac{1.75}{a\phi^3}\left(\frac{d_p U_f \rho_g}{\eta_g}\right)^2 + 150\left(\frac{1-\phi}{a^2\phi^3}\right)\left(\frac{d_p U_f \rho_g}{\eta_g}\right) = \frac{d_p^3 \rho_g \left(\rho_w - \rho_g\right) g}{\eta_g^2}, \qquad (160)$$

where

a = particle shape factor (unitless),

d_p = particle diameter (m).

Fluidization occurs in the failed material to the depth at which gas velocity does not exceed the fluidization velocity; this depth is denoted by r_{fluid} and is used to determine cavity radius (Section PA-4.6.2.3.3). If fluidization occurs, the gas and waste particles mix into the cavity at the bottom of the wellbore. To account for the fact that this mixing cannot be instantaneous, which would be non-physical (much as allowing instantaneous tensile failure propagation would be non-physical), a small artificial relaxation time, equal to the cavity radius r_{cav} divided by the superficial gas velocity $u\left(r_{cav}\right)$, is imposed upon the mixing phenomenon. The fluidized material is released into the cavity uniformly over the relaxation time.

PA-4.6.3 Numerical Model

The numerical model implements the conceptual and mathematical models described above. Both the wellbore and the repository domain calculations use time-marching finite differences.

These are part of a single computational loop and therefore use the same time step. The differencing schemes for the wellbore and repository calculations are similar, but not identical.

PA-4.6.3.1 Numerical Method – Wellbore

The wellbore is zoned for finite differencing as shown in Figure PA-19. This shows zones, zone indices, grid boundaries, volumes, and interface areas. The method is Eulerian; i.e., zone boundaries are fixed, and fluid flows across the interfaces by advection. Quantities are zone-centered and integration is explicit in time.

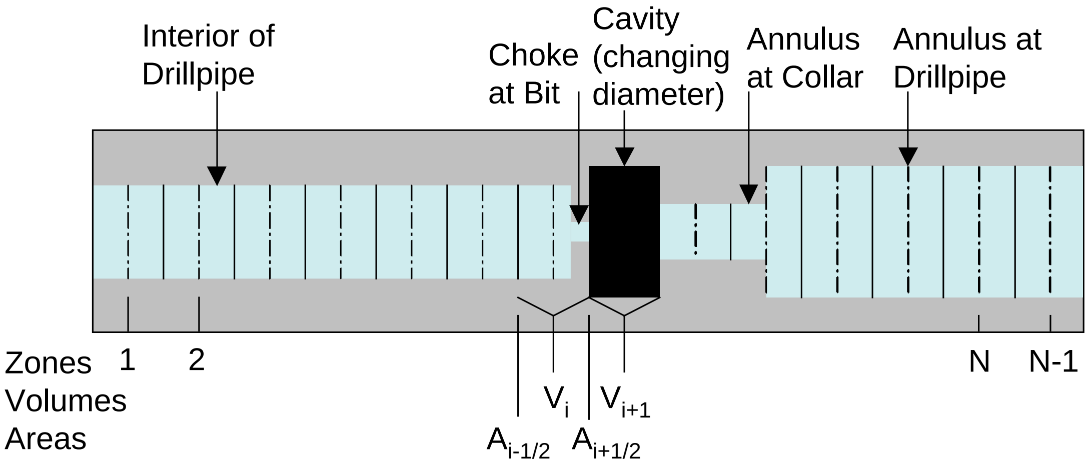

Figure PA-19. Finite Difference Zoning for Wellbore.

To reduce computation time, an iterative scheme is employed to update the wellbore flow solution. The finite difference scheme first solves Equation (125) for the mass of each phase in each grid cell and the momentum in each grid cell.

The updated solution to Equation (125) is then used to compute the volume of each phase, the pressure, and the mixture velocity in each grid cell.

All of the materials (mud, salt, gas, and waste) are assumed to move together as a mixture. Since fluid moves through the cell boundaries, the calculation requires values for the flow through cell boundaries during a timestep. These values are obtained by averaging the fluid velocities at the zone centers, given by:

$$u_{i+1/2} = \frac{1}{2}\left(u_{i+1}^{n-1} + u_i^{n-1}\right). \tag{161}$$

The mass transport equation, prior to any volume change, becomes

$$V_i \rho_i^* = V_i \rho_i^{n-1} - \Delta t\left(A_{i+1/2}\rho_{i+1/2}^{n-1}u_{i+1/2} - A_{i-1/2}\rho_{i-1/2}^{n-1}u_{i-1/2}\right) + \Delta t S_{m,i}. \tag{162}$$

Here, the source terms $\left(S_{m,i}\right)$ are set to correspond to material entering or exiting at the pump, cavity, and surface. The "upwind" zone centered densities are used for the interfaces values, $\rho_{i+1/2}^{n-1}$ and $\rho_{i-1/2}^{n-1}$.

Finally any changed volumes are incorporated and numerical mass diffusion is added for stability:

$$V_i \rho_i^n = V_i \rho_i^* + \Delta z_i \sum_{q=w,m,s,g} \zeta_q D_{i,q}, \tag{163}$$

where

$$D_{i,q} = \left[A_{i+1/2}\left(\left(\rho f_q\right)_{i+1}^{n-1} - \left(\rho f_q\right)_i^{n-1}\right) - A_{i-1/2}\left(\left(\rho f_q\right)_i^{n-1} - \left(\rho f_q\right)_{i-1}^{n-1}\right)\right]$$

and ζ_q is the diffusion coefficient for phase q. The density ρf_q for the phase q being diffused is calculated from the mixture density, ρ, and the mass fraction, f_q, of the phase q in the referenced cell ($f_q = \rho V_{q,i} / \rho V_i$). The numerical diffusion coefficient ζ_q is chosen empirically for stability. Separate diffusion coefficients could be used for the different materials (mud, gas, etc.). However, sufficient stability is obtained by only diffusing mud and salt using the same coefficient ($\zeta_m = \zeta_s = 0.0001$ and $\zeta_w = \zeta_g = 0$ in the CRA-2004 PA).

Momentum is differenced as:

$$\begin{aligned} V_i \left(\rho u\right)_i^* = {} & V_i \left(\rho u\right)_i^{n-1} - \Delta t\left(A_{i+1/2}\left(\rho u\right)_{i+1/2}^{n-1} u_{i+1/2} - A_{i-1/2}\left(\rho u\right)_{i-1/2}^{n-1} u_{i-1/2}\right) \\ & - V_i \Delta t\left(\frac{P_{i+1}^{n-1} - P_{i-1}^{n-1}}{2\Delta z} - \rho_i^{n-1} g + F_i^{n-1}\right) + \Delta t S_{mom,i}, \end{aligned} \tag{164}$$

where the dissipation term F_i^{n-1} is obtained from Equation (130) and is constrained by:

$$\left|F_i^{n-1}\right| \le \left|\frac{P_{i+1}^{n-1} - P_{i-1}^{n-1}}{2\Delta z} - \rho_i^{n-1} g\right|, \qquad 165)$$

and the sign of F_i^{n-1} is chosen to oppose flow. Finally, numerical momentum diffusion is added without distinguishing between phases in the mixture (ρ is the mixture density).

$$V_i \left(\rho u\right)_i^n = V_i \left(\rho u\right)_i^* - \zeta_p \Delta x_i \left[A_{i+1/2}\left(\left(\rho u\right)_{i+1}^{n-1} - \left(\rho u\right)_i^{n-1}\right) - A_{i-1/2}\left(\left(\rho u\right)_i^{n-1} - \left(\rho u\right)_{i-1}^{n-1}\right)\right]. \tag{166}$$

In the CRA-2004 PA, $\zeta_p = 0.01$.

Equation (127), Equation (128), and Equation (129) comprise a simultaneous system of equations for the volumes of gas and mud, and the pressure in the wellbore. The volumes of salt and waste will be known, since they are considered incompressible. Equation (127) and Equation (128) combine into a quadratic equation for gas volume

$$aV_g^2 + bV_g - c = 0\,, \tag{167}$$

where

$$\begin{aligned} a &= 1 - c_m P_{atm}, \\ b &= c_m P_{atm} V_{g,0} - aV^* + V_{m,0}, \\ c &= V^* c_m P_{atm} V_{g,0}, \\ V_{g,0} &= m_g / \rho_{g,0}, \\ V_{m,0} &= m_m / \rho_{m,0}, \end{aligned}$$

and

$$V^* = V_m + V_g = V - V_s - V_w$$

The volume of the mud phase follows from Equation (127) and the pressure from Equation (126). Once mixture density in each cell (ρ_i) is updated by Equation (128), mixture velocity in each cell (u_i) is computed by

$$u_i = \frac{(\rho u)_i}{\rho_i}\,,$$

where the quantity $\rho\, u$ is determined by Equation (166).

PA-4.6.3.2 Numerical Method – Repository

The time integration method for the repository flow is implicit, with spatial derivatives determined after the time increment. This method requires the inversion of a matrix for the entire repository, which is usually straightforward. The implicit scheme is unconditionally stable. However, it is still necessary to use small time steps to ensure gradient accuracy.

The numerical method follows Press et al. (1989). For simplicity, the equations are presented for constant zone size, although DRSPALL implements difference equations that allow for a variable zone size. Near the cavity, a small, constant zone size is used, and then zones are allowed to grow geometrically as the outer boundary is approached. This procedure greatly increases computational efficiency without sacrificing accuracy in the region of interest.

For an isothermal ideal gas, the pseudopressure is defined as

$$\psi = \frac{P^2}{\eta} \quad \text{or} \quad P = \sqrt{\eta\psi}\,. \tag{168}$$

Using Equation (168), Equation (145) is expanded to

$$\frac{\partial\psi}{\partial t} = D(\psi)\left[\frac{\partial^2\psi}{\partial r^2} + \frac{(m-1)}{r}\frac{\partial\psi}{\partial r} + \frac{1}{k'}\frac{\partial k'}{\partial r}\frac{\partial\psi}{\partial r}\right], \tag{169}$$

where $D(\psi) = \frac{k'}{\phi}\sqrt{\frac{\psi}{\eta}} = \frac{k'P}{\phi\eta}$; Equation (169) is then converted to a difference equation by treating $D(\psi)$ as constant over a zone, using its zone-centered value at the current time D_j^n:

$$\frac{\psi_j^{n+1} - \psi_j^n}{\Delta t} = \frac{D_j^n}{\Delta r}\left[\frac{\psi_{j+1}^{n+1} - 2\psi_j^{n+1} + \psi_{j-1}^{n+1}}{\Delta r} + \frac{(m-1)\left(\psi_{j+1}^{n+1} - \psi_{j-1}^{n+1}\right)}{2r_j} + \frac{\left(k'^{\,n+1}_{j+1} - k'^{\,n+1}_{j-1}\right)\left(\psi_{j+1}^{n+1} - \psi_{j-1}^{n+1}\right)}{4k'\Delta r}\right]. \tag{170}$$

Collecting similar terms in ψ leads to a tridiagonal system:

$$-\alpha 1\psi_{j-1}^{n+1} + (1+2\alpha\alpha)\,{}_j^{n+1} - \alpha 2\psi_{j+1}^{n+1} = \psi_j^n - \alpha_1\Psi_{j-1}^{n+1} + (1+2\alpha \quad \text{j = 1,2….,} \tag{171}$$

where

$$\alpha = \frac{D_j^n \Delta t}{(\Delta r)^2},$$

$$\alpha_1 = \left(\frac{D_j^n}{\Delta r}\right)\left(\frac{1}{\Delta r} - \frac{(m-1)}{2r_j} - \frac{k'^{\,n+1}_{i+1} - k'^{\,n+1}_{i-1}}{4k'\Delta r}\right)\Delta t,$$

$$\alpha_2 = \left(\frac{D_j^n}{\Delta r}\right)\left(\frac{1}{\Delta r} + \frac{(m-1)}{2r_j} + \frac{k'^{\,n+1}_{i+1} - k'^{\,n+1}_{i-1}}{4k'\Delta r}\right)\Delta t.$$

Equation (171) may be solved by simplified LU decomposition as presented in Press et al. (1989).

The boundary condition at the inner radius is implemented by noting that for i = 1 (the first intact or non-fluidized cell), ψ_{i-1} is the cavity pseudopressure, which is known, and therefore can be moved to the right hand side of Equation (171):

$$\left(1+2\alpha\right)\psi_1^{n+1}-\alpha_2\psi_2^{n+1}=\psi_1^n+\alpha_1\psi_{cav}^{n+1}. \tag{172}$$

The far field boundary condition is a zero gradient, which is implemented by setting $\psi_{j+1}^{n+1}=\psi_j^{n+1}$ in Equation (172), recognizing that $1+2\alpha=1+\alpha_1+\alpha_2$ and rearranging, which gives

$$-\alpha_1\psi_{j-1}^{n+1}+\left(1+\alpha_1\right)\psi_j^{n+1}=\psi_j^n, \tag{173}$$

where j is the index of the last computational cell.

PA-4.6.3.3 Numerical Method – Wellbore to Repository Coupling

The term u_{rep}, appearing in Equation (150), is the gas velocity in the repository at the waste-cavity interface and is determined from the pressure gradient inside the waste. The CRA-2004 PA uses the pressure (P_1) at the center of the first numerical zone in the waste to determine u_{rep} :

$$u_{rep}=\frac{k\left(P_1-P_{cav}\right)}{\Delta r\eta_g\phi}. \tag{174}$$

PA-4.6.4 Implementation

During development of the spallings model, a total of five parameters were determined to be both uncertain and potentially significant to model results (Hansen et al. 2003; Lord and Rudeen 2003). All five parameters relate to the repository conditions or the state of the waste at the time of intrusion. Table PA-14 lists the uncertain parameters in the DRSPALL calculations.

The computational requirements of DRSPALL prohibit calculation of spall volumes for all possible combinations of initial conditions and parameter values. Since repository pressure is a time-dependent value computed by the BRAGFLO model (see Section PA-4.2), DRSPALL calculations were performed for a small number of pressures. Sensitivity studies showed that spall does not occur at pressures below 10 MPa; this value was used as the lower bound on

Table PA-14. Uncertain Parameters in the DRSPALL Calculations

Parameter	Variable	Implementation
Repository Pressure	REPIPRES	Initial repository pressure (Pa); spall calculated for values of 10, 12, 14, and 14.8 MPa. Defines initial repository pressure in Equation (145) (see Section PA-4.6.2.2) and Pff in Equation (158).
Repository Permeability	REPIPERM	Permeability (m^2) of waste, implemented by parameter SPALLMOD/REPIPERM. Loguniform distribution from 2.4×10^{-14} to 2.4×10^{-12}. Defines k in Equation (142c).
Repository Porosity	REPIPOR	Porosity (dimensionless) of waste, implemented by parameter SPALLMOD/REPIPOR. Uniform distribution from 0.35 to 0.66. Defines ϕ in Equation (142b).
Particle Diameter	PARTDIAM	Particle diameter of waste (m) after tensile failure, implemented by parameter SPALLMOD/PARTDIAM. Loguniform distribution from 0.001 to 0.1 (m). Defines d_p in Equation (160).
Tensile Strength	TENSLSTR	Tensile strength of waste (Pa), implemented by parameter SPALLMOD/TENSLSTR. Uniform distribution from 0.12 MPa to 0.17 MPa. Defines $\bar{\sigma}_r$ in Section PA-4.6.2.3.5.

pressure. In DRSPALL, the repository pressure cannot exceed the far-field confining stress (14.9 MPa in the CRA-2004 PA); consequently, 14.8 MPa was used as the upper bound on pressure. Computations were also performed for intermediate pressures of 12 and 14 MPa.

The remaining four parameters listed in Table PA-14 were treated as subjectively uncertain. The uncertainty represented by these parameters pertains to the future state of the waste, which is modeled in PA as a homogeneous material with uncertain properties. In order to ensure that sampled values are independent and that the extremes of each parameter's range are represented in the results, the CRA-2004 PA uses Latin hypercube sampling to generate a sample of 50 elements. The LHS generated for DRSPALL calculations is independent of the LHS generated for the general PA calculations. Spall volumes are computed for each combination of initial pressure and sample element, for a total of 4 × 50 = 200 model runs. Although repository porosity could be treated as an initial condition (using the time-dependent value computed by BRAGFLO), to reduce the number of computational cases, and to ensure that extreme porosity values were represented, repository porosity was included as a sampled parameter. The LHS for DRSPALL and the results of the DRSPALL calculations are presented in Lord et al. (2003).

The spallings submodel of the code CUTTINGS_S uses the DRSPALL results to compute the spall volume for a given initial pressure P. An uncertain parameter SPALLMOD/RNDSPALL is included in the LHS for performance assessment (see Section PA-5.2) and is sampled from a uniform distribution on $[0,1]$. This parameter selects a sample element from the LHS for DRSPALL. The DRSPALL results for the selected sample element are used to construct the spall volume. If $P < 10$ MPa or $P > 14.8$ MPa, the spall volume is the value computed for REPIPRESS = 10 MPa or REPIPRESS = 14.8 MPa, respectively. If P falls between 10 and 14.8 MPa, the spall volume is constructed by linear interpolation between the DRSPALL results for pressures which bracket P.

PA-4.6.5 Additional Information

Additional information on DRSPALL and its use in the CRA-2004 PA to determine spallings releases can be found in the User's Manual for DRSPALL (WIPP PA 2003h) and in the analysis package for spallings releases (Lord et al. 2003). Additional information on the construction of spall volumes by the code CUTTINGS_S can be found in the CUTTINGS_S Design Document (WIPP PA 2003i).

PA-4.7 Direct Brine Release to Surface: BRAGFLO

This section describes the model for direct brine release (DBR) volumes, which are volumes of brine released to the surface at the time of a drilling intrusion. DBR volumes are calculated by the code BRAGFLO, the same code used to compute two-phase flow in and around the repository (see Section PA-4.2).

PA-4.7.1 Overview of Conceptual Model

DBRs could occur if the pressure in the repository at the time of a drilling intrusion exceeds 8 MPa, which is the pressure exerted by a column of brine-saturated drilling fluid at the depth of the repository (Stoelzel and O'Brien 1996). For repository pressures less than 8 MPa, no DBRs are assumed to occur. However, even if the repository pressure exceeds 8 MPa at the time of a drilling intrusion, a DBR is not assured, as there might not be sufficient mobile brine in the repository to result in movement towards the borehole.

DBRs are estimated for the following cases: (1) an initial intrusion into the repository into either a lower (down-dip), middle, or upper (up-dip) panel, (2) an intrusion into a waste panel that has been preceded by an E1 intrusion into either the same waste panel, an adjacent panel, or a non-adjacent panel, and (3) an intrusion into a waste panel that has been preceded by an E2 intrusion into either the same waste panel, an adjacent panel, or a non-adjacent panel (see Section PA-6.7). To determine releases for the above cases, the DBR calculations use a computational grid that explicitly includes all 10 waste panels (Figure PA-20).

The DBRs are assumed to take place over a relatively short period of time (i.e., 3 to 11 days) following the drilling intrusion. The initial value conditions for determining DBR volumes are obtained by mapping solutions of Equation (25) obtained from BRAGFLO with the computational grid in Figure PA-8 onto the grid in Figure PA-20.

In concept, the DBR for a drilling intrusion has the form

$$\boldsymbol{DBR = \int_0^{t_e} rDBR\left(t\right) dt}\,, \tag{175}$$

where

DBR = direct brine release volume (m^3) for drilling intrusion,

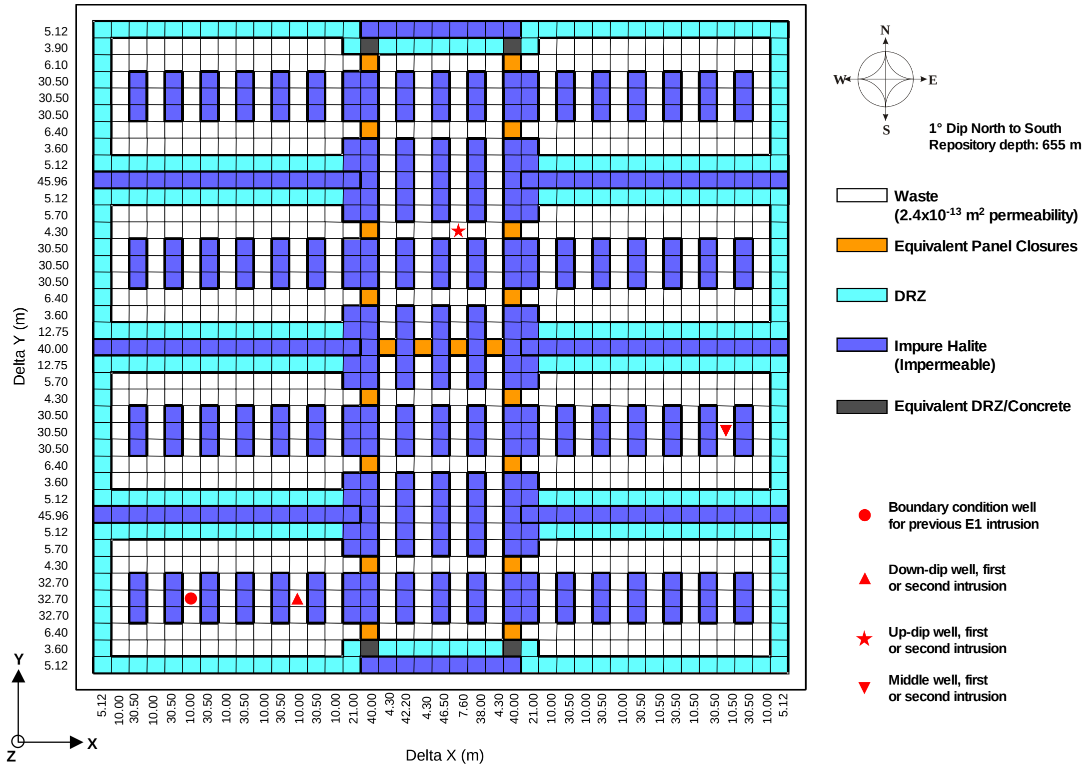

Note: Model cells are not to scale. The actual dimensions of the grid blocks are indicated along the edge of the diagram.

Figure PA-20. DBR Logical Mesh.

$\boldsymbol{rDBR}(\boldsymbol{t})$ = rate (m^3) at time t at which brine flows up intruding borehole,

t = elapsed time (s) since drilling intrusion,

t_e = time (s) at which direct brine release ends.

The definition of $\boldsymbol{rDBR}(\boldsymbol{t})$ is discussed in the following sections and is based on the two-phase flow relationships in Equation (25) and use of the Poettmann-Carpenter correlation (Poettmann and Carpenter 1952) to determine a boundary pressure at the connection between the intruding borehole and the repository. The time t_e is based on current drilling practices in the Delaware Basin (Section PA-4.7.8).

PA-4.7.2 Linkage to Two-Phase Flow Calculation

The mesh in Figure PA-20 was linked to the mesh in Figure PA-8 by subdividing the waste disposal area in the mesh in Figure PA-8 into three regions (Figure PA-21). Region 1 represents the northern rest of repository North RoR area in Figure PA-8. Region 2 represents the southern rest of repository South RoR area in Figure PA-8. Region 3 represents the farthest down-dip repository area Waste Panel in Figure PA-8 that contained waste and thus corresponds to the single down-dip waste panel. The linkage between the solutions to

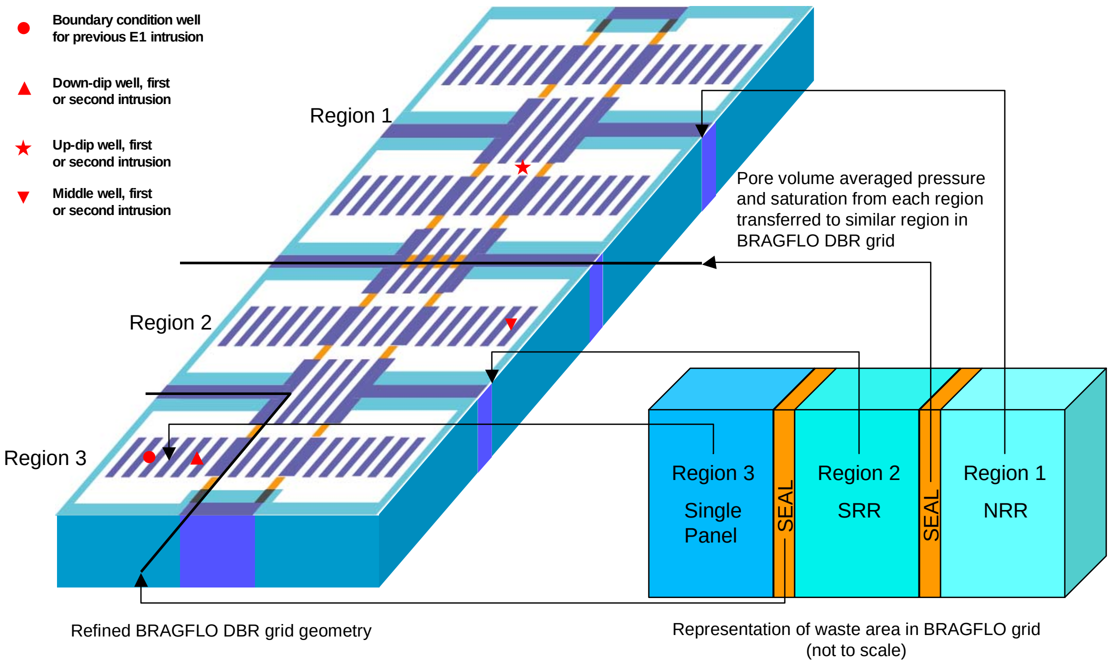

Figure PA-21. Assignment of Initial Conditions for DBR Calculation at Each Intrusion Time.

Equation (25) and the DBR calculations was made by assigning quantities calculated by BRAGFLO for each region in Figure PA-8 to the corresponding waste region in Figure PA-20.

The height of the grid in Figure PA-20 was assigned a value that corresponded to the crushed height h (m) of the waste as predicted by the solution of Equation (25). Specifically,

$$h = h_i \frac{1-\phi_i}{1-\phi}, \tag{176}$$

where h_i and ϕ_i are the initial height (m) and porosity of the waste and ϕ is the volume-averaged porosity of the waste at the particular time under consideration (Section PA-4.2.3). The areas designated equivalent panel closures, DRZ, and impure halite in Figure PA-20 were assigned the same pressures and saturations as the corresponding grid blocks in the 10,000 year BRAGFLO calculations. The area designated equivalent DRZ/concrete (Figure PA-20) was assigned the same pressures and saturations as the DRZ. These areas were assigned porosities that resulted in a conservation of the initial pore volumes used for these areas in the solution of Equation (25) on the grid in Figure PA-8. Specifically, the pore volumes associated with the panel closures, DRZ, and impure halite do not change with time, with this constancy implemented by the definitions of $\varphi(x,y,0)$ in Table PA-15.

The initial brine pressure $p_b(x,y,0)$ and gas saturation $S_g(x,y,0)$ in the grid in Figure PA-20 are assigned by:

$$p_b\left(x,y,0\right)=\int_R \tilde{p}_b\left(\tilde{x},\tilde{y},t_{int}\right)dV \,/\int_R dV\,, \tag{177}$$

$$S_g\left(x,y,0\right)=\int_R \tilde{S}_g\left(\tilde{x},\tilde{y},t_{int}\right)dV \,/\int_R dV\,, \tag{178}$$

where $\left(x,y\right)$ designates a point in the grid in Figure PA-20, $\tilde{p}_b$ and $\tilde{S}_g$ denote solutions to Equation (25), $\tilde{x}$ and $\tilde{y}$ denote the variables of integration, tint is the time at which the drilling intrusion occurs, and R corresponds to the region in the computational grid for BRAGFLO (Figure PA-8) that is mapped into the region in the computational grid for BRAGFLO for DBR (Figure PA-20) that contains the point $\left(x,y\right)$ (Figure PA-21). Note that t_{int} defines a time in the solution of Equation (25); t = 0 defines the start time for the DBR calculation and corresponds to t_{int} in the solution of Equation (25).

The initial porosity $\phi\left(x,y,0\right)$ in the grid in Figure PA-20 is set by the equations listed in Table PA-15. In Table PA-15, hi is initial height of waste panels (3.96 m), $\phi_{WP,i}$ is initial porosity of waste panels (0.848), $h\left(t_{int}\right)$ is height of repository at time of intrusion (typically 1 to 1.5 m; corresponds to h in Equation (25)), $h_{DRZ,i}$ is initial height for DRZ (43.60 m) that results in DRZ in Figure PA-20 having the same pore volume as the initial pore volume of the DRZ in Figure PA-8, A_{DRZ} is area associated with DRZ in Figure PA-20, and $\phi_{DRZ,i}$ is initial porosity of DRZ (see Table PA-2). The quantity $h_{DRZ,i} \times A_{DRZ} \times \phi_{DRZ,i}$ is equal to pore volume of DRZ above and below the waste filled regions in Figure PA-8. In Table PA-15, the term ϕ_C is the porosity of the panel closure concrete material (CONC_PCS; see Table PA-2), d_1 is the length of the drift/explosion wall portion of the panel closure (32.1 m; see Figure PA-13), and d_2 is the length of the concrete portion of the panel closure (7.9 m; see Figure PA-13). The porosity of the panel closure and the equivalent DRZ/concrete materials are defined as the volume-weighted mean porosity of the component materials; this definition results in the same brine volume within the pore space in each set of panel closures in Figure PA-8 and Figure PA-20. In Table PA-15, $h_{H,i}$ is initial height of undisturbed halite in Figure PA-20, which is arbitrarily taken to be 8.98 m. However, this value is unimportant because of the extremely low permeability of the undisturbed halite ($\sim 3.16 \times 10^{-23}$ m^2); any brine in the halite could not flow into the waste over the short time period of the DBR calculation, so no effort was made to preserve halite pore volume when mapping from the computational grid in Figure PA-8 to the computational grid in Figure PA-20. The quantity $\phi_{H,i}$ is initial porosity of halite (HALPOR, see Table PA-17).

PA-4.7.3 Conceptual Representation for Flow Rate rDBR(t)

The driving force that would give rise to the DBR is a difference between waste panel pressure, p_w (Pa), and the flowing bottomhole pressure in the borehole, p_{wf} (Pa) at the time of the intrusion. The flowing bottomhole pressure p_{wf}, defined as the dynamic pressure at the

Table PA-15. Initial Porosity in the DBR Calculation

Grid region	Initial Porosity $\varphi(x, y, 0)$
Waste	$1 - h_i \dfrac{1 - \phi_{WP,i}}{h\left(t_{\mathrm{int}}\right)}$
Panel Closures	$\dfrac{\phi_C d_2 + d_1\left[1 - h_i\left(1 - \phi_{WP,i}\right)/h\left(t_{int}\right)\right]}{d_1 + d_2}$
DRZ	$\dfrac{h_{DRZ,i}\phi_{DRZ,i}}{h\left(t_{int}\right)}$
Impure Halite	$\dfrac{h_{H,i}\phi_{H,i}}{h\left(t_{int}\right)}$
Equivalent DRZ/Concrete	$\dfrac{\phi_C d_1 + \phi_{DRZ,i} d_2}{d_1 + d_2}$

inlet of the intruding borehole to the waste panel, is less than the static pressure p_w due to elevation, friction and acceleration effects. The rate at which brine and gas are transported up the intruding borehole is determined by the difference $p_w - p_{wf}$ and a productivity index J_p for the intruded waste panel (Mattax and Dalton 1990, p. 79):

$$q_p(t) = J_p\left[p_w(t) - p_{wf}\right], \tag{179}$$

where

$q_p(t)$ = flow rate (m^3/s) at time t for phase p (p = b ~ brine, p = g ~ gas),

J_p = productivity index (m^3/Pa·s) for phase p

and p_w and p_{wf} are defined above. As indicated by the inclusion/exclusion of a dependence on t, the terms J_p and p_{wf} are constant during the determination of $q_p(t)$ for a particular drilling intrusion in the present analysis, and $p_w(t)$ changes as a function of time. In concept, the DBR is given by

$$DBR = \int_0^{t_e} rDBR(t)\,dt = \int_0^{t_e} J_b\left[p_w(t) - p_{wf}\right]dt, \tag{180}$$

once J_p, p_w and p_{wf} are determined. Section PA-4.7.4 discusses the determination of J_p; Section PA-4.7.5 presents the numerical determination of p_w and DBR; and the determination of

p_{wf} is discussed in Section PA-4.7.6. The associated gas release is given by the corresponding integral with J_g rather than J_b. In the computational implementation of the analysis, DBR is determined as part of the numerical solution of the system of partial differential equations that defines p_w (Section PA-4.7.5).

PA-4.7.4 Determination of Productivity Index J_p

In a radial drainage area with uniform saturation, which is assumed to be valid throughout the DBR, the following representation for J_p can be determined from Darcy's law (Mattax and Dalton 1990, p. 79; Williamson and Chappelear 1981; Chappelear and Williamson 1981):

$$J_p = \frac{2\pi\pi k_{rp} h}{\mu_p \left[\ln(r_e / r_w) + s + c \right]}, \tag{181}$$

where

k = absolute permeability (assumed to be constant through time at 2.4 × 10^{-13} m^2),

k_{rp} = relative permeability to phase p (calculated with modified Brooks-Corey model in Equation (32) and brine and gas saturations, S_b and S_g, obtained by mapping solutions of Equation (25) obtained with grid in Figure PA-8 onto grid in Figure PA-20),

h = crushed panel height (Equation (176)),

μ_p = viscosity of fluid phase (assumed to be constant through time with $\mu_b = 1.8 \times 10^{-3}$ Pa·s, and $\mu_g = 8.92 \times 10^{-6}$ Pa·s (Kaufmann 1960)),

r_e = external drainage radius (for use with the rectangular grid-blocks in Figure PA-20, r_e is taken to be the equivalent areal radius; see Equation (182)),

r_w = wellbore radius (assumed to be constant through time at 0.1556 m (Table 14.7, Gatlin 1960)),

c = –0.50 for pseudo steady-state flow,

s = skin factor, which is used to incorporate flow stimulation caused by spallings release (see Equation (183)).

In the present analysis,

$$r_e = \sqrt{(\Delta\Delta x)(\Delta y)}/, \tag{182}$$

where Δx is the x-dimension (m) and Δy is the y-dimension (m) of the grid block containing the down-dip well in Figure PA-20 ($\Delta x = 10$ m and $\Delta y = 32.7$ m).

The skin factor s is derived from the spallings release through the following petroleum engineering well testing relationship (pp. 5-7, Lee 1982):

$$s = \left(\frac{k}{k_s} - 1 \right) \ln\left(\frac{r_s}{r_w} \right), \tag{183}$$

where

k_s = permeability (m^2) of an open channel as a result of spallings releases (assumed to be infinite),

r_s = effective radius (m) of the wellbore with the spalled volume removed.

In the CCA PA, the effective radius r_s was obtained by converting the spalled volume release V_i into a cylinder of equal volume, then computing the radius of the cylinder. The area of the cylinder A_i is

$$A_i = \frac{V_i}{h_i}. \tag{184}$$

Then,

$$r_s = \sqrt{A_i / \pi} \tag{185}$$

and substitution of r_s into Equation (183) with $k_s = \infty$ yields

$$s = -\ln\left[\frac{\sqrt{A_i / \pi}}{r_w} \right]. \tag{186}$$

For the CRA-2004 PA, calculation of the skin factor was simplified by assuming that the spalled volume, V_i, would be equal to 4 m^3 for all intrusions. This assumption was made only for the calculation of the skin factor to determine DBRs. This assumption is conservative since it will overestimate the well productivity index and consequently overestimate DBRs for all intrusions where the spalled volume is less than 4 m^3.

PA-4.7.5 Determination of Waste Panel Pressure $p_w(t)$ and Direct Brine Release

The repository pressure $p_w(t)$ in Equation (180) after a drilling intrusion is determined with the same system of nonlinear partial differential equations discussed in Section PA-4.2. These equations are solved numerically by the code BRAGFLO used with the computational grid in

Figure PA-20 and assumptions (i.e., parameter values, initial value conditions, and boundary value conditions) that are appropriate for representing brine flow to an intruding borehole over a relatively short time period immediately after the intrusion (i.e., 3 – 11 days). Due to the short time periods under consideration, the model for DBR does not include gas generation due to either corrosion or microbial action and also does not include changes in repository height due to creep closure. Furthermore, to stabilize the calculation and thus allow longer time steps in the numerical solution, the capillary pressure was assigned a value of 0 Pa in all modeled regions (Figure PA-20); in the analysis of the full system in Section PA-4.2, capillary pressure had a value of 0 Pa in the waste regions and the DRZ but a nonzero value in the panel closures (Table PA-3). Use of a capillary pressure of 0 Pa results in the brine pressure $p_b(x,y,t)$ and the gas pressure $p_g(x,y,t)$ being equal, with the pressure $p_w(t)$ in Equation (180) given by

$$p_w(t) = p_b(x,y,t). \tag{187}$$

Although the determination of DBR can be conceptually represented by the integral in Equation (175), in the numerical implementation of the analysis, DBR is determined within the numerical solution of the system of partial differential equations that defines $p_b(x,y,t)$.

With the specific assumptions for DBR, Equation (25) becomes:

Gas Conservation $$\nabla \bullet \left[\frac{\alpha \rho_g K_g k_{rg}}{\mu_g} \left(\nabla p_g + \rho_g g \nabla h \right) \right] = \alpha \frac{\partial \left(\phi \rho_g S_g \right)}{\partial t}, \tag{188a}$$

Brine Conservation $$\nabla \bullet \left[\frac{\alpha \rho_b K_b k_{rb}}{\mu_b} \left(\nabla p_b + \rho_b g \nabla h \right) \right] = \alpha \frac{\partial \left(\phi \rho_b S_b \right)}{\partial t}, \tag{188b}$$

Saturation Constraint $$S_g + S_b = 1, \tag{188c}$$

Capillary Pressure Constraint $$p_g - p_b = 0, \tag{188d}$$

Gas Density ρ_g determined by Redlich-Kwong-Soave equation of state (Equation (45)) (188e)

Brine Density $$\rho_b = \rho_0 \exp\left[\beta_b \left(p_b - p_{b0} \right) \right], \tag{188f}$$

Formation Porosity $$\phi = \phi_0 \exp\left[\beta_f \left(p_b - p_{b0} \right) \right], \tag{188g}$$

with all symbols having the same definitions as in Equation (25).

The primary differences between the BRAGFLO calculations described in Section PA-4.2 and the BRAGFLO calculations described in this section are in the computational meshes used (Figure PA-20 and Figure PA-8), the initial values used (Table PA-2 and Section PA-4.7.2), and the boundary conditions used (Table PA-16). In particular, brine and gas flow associated with intruding boreholes in the DBR calculations are incorporated by the appropriate assignment of boundary conditions. Specifically, brine flow up an intruding borehole is incorporated into Equation (188) by using the Poettmann-Carpenter wellbore model to determine the pressure at the outflow point in a waste panel (Figure PA-20), with this pressure entering the calculation as a boundary value condition (Table PA-16). The details of this determination are discussed in Section PA-4.7.6. Further, for calculations that assume a prior E1 intrusion, the effects of this intrusion are also incorporated into the analysis by specifying a pressure specified as a boundary condition (Table PA-16). The determination of this pressure is discussed in Section PA-4.7.6.

Table PA-16. Boundary Conditions for p_b and S_g in DBR Calculations

***(x, y)* on Upper (Northern) or Lower (Southern) Boundary in Figure PA-20, 0 ≤ t**	
$\left(\nabla p_g + \rho_g g \nabla h\right)\Big\rvert_{(x,y,t)} \cdot \boldsymbol{j} = 0 \;\; Pa/m$	no gas flow condition
$\left(\nabla p_b + \rho_b g \nabla h\right)\Big\rvert_{(x,y,t)} \cdot \boldsymbol{j} = 0 \;\; Pa/m$	no brine flow condition
***(x, y)* on Right (Eastern) or Left (Western) Boundary in Figure PA-20, 0 ≤ t**	
$\left(\nabla p_g + \rho_g g \nabla h\right)\Big\rvert_{(x,y,t)} \cdot \boldsymbol{i} = 0 \;\; Pa/m$	no gas flow condition
$\left(\nabla p_b + \rho_b g \nabla h\right)\Big\rvert_{(x,y,t)} \cdot \boldsymbol{i} = 0 \;\; Pa/m$	no brine flow condition
***(x, y)* at Location of Drilling Intrusion under Consideration (see indicated points in Figure PA-20), 0 ≤ t**	
$P_b(x, y, t) = P_{wf}$ (see Section PA.4.7.6)	constant pressure condition
***(x, y)* at Location of Prior Drilling Intrusion into Pressurized Brine (see indicated point in Figure PA-20), 0 ≤ t**	
$P_b(x, y, t) = P_{wE1}$ (see Section PA.4.7.7)	constant pressure condition

For perspective, the following provides a quick comparison of the assumptions that underlie the solution of Equation (25) on the mesh in Figure PA-8 (i.e., the BRAGFLO mesh) and the solution of Equation (188) on the mesh in Figure PA-20 (i.e., the BRAGFLO mesh for DBR):

1. The BRAGFLO mesh for DBR is defined in the areal plane with the z-dimension (height) one element thick; the BRAGFLO mesh is defined as a cross-section, with multiple layers in height and the thickness (y-dimension) one element thick.

2. The BRAGFLO mesh for DBR uses constant thickness, while BRAGFLO uses rectangular flaring to account for three-dimensional volumes in a two-dimensional grid (Figure PA-9).

3. The BRAGFLO mesh for DBR represents flow only in the waste area. The BRAGFLO model includes the surrounding geology as well as the entire WIPP excavation (including operations, experimental, and shaft regions).

4. Local scale heterogeneities are included in the BRAGFLO mesh for DBR, including the salt pillars, rooms, panel closures, and passageways that contain waste. These are not fully represented in the BRAGFLO mesh.

5. The DRZ is included in both models, but exists above and below the excavated regions in the BRAGFLO model, whereas the DRZ surrounds the waste rooms on the sides of the BRAGFLO mesh for DBR.

6. Both models include a one-degree formation dip through the excavated regions (Equation (27)).

PA-4.7.6 Boundary Value Pressure p_{wf}

The boundary value pressure p_{wf} at the inlet of the intruding borehole is defined by a system of equations of the following form:

$$\frac{dp}{dh} = G\left(q_b\left[p(0)\right], q_g\left[p(0)\right], p(h), h\right), \quad 0 \le h \le 655m, \tag{189a}$$

$$p(655) = 1.013 \times 10^5 \ Pa, \tag{189b}$$

$$q_b\left[p(0)\right] = J_b\left[p_w - p(0)\right], \tag{189c}$$

$$q_g\left[p(0)\right] = J_g\left[p_w - p(0)\right], \tag{189d}$$

where $p(h)$ is pressure (Pa) at elevation h (m) in the borehole with h = 0 m corresponding to the entry point of the borehole into the waste panel and h = 655 m corresponding to the land surface (Figure PA-22), G is a function (Pa/m) characterizing the change of pressure with elevation in the borehole, $p(655)$ is an initial value condition requiring that pressure at the land surface (i.e., the outlet point of the borehole) be equal to atmospheric pressure, $q_b\left[p(0)\right]$ and $q_b\left[p(0)\right]$ define brine and gas flow rates (m^3/s) into the borehole, J_b and J_g are productivity indexes (m^3/Pa s) (see Equation (181)), and p_w is the pressure (Pa) in the repository at the time of the drilling intrusion.

The boundary value pressure p_{wf} is defined by

$$p_{wf} = p(0). \tag{190}$$

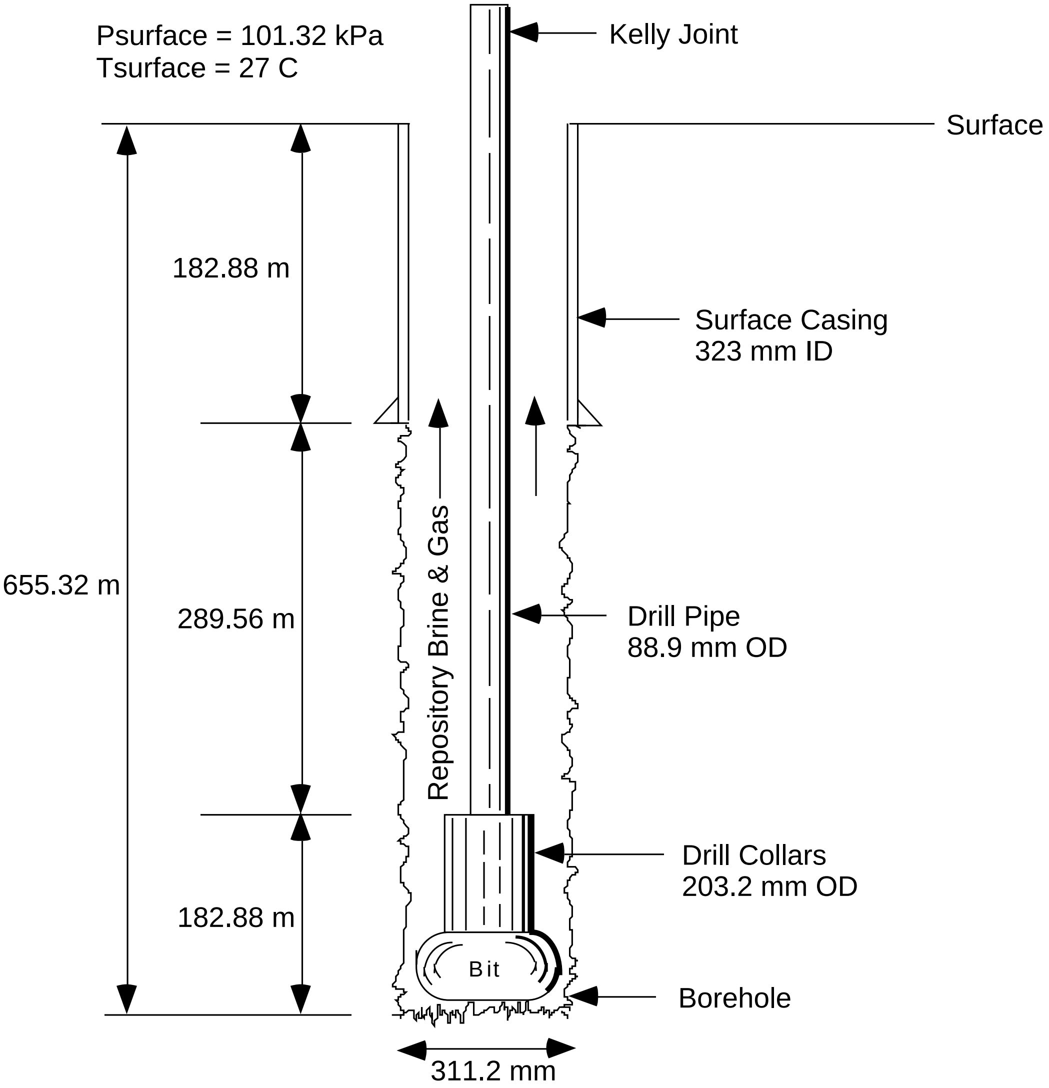

Figure PA-22. Borehole Representation Used for Poettmann-Carpenter Correlation.

Thus, p_{wf} is determined by the numerical solution of Equation (189a) for $p(0)$ subject to the constraints in Equation (189b), Equation (189c) and Equation (189d).

The pressure p_W corresponds to the pressure $p_w(0)$ in Equation (187) and is obtained from the solution of Equation (25) with the computational grid in Figure PA-8 (see Section PA-4.7.2). The production indexes J_b and J_g are defined in Equation (181). Thus, the only quantity remaining to be specified in Equation (189) is the function G.

Brine and gas flow up a borehole is governed by complex physics dependent on frictional effects and two-phase fluid properties. This phenomenon has been widely studied in the petroleum industry and many modeling procedures have been developed to predict flow rates and pressures in vertical two-phase pipe flow (i.e., to define G in Equation (189a)) (Brill and Beggs 1986). For this analysis, the Poettmann-Carpenter model (Poettmann and Carpenter 1952, Welchon et al.

1962) was used to define G because it accounts for multiphase frictional effects based on empirical (i.e., field) data from flowing wells, is one of the few modeling approaches that included annular flow data in its development, and is relatively easy to implement. Specifically, the Poettmann-Carpenter model defines G by:

$$\begin{aligned} &G\left(q_b\left[p(0)\right], q_g\left[p(0)\right], p(h), h\right) \\ &\qquad = gm(h) + f'\left(m(h), D(h), q_b\left[p(0)\right]\right) gm(h) F^2(h) / D^5(h) \end{aligned}, \tag{191}$$

where

g = acceleration due to gravity (9.8 m/s^2),

$m(h)$ = density (kg/m^3) of fluids (i.e., gas and brine) in wellbore at elevation h (Note: $m(h)$ is a function of $q_b\left[p(0)\right]$ and $q_g\left[p(0)\right]$; see Equation (192), below),

$f'\left\{m(h), D(h) q_b\left[p(0)\right]\right\}$ = empirically defined scale factor (m/s^2) (Note: f' is the scale factor in the Poettmann-Carpenter model for fluid flow in a wellbore [Poettmann and Carpenter 1952]; see discussion below),

$F(h)$ = flow rate (m^3/s) of fluids (i.e., gas and brine) in wellbore at elevation h (Note: $F(h)$ is a function of $q_b\left[p(0)\right]$ and $q_g\left[p(0)\right]$; see Equation (193), below),

$D(h)$ = effective diameter (m) of wellbore (see Equation (196), below).

The first term, $gm(h)$, in Equation (191) results from the contribution of elevation to pressure; the second term results from frictional effects (Poettmann and Carpenter 1952). The fluid density $m(h)$ at elevation h is given by

$$m(h) = \frac{q_b\left[p(0)\right]\rho_b\left[p(0)\right] + q_g\left[p(0)\right]\rho_g\left[p(0)\right]}{F(h)}, \tag{192}$$

where

$$F(h) = q_b\left[p(0)\right] + \frac{z(h)p(h)}{p(0)} q_g\left[p(0)\right], \tag{193}$$

and

$\rho_b\left[p(0)\right]$ = density (kg/m^3) of brine at pressure $p(0)$ and temperature 300.1°K, which is fixed at 1230 kg/m^3,

$\rho_g [p(0)]$ = density (kg/m^3) of H_2 at pressure $p(0)$ and temperature 300.1°K (see Equation (194), below),

$z(h)$ = z-factor for compressibility of H_2 at elevation h (Note: $z(h)$ is a function of $p(h)$; see Equation (195), below), and $q_g [p(0)]$ and $q_g [p(0)]$ are defined in Equation (189).

The gas density in Equation (192) is obtained from the universal gas law, PV = nRT, by

$$\rho_g [p(0)] = C_{m,kg} \frac{n}{V} = C_{m,kg} \frac{P}{RT}, \tag{194}$$

where n is the amount of gas (mol) in a volume V, $C_{m,kg}$ is the conversion factor from moles to kilograms for H_2 (i.e., 2.02×10^{-3} kg/mol), $P = p(0)$, R = 8.3145 kg m^2/mol°K s^2, and T = 300.1°K. The z-factor is given by

$$z(h) = 1 + (8.54 \times 10^{-8}\ Pa^{-1})p(h), \tag{195}$$

and was obtained from calculations performed with the SUPERTRAPP program (Ely and Huber 1992) for pure H_2 and a temperature of 300.1°K (Stoelzel and O’Brien 1996, Figure 4.7.4). The preceding approximation to $z(h)$ was obtained by fitting a straight line between the results for pressures of 0 psi and 3000 psi and a hydrogen mole fraction of 1 in Stoelzel and O’Brien (1996, Figure 4.7.4); the actual calculations used the more complex, but numerically similar, regression model given in Stoelzel and O’Brien (1996, Figure 4.7.4). The numerator and denominator in Equation (192) involve rates, with the time units canceling to give $m(h)$ in units of kg/m^3.

The effective diameter $D(h)$ in Equation (191) is defined with the hydraulic radius concept. Specifically,

$$D^5(h) = [D_0(h) + D_i(h)]^2 [D_0(h) - Di/(h)]^3, \tag{196}$$

where $D_i(h)$ and $D_0(h)$ are the inner and outer diameters (m) of the wellbore at elevation $h(m)$ (see Figure PA-22). The factor f' in Equation (191) is a function of $m(h)$, $D(h)$ and $q_g [p(0)]$.

In the original development by Poettmann and Carpenter (1952, Figure 4), f' is defined in terms of quantities commonly used to measure production from oil and gas wells. The result is that f' is expressed in quantities that are unfamiliar outside of the oil and gas industry. For clarity, Equation (191) and the quantities contained in it are expressed in SI units. However, to allow use of the original correlations developed by Poettmann and Carpenter to define f', the calculations within the CCA PA (Stoelzel and O’Brien 1996) were performed in the same oilfield units originally used by Poettmann and Carpenter (1952).

Subsequent to submittal of the CCA PA, it was discovered that the factor of 2π was omitted from Equation (181). This error was determined to be of no consequence to the conclusions of the CCA PA (Hadgu et al. 1999) and has been corrected in the CRA-2004 PA. As a consequence of the error correction, the regression models used to determine the boundary pressure p_{wf} were recalculated (Hadgu et al. 1999). The corrected regression models are reported in this appendix.

The following iterative procedure based on bisection method was used to approximate solutions to Equation (189).

Step 1. Estimate $p(0)$ using a bisection algorithm. (Initial guess for $p(0)$ is the midpoint $\frac{1}{2}p_w$ of interval $\left[0, p_w\right]$, where p_w is the pressure in the repository at the time of the drilling intrusion used in Equation (189)). Next guess for $p(0)$ is at the midpoint of either $\left[0, \frac{1}{2}p_w\right]$ or $\left[\frac{1}{2}p_w, p_w\right]$ depending on whether resultant approximation to $p(655)$ is above or below atmospheric pressure. Subsequent guesses for $p(0)$ are made in a similar manner.

Step 2. Use $p(0)$, known values for J_b, J_g and p_w, and Equation (189) to determine $q_b\left[p(0)\right]$ and $q_g\left[p(0)\right]$.

Step 3. Use the bisection method with $\Delta h = 25$ ft $= 7.62$ m and appropriate changes in annular diameter (Figure PA-22) to determine $p(655)$ (i.e., $p(h+\Delta h) = p(h) + G\left(q_b\left[p(0)\right], q_g\left[p(0)\right], p(h), h\right)\Delta h$).

Step 4. Stop if $p(655)$ is within 0.07% of atmospheric pressure (i.e., if $\left|1.013 \times 10^5 \text{ Pa} - p(655)\right| \le 70 \text{ Pa}$). Otherwise, return to Step 1 and repeat process.

The preceding procedure is continued until the specified error tolerance (i.e., 0.07percent) has been met. The computational design of the PA has the potential to require more than 23,000 separate DBR calculations (3 replicates × 5 scenarios × 3 drilling locations × 100 vectors × 5 to 6 intrusion times per scenario). In concept, each of these cases requires the solution of Equation (189) with the iterative procedure just presented to obtain the boundary value condition $p_{wf} = p(0)$ (Table PA-16). To help hold computational costs down, $p(0)$ was calculated for approximately 2000 randomly generated vectors of the form

$$\mathbf{v} = \left[p_w, h, S_{br}, S_{gr}, S_b, A_i\right], \tag{197}$$

where p_w is the repository pressure (used in definition of $q_b\left[p(0)\right]$ and $q_g\left[p(0)\right]$ in Equation (189)), h is the crushed height of the repository (used in definition of J_p in Equation (181)), S_{br} and S_{gr} are the residual saturations for gas and brine in the repository (used in definition of k_{rp} in Equation (181)), S_b is the saturation of brine in the repository (used in definition of k_{rp} in Equation (181)), and A_i is the equivalent area of material removed by spallings (used in definition of skin factor s in Equation (186)). The outcomes of these calculations were divided into three cases:

1. mobile brine only (i.e., $k_{rg} = 0$ in Equation (188a))
2. brine-dominated flow (i.e., $k_{rb} > k_{rg}$), and
3. gas-dominated flow (i.e., $k_{rg} > k_{rb}$).

Then, regression procedures were used to fit algebraic models that can be used to estimate $p(0)$. These regression models were then used to determine $p(0)$, and hence p_{wf}. The resulting three regression models (or curve fit equations) for flowing bottomhole pressure (p_{wf}) are as follows.

1. For a system with only mobile brine (i.e., $k_{rg} = 0$)

$$p_{wf} = a + bx + cy + dx^2 + ey^2 + fxy + gx^3 + hy^3 + ixy^2 + jx^2y\,, \tag{198a}$$

where $x = \log(J_b)$ and $y = p_w$ (= repository pressure). The coefficients in Equation (198a) were determined to be:

$a = 3.2279346 \times 10^{11}$,
$b = 9.4816648 \times 10^{10}$,
$c = -6.2002715 \times 10^{3}$,
$d = 9.2450601 \times 10^{9}$,
$e = 4.1464475 \times 10^{-6}$,
$f = -1.2886068 \times 10^{3}$,
$g = 2.9905582 \times 10^{8}$,
$h = 1.0857041 \times 10^{-14}$,
$i = 4.7119798 \times 10^{-7}$,
$j = -6.690712 \times 10^{-1}$,

with resulting coefficient of determination $R^2 = 0.974$.

2. For brine dominated flow ($k_{rb} > k_{rg}$):

$$Pwf = \frac{a + bx + cx^2 + dy}{1 + ex + fx^2 + gx^3 + hy}, \tag{198b}$$

where $x = \log\left(\frac{k_{rg}}{k_{rb}}\right)$ and $y = p_w$ (= repository pressure). The coefficients in Equation (198b) were determined to be:

a = 1.6065077×10^{6},
b = 2.6243397×10^{6},
c = 2.4768899×10^{6},
d = $-5.3635476 \times 10^{-2}$,
e = 7.0815693×10^{-1},
f = 3.8012696×10^{-1},
g = 4.1916956×10^{-3},
h = $-2.4887085 \times 10^{-8}$,

with resulting coefficient of determination $R^2 = 0.997$.

3. For gas dominated flow ($k_{rg} > k_{rb}$):

$$p_{wf} = a + b\frac{1}{x} + cy + d\frac{1}{x^2} + ey^2 + f\frac{x}{y} + g\frac{1}{x^3} + hy^3 + i\frac{y^2}{x} + j\frac{y}{x^2}, \tag{198c}$$

where $x = \log\left(J_g\right)$ and $y = p_w$ (= repository pressure). The coefficients in Equation (198c) were determined to be:

a = -1.0098405×10^{9},
b = $-2.3044622 \times 10^{10}$,
c = 9.8039146,
d = $-1.7426466 \times 10^{11}$,
e = 1.8309137×10^{-7},
f = 1.7497064×10^{2},
g = $-4.3698224 \times 10^{11}$,
h = $-1.4891198 \times 10^{-16}$,
i = 1.3006196×10^{-6},
j = 7.5744833×10^{2},

with resulting coefficient of determination $R^2 = 0.949$.

PA-4.7.7 Boundary Value Pressure p_{wE1}

Some of the calculations for DBR are for a drilling intrusion that has been preceded by an E1 intrusion in either the same waste panel, an adjacent waste panel, or a nonadjacent waste panel (Section PA-6.7.5). The effects of these prior E1 intrusions are incorporated into the solution of Equation (188), and hence into the DBR, by the specification of a boundary pressure p_{wE1} at the location of the E1 intrusion into the repository (Table PA-16).

Two cases are considered for the definition of p_{wE1}: (1) an open borehole between the brine pocket and the repository, and (2) a borehole between the brine pocket and the repository filled with material with properties similar to silty sand. The first case corresponds to the situation in which the drilling intrusion under consideration has occurred within 200 years of a prior drilling intrusion that penetrated the pressurized brine pocket, and the second case corresponds to the situation in which the drilling intrusion under consideration has occurred more than 200 years after a prior drilling intrusion that penetrated the pressurized brine pocket.

PA-4.7.7.1 Solution for Open Borehole

In this case, p_{wE1} is set equal to the flowing well pressure p_{wfBP} of an open borehole between the brine pocket and the repository and is given by:

$$Q = f_1\left(p_{BP}, p_{wfBP}\right), \tag{199a}$$

$$Q = f_2\left(p_{wfBP}, p_{wfBI}\right), \tag{199b}$$

$$Q = f_3\left(p_{wfBI}, p_{wfBO}\right), \tag{199c}$$

where

pB = pressure (Pa) in brine pocket,

p_{wfBP} = flowing well pressure (Pa) at outlet from brine pocket,

p_{wfBI} = flowing well pressure (Pa) at inlet to repository from brine pocket,

p_{wfBO} = flowing well pressure (Pa) at outlet from repository due to intruding borehole (Note: The boreholes associated with p_{wfBI} and p_{wfBO} arise from different drilling intrusions and hence are at different locations; see Figure PA-20),

Q = brine flow rate (m^3/s) from brine pocket to repository, through repository, and then to surface,

and f_1, f_2 and f_3 are linear functions of their arguments. In the development, p_{BP} and p_{wfBO} are assumed to be known, with the result that Equation (199) constitutes a system of three linear equations in three unknowns (i.e., p_{wfBP}, p_{wfBI}, Q) that can be solved to obtain p_{wfBI}. In the determination of $p_{wfBI} = p_{wE1}$ for use in a particular solution of Equation (188), p_{BP} is the pressure in the brine pocket at the time of the intrusion obtained from the solution of Equation (25) with BRAGFLO, and p_{wfBO} is the flowing well pressure obtained from conditions at the time of the intrusion (from the solution of Equation (25)) and the solutions of the Poettmann-Carpenter model embodied in Equation (198) (i.e., given pressure, k_{rg} and k_{rb} at the time of the intrusion from the solution of Equation (25) with BRAGFLO and J_b from both the solution of Equation (25) with BRAGFLO and the evaluation of the spallings release (assumed to be a constant of 4 m^3), p_{wfBO} is determined from the regression models indicated in Equation (198).

The definition of Equation (199) is now discussed. Equation (199a) characterizes flow out of the brine pocket into an open borehole and has the form (Williamson and Chappelear 1981, Chappelear and Williamson 1981):

$$Q = \left(\frac{2\pi k_{BP} h_{BP}}{\mu \left[\ln\left(r_{eBP} / r_w \right) - 0.5 \right]} \right) \left(p_{BP} - p_{wfBP} \right), \tag{200}$$

where

k_{BP} = brine pocket permeability (m^2),

h_{BP} = effective brine pocket height (m),

r_{eBP} = effective brine pocket radius (m),

r_w = wellbore radius (m),

μ = brine viscosity (Pa s).

In the present analysis, k_{BP} is an uncertain analysis input (see BHPRM in Table PA-17), $h_{BP} = 125.83$ m, $r_{eBP} = 114$ m (Stoelzel and O'Brien 1996), which corresponds to the size of the largest brine pocket that could fit under one waste panel, r_w = (8.921 in.) / 2 = 0.1133 m, which is the inside radius of a 9 5/8 in. outside diameter casing (Gatlin 1960, Table 14.7), $\mu = 1.8 \times 10^{-3}$ Pa s, and p_{BP} is determined from the solution of Equation (25) as previously indicated.

Equation (199b) characterizes flow up an open borehole from the brine pocket to the repository and is based on Poiseuille's Law (Prasuhn 1980, Eqs. 7-21, 7-22). Specifically, Equation (199b) has the form

$$Q = \left[\frac{\pi D^4}{128\mu \left(y_{BP} - y_{rep} \right)} \right] \left[\left(p_{wfBP} - p_{wfBI} \right) + g\rho \left(y_{rep} - y_{BP} \right) \right], \tag{201}$$

where

D = wellbore diameter (m),

y_{rep} = elevation of repository (m) measured from surface,

y_{BP} = elevation of brine pocket (m) measured from surface,

g = acceleration due to gravity (9.8 m/s^2),

ρ = density of brine (kg/m^3),

and the remaining symbols have already been defined.

In the present analysis, $D = 2r_w = 0.2266$ m, $\rho = 1230$ kg/m^3, and $y_{rep} - y_{BP} = 247$ m. With the preceding values,

$$128\mu\left(y_{BP} - y_{rep}\right)/\pi D^4 = 6.87 \times 10^3 \ Pa\ s/m^3 , \tag{202}$$

$$g\rho\left(y_{rep} - y_{BP}\right) == 2.98 \times 10^6 \ Pa . \tag{203}$$

Thus,

$$p_{wfBI} = p_{wfBP} - 2.98 \times 10^6 \ Pa . \tag{204}$$

when Q is small (≤ 0.1 m^3/s). When appropriate, this approximation can be used to simplify the construction of solutions to Equation (199).

Equation (199c) characterizes flow through the repository from the lower borehole to the bottom of the borehole associated with the drilling intrusion under consideration and has the same form as Equation (200). Specifically,

$$Q = \left(\frac{2\pi k_{rep} h_{rep}}{\mu\left[\ln\left(r_{e,rep}/r_w\right) - 0.5\right]}\right)\left(p_{wfBI} - p_{wfBO}\right), \tag{205}$$

where

k_{rep} = repository permeability (m^2),

h_{rep} = repository height (m),

$r_{e,rep}$ = effective repository radius (m), and the remaining symbols have already been defined. In the present analysis, $k_{rep} = 2.4 \times 10^{-13}\, m^2$; h_{rep} at the time of the drilling intrusion under consideration is obtained from the solution of Equation (25) (see Equation (176)); and $r_{e,rep}$ is the same as the radius r_e defined in Equation (182). As previously indicated, p_{wfBO} is obtained from the solutions to the Poettmann-Carpenter model summarized in Equation (198).

Three equations (i.e., Equation (200), Equation (201) and Equation (205)) in three unknowns (i.e., p_{wfBP}, p_{wfBI} and Q) have now been developed. The solution for p_{wfBI} defines the initial value p_{wE1} in Table PA-16. When the simplification in Equation (204) is used, the resultant solution for p_{wfBI} is

$$p_{wfBI} = \frac{p_{wfBO} + \left(p_{BP} - 2.98 \times 10^6\right) K_1}{1 + K_1}, \tag{206}$$

where

$$K_1 = \frac{k_{BP} h_{BP} \left[\ln\left(\frac{r_{e,rep}}{r_w}\right) - \frac{1}{2} \right]}{k_{rep} h_{rep} \left[\ln\left(\frac{r_{eBP}}{r_w}\right) - \frac{1}{2} \right]}, \tag{207}$$

and -2.98×10^6 comes from Equation (203). The expression in Equation (207) was used to define p_{wE1} in the CCA PA in the determination of DBRs for a drilling intrusion that occurred within 200 years of a preceding E1 intrusion (see Table PA-5). The same approach was used for the CRA-2004 PA.

PA-4.7.7.2 Solution for Sand-Filled Borehole

The determination of the pressure p_{wfBI} with the assumption that a borehole filled with material with properties similar to silty sand connects the brine pocket and the repository is now considered. The approach is similar to that used for the open borehole except that Equation (199a) and Equation (199b) are replaced by a single equation based on Darcy's Law. Specifically, flow from the brine pocket to the repository is represented by

$$Q = \frac{k_{BH} A_{BH} \left[\left(p_{wfBP} - p_{wfBI}\right) + g\rho \right]}{\mu\left(y_{BP} - y_{rep}\right)}, \tag{208}$$

where

k_{BH} = borehole permeability (m^2),

A_{BH} = borehole cross-sectional area (m^2),

and the remaining symbols have been defined previously. In the present analysis, k_{BH} is an uncertain input (see BHPRM in Table PA-17) and A_{BH} is defined by the assumption that the borehole diameter is the same as the drill bit diameter (i.e., 12.25 in. = 0.311 m).

The representation for flow from the brine pocket inlet point to the repository to the outlet point associated with the drilling intrusion under consideration remains as defined in Equation (205). Thus, two equations (i.e., Equation (208) and Equation (205)) and two unknowns (i.e., p_{wfBI} and Q) are under consideration. Solution for p_{wfBI} and yields

$$p_{wfBI} = \frac{p_{wfBO} + K_2 p_{BP} - 2.98 \times 10^6 K_2}{1 + K_2} \tag{209}$$

where

$$K_2 = \frac{\pi k_{BH} r_w^2 \left[\ln\left(\frac{r_{eBP}}{r_w} \right) - \frac{1}{2} \right]}{2\pi h_{rep} k_{rep} \left(y_{BP} - y_{rep} \right)} \tag{210}$$

and -2.98×10^6 comes from Equation (203). The expression in Equation (209) was used to define p_{wE1} in the determination of DBRs for a drilling intrusion that occurred more than 200 years after a preceding E1 intrusion (see Table PA-5).

PA-4.7.8 End of Direct Brine Release

The CRA-2004 PA has 23,400 cases that potentially required solution of Equation (188) to obtain the DBR volume (See Section PA-6.7.5). However, the DBR was set to zero without solution of Equation (188) when there was no possibility of a release (i.e., the intruded waste panel at the time of the intrusion had either a pressure less than 8 MPa or a brine saturation below the residual brine saturation S_{br}).

For the remaining cases, Equation (188) was solved for a time period of 50 days, although the value used for t_e was always less than 50 days. The minimum value used for t_e was three days, which is an estimate of the time required to drill from the repository through the Castile Formation and then cement the intermediate casing. If there is little or no gas flow associated with brine inflow into the borehole during drilling in the Salado Formation, current industry practice is to allow the brine to “seep” into the drilling mud and be discharged to the mud pits until the salt section is cased.

If there is a significant amount of gas flow, then it is possible that the driller will lose control of the well. In such cases, DBRs will take place until the gas flow is brought under control. Two possibilities exist: (1) the driller will regain control of the well when the gas flow drops to a manageable level, and (2) aggressive measures will be taken to shut off the gas flow before it drops to a manageable level. In the CCA PA, the driller was assumed to be able to regain control of the well when the gas flow dropped to a "cut-off" rate of 1×10^5 standard cubic feet per day (SCF/d in commonly used oil field units). Experience at the South Culebra Bluff Unit #1, which blew out in January 1978, suggests that approximately 11 days may be needed to bring a well under control before the gas flow drops to a manageable level (i.e., 1×10^5 SCF/d) (DOE 1996, Appendix MASS Attachment MASS 16-2). In particular, it took 11 days to assemble the equipment and personnel needed to bring that well under control.

Given the preceding, t_e is defined by

$$t_e = \begin{cases} \max\left\{3\ d, t_f\right\} & if\ t_f \le 11\ d \\ 11\ d & if\ t_f > 11\ d \end{cases} \tag{211}$$

in the CRA-2004 PA, where t_f is the time at which the gas flow out of the well drops below 1×10^5 SCF/d. As a reminder, gas flow out of the repository in the intruding borehole, and hence t_e, is determined as part of the solution to Equation (188).

PA.-4.7.9 Numerical Solution

As previously indicated, the BRAGFLO program is used to solve Equation (188) with the computational grid in Figure PA-20, the initial value conditions in Section PA-4.7.2, the boundary value conditions in Table PA-16, and parameter values appropriate for modeling DBRs. Thus, the numerical procedures in use for Equation (188) are the same as those described in Section PA-4.2.10 for the solution of Equation (25).

In this solution, the boundary value conditions associated with drilling intrusions (i.e., p_{wf} and pwE1 in Table PA-16) are implemented through the specification of fluid withdrawal terms (i.e., q_{wg} and q_{wb} in Equation (25)) rather than as defined boundary value conditions. With this implementation, the representations in Equation (188a) and Equation (188b) for gas and brine conservation become

$$\nabla \cdot \left[\frac{\alpha \rho_g K_g k_{rg}}{\mu_g} \left(\nabla p_g + \rho_g g \nabla h \right) \right] + \alpha q_{wg} = \alpha \frac{\partial \left(\phi \rho_g S_g \right)}{\partial t} \tag{212a}$$

$$\nabla \cdot \left[\frac{\alpha \rho_b K_b k_{rb}}{\mu_b} \left(\nabla p_b + \rho_b g \nabla h \right) \right] + \alpha q_{wb} = \alpha \frac{\partial \left(\phi \rho_b S_b \right)}{\partial t}, \tag{212b}$$

and the constraints in Equation (188) remain unchanged. As used in Equation (212), q_{wg} and q_{wb} are independent of the computational grid in use (Figure PA-20). In practice, q_{wg} and q_{wb} are defined with a productivity index (see Equation (181)) that is a function of the specific computational grid in use, with the result that these definitions are only meaningful in the context of the computational grid that they are intended to be used with. This specificity results because

q_{wg} and q_{wb} as used in Equation (212) are defined on a much smaller scale than can typically be implemented with a reasonable-sized computational grid. As a result, the values used for q_{wg} and q_{wb} in the numerical solution of Equation (212) must incorporate the actual size of the grid in use.

In the solution of Equation (212) with the computational grid in Figure PA-20, q_{wg} is used to incorporate gas flow out of the repository and q_{wb} is used to incorporate both brine inflow to the repository from a pressurized brine pocket and brine flow out of the repository. For gas flow out of the repository,

$$q_{wg}(x,y,t) = \frac{kk_{rg}(x,y,t)[p_g(x,y,t) - p_{wf}]}{\mu_g[\ln(r_e/r_w) + s + c]}, \tag{213}$$

if (x,y) is at the center of the grid cell containing the drilling intrusion (Figure PA-20) and $q_{wg}(x,y,t)$ = 0 (kg/m^3)/s otherwise, where k, k_{rg}, μ_g, r_e, r_w, s and c are defined in conjunction with Equation (181), p_g is gas pressure, and p_{wf} is the flowing well pressure at the outlet borehole (i.e., the boundary value condition in Table PA-16). The factor h in Equation (181) is the crushed height of the repository as indicated in Equation (176) and defines the factor α in Equation (212). In the numerical solution, $q_{wg}(x,y,t)$ defines $q_{wgi,j}^{n+1}$ in Equation (79), with $q_{wgi,j}^{n+1}$ having a nonzero value only when i, j correspond to the grid cell containing the borehole through which gas outflow is taking place (i.e., the grid cells containing the down-dip and up-dip wells in Figure PA-20).

For brine flow,

$$q_{wb}(x,y,t) = \frac{kk_{rb}(x,y,t)[p_b(x,y,t) - p_{wf}]}{\mu_b[\ln(r_e/r_w) + s + c]}, \tag{214}$$

if (x,y) is at the center of the grid cell containing the drilling intrusion through which brine outflow from the repository is taking place (Figure PA-20);

$$q_{wb}(x,y,t) = \frac{kk_{rb}(x,y,t)[p_{wE1} - p_b(x,y,t)]}{\mu_b[\ln(r_e/r_w) + c]}, \tag{215}$$

if (x,y) is at the center of the grid cell containing a prior drilling intrusion into a pressurized brine pocket (Figure PA-20), where p_{wE1} is the boundary value condition defined in Table PA-16; and $q_{wb}(x,y,t)$ = 0 otherwise. In the numerical solution of Equation (212a), $q_{wb}(x,y,t)$ defines $q_{wbi,j}^{n+1}$ in a discretization for Equation (212b) that is equivalent to the discretization for Equation (212a) shown in Equation (79), with $q_{wbi,j}^{n+1}$ having a nonzero value only when i, j correspond to the grid cell containing the borehole through which brine outflow is taking place (i.e., the grid cells containing the down-dip and up-dip wells in Figure PA-20, in which case, Equation (214) defines $q_{wbi,j}^{n+1}$ or to the grid cell containing the borehole through which brine inflow to the repository from a pressurized brine pocket is taking place (i.e., the grid cell containing the E1 intrusion in Figure PA-20; in which case, Equation (215) defines $q_{wbi,j}^{n+1}$.

PA-4.7.10 Additional Information

Additional information on BRAGFLO and its use in the CRA-2004 PA to determine DBRs can be found in the analysis package for DBR (Stein 2003) and in the BRAGFLO User's Manual (WIPP PA 2003c).

PA-4.8 Brine Flow in Culebra: MODFLOW

This section describes the model for the calculation of brine flow in the Culebra.

PA-4.8.1 Mathematical Description

Groundwater flow in the Culebra Dolomite is represented by the partial differential equation

$$S\left(\frac{\partial h}{\partial t}\right) = \nabla \cdot \left(bK\nabla h\right) - Q , \tag{216}$$

where

S = medium storativity (dimensionless),

h = hydraulic head (m),

t = time (s),

b = aquifer thickness (m),

K = hydraulic conductivity tensor (m/s),

Q = source/sink term expressed as the volumetric flux per unit area ((m^3/m^2)/s = m/s).

Further, the Culebra is assumed to be isotropic, and as a result, K is defined by

$$K(x, y) = k(x, y)\begin{bmatrix} 1 & 0 \\ 0 & 1 \end{bmatrix}, \tag{217}$$

where $k\left(x, y\right)$ is the hydraulic conductivity (m/s) at the point $\left(x, y\right)$. The following simplifying assumptions are also made: fluid flow in the Culebra is at steady state (i.e., $\partial h/\partial t = 0$), and source and sink effects arising from borehole intrusions and infiltration are negligible (i.e., Q = 0). Given these assumptions, Equation (216) simplifies to

$$\nabla \cdot \left(b\boldsymbol{K} \nabla \boldsymbol{h} \right) = \boldsymbol{0}\,, \tag{218}$$

which is the equation actually solved to obtain fluid flow (i.e., $\boldsymbol{K}\nabla \boldsymbol{h}$) in the Culebra. In the CRA-2004 PA, b = 7.75 m, and $\boldsymbol{k}\left(\boldsymbol{x},\boldsymbol{y}\right)$ in Equation (217) is a function of an imprecisely known transmissivity field, as discussed in Section PA-4.8.2.

PA-4.8.2 Implementation

The first step in the analysis of fluid flow in the Culebra is to generate transmissivity fields $\boldsymbol{t(x,y)}$ (m^2/s) for the Culebra and to characterize the uncertainty in these fields. This was accomplished by generating a large number of plausible transmissivity fields. A description of the method used to construct these transmissivity fields is included in Attachment TFIELD. Below, a brief outline of the method is presented.

The transmissivity fields used for the CRA-2004 PA are based on several types of information, including a regression model developed on WIPP-site geologic data, measured head levels in the Culebra for the year 2000, and well drawdown test results. The following steps led to the final transmissivity fields used in this analysis:

Geologic data including: (1) depth to the top of the Culebra, (2) reduction in thickness of the upper Salado Formation by dissolution, and (3) the spatial distribution of halite in the Rustler Formation below and above the Culebra were used to define a geologic regression model that relates transmissivity at any location to a set of geologically defined parameters.

Base transmissivity fields are defined for a modeling domain measuring 22.4 km east-west by 30.7 km north-south using a method of stochastic simulation. The base transmissivity fields were constructed from information on the depth to the Culebra, indicator functions defining the location of Salado dissolution, halite occurrence, and high transmissivity zones.

Seed transmissivity fields are defined by conditioning base transmissivity fields to measured values of transmissivity. This conditioning is performed with a Gaussian geostatistical simulation algorithm.

The seed transmissivity fields are calibrated to transient water level data from the year 2000 in 37 wells across the region using parameter estimation program PEST (Doherty 2002). The PEST program iteratively changes the seed transmissivity field values to minimize an objective function, using MODFLOW to rerun the flow solution between each iteration. The objective function minimized by PEST is a combination of the weighted sum of the squared residuals between the measured and modeled head data and a second weighted sum of the squared differences in the estimated transmissivity between pairs of pilot points. The second weighted sum is designed to keep the transmissivity field as homogeneous as possible and to provide numerical stability when estimating more parameters than there are data.

The calibrated transmissivity fields produced by PEST and MODFLOW are screened according to specific acceptance criteria. Calibrated transmissivity fields that meet the acceptance criteria are modified for the partial and full mining scenarios. This modification increases transmissivity by a random factor between 1 and 1000 in areas identified as containing potash reserves, as described below. Steady-state flow simulations are then run using the mining-modified transmissivity fields.

The transport code SECOTP2D uses a grid with uniform cells of 50 × 50 m. Thus as a final step, MODFLOW runs with a 50 × 50 m grid to calculate the flow fields required for the transport code. The hydraulic conductivities for the finer grid are obtained by dividing each 100 × 100 m cell into four 50 × 50 m cells. The conductivity assigned to each of the four cells is equal to the conductivity of the larger cell (Leigh et al. 2003).

The hydraulic conductivity $\boldsymbol{k}\left(\boldsymbol{x},\boldsymbol{y}\right)$ in Equation (217) is defined in terms of the transmissivity fields $\boldsymbol{t}\left(\boldsymbol{x},\boldsymbol{y}\right)$ by

$$\boldsymbol{k}(\boldsymbol{x},\boldsymbol{y}) = \boldsymbol{t}(\boldsymbol{x},\boldsymbol{y})/\boldsymbol{b}. \quad (219)$$

Fluid flow (i.e., $\boldsymbol{K}\nabla\boldsymbol{h}$) is determined by solving Equation (218) for two different cases: (1) a partial mining case (mining of potash deposits outside the land withdrawal boundary), and (2) a full mining case (mining of potash deposits inside and outside the land withdrawal boundary) (Figure PA-23). As specified by guidance in 40 CFR Part 194 (p. 5229, EPA 1996), potash mining increases the hydraulic conductivity in the Culebra in the vicinity of such mining by an uncertain factor with a value between 1 and 1000. As specified in 40 CFR § 194.32 and described in Section PA-3.8, economic potash reserves outside the land withdrawal boundary are assumed to have been fully mined by the end of the 100 year-period of active institutional controls, after which the occurrence of potash mining within the land withdrawal boundary follows a Poisson process with a rate constant of $\lambda_m = 1 \times 10^{-4}$ yr^{-1}.

In the partial mining case, the hydraulic conductivity $\boldsymbol{k_{PM}}\left(\boldsymbol{x},\boldsymbol{y}\right)$ is defined by Equation (219) inside the WIPP boundary and by $\boldsymbol{k_{PM}}\left(\boldsymbol{x},\boldsymbol{y}\right) = \boldsymbol{k}\left(\boldsymbol{x},\boldsymbol{y}\right) \times \boldsymbol{MF}$ outside the WIPP boundary, where MF is determined by the uncertain parameter CTRANSFM (see Table PA-17). In the full mining case, the hydraulic conductivity $\boldsymbol{k_{FM}}\left(\boldsymbol{x},\boldsymbol{y}\right) = \boldsymbol{k}\left(\boldsymbol{x},\boldsymbol{y}\right) \times \boldsymbol{MF}$ in all areas of the modeling domain.

In turn, $\boldsymbol{k_{PM}}\left(\boldsymbol{x},\boldsymbol{y}\right)$ and $\boldsymbol{k_{FM}}\left(\boldsymbol{x},\boldsymbol{y}\right)$ result in the following definition for the hydraulic conductivity tensor K:

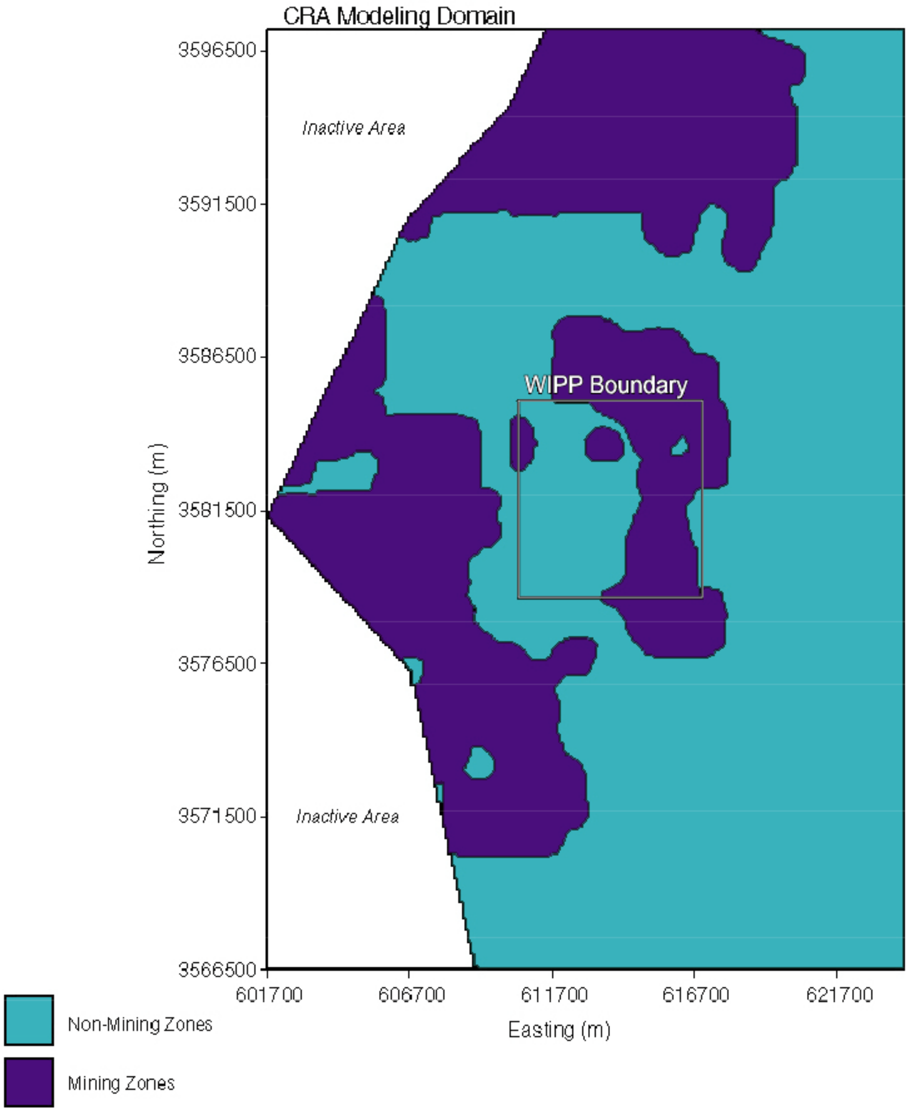

Figure PA-23. Areas of Potash Mining in the McNutt Potash Zone.

$$\boldsymbol{K}_i(x,y) = k_i(x,y)\begin{bmatrix}1 & 0\\ 0 & 1\end{bmatrix}, \quad i = PM, FM\ . \tag{220}$$

In the analysis, Equation (218) is solved with each of the preceding definitions of $\boldsymbol{K}_i$ to obtain characterizations of fluid flow in the Culebra for partially-mined conditions (i.e., $\boldsymbol{K}_{PM}\nabla \boldsymbol{h}$) and fully-mined conditions (i.e., $\boldsymbol{K}_{FM}\nabla \boldsymbol{h}$).

The determination of fluid flow in the Culebra through the solution of Equation (218) does not incorporate the potential effects of climate change on fluid flow. Such effects are incorporated into the analysis by an uncertain scale factor to introduce the potential effects of climate change into the analysis (Corbet and Swift 1996a, 1996b). Specifically, the Darcy fluid velocity $\mathbf{v}_i(x,y)$ actually used in the radionuclide transport calculations is given by

$$\mathbf{v}_i(x,y) = \left[u_i(x,y), v_i(x,y)\right] = SFC\left[\mathbf{K}_i(x,y)\nabla h_i(x,y)\right]^T, \tag{221}$$

where $u_i(x,y)$ and $v_i(x,y)$ represent Darcy fluid velocities (m/s) at the point (x,y) in the x and y directions, respectively, $\nabla h_i(x,y)$ is obtained from Equation (218) with $\mathbf{K} = \mathbf{K}_i$, and SFC is a scale factor used to incorporate the uncertainty that results from possible climate changes. The scale factor SFC is determined by the uncertain parameter CCLIMSF (see Table PA-17).

PA-4.8.3 Computational Grids and Boundary Value Conditions

The representation for fluid flow in the Culebra in Equation (218) is evaluated on a numerical grid 22.4 km east-west by 30.7 km north-south, aligned with the compass directions (Figure PA-24). The modeling domain is discretized into 68,768 uniform 100-m × 100-m cells. The northern model boundary is slightly north of the northern end of Nash Draw, 12 km north of the northern WIPP site boundary, and about 1 km north of Mississippi Potash Incorporated's east tailings pile. The eastern boundary lies in a low-T region that contributes little flow to the modeling domain. The southern boundary lies 12.2 km south of the southern WIPP site boundary, 1.7 km south of WIPP's southernmost well (H-9), and far enough from the WIPP site to have little effect on transport rates on the site. The western model boundary passes through the IMC tailings pond (Laguna Uno; see Hunter (1985)) due west of the WIPP site in Nash Draw.

Two types of boundary conditions are specified: constant-head and no-flow (Figure PA-25). Constant-head conditions are assigned along the eastern boundary of the model domain, and along the central and eastern portions of the northern and southern boundaries. Values of these heads are obtained from the kriged initial head field. The western model boundary passes through the IMC tailings pond (Laguna Uno) due west of the WIPP site in Nash Draw. A no-flow boundary (a flow line) is specified in the model from this tailings pond up the axis of Nash Draw to the northeast, reflecting the concept that groundwater flows down the axis of Nash Draw, forming a groundwater divide. Similarly, another no-flow boundary is specified from the tailings pond down the axis of the southeastern arm of Nash Draw to the southern model boundary, coinciding with a flow line in the regional modeling of Corbet and Knupp (1996). Thus, the northwestern and southwestern corners of the modeling domain are specified as inactive cells in MODFLOW.

PA-4.8.4 Numerical Solution

The flow model in Equation (218) is evaluated with a second-order difference procedure (McDonald and Harbaugh 1988, p. 126) on the computational grid described in Section PA.4.8.3. Specifically, the discretized form of Equation (218) is

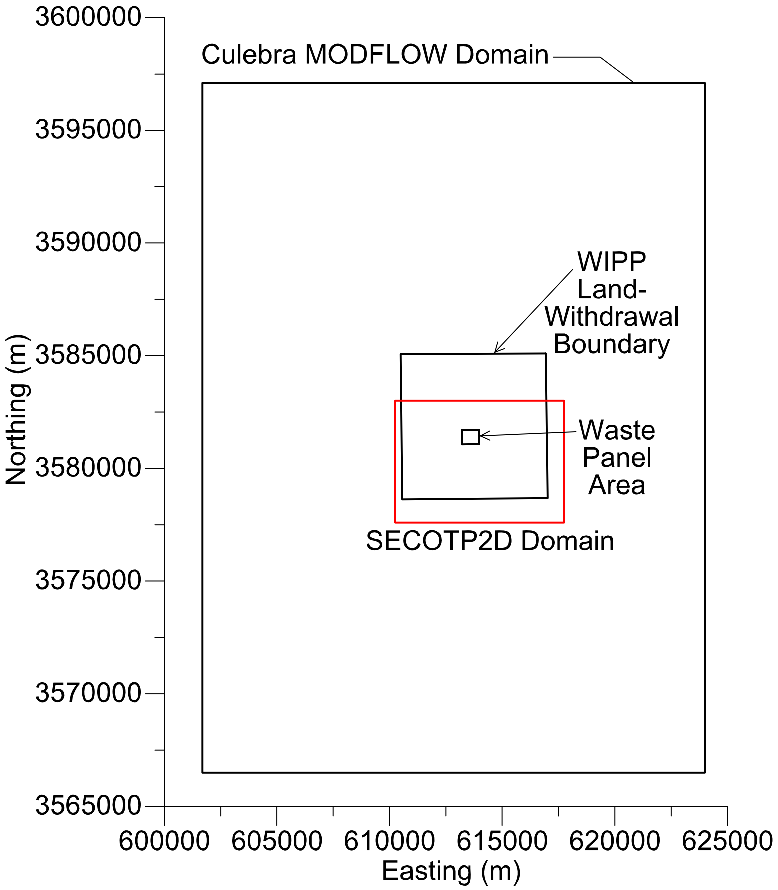

Figure PA-24. Modeling Domain for Groundwater Flow (MODFLOW) and Transport (SECOTP2D) in the Culebra.

$$\begin{aligned} 0 = {} & CR_{i,j-1/2}\left(h_{i,j-1} - h_{i,j}\right) + CR_{i,j+1/2}\left(h_{i,j+1} - h_{i,j}\right) \\ & + CC_{i-1/2,j}\left(h_{i-1,j} - h_{i,j}\right) + CC_{i+1/2,j}\left(h_{i+1,j} - h_{i,j}\right) , \end{aligned} \tag{222}$$

where CR and CC are the row and column hydraulic conductances at the cell interface between node i, j and a neighboring node (m^2/s). Since the grid is uniform, the hydraulic conductance is simply the harmonic mean of the hydraulic conductivity in the two neighboring cells multiplied by the aquifer thickness. For example, the hydraulic conductance between cells (i, j) and $(i, j-1)$ is given by $CR_{i,j-1/2}$ and the hydraulic conductance between cells (i, j) and $(i+1, j)$ is given by $CC_{i+1/2,j}$:

$$CR_{i,j-1/2} = \frac{2k_{i,j}k_{i,j-1}}{k_{i,j} + k_{i,j-1}} \times b \quad \text{and} \quad CC_{i+1/2,j} = \frac{2k_{i,j}k_{i+1,j}}{k_{i,j} + k_{i+1,j}} \times b ,$$

where $k_{i,j}$ is the hydraulic conductivity in cell i, j (m/s) and b is the aquifer thickness (m).

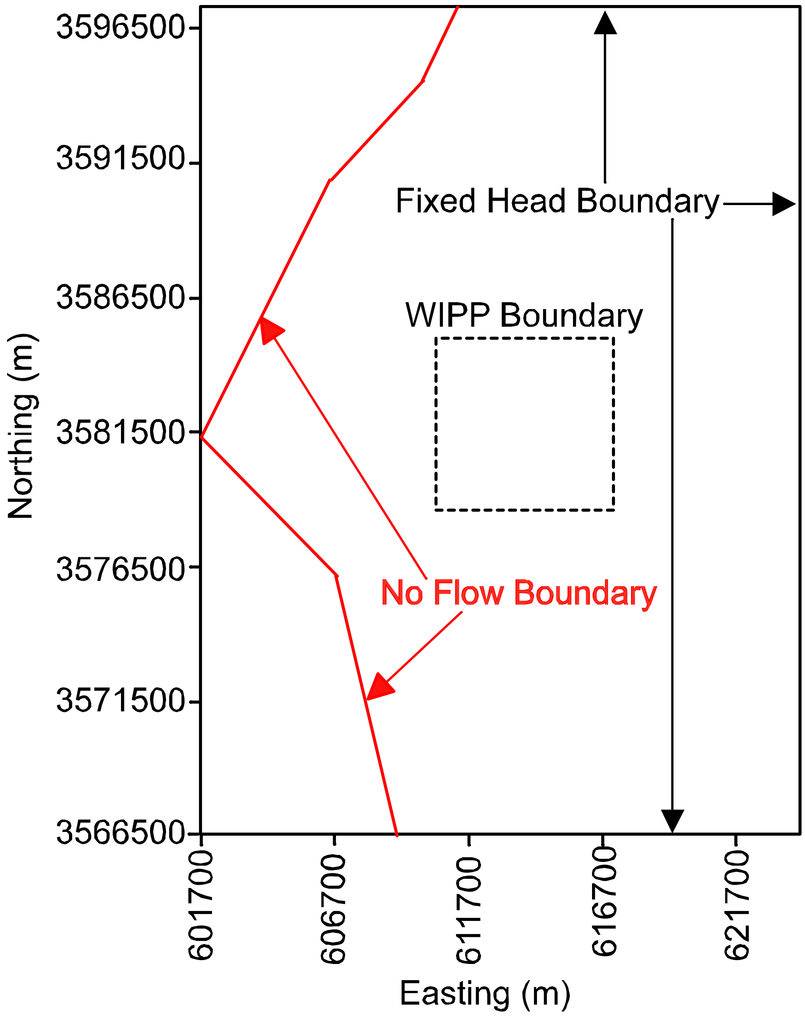

Figure PA-25. Boundary Conditions Used for Simulations of Brine Flow in the Culebra.

Figure PA-26 illustrates the cell numbering convention used in the finite difference grid for MODFLOW. The determination of h is then completed by the solution of the linear system of equations in Equation (222) for the unknown heads $h_{i,j}$. The solution is accomplished using the algebraic multigrid solver (AMG) (Ruge and Stuben 1987) that is part of the Link-AMG (LMG) package within MODFLOW (Mehl and Hill 2001). The AMG method solves Equation (222) with the successive over-relaxation (SOR) iterative method (Roache 1972) on different grids that are coarser than the original grid. The coarser grid solutions provide the initial condition to the next finer solution until a solution based on the original grid size is obtained. The advantage of the AMG method is that the larger grid solutions reduce the large frequency oscillations in the numerical solution much faster than if solved on a finer grid. The finer grid solutions are then able to remove the small frequency oscillations to obtain the final solution. While memory intensive, the AMG method produces solutions faster than ordinary iterative methods (Mehl and Hill 2001). Brine fluxes at cell interfaces are calculated from the values for $h_{i,j}$ internally in MODFLOW.

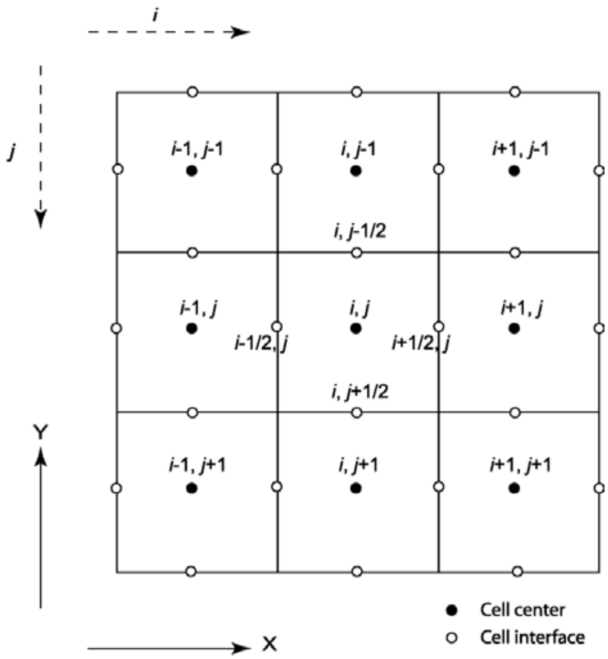

Figure PA-26. Finite Difference Grid Showing Cell Index Numbering Convention Used by MODFLOW.

PA-4.8.5 Additional Information

Additional information on MODFLOW and its use in the CRA-2004 PA to determine fluid flow in the Culebra can be found in the MODFLOW-2000 User's Manual (Harbaugh et al. 2000) and in McKenna and Hart (2003) and Lowry (2003). The flow fields computed for the CRA-2004 PA are presented in Attachment TFIELD.

PA-4.9 Radionuclide Transport in Culebra: SECOTP2D

Radionuclide transport in the Culebra formation is computed using the SECOTP2D computer code. The mathematical equations solved by the code SECOTP2D and the numerical methods used are described in the following sections.

PA-4.9.1 Mathematical Description

Radionuclide transport in the Culebra Dolomite is described by a parallel plate dual porosity model (Meigs and McCord 1996). The parallel plate dual porosity conceptualization assumes that the numerous fractures within the formation are aligned in a parallel fashion and treats the fractured porous media as two overlapping continua: one representing the fractures and the other representing the surrounding porous rock matrix (See Figure PA-27). In this model, one system of partial differential equations (PDEs) is used to represent advective transport in fractures within the Culebra Dolomite and another PDE system is used to represent diffusive transport and sorption in the matrix that surrounds the fractures.

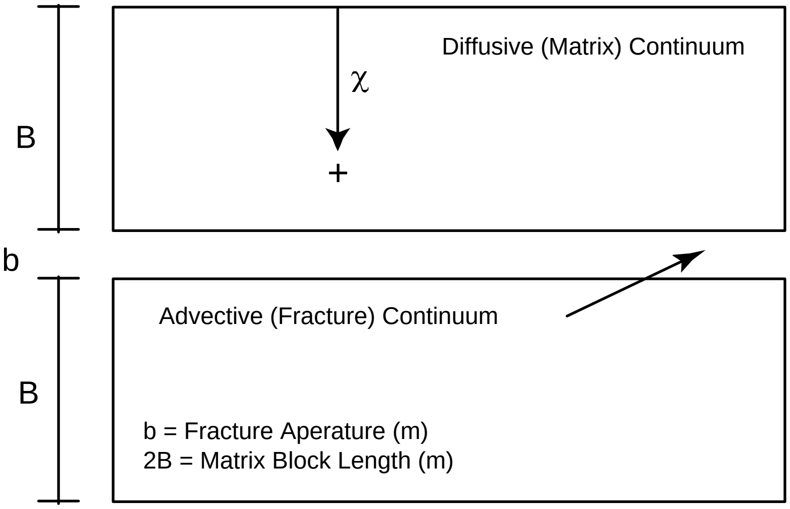

Figure PA-27. Parallel Plate Dual Porosity Conceptualization.

PA-4.9.1.1 Advective Transport in Fractures

The PDE system used to represent advective transport in fractures is given by (WIPP PA 1997b)

$$\nabla \bullet \left[\phi \boldsymbol{D}_k \nabla C_k - \boldsymbol{v} C_k \right] = \phi R_k \left(\frac{\partial C_k}{\partial t} \right) + \phi R_k \lambda_k C_k - \phi R_{k-1} \lambda_{k-1} C_{k-1} - Q_k - \Gamma_k , \qquad (223)$$

for k = 1, 2, …, nR, where

nR = number of radionuclides under consideration,

C_k = concentration of radionuclide k in brine (kg/m^3),

D_k = hydrodynamic dispersion tensor (m^2/s),

v = Darcy velocity (i.e., specific discharge) of brine (m/s = (m^3/m^2)/s),

ϕ = advective (i.e., fracture) porosity (dimensionless),

R_k = advective retardation coefficient (dimensionless),

λ_k = decay constant for radionuclide k (s^{-1}),

Q_k = injection rate of radionuclide k per unit bulk volume of formation ((kg/s)/m^3) (Note: $Q_k > 0$ corresponds to injection into the fractures),

$\boldsymbol{\Gamma}_k$ = mass transfer rate of radionuclide k per unit bulk volume of formation due to diffusion between fractures and surrounding matrix ((kg/s)/m^3) (Note: $\boldsymbol{\Gamma}_k > 0$ corresponds to diffusion into fractures).

The Darcy velocity $\mathbf{v}$ is obtained from the solution of Equation (218); specifically, $\mathbf{v}$ is defined by the relationship in Equation (221). The advective porosity ϕ, defined as the ratio of the interconnected fracture pore volume to the total volume, is determined by an uncertain parameter (see CFRCPOR in Table PA-17).

The hydrodynamic dispersion tensor is defined by (WIPP PA 1997b; Bear 1972)

$$\mathbf{D}_k = \frac{1}{\|\mathbf{v}\|\phi}\begin{bmatrix} u & -v \\ v & u \end{bmatrix}\begin{bmatrix} \alpha_L & 0 \\ 0 & \alpha_T \end{bmatrix}\begin{bmatrix} u & v \\ -v & u \end{bmatrix} + \tau D_k^* \begin{bmatrix} 1 & 0 \\ 0 & 1 \end{bmatrix}, \qquad (224)$$

where α_L and α_T are the longitudinal and transverse dispersivities (m); u and v are the x and y components of $\mathbf{v}$ (i.e., $\mathbf{v} = [u, v]$); D_k^* is the free water molecular diffusion coefficient (m^2 s^{-1}) for radionuclide k; and τ is the advective tortuosity, defined as the ratio of the true length of the flow path of a fluid particle to the straight-line distance between the starting and finishing points of the particle's motion. As in the CCA PA (Helton et al. 1998), the CRA-2004 PA uses $\alpha_L = \alpha_T = 0$ m and $\tau = 1$. Thus, the definition of $\mathbf{D}_k$ used in the CRA-2004 PA reduces to

$$\mathbf{D}_k = D_k^* \begin{bmatrix} 1 & 0 \\ 0 & 1 \end{bmatrix}. \qquad (225)$$

The diffusion coefficient D_k^* equals 3×10^{-10} m^2/s for radionuclides in the +3 oxidation state (i.e., Am(III), Pu(III)), 1.53×10^{-10} m^2/s for radionuclides in the +4 oxidation state (i.e., Pu(IV), Th(IV), U(IV)), and 4.26×10^{-10} m^2/s for radionuclides in the +6 oxidation state (i.e., U(VI)) (Attachment PAR, Table PAR-35). The existence of Pu in the +3 or +4 oxidation state (i.e., as Pu(III) or Pu(IV)) and the existence of U in the +4 or +6 oxidation state (i.e., as U(IV) or U(VI)) is determined by an uncertain parameter (see WOXSTAT in Table PA-17).

The advective retardation coefficient R_k is defined by

$$R_k = 1 + (1 - \phi)\rho_A K_{Ak} / \phi, \qquad (226)$$

where

ρ_A = surface area density of fractures in Culebra (m^2/m^3 = 1/m) (i.e., surface area of fractures (m^2) divided by volume of fractures (m^3)),

K_{Ak} = surface area distribution coefficient ((kg/m^2)/(kg/m^3) = m) (i.e., concentration of radionuclide k sorbed on fracture surfaces (kg/m^2) divided by concentration of radionuclide k dissolved in brine within fractures (kg/m^3)).

Following the logic of the CCA PA (Helton et al. 1998), $K_{Ak} = 0$ and thus $R_k = 1$ in the 2004 PA.

In concept, the term Q_k in Equation (223) provides the link between the releases to the Culebra calculated with NUTS and PANEL (Section PA-6.7) and transport within the Culebra. In the computational implementation of the CRA-2004 PA, radionuclide transport calculations in the Culebra were performed for unit radionuclide releases to the Culebra and then the outcomes of these calculations were used to construct the release to the accessible environment associated with time-dependent releases into the Culebra derived from NUTS and PANEL calculations (Section PA-6.8.7). The definition of Q_k is discussed in more detail in Section PA-4.9.1.4.

The initial condition for Equation (223) is

$$C_k\left(x, y, 0\right) = 0 \text{ kg / m}^3. \tag{227}$$

Furthermore, the boundary value conditions for Equation (223) are defined at individual points on the boundary of the grid in Figure (PA-24) on the basis of whether the flow vector $\mathbf{V} = [u, v]$ defines a flow entering the grid or leaving the grid. The following Neumann boundary value condition is imposed at points $\left(x, y\right)$ where flow leaves the grid:

$$\nabla C_k\left(x, y, t\right) \cdot \mathbf{n}\left(x, y\right) = 0 \text{ (kg/m}^3\text{)/m}, \tag{228}$$

where $\mathbf{n}\left(x, y\right)$ is an outward-pointing unit normal vector defined at $\left(x, y\right)$. The following Dirichlet boundary value condition is imposed at points $\left(x, y\right)$ where flow enters the grid:

$$C_k\left(x, y, t\right) = 0 \text{ kg/m}^3. \tag{229}$$

PA-4.9.1.2 Diffusive Transport in the Matrix

The system of PDEs used to represent diffusive transport in the matrix surrounding the fractures is given by (WIPP PA 1997b)

$$\frac{\partial}{\partial \chi}\left(\phi'_k D'_k \frac{\partial C'_k}{\partial \chi}\right) = \phi' R'_k \left(\frac{\partial C'_k}{\partial t}\right) + \phi' R'_k \lambda_k C'_k - \phi' R'_{k-1} \lambda_{k-1} C'_{k-1}\ , \tag{230}$$

where χ is the spatial coordinate in Figure PA-27, D'_k is the matrix diffusion coefficient (m^2/s) for radionuclide k defined by $D'_k = D^*_k \tau'$, and τ' is the matrix tortuosity. The remaining terms have the same meaning as those in Equation (223) except that the prime denotes properties of the matrix surrounding the fractures. A constant value ($\tau' = 0.11$) for the matrix (i.e., diffusive) tortuosity is used in the CRA-2004 PA (Meigs 1996). The matrix (i.e., diffusive) porosity φ' is an uncertain input to the analysis (see CMTRXPOR in Table PA-17). The matrix retardation R'_k is defined by

$$R'_k = 1 + \left(1 - \phi'\right)\rho_s K_{dk} / \phi' , \tag{231}$$

where ρ_s is the particle density (kg/m^3) of the matrix and K_{dk} is the distribution coefficient ((Ci/kg)/(Ci/m^3) = m^3/kg) for radionuclide k in the matrix. The density ρ_s is assigned a value of 2.82×10^3 kg/m^3 (Martell 1996b). The distribution coefficients K_{dk} are uncertain inputs to the analysis and dependent on the uncertain oxidation state of the relevant element (see CMKDAM3, CMKDPU3, CMKDPU4, CMKDTH4, CMKDU4, CMKDU6, and WOXSTAT in Table PA-17).

The initial and boundary value conditions used in the formulation of Equation (230) are

$$C'_k\left(x, y, \chi, 0\right) = 0 \ kg / m^3 , \tag{232}$$

$$\partial C'_k\left(x, y, 0, t\right) / \partial z = 0 \ \ kg / m^2 , \tag{233}$$

$$C'_k\left(x, y, B, t\right) = C_k(x, y, t), \tag{234}$$

where $\left(x, y\right)$ corresponds to a point in the domain on which Equation (223) is solved and B is the matrix half block length (m) in Figure PA-27 (i.e., 2B is the thickness of the matrix between two fractures). The initial condition in Equation (232) means that no radionuclide is present in the matrix at the beginning of the calculation. The boundary value condition in Equation (233) implies that no radionuclide movement can take place across the centerline of a matrix block separating two fractures. The boundary value condition in Equation (234) ensures that the dissolved radionuclide concentration in the matrix at the boundary with the fracture is the same as the dissolved radionuclide concentration within the fracture. The matrix half block length B is an uncertain input to the analysis (see CFRCSP in Table PA-17).

PA-4.9.1.3 Coupling Between Fracture and Matrix Equations

The linkage between Equation (223) and Equation (230) is accomplished through the term Γ_k, defining the rate at which radionuclide k diffuses across the boundary between a fracture and the adjacent matrix (see Figure PA-27). Specifically,

$$\Gamma_k = -\frac{2\phi}{b}\left(\phi' D'_k \left.\frac{\partial C'_k}{\partial \chi}\right|_{z=\chi} \right), \tag{235}$$

where b is the fracture aperture (m) defined by

$$b = \phi B\left(1 - \phi\right). \tag{236}$$

PA-4.9.1.4 Source Term

As already indicated, Equation (223) and Equation (230) are solved for unit radionuclide releases to the Culebra. Specifically, a release of 1 kg of each radionuclide under consideration was assumed to take place over a time interval from 0 to 50 years, with this release taking place into the computational cell WPAc , located at the center of the Waste Panel Area in Figure PA-24, that has dimensions of 50 m × 50 m. The volume of this cell is given by

$$V = (50m)(50m)(4m) = 1 \times 10^4 \ m^3 , \tag{237}$$

where 4 m is the assumed thickness of the Culebra Dolomite (Meigs and McCord 1996). As a result, $Q_k(x, y, t)$ has the form

$$Q_k(x, y, t) = \frac{1 \ kg}{\left(1 \times 10^4 \ m^3\right)\left(50 \ yr\right)\left(3.16 \times 10^7 \ s / yr\right)} = 6.33 \times 10^{-14} \ kg / m^3 / s \tag{238}$$

for $0 \le t \le 50$ yr and (x, y) is in cell WPAC and $Q_k(x, y, t) = 0$ (kg/m^3/s) otherwise.

PA-4.9.1.5 Cumulative Releases

If $\mathcal{B}$ denotes an arbitrary boundary (e.g., the land withdrawal boundary) in the domain of Equation (223) (i.e., Figure PA-24), then the cumulative transport of $C_k(t, \mathcal{B})$ of radionuclide k from time 0 to time t across $\mathcal{B}$ is given by

$$C_k(t, \mathcal{B}) = \int_0^t \left[\int_{\mathcal{B}} \left\{ \boldsymbol{v}(x, y) C_k(x, y, \tau) - \phi \boldsymbol{D}_k(x, y, t) \nabla C_k(x, y, \tau) \right\} b \bullet \boldsymbol{n}(x, y) ds \right] d\tau , \tag{239}$$

where h is the thickness of the Culebra (4 m), ϕ is the advective porosity in Equation (223), $\boldsymbol{n}(x, y)$ is an outward pointing unit normal vector, and $\int_{\mathcal{B}} ds$ denotes a line integral over $\mathcal{B}$.

PA-4.9.2 Numerical Solution

The numerical solution to the coupled PDE system represented by Equation (223), and Equation (230) is computed using SECOTP2D, an implicit finite volume code for the simulation of multispecies reactive transport. A high-level description of the numerical procedures implemented in SECOTP2D follows, with more detail available in WIPP PA (1997b).

PA-4.9.2.1 Discretization of Fracture Domain

The fracture domain is discretized in space using the block centered finite difference method indicated in Figure PA-28. In this formulation, cell concentrations are defined at grid block centers while the velocity components $[u, v]$ are defined on grid cell faces. A uniform mesh with 50 m × 50 m cells is used for the spatial discretization. Ghost cells are placed outside the problem domain for the purpose of implementing boundary conditions. The temporal discretization is accomplished using variable time step sizes.

The dispersive term, $\nabla \cdot \left(\boldsymbol{\phi D_k} \nabla \boldsymbol{C_k} \right)$, in Equation (223) is approximated using a second-order central difference formula (Fletcher 1988).

The advective term, $\nabla \cdot \boldsymbol{v C_k}$, is approximated using the Total Variation Diminishing (TVD) method (Sweby 1984). The TVD method provides a way of accurately resolving advection dominated transport problems without the occurrence of nonphysical oscillations commonly present in second-order solutions. This method invokes a weighted upstream differencing scheme that locally adjusts the weighting to prevent oscillatory behavior and maximize solution accuracy. The weighting parameters are known as the TVD flux limiters $\Phi\left(x, y, r\right)$, where r is a function of the concentration gradient and direction of flow. PA uses the van Leer TVD limiter (Sweby 1984, p. 1005), which is defined as

$$\Phi\left(x, y, r\right) = \mathbf{max}\left\{0, \mathbf{min}\left\{2r, \frac{r + |r|}{1 + |r|}\right\}\right\}. \tag{240}$$

At locations where u (i.e., the Darcy velocity in the x direction) is positive, r is defined at the j−1/2, k interface by

$$r_{j-1/2,k} = \frac{\partial C/\partial x|_{j-3/2,k}}{\partial C/\partial x|_{j-1/2,k}}, \tag{241}$$

and at locations where u is negative, r is defined by

$$r_{j-1/2,k} = \frac{\partial C/\partial x|_{j+1/2,k}}{\partial C/\partial x|_{j-1/2,k}}. \tag{242}$$

Similar definitions are made for r at the j, k−1/2 interface in the y-direction with $\mathbf{v}$ (i.e., the Darcy velocity in the y direction) used instead of u.

Because Φ_k is a function of C_k, the discretized set of equations is nonlinear. This nonlinearity is addressed by treating the flux limiters explicitly (i.e., time lagged). Explicit treatment of the limiter functions, however, can lead to oscillatory and sometimes unstable solutions when the Courant number exceeds unity (Cr > 1), where Cr is defined by

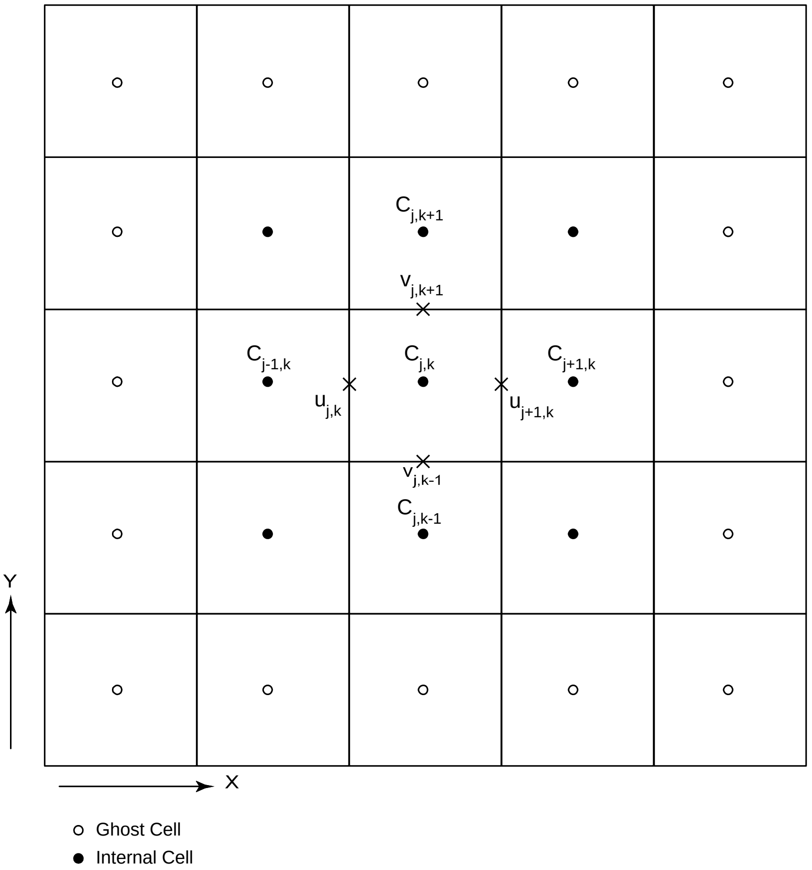

Figure PA-28. Schematic of Finite Volume Staggered Mesh Showing Internal and Ghost Cells.

$$Cr = \max\left\{Cr_x, Cr_y\right\}, \text{ where } Cr_x = |u|\Delta t / \phi\Delta x \text{ and } Cr_y = |v|\Delta t / \phi\Delta y. \qquad (243)$$

To avoid this behavior, the application of the TVD method is restricted to regions in which the Courant numbers are less than one. In regions where Cr > 1, a first order full upwinding scheme is invoked, which is unconditionally stable and nonoscillatory.

The discretized form of Equation (223) can be expressed in a delta formulation as

$$\left(\boldsymbol{I} + \boldsymbol{L}_{xx} + \boldsymbol{L}_{yy} + \boldsymbol{S}\right)\Delta \boldsymbol{C}^{n+1} = \boldsymbol{RHS}^{n}, \qquad (244)$$

where $\boldsymbol{I}$ is the identity matrix, $\boldsymbol{L}_{xx}$ and $\boldsymbol{L}_{yy}$ are finite difference operators in the x and y directions, $\boldsymbol{S}$ is an implicit source term that accounts for decay and mass transfer between the matrix and the fracture, $\boldsymbol{RHS}$ consists of the right hand side known values at time level n, and $\Delta \boldsymbol{C}_{n+1} = \boldsymbol{C}_{n+1} - \boldsymbol{C}_{n}$. Direct inversion of Equation (244) for a typical Culebra transport problem is very computationally intensive, requiring large amounts of memory and time. To reduce these requirements, the operator in Equation (244) is factored as follows:

$$\left(\boldsymbol{I} + \boldsymbol{L}_{xx} + \alpha_x \boldsymbol{S}\right)\left(\boldsymbol{I} + \boldsymbol{L}_{yy} + \alpha_y \boldsymbol{S}\right)\Delta \boldsymbol{C}^{n+1} = \boldsymbol{RHS}^{n}, \qquad (245)$$

where α_x and α_y are constants that must sum to one (i.e., $\alpha_x + \alpha_y = 1$). The left hand sides in Equation (244) and Equation (245) are not equivalent, with the result that the factorization of Equation (244) in Equation (245) is referred to as an approximate factorization (Fletcher 1988). The advantage of approximately factoring Equation (244) is that the resulting equation consists of the product of two finite difference operators that are easily inverted independently using a tridiagonal solver. Hence, the solution to the original problem is obtained by solving a sequence of problems in the following order:

$$\left(\boldsymbol{I} + \boldsymbol{L}_{xx} + \alpha_x \boldsymbol{S}\right)\Delta \overline{\boldsymbol{C}} = \boldsymbol{RHS}^{n}, \qquad (246)$$

$$\left(\boldsymbol{I} + \boldsymbol{L}_{yy} + \alpha_y \boldsymbol{S}\right)\Delta \boldsymbol{C}^{n+1} = \Delta \overline{\boldsymbol{C}}, \qquad (247)$$

$$\boldsymbol{C}^{n+1} = \boldsymbol{C}^{n} + \Delta \boldsymbol{C}^{n+1}. \qquad (248)$$

PA-4.9.2.2 Discretization of Matrix Equation

The nonuniform mesh used to discretize the matrix equation is shown in Figure PA-29. Straightforward application of standard finite difference or finite volume discretizations on nonuniform meshes results in truncation error terms which are proportional to the mesh spacing variation (Hirsch 1988). For nonuniform meshes, the discretization can be performed after a transformation from the Cartesian physical space (χ) to a stretched Cartesian computational space (ξ). The transformation is chosen so that the nonuniform grid spacing in physical space is transformed to a uniform spacing of unit length in computational space (the computational space is thus a one-dimensional domain with a uniform mesh). The transformed equations contain metric coefficients that must be discretized, introducing the mesh size influence into the difference formulas. Then standard unweighted differencing schemes can then be applied to the governing equations in the computational space.

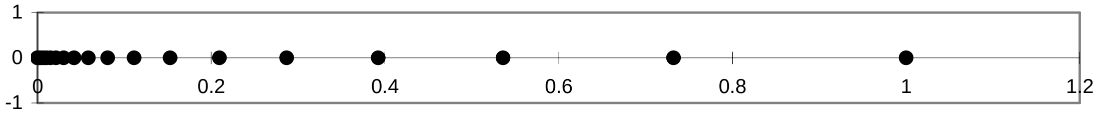

Figure PA-29. Illustration of Stretched Grid Used for Discretization of Matrix Domain.

The SECOTP2D code applies such a coordinate transformation to the nonuniform diffusion domain mesh, solving the transformed system of equations in the uniform computational space. The transformed matrix equation is written as:

$$\phi' R'_k \frac{\partial \hat{C}'_k}{\partial t} - \frac{\partial \hat{F}'_v}{\partial \xi'} = -\phi' R'_k \lambda_k \hat{C}'_k + \phi' R'_{k-1} \lambda_{k-1} \hat{C}'_{k-1}, \qquad (249)$$

where

$$\hat{C}'_k = \frac{C'_k}{J}, \tag{250}$$

$$\hat{F}'_v = D'\xi'_x \frac{\partial C'_k}{\partial \xi'}. \tag{251}$$

In the uniform computational space, a first-order backwards difference formula is used to approximate the temporal derivative while a second-order accurate central difference is used to approximate spatial derivatives.

PA-4.9.2.3 Fracture-Matrix Coupling

The equations for the fracture and the matrix are coupled through the mass transfer term Γ_k. In the numerical solution, these equations are coupled in a fully implicit manner and solved simultaneously. A procedure outlined in (Huyakorn et al. 1983) was adapted and redeveloped for an approximate factorization algorithm with the delta formulation and a finite volume grid. The coupling procedure consists of three steps.

Step 1. Write the mass transfer term Γ_k in a delta (Δ) form.

Step 2. Evaluate Δ terms that are added to the implicit part of the fracture equation. This is accomplished using the inversion process (LU factorization) in the solution of the matrix equation. After the construction of the lower tridiagonal matrix L and the intermediate solution, there is enough information to evaluate the Δ terms. This new information is fed into the fracture equation that subsequently is solved for concentrations in the fracture at the new time level (n+1).

Step 3. Construct the boundary condition for the matrix equation at the fracture-matrix interface using fracture concentrations at the (n+1) time level. Matrix concentrations are then obtained using the upper tridiagonal matrix U by back substitution. A detailed description of this technique and its implementation is given in the SECOTP2D User's Manual (WIPP PA 1997b).

PA-4.9.2.4 Cumulative Releases

The cumulative transport $C_k(t,\mathcal{B})$ of individual radionuclides across specified boundaries indicated in Equation (239) is also accumulated during the numerical solution of Equation (223) and Equation (230).

PA-4.9.3 Additional Information

Additional information on SECOTP2D and its use in the CRA-2004 PA to determine radionuclide transport in the Culebra Dolomite can be found in the SECOTP2D User's Manual (WIPP PA 1997b) and in the analysis package for radionuclide transport in the Culebra Dolomite (Kanney 2003).

PA-5.0 PROBABILISTIC CHARACTERIZATION OF SUBJECTIVE UNCERTAINTY

This section summarizes the uncertain parameters in the CRA-2004 PA that constitute the space for subjective uncertainty defined in Section PA-2.4.

PA-5.1 Probability Space

As discussed in Section PA-2.4, the third entity (EN3) that underlies the CRA-2004 PA is a probabilistic characterization of the uncertainty in important variables used as input to the analysis. This entity is defined by a probability space $\left(\boldsymbol{X}_{su}, \boldsymbol{S}_{su}, \boldsymbol{p}_{su}\right)$ that characterizes subjective uncertainty. The individual elements of S_{su} are vectors $\boldsymbol{x}_{su}$ of the form

$$\boldsymbol{x}_{su} = \left[x_1, x_2, \ldots x_{nV}\right], \tag{252}$$

where each x_j is an imprecisely-known input to the analysis and nV is the number of such inputs.

The uncertainty in the x_j, and hence in $\boldsymbol{x}_{su}$, is characterized by developing a distribution

$$D_j,\ j = 1, 2, \ldots, nV, \tag{253}$$

for each x_j. Each distribution is based on all available knowledge about the corresponding variable and describes a degree of belief as to where the appropriate value to use for this variable is located. This degree of belief is conditional on the numerical, spatial, and temporal resolution of the models selected for use in the CRA-2004 PA (Chapter PA-4.0). When appropriate, correlations between imprecisely-known variables are also possible, with such correlations indicating a dependency in the knowledge about the correlated variables. It is the distributions in Equation (253) and any associated correlations between the x_j that define $\left(\boldsymbol{X}_{su}, \boldsymbol{S}_{su}, \boldsymbol{p}_{su}\right)$.

The uncertain variables (i.e., x_j) incorporated into the CRA-2004 PA are discussed in Section PA-5.2. Then, the distributions and correlations assigned to these variables are described in Section PA-5.3 and Section PA-5.4. Finally, a discussion of the concept of a scenario is given in Section PA-5.5.

PA-5.2 Variables Included For Subjective Uncertainty

The CRA-2004 PA selected nV = 64 imprecisely-known variables for inclusion in the analysis (Table PA-17). The individual variables in Table PA-17 correspond to the elements x_j of the vector $\boldsymbol{x}_{su}$ in Equation (252). Most variables listed in Table PA-17 were also treated as uncertain in the CCA PA (CCA Appendix PAR). Table PA-18 lists the differences between the set of subjectively uncertain variables in the CCA PA and the CRA-2004 PA. Most differences result from the inclusion of additional uncertain variables from the 1997 PAVT. All subjectively uncertain variables incorporated into the CRA-2004 PA are used as input to the models discussed in Section PA-2.3 and Chapter 4.0.

PA-5.3 Variable Distributions

Each uncertain variable is assigned a distribution that characterizes the subjective uncertainty in that variable. Distributions for each parameter are described in Attachment PAR. Attachment PAR contains documentation for each of the 64 parameters that were sampled by the LHS code during the PA.

PA-5.4 Correlations

Most of the variables in Table PA-17 are assumed to be uncorrelated. However, the pairs (ANHCOMP, ANHPRM), (HALCOMP, HALPRM), and (BPCOMP, BPPRM) are assumed to have rank correlations of –0.99, –0.99, and –0.75, respectively (Figure PA-30, Figure PA-31, and Figure PA-32). These correlations result form a belief that the underlying physics implies that a large value for one variable in a pair should be associated with a small value for the other variable in the pair. The scatterplots in Figure PA-29, Figure PA-30, and Figure PA-31 result from the LHSs described in Section PA-6.4, with the rank correlations within the pairs (ANHCOMP, ANHPRM), (HALCOMP, HALPRM), and (BPCOMP, BPPRM) induced with the Iman and Conover (1982) restricted pairing technique.

The distributions and associated correlations indicated in Table PA-17 and Figure PA-29, Figure PA-30, and Figure PA-31 define the probability space $\left(\boldsymbol{X}_{su}, \boldsymbol{S}_{su}, \boldsymbol{p}_{su}\right)$ for subjective uncertainty in Section PA.2.4. The vector $\boldsymbol{x}_{su}$ in Equation (252) has the form

$$\boldsymbol{x}_{su} = \left[\boldsymbol{ANHBCEXP, ANHBCVGP, ..., WTAUFAIL}\right], \tag{254}$$

where the individual elements of $\boldsymbol{x}_{su}$ are the subjectively uncertain variables described in Table PA-17.

PA-5.5 Separation of Stochastic and Subjective Uncertainty

The CRA-2004 PA uses the term “scenario” to refer to subsets E_{st} of the sample space, S_{st} for stochastic uncertainty, with scenario probabilities $\boldsymbol{p}_{st}\left(\boldsymbol{E}_{st}\right)$ being defined by the function p_{st} associated with the probability space $\left(\boldsymbol{X}_{st}, \boldsymbol{S}_{st}, \boldsymbol{p}_{st}\right)$ (Section PA-3.9). This definition is consistent with the concept that a scenario is something that could happen in the future. Subsets E_{su} of the sample space for subjective uncertainty S_{su} are not referred to as scenarios to maintain the important distinction between the two sample spaces. In particular, a scenario E_{st} contains vectors $\boldsymbol{x}_{st}$ of the form defined in Equation (3), and the probability $\boldsymbol{p}_{st}\left(\boldsymbol{E}_{st}\right)$ for E_{st} characterizes the likelihood that a vector $\boldsymbol{x}_{st}$ in E_{st} will match the occurrences that will take place at the WIPP over the next 10,000 years. In contrast, a subset E_{su} from the space of subjective uncertainty X_{su} contains vectors $\boldsymbol{x}_{su}$ of the form defined in Equation (252) and the probability $\boldsymbol{p}_{su}\left(\boldsymbol{E}_{su}\right)$ characterizes a degree of belief that a vector $\boldsymbol{x}_{su}$ in E_{su} contains the appropriate values for the 64 uncertain variables in Table PA-17.

Table PA-17. Variables Representing Subjective Uncertainty in the CRA-2004 PA

Sample Position	Variable Name	Material Name	Property Name	Description
1	WGRCOR	STEEL	CORRMCO2	Rate of anoxic steel corrosion (m/s) under brine inundated conditions and with no CO_2 present. Defines R_{ci} in Equation (59) for areas Waste Panel, South RoR, and North RoR in Figure PA-8.
2	WMICDFLG	WAS_AREA	PROBDEG	Index for model of microbial degradation of CPR materials (dimensionless). Used in areas Waste Panel, South RoR, and North RoR in Figure PA-8.
3	WGRMICI	WAS_AREA	GRATMICI	Rate of CPR biodegradation (mol $C_6H_{10}O_5$ / kg $C_6H_{10}O_5$ / s) under anaerobic, brine-inundated conditions. Defines R_{mi} in Equation (61) for areas Waste Panel, South RoR, and North RoR, in Figure PA-8.
4	WGRMICH	WAS_AREA	GRATMICH	Rate of CPR biodegradation (mol $C_6H_{10}O_5$ / kg $C_6H_{10}O_5$ / s) under anaerobic, humid conditions. Defines R_{mh} in Equation (61) for areas Waste Panel, South RoR, and North RoR, in Figure PA-8.
5	WFBETCEL	CELLULS	FBETA	Scale factor used in definition of stoichiometric coefficient for microbial gas generation (dimensionless). Defines β in Equation (77) for areas Waste Panel, South RoR, and North RoR, in Figure PA-8.
6	WRGSSAT	WAS_AREA	SAT_RGAS	Residual gas saturation in waste (dimensionless). Defines S_{gr} in Equation (35) for areas Waste Panel, South RoR, and North RoR in Figure PA-8; also used in waste material in Figure PA-20 for calculation of DBR; see Section PA-4.7.
7	WRBRNSAT	WAS_AREA	SAT_RBRN	Residual brine saturation in waste (dimensionless). Defines S_{br} in Equation (34) for areas Waste Panel, South RoR, and North RoR, in Figure PA-8; also used in waste material in Figure PA-20 for calculation of DBR; see Section PA-4.7.
8	WASTWICK	WAS_AREA	SAT_WICK	Increase in brine saturation of waste due to capillary forces (dimensionless). Defines S_{wick} in Equation (78) for areas Waste Panel, South RoR, and North RoR, in Figure PA-8.

Table PA-17. Variables Representing Subjective Uncertainty in the CRA-2004 PA — Continued

Sample Position	Variable Name	Material Name	Property Name	Description
9	DRZPCPRM	DRZ_PCS	PRMX_LOG	Logarithm of intrinsic permeability (m^2) of the DRZ immediately above the panel closure concrete (Section PA-4.2.8.3). Used in region DRZ_PCS in Figure PA-8.
10	CONPRM	CONC_PCS	PRMX_LOG	Logarithm of intrinsic permeability (m^2) for the concrete portion of the panel closure. (Section PA-4.2.8.1). Used in region CONC_PCS in Figure PA-8.
11	WSOLU4C	SOLU4	SOLCIM	Uncertainty factor (dimensionless) for solubility of U in the +IV oxidation state in Castile brine. Defines UF(Castile, +4, U) in Equation (90).
12	WSOLTH4C	SOLTH4	SOLCIM	Uncertainty factor (dimensionless) for solubility of Th in the +IV oxidation state in Castile brine. Defines UF(Castile, +4, Th) in Equation (90).
14	CONGSSAT	CONC_PCS	SAT_RGAS	Residual gas saturation (dimensionless) in panel closure concrete (Section PA-4.2.8.1). Defines S_{gr} in Equation (35) for area CONC_PCS in Figure PA-8.
15	CONBRSAT	CONC_PCS	SAT_RBRN	Residual brine saturation (dimensionless) in panel closure concrete (Section PA-4.2.8.1). Defines S_{br} in Equation (35) for use in region CONC_PCS in Figure PA-8.
16	CONBCEXP	CONC_PCS	PORE_DIS	Brooks-Corey pore distribution parameter (dimensionless) for panel closure concrete (Section PA-4.2.8.1). Defines λ in Equation (32) for region CONC_PCS of Figure PA-8 for use with Brooks-Corey model; defines λ in $m = \lambda/(1+\lambda)$ in Equation (36) for use with van Genuchten-Parker model in region CONC_PCS.
17	HALPOR	S_HALITE	POROSITY	Halite porosity (dimensionless). Defines ϕ_0 in Equation (25g) for region Salado in Figure PA-8.
18	HALPRM	S_HALITE	PRMX_LOG	Logarithm of intrinsic halite permeability (m^2). Used in region Salado in Figure PA-8.
19	HALCOMP	S_HALITE	COMP_RCK	Bulk compressibility of halite (Pa^{-1}). Defines β_{fB} in Equation (31) for region Salado of Figure PA-8.
20	ANHPRM	S_MB139	PRMX_LOG	Logarithm of intrinsic anhydrite permeability (m^2). Used in regions MB 138, Anhydrite AB, and MB 139 in Figure PA-8.
21	ANHCOMP	S_MB139	COMP_RCK	Bulk compressibility of anhydrite (Pa^{-1}). Defines β_{fB} in Equation (31) for regions MB 138, Anhydrite AB and MB 139 in Figure PA-8.

Table PA-17. Variables Representing Subjective Uncertainty in the CRA-2004 PA — Continued

Sample Position	Variable Name	Material Name	Property Name	Description
22	ANHBCVGP	S_MB139	RELP_MOD	Indicator for relative permeability model (dimensionless) for regions MB 138, Anhydrite AB and MB 139 in Figure PA-8. See Table PA-3.
23	ANRBRSAT	S_MB139	SAT_RBRN	Residual brine saturation in anhydrite (dimensionless). Defines S_{br} in Equation (35) for regions MB 138, Anhydrite AB, and MB 139 in Figure PA-8.
24	ANRGSSAT	S_MB139	SAT_RGAS	Residual gas saturation in anhydrite (dimensionless). Defines S_{gr} in Equation (34) for regions MB 138, Anhydrite AB, and MB 139 in Figure PA-8.
25	ANHBCEXP	S_MB139	PORE_DIS	Brooks-Corey pore distribution parameter for anhydrite (dimensionless). Defines λ in Equation (32) for regions MB 138, Anhydrite AB, and MB 139 of Figure PA-8 for use with Brooks-Corey model; defines λ in $m = \lambda/(1 + \lambda)$ in Equations (36) for use with van Genuchten-Parker model in the same regions.
26	SALPRES	S_HALITE	PRESSURE	Initial brine pore pressure (Pa) in the Salado halite, applied at an elevation consistent with the intersection of MB 139. Defines $p_{b,ref}$ for Equation (49) for region Salado in Figure PA-8.
27	BPINTPRS	CASTILER	PRESSURE	Initial brine pore pressure in the Castile brine reservoir. Defines $Pb^{(x,y,-5)}$ in Equation (50) for region CASTILER in Figure PA-8.
28	BPPRM	CASTILER	PRMX_LOG	Logarithm of intrinsic permeability (m^2) of the Castile brine reservoir. Used in region CASTILER in Figure PA-8.
29	BPCOMP	CASTILER	COMP_RCK	Bulk compressibility (Pa^{-1}) of Castile brine reservoir. Defines β_{fB} in Equation (29) for region CASTILER of Figure PA-8
30	BHPERM	BH_SAND	PRMX_LOG	Logarithm of intrinsic permeability (m^2) of the silty sand-filled borehole (Table PA-5). Used in regions Upper Borehole and Lower Borehole in Figure PA-8.
31	DRZPRM	DRZ_1	PRMX_LOG	Logarithm of intrinsic permeability (m^2) of the DRZ. Used in regions Upper DRZ and Lower DRZ in Figure PA-8.
32	PLGPRM	CONC_PLG	PRMX_LOG	Logarithm of intrinsic permeability (m^2) of the concrete borehole plugs (Table PA-5). Used in region Borehole Plugs in Figure PA-8.
34	WSOLAM3S	SOLAM3	SOLSIM	Uncertainty factor (dimensionless) for solubility of Am in the +III oxidation state in Salado brine. Defines UF(Salado, +3, Am) in Equation (90).

Table PA-17. Variables Representing Subjective Uncertainty in the CRA-2004 PA — Continued

Sample Position	Variable Name	Material Name	Property Name	Description
35	WSOLAM3C	SOLAM3	SOLCIM	Uncertainty factor (dimensionless) for solubility of Am in the +III oxidation state in Castile brine. Defines UF(Castile, +3, Am) in Equation (90).
36	WSOLPU3S	SOLPU3	SOLSIM	Uncertainty factor (dimensionless) for solubility of Pu in the +III oxidation state in Salado brine. Defines UF(Salado, +3, Pu) in Equation (90).
37	WSOLPU3C	SOLPU3	SOLCIM	Uncertainty factor (dimensionless) for solubility of Pu in the +III oxidation state in Castile brine. Defines UF(Castile, +3, Pu) in Equation (90).
38	WSOLPU4S	SOLPU4	SOLSIM	Uncertainty factor (dimensionless) for solubility of Pu in the +IV oxidation state in Salado brine. Defines UF(Salado, +4, Pu) in Equation (90).
39	WSOLPU4C	SOLPU4	SOLCIM	Uncertainty factor (dimensionless) for solubility of Pu in the +IV oxidation state in Castile brine. Defines UF(Castile, +4, Pu) in Equation (90).
40	WSOLU4S	SOLU4	SOLSIM	Uncertainty factor (dimensionless) for solubility of U in the +IV oxidation state in Salado brine. Defines UF(Salado, +4, U) in Equation (90).
41	WSOLU6S	SOLU6	SOLSIM	Uncertainty factor (dimensionless) for solubility of U in the +VI oxidation state in Salado brine. Defines UF(Salado, +6, U) in Equation (90).
42	WSOLU6C	SOLU6	SOLCIM	Uncertainty factor (dimensionless) for solubility of U in the +VI oxidation state in Castile brine. Defines UF(Castile, +6, U) in Equation (90).
43	WSOLTH4S	SOLTH4	SOLSIM	Uncertainty factor (dimensionless) for solubility of Th in the +IV oxidation state in Salado brine. Defines UF(Salado, +4, Th) in Equation (90).
44	WPHUMOX3	PHUMOX3	PHUMCIM	Ratio (dimensionless) of concentration of actinides attached to humic colloids to dissolved concentration of actinides for oxidation state +III in Castile brine. Defines SF_{Hum}(Castile, +3, Am) and SF_{Hum}(Castile, +3, Pu) for Equation (90).
45	WOXSTAT	GLOBAL	OXSTAT	Indicator variable for elemental oxidation states (dimensionless). WOXSTAT = 0 indicates use of CMKDPU3, CMKDU4, WSOLPU3C, WSOLPUS, , WSOLU4C, and WSOLU4S. WOXSTAT = 1 implies use of CMKDPU4, CMKDU6, WSOLPU4C, WSOLPU4S, WSOLU6C, and WSOLU6S.

Table PA-17. Variables Representing Subjective Uncertainty in the CRA-2004 PA — Continued

Sample Position	Variable Name	Material Name	Property Name	Description
46	CTRANSFM	CULEBRA	MINP_FAC	Multiplier (dimensionless) applied to transmissivity of the Culebra within the land withdrawal boundary after mining of potash reserves. Defines MF in Equation (216) (see section PA-4.8.2).
47	CTRAN	GLOBAL	TRANSIDX	Indicator variable for selecting transmissivity field. See Section PA-4.8.2.
48	CCLIMSF	GLOBAL	CLIMTIDX	Climate scale factor (dimensionless) for Culebra flow field. Defines SFC in Equation (221).
49	CFRACSP	CULEBRA	HMBLKLT	Culebra fracture spacing (m). Equal to half the distance between fractures (i.e., the Culebra half matrix block length). Defines B in Equation (236) and Figure PA-26.
50	CFRACPOR	CULEBRA	APOROS	Culebra fracture (i.e., advective) porosity (dimensionless). Defines ϕ in Equation (223).
51	CMTRXPOR	CULEBRA	DPOROS	Culebra matrix (i.e., diffusive) porosity (dimensionless). Defines ϕ' in Equation (230).
52	CMKDU6	U+6	MKD_U	Matrix distribution coefficient (m^3/kg) for U in +6 oxidation state. Defines K_{dk} in Equation (231).
53	CMKDU4	U+4	MKD_U	Matrix distribution coefficient (m^3/kg) for U in +4 oxidation state. Defines K_{dk} in Equation (231).
54	CMKDPU3	PU+3	MKD_PU	Matrix distribution coefficient (m^3/kg) for Pu in +3 oxidation state. Defines K_{dk} in Equation (231).
55	CMKDPU4	PU+4	MKD_PU	Matrix distribution coefficient (m^3/kg) for Pu in +4 oxidation state. Defines K_{dk} in Equation (231).
56	CMKDTH4	TH+4	MKD_TH	Matrix distribution coefficient (m^3/kg) for Th in +4 oxidation state. Defines K_{dk} in Equation (231).
57	CMKDAM3	AM+3	MKD_AM	Matrix distribution coefficient (m^3/kg) for Am in +3 oxidation state. Defines K_{dk} in Equation (231).
58	WTAUFAIL	BOREHOLE	TAUFAIL	Shear strength of waste (Pa). Defines $r(R,1)$ in Equation (111).
60	PBRINE	GLOBAL	PBRINE	Probability that a drilling intrusion penetrates pressurized brine in the Castile Formation. Defines p_{B1}; see Section PA-3.5.

Table PA-17. Variables Representing Subjective Uncertainty in the CRA-2004 PA — Continued

Sample Position	Variable Name	Material Name	Property Name	Description
61	DOMEGA	BOREHOLE	DOMEGA	Drill string angular velocity (rad/s). Defines $\Delta\Omega$ in Equation (112b).
62	SHURBRN	SHFTU	SAT_RBRN	Residual brine saturation in upper shaft seal materials (dimensionless). Defines S_{br} in Equation (35) for region Upper Shaft in Figure PA-8.
63	SHURGAS	SHFTU	SAT_RGAS	Residual gas saturation in upper shaft seal materials (dimensionless). Defines S_{gr} in Equation (34) for region Upper Shaft in Figure PA-8.
64	SHUPRM	SHFTU	PRMX_LOG	Logarithm of intrinsic permeability (m^2) of upper shaft seal materials. Used in region Upper Shaft in Figure PA-8.
65	SHLPRM1	SHFTL_T1	PRMX_LOG	Logarithm of intrinsic permeability (m^2) of lower shaft seal materials for the first 200 years after closure. Used in region Lower Shaft in Figure PA-8.
66	SHLPRM2	SHFTL_T2	PRMX_LOG	Logarithm of intrinsic permeability (m^2) of lower shaft seal materials from 200 years to 10,000 years after closure. Used in region Lower Shaft in Figure PA-8.
75	RNDSPALL	SPALLMOD	RNDSPALL	Indicator variable for selecting element from the LHS for DRSPALL. See Section PA-4.6.4.

1

Table PA-18. Differences in Uncertain Parameters in the CCA PA and CRA-2004 PA

Material Name	Property Name	Description	When Used	Reason for Removal or Addition
DRZ_PCS	PRMX_LOG	Logarithm of intrinsic permeability (m^2) of the DRZ immediately above the panel closure concrete.	2003	Added due to the addition of the Option D panel closures.
CONC_PCS	PRMX_LOG	Logarithm of intrinsic permeability (m^2) for the concrete portion of the panel closure.	2003	Added due to the addition of the Option D panel closures.
SOLU4	SOLCIM	Uncertainty factor (dimensionless) for solubility of U in the +IV oxidation state in Castile brine.	2003	Added for completeness.
SOLTH4	SOLCIM	Uncertainty factor (dimensionless) for solubility of Th in the +IV oxidation state in Castile brine.	2003	Added for completeness.
DRZ_1	PRMX_LOG	Logarithm of intrinsic permeability (m^2) of the DRZ.	2003	Added from 1997 PAVT (Hansen and Leigh 2003).
CONC_PLG	PRMX_LOG	Logarithm of intrinsic permeability (m^2) of the concrete borehole plugs.	2003	Added from 1997 PAVT (Hansen and Leigh 2003).
GLOBAL	PBRINE	Probability that a drilling intrusion penetrates pressurized brine in the Castile Formation.	2003	Added due to change in Castile Brine pocket modeling (Section 6.12.4.6).
BOREHOLE	DOMEGA	Drill string angular velocity (rad/s).	2003	Added from 1997 PAVT (Hansen and Leigh 2003).
SHFTU	SAT_RBRN	Residual brine saturation in upper shaft seal materials (dimensionless).	2003	Added due to the simplified shaft model.
SHFTU	SAT_RGAS	Residual gas saturation in upper shaft seal materials (dimensionless).	2003	Added due to the simplified shaft model.
SHFTU	PRMX_LOG	Logarithm of intrinsic permeability (m^2) of upper shaft seal materials.	2003	Added due to the simplified shaft model.
SHFTL_T1	PRMX_LOG	Logarithm of intrinsic permeability (m^2) of lower shaft seal materials for the first 200 years after closure.	2003	Added due to the simplified shaft model.
SHFTL_T2	PRMX_LOG	Logarithm of permeability of lower shaft seal materials (m^2) from 200 years to 10,000 years after closure.	2003	Added due to the simplified shaft model.
SPALLMOD	RNDSPALL	Indicator variable for selecting element from the LHS for DRSPALL.	2003	Use of DRSPALL to calculate spall volumes.

Table PA-18. Differences in Uncertain Parameters in the CCA PA and CRA-2004 PA — Continued

Material Name	Property Name	Description	When Used	Reason for Removal or Addition
CL_L_T1	PRMX_LOG	Logarithm of intrinsic permeability (m^2) for clay components of shaft.	1996	Removed due to the simplified shaft model.
CONC_T1	PRMX_LOG	Logarithm of intrinsic permeability (m^2) for concrete component of shaft seal for 0 to 400 years.	1996	Removed due to the simplified shaft model.
ASPHALT	PRMX_LOG	Logarithm of intrinsic permeability (m^2) for clay components of shaft seal (m^2).	1996	Removed due to the simplified shaft model.
SHFT_DRZ	PRMX_LOG	Logarithm of intrinsic permeability (m^2) of DRZ surrounding shaft.	1996	Removed due to the simplified shaft model.
SALT_T1	CUMPROB	Pointer variable used to select intrinsic permeability in crushed salt component of shaft seal at different times.	1996	Removed due to the simplified shaft model.
CASTILER	GRIDFLO	Pointer variable for selection of brine pocket volume.	1996	Removed due to changes in Castile Brine pocket modeling (Section 6.12.4.6).
BLOWOUT	PARTDIA	Waste particle diameter (m).	1996	Removed due to replacement of spall model.

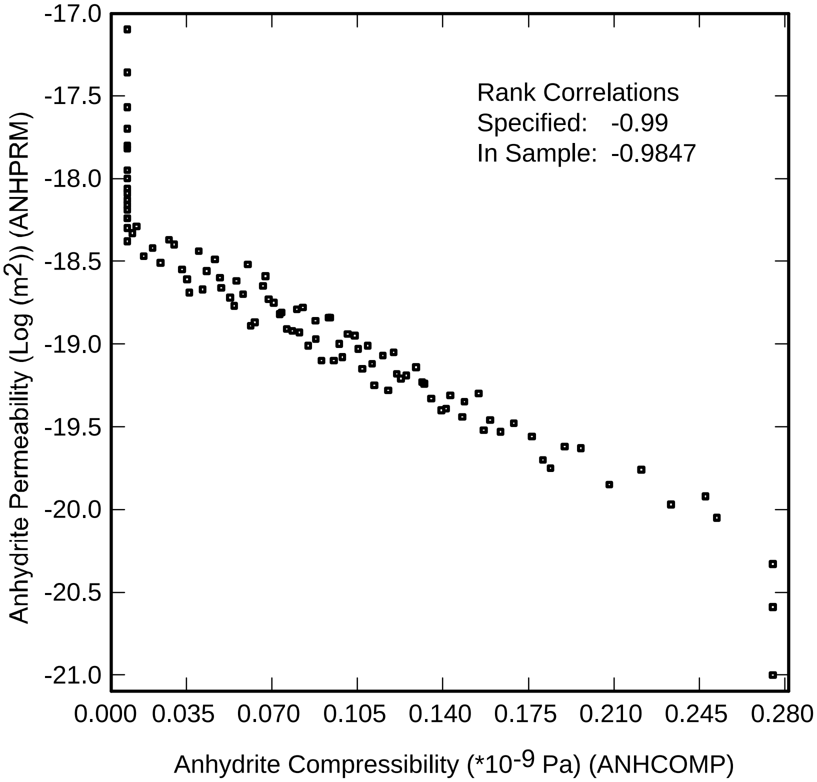

Figure PA-30. Correlation Between ANHCOMP and ANHPRM.

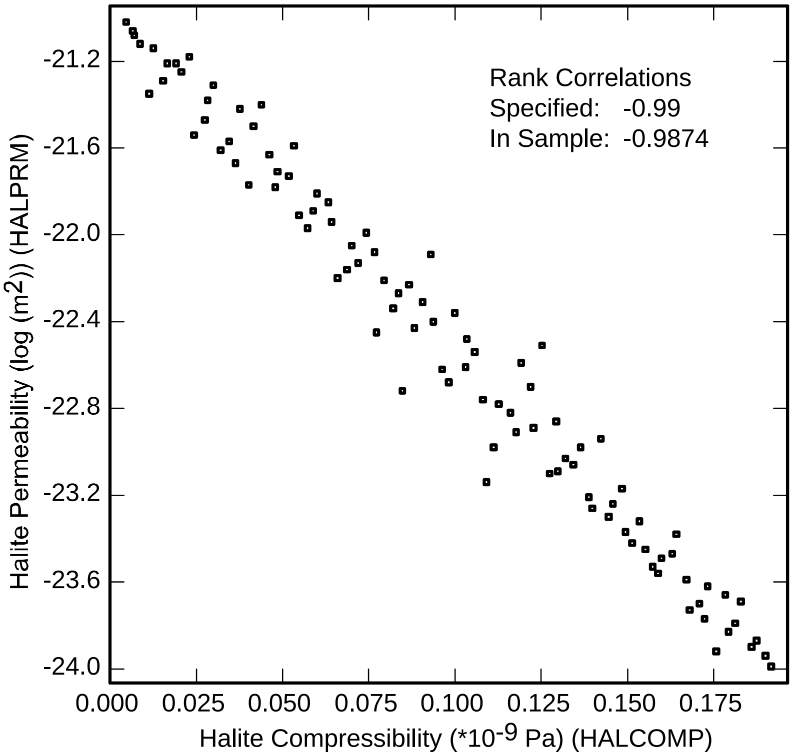

Figure PA-31. Correlation Between HALCOMP and HALPRM.

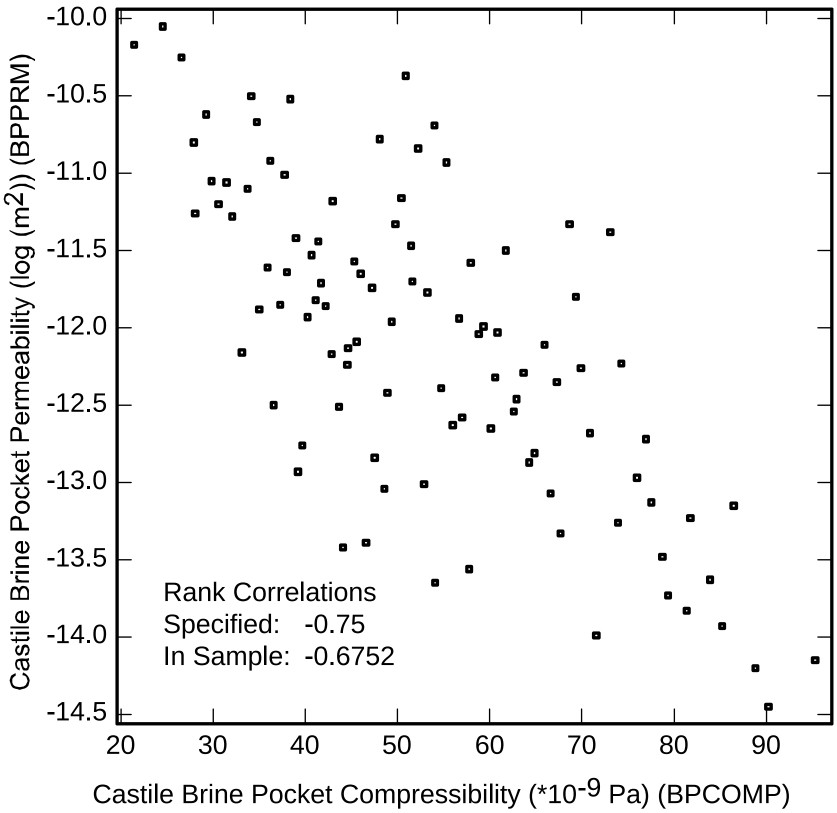

1

2 **Figure PA-32. Correlation between BPCOMP and BPPRM.**

PA-6.0 COMPUTATIONAL PROCEDURES

This section outlines the computational procedures used to execute the CRA-2004 PA. First, this section outlines the sampling procedures applied to evaluate performance accounting for subjective and stochastic uncertainty. The mechanistic calculations used to evaluate the function f in Equation (24) are tabulated, followed by a description of the algorithms used to compute releases. This section concludes with a discussion of sensitivity analysis techniques used to identify which uncertain parameters are primary contributors to the uncertainty in the PA results.

PA-6.1 Sampling Procedures

Extensive use is made of sampling procedures in the CRA-2004 PA. In particular, random sampling is used in the generation of individual CCDFs (i.e., for integration over the probability space $(\mathcal{X}_{st}, \mathcal{S}_{st}, p_{st})$ for stochastic uncertainty; see Section PA-2.3) and Latin hypercube sampling is used for the assessment of the effects of imprecisely known analysis inputs (i.e., for integration over the probability space $(\mathcal{X}_{su}, \mathcal{S}_{su}, p_{su})$ for subjective uncertainty; see Section PA-2.4).

In random sampling, sometimes also called simple random sampling, the observations

$$\mathbf{x}_k = \left[x_{k1}, x_{k2}, \ldots, x_{knV}\right], \text{ k = 1, 2, ..., nR,} \tag{255}$$

where nR is the sample size, are selected according to the joint probability distribution for the elements of x as defined by $(\mathcal{X}_{st}, \mathcal{S}_{st}, p_{st})$. In practice, $(\mathcal{X}_{st}, \mathcal{S}_{st}, p_{st})$ is defined by specifying a distribution D_j for each element x_j of $\mathbf{x}$. Points from different regions of the sample space S_{st}, occur in direct relationship to the probability of occurrence of these regions. Furthermore, each sample element is selected independently of all other sample elements. The random sampling provides unbiased estimates for means, variances, and distributions of the elements x that comprise $(\mathcal{X}_{st}, \mathcal{S}_{st}, p_{st})$.

The random sampling to integrate over the probability space for $(\mathcal{X}_{st}, \mathcal{S}_{st}, p_{st})$ for stochastic uncertainty is implemented in the WIPP PA code CCDFGF. The code CCDFGF is capable of generating and evaluating thousands of possible futures; the CRA-2004 PA uses a sample size nS = 10,000 from the space $(\mathcal{X}_{st}, \mathcal{S}_{st}, p_{st})$ to estimate repository releases. This sample size is sufficient to estimate the 0.999 quantile of the distribution of releases to the accessible environment.

Latin hypercube sampling is used to integrate over the space for subjective uncertainty $(\mathcal{X}_{su}, \mathcal{S}_{su}, p_{su})$. This technique was first introduced by McKay et al (1979). In Latin hypercube sampling, the range of each variable (i.e., the x_j) is divided into nLHS intervals of equal probability and one value is selected at random from each interval. The nLHS values thus obtained for x_1 are paired at random without replacement with the nLHS values obtained for x_2. These nLHS pairs are combined in a random manner without replacement with the nLHS values of x_3 to form nLHS triples. This process is continued until a set of nLHS nV-tuples is formed. These nV-tuples are of the form

$$\mathbf{x}_k = \left[x_{k1}, x_{k2}, \ldots, x_{knV} \right], \text{ k = 1, ..., nLHS,} \tag{256}$$

and constitute the Latin hypercube sample. The individual x_j must be independent for the preceding construction procedure to work; a method for generating Latin hypercube and random samples from correlated variables was developed by Iman and Conover (1982) and is used in WIPP PA. For more information about Latin hypercube sampling and a comparison with other sampling techniques, see Helton and Davis (2003).

Latin hypercube sampling provides unbiased estimates for means and distribution functions and dense stratification across the range of each sampled variable (McKay et al. 1979), ensuring that the sampled values cover the full range of each uncertain element x_j of $\mathbf{x}$. In particular, uncertainty and sensitivity analysis results obtained with Latin hypercube sampling are robust even when relatively small samples (i.e., nLHS = 50 to 200) are used (Iman and Helton 1988, 1991; Helton et al. 1995).

PA-6.2 Sample Size for Incorporation of Subjective Uncertainty

Section 194.34(d) states that "The number of CCDFs generated shall be large enough such that, at cumulative releases of 1 and 10, the maximum CCDF generated exceeds the 99th percentile of the population of CCDFs with at least a 0.95 probability." For an LHS of size nLHS, the preceding guidance is equivalent to the inequality

$$1 - 0.99^{nLHS} > 0.95, \tag{257}$$

which results in a minimum value of 298 for nLHS. The CRA-2004 PA uses a total sample size of 300 to integrate over the probability space $\left(X_{su}, S_{su}, p_{su} \right)$ for subjective uncertainty. As discussed in the next section, however, in order to demonstrate convergence of the mean for the population of CCDFs, the total sample of 300 is created by means of three replicated samples of size 100 each.

PA-6.3 Statistical Confidence on Mean CCDF

Section 194.34(f) states that "Any compliance assessment shall provide information which demonstrates that there is at least a 95 percent level of statistical confidence that the mean of the population of CCDFs meets the containment requirements of § 191.13 of this chapter." Given that Latin hypercube sampling is used, the confidence intervals required by Section 194.34(f) are obtained with a replicated sampling technique proposed by Iman (1982). In this technique, the sampling in Equation (256) is repeated nR times with different random seeds. These samples lead to a sequence $\bar{P}_r(R),\ r = 1, 2, \ldots, nR,$ of estimated mean exceedance probabilities, where $\bar{P}_r(R)$ defines the mean CCDF obtained for sample r (i.e., $\bar{P}_r(R)$ is the mean probability that a normalized release of size R will be exceeded; see Section PA-2.4) and nR is the number of independent samples generated with different random seeds. Then,

$$\bar{P}(R) = \sum_{r=1}^{nR} \bar{P}_r(R) / nR \tag{258}$$

and

$$SE(R) = \left\{ \sum_{r=1}^{nR} \left[\bar{P}_r(R) - \bar{P}(R) \right]^2 / nR(nR-1) \right\}^{1/2} \tag{259}$$

provide an additional estimate of the mean CCDF and an estimate of the standard error associated with the mean exceedance probabilities. The t-distribution with nR−1 degrees of freedom can be used to place confidence intervals around the mean exceedance probabilities for individual R values (i.e., around $\bar{P}(R)$). Specifically, the 1−α confidence interval is given by $\bar{P}_r(R) \pm t_{1-\alpha/2} SE(R)$, where $t_{1-\alpha/2}$ is the $1-\alpha/2$ quantile of the t-distribution with nR−1 degrees of freedom (e.g., $t_1 - \alpha/2 = 4.303$ for $\alpha = 0.05$ and nR = 3). The same procedure can also be used to place pointwise confidence intervals around percentile curves.

PA-6.4 Generation of LHSs

The LHS program (WIPP PA 1996) is used to produce three independently generated LHSs of size nLHS = 100 each, for a total of 300 sample elements. Each individual replicate is an LHS of the form

$$\mathbf{x}_{su,k} = \left[x_{k1}, x_{k2}, \ldots, x_{knV} \right],\ \text{k} = 1, 2, \ldots, \text{nLHS} = 100. \tag{260}$$

In the context of the replicated sampling procedure described in Section PA-6.2, nR = 3 replicates of 100 are used. For notational convenience, the replicates are designated by R1, R2, and R3.

The restricted pairing technique described in Section PA-6.2 is used to induce requested correlations and also to assure that uncorrelated variables have correlations close to zero. The variable pairs (ANHCOMP, ANHPRM), (HALCOMP, HALPRM), and (BPCOMP, BPPRM) are assigned rank correlations of −0.99, −0.99, and −0.75, respectively (Section PA-5.4). All other variable pairs are assigned rank correlations of zero. The restricted pairing technique is very successful in producing these correlations (Table PA-19). Specifically, the correlated variables have correlations that are close to their specified values and uncorrelated variables have correlations that are close to zero.

Table PA-19. Example Correlations in Replicate R1

WGRCOR	1.0000							
WMICDFLG	-0.0993	1.0000						
WGRMICI	0.0152	0.0495	1.0000					
WGRMICH	0.0191	-0.0098	0.0150	1.0000				
WFBETCEL	0.0113	-0.0139	-0.0273	0.0033	1.0000			
WRGSSAT	0.0004	0.0712	-0.0451	-0.0058	-0.0517	1.0000		
WRBRNSAT	0.0192	0.0244	-0.0558	0.0321	-0.0128	-0.0260	1.0000	
WASTWICK	-0.0096	0.0955	-0.0099	0.0043	0.0057	-0.0147	0.0076	1.0000
	WGRCOR	**WMICDFLG**	**WGRMICI**	**WGRMICH**	**WFBETCEL**	**WRGSSAT**	**WRBRNSAT**	**WASTWICK**

PA-6.5 Generation of Individual Futures

Random sampling (Section PA-6.1) is used to generate elements $\mathbf{x}_{st}$ of S_{st} for CCDF construction. Table PA-20 outlines the algorithm used to generate a single future $\mathbf{x}_{st}$ in the CRA-2004 PA. For each LHS element $\mathbf{x}_{su,k}$, k = 1, 2, …, 300, a total of nS = 10,000 individual futures of the form

$$\mathbf{x}_{st,i} = \left[t_{i1}, e_{i1}, l_{i1}, b_{i1}, p_{i1}, \mathbf{a}_{i1}, t_{i2}, e_{i2}, l_{i2}, b_{i2}, p_{i2}, \mathbf{a}_{i2}, \ldots, t_{in}, e_{in}, l_{in}, b_{in}, p_{in}, \mathbf{a}_{in}, t_{i,min} \right], \quad i = 1, 2, \ldots, nS = 10{,}000 \tag{261}$$

are generated in the construction of all CCDFs for that LHS element. A different random seed is used to initiate the sampling of $\mathbf{x}_{st}$ for each LHS element, with the result that each LHS element uses different values for $\mathbf{x}_{st}$ in CCDF construction. As 300 LHS elements are used in the analysis and 10,000 futures are sampled for each LHS element, the total number of futures $\mathbf{x}_{st}$ used in the analysis in CCDF construction is 3×10^6.

The drilling rate λ_d is used to generate the times at which drilling intrusions occur. For a Poisson process with a constant λ_d (i.e., a stationary process), the CDF for the time Δt between the successive events is given by (Ross 1987, p. 113)

$$prob(t \le \Delta t) = 1 - \exp(-\lambda_d \Delta t). \tag{262}$$

A uniformly distributed random number is selected from [0, 1]. Then, solution of

$$r_1 = 1 - \exp(-\lambda_d t_1) \tag{263}$$

Table PA-20. Algorithm to Generate a Single Future $\mathbf{x}_{st}$ from S_{st}

1. Sample t_1 with a time dependent λ_d given by

$$\lambda_d(t) = \begin{cases} 0 & \text{if } 0 \le t \le tA \\ \lambda_d & \text{if } t > tA \end{cases},$$

where tA = 100 yr (i.e., time at which administrative control ends) and $\lambda_d = 3.30 \times 10^{-3}\ \text{yr}^{-1}$ (see Section PA-3.2).

2. Sample e_1 with a probability of $pE_0 = 0.797$ that the intrusion will be in an unexcavated area and a probability of $pE_1 = 0.203$ that the intrusion will be in an excavated area (see Section PA-3.3).

3. Sample l_1 with a probability of $pL_j = 6.74 \times 10^{-3}$ for each of the j = 1, 2, …, 144 nodes in Figure PA-6 (see Section PA-3.4).

4. Sample b_1 with a probability of $pB_1 = p(\mathbf{x}_{su})$ that the intrusion will penetrate pressurized brine (see Section PA-3.5).

5. Sample p_1 with probabilities of $pPL_1 = 0.015$, $pPL_2 = 0.696$, and $pPL_3 = 0.289$ that plugging pattern 1, 2, or 3, respectively, will be used (see Section PA-3.6).

6. Sample a_1 (see Section PA-3.7).

6.1 Penetration of nonexcavated area (i.e., $e_1 = 0$): $\mathbf{a}_i = a_1 = 0$.

6.2 Penetration of excavated area (i.e., $e_1 = 1$): Sample to determine if intrusion penetrates RH-TRU or CH-TRU waste with probabilities of pRH = 0.124 and pCH = 0.876 of penetrating RH-TRU and CH-TRU waste, respectively.

6.3 Penetration of RH-TRU waste: $\mathbf{a}_i = a_1 = 1$.

6.4 Penetration of CH-TRU waste: Use probabilities pCH_j of intersecting waste stream j, j = 1, 2, …, 693, (see Attachment PAR, Table PAR-50) to independently sample three intersected waste streams iCH_{11}, iCH_{12}, iCH_{13} (i.e., each of iCH_{11}, iCH_{12}, iCH_{13} is an integer between 1 and 693). Then, $\mathsf{a}_1 = [2, iCH_{11}, iCH_{12}, iCH_{13}]$.

7. Repeat steps 1 - 6 to determine properties (i.e., t_i, e_i, l_i, b_i, p_i, a_i) of the i^{th} drilling intrusion.

8. Continue until $t_{n+1} > 10{,}000$ yr; the n intrusions thusly generated define the drilling intrusions associated with $\mathbf{x}_{st}$.

9. Sample t_{min} with a time dependent λ_m given by

$$\lambda_m(t) = \begin{cases} 0 & \text{if } 0 \le t \le tA \\ \lambda_m & \text{if } t > tA \end{cases}$$

where tA = 100 yr and $\lambda_m = 1 \times 10^{-4}\ \text{yr}^{-1}$ (see Section PA-3.8).

for t_1 gives the time of the first drilling intrusion. An initial period of 100 years of administrative control is assumed, thus 100 years is added to the t_1 obtained in Equation (263) to obtain the time of the first drilling intrusion. Selection of a second random number r_2 and solution of

$$r_2 = 1 - \exp(-\lambda_d \, \Delta t_1) \tag{264}$$

for Δt_1 gives the time interval between the first and second drilling intrusions, with the outcome that $t_2 = t_1 + \Delta t_1$. This process is continued until t_{n+1} exceeds 10,000 yr. The times t_1, t_2, …, t_n then constitute the drilling times in $\mathbf{x}_{st}$ in Equation (261).

The mining time t_{min} is sampled in a manner similar to sampling the drilling times. Additional uniformly distributed random numbers from $[0,1]$ are used to generate the elements e_i , l_i , b_i , p_i , $\mathbf{a}_i$ of $\mathbf{x}_{st}$ from their assigned distributions (see Section PA-3.0).

PA-6.6 Construction of CCDFs

In the CRA-2004 PA, the sampling of individual futures (Section PA-6.5) and associated CCDF construction is carried out by the CCDFGF program (WIPP PA 2003d). The sampled futures $\mathbf{x}_{st,i}$ in Equation (261) are used to construct CCDFs for many different quantities (e.g., cuttings and cavings releases, spallings releases, direct brine releases, etc.). The construction process is the same for each quantity. For notational convenience, assume that the particular quantity under consideration can be represented by a function $f\left(\mathbf{x}_{st,i}\right)$, with the result that 10,000 values

$$f\left(\mathbf{x}_{st,i}\right), \mathrm{i} = 1, 2, \ldots, 10{,}000 \tag{265}$$

are available for use in CCDF construction. Formally, the resultant CCDF is defined by the expression in Equation (4). In practice, the indicator function δ_R is not directly used and the desired CCDF is obtained after an appropriate ordering of the $f\left(\mathbf{x}_{st,i}\right)$ (i.e., from smallest to largest or largest to smallest) as described below.

The CRA-2004 PA uses a binning procedure in CCDF construction to simplify sorting the individual $f\left(\mathbf{x}_{st,i}\right)$ and to reduce the number of plot points. Specifically, the range of f is divided into intervals (i.e., bins) by the specified points

$$f_{min} = b_0 < b_1 < b_2 < \ldots < b_n = f_{max}, \tag{266}$$

where f_{min} is the minimum value of f to be plotted (typically 10^{-6} or 10^{-5} when an EPA normalized release is under consideration), f_{max} is the maximum value of f to be plotted (typically 100 when an EPA normalized release is under consideration), n is the number of bins in use, and the b_i are typically loguniformly placed with 20 values per order of magnitude. A counter nB_j is used for each interval $\left[b_{j-1}, b_j\right]$. All counters are initially set to zero. Then, as individual values $f\left(\mathbf{x}_{st,i}\right)$ are generated, the counter nB_j is incremented by 1 when the inequality

$$b_{j-1} < f\left(\mathbf{x}_{st,i}\right) \le b_j \tag{267}$$

is satisfied. When necessary, f_{max} is increased in value so that the inequality $\boldsymbol{f}\left(\boldsymbol{x}_{st,i}\right) < \boldsymbol{f_{max}}$ will always be satisfied. Once the 10,000 values for $\boldsymbol{f}\left(\boldsymbol{x}_{st,i}\right)$ have been generated, a value of nB_j exists for each interval $\left[\boldsymbol{b}_{j-1}, \boldsymbol{b}_j\right]$. The quotient

$$pB_j = nB_j / 10{,}000 \tag{268}$$

provides an approximation to the probability that $\boldsymbol{f}\left(\boldsymbol{x}_{st}\right)$ will have a value that falls in the interval $\left[\boldsymbol{b}_{j-1}, \boldsymbol{b}_j\right]$. The resultant CCDF is then defined by the points

$$\left(b_j, prob\left(value > b_j\right)\right) = \left(b_j, \sum_{k=j+1}^{n} pB_k\right) \tag{269}$$

for j = 0, 1, 2, …, n−1, where $prob\left(value > b_j\right)$ is the probability that a value greater than b_j will occur.

The binning technique produces histograms that are difficult to read when multiple CCDFs appear in a single plot. As the number of futures is increased and the bins are refined, the histogram CCDF should converge to a continuous CCDF as additional points (i.e., elements $\boldsymbol{x}_{st}$ of S_{st}) are used in its construction. The continuous CCDF is approximated by drawing diagonal lines from the left end of one bin to the left end of the next bin.

When multiple CCDFs appear in a single plot, the bottom of the plot becomes very congested as the individual CCDFs drop to zero on the abscissa. For this reason, each CCDF stops at the largest observed consequence value among the 10,000 values calculated for that CCDF. Stopping at the largest consequence value rather than the left bin boundary of the bin that contains this value permits the CCDF to explicitly show the largest observed consequence. Due to the use of a sample size of 10,000 in the generation of CCDFs for comparison with the EPA release limits, the last nonzero exceedance probability in the resultant CCDFs is typically 10^{-4}; Figure PA-5 shows an example of CCDFs from the 2004 PA.

PA-6.7 Mechanistic Calculations

For the CRA-2004 PA, calculations were performed with the models described in Chapter PA-4.0 for selected elements of S_{st} (see Section PA-3.9) and the results were used to determine the releases to the accessible environment for the large number (i.e., 10,000) of randomly sampled futures used in the estimation of individual CCDFs. The same set of mechanistic calculations was performed for each LHS element. This section summarizes the calculations performed with each of the models described in Chapter PA-4.0; Section PA-6.8 outlines the algorithms used to construct releases for the randomly sampled elements $\boldsymbol{x}_{st,i}$ of S_{st} from the results of the mechanistic calculations. Long (2003) documents execution of the calculations and archiving of calculation results.

PA-6.7.1 BRAGFLO Calculations

The BRAGFLO code (Section PA-4.2) computes two-phase (brine and gas) flow in and around the repository. BRAGFLO results are used as initial conditions in the models for Salado Transport (implemented in NUTS and PANEL), spallings (implemented in CUTTINGS_S) and DBR (also calculated by BRAGFLO). Thus, the BRAGFLO scenarios are used to define scenarios for other codes.

The four fundamental scenarios for the CRA-2004 PA (Section PA-3.9) define four categories of calculations to be performed with BRAGFLO (i.e., E0, E1, E2, and E1E2). These four fundamental scenarios were expanded into six general scenarios by specifying the time of drilling intrusions. Table PA-21 summarizes the specific scenarios used in the CRA-2004 PA. A total of 6 scenarios × nR × nLHS = 6 × 3 × 100 = 1800 BRAGFLO calculations were conducted for the CRA-2004 PA.

Table PA-21. BRAGFLO Scenarios in the CRA-2004 PA

Fundamental Scenario (Section PA-3.9)	***Specific Scenario***	***Time of drilling intrusion(s)***
E0: no drilling intrusions	S1	N/A
E1: single intrusion into excavated area ($e_1 = 1$), pressurized brine is penetrated ($b_1 = 1$), and plugging pattern 2 is used ($p_1 = 2$).	S2	350 years
	S3	1,000 years
E2: single intrusion into excavated area ($e_1 = 1$), pressurized brine is penetrated ($b_1 = 1$) and plugging pattern 3 is used ($p_1 = 3$), or pressurized brine is not penetrated ($b_1 = 0$).	S4	350 years
	S5	1,000 years
E1E2: two intrusions into the same waste panel ($e_1 = e_2 = 1$), the first being an E2 intrusion and the second being an E1 intrusion.	S6	800 years for E2 intrusion 2,000 years for E1 intrusion

Values for the activity level $\boldsymbol{a_1}$ and for mining time t_{min} are not needed for the mechanistic calculations; these values are used in the construction of the releases from the results of the mechanistic calculations (Section PA-6.8). Although a value for drilling location l_1 is not specified, a drilling location is required for the BRAGFLO calculations. If equivalent grids were used in the definition of $\boldsymbol{x_{st}}$ (Figure PA-6) and in the numerical solution of the partial differential equations on which BRAGFLO is based (Figure PA-8), the location of the drilling intrusion used in the BRAGFLO calculations could be specified as a specific value for l_1, which in turn would correspond to one of the 144 locations in Figure PA-6 that are designated by l in the definition of $\boldsymbol{x_{st}}$. However, as these grids are not the same, a unique pairing between a value for l_1 and the location of the drilling intrusion used in the computational grid employed with BRAGFLO is not possible. The BRAGFLO computational grid divides the repository into a lower waste panel (area Waste Panel), a middle group of four waste panels (area South RoR), and an upper group of five waste panels (area North RoR), with the drilling intrusion taking place through the center of the lower panel (Figure PA-8). Thus, in the context of the locations in Figure PA-6 potentially indexed by l_1, the drilling intrusions in Scenario S2, Scenario S3, Scenario S4 and Scenario S5 occur at a location in Panel 5. In Scenario S6, both intrusions occur at a location in Panel 5, with the effects of flow between the two boreholes implemented through assumptions involving the time-dependent behavior of borehole permeability (Table PA-5).

PA-6.7.2 NUTS Calculations

Transport through the Salado is computed by the code NUTS (Section PA-4.3) using the flow fields computed by BRAGFLO. Two types of calculations are performed with NUTS. First, a set of screening calculations identifies elements of the sample from S_{su} for which radionuclide transport is possible through the Salado to the LWB or to the Culebra. The screening calculations identify a subset of the sample from S_{st} for which transport is possible and for which releases calculations are performed. Screening calculations are performed for all BRAGFLO cases, for a total of 1500 screening calculations with NUTS (Table PA-21). Table PA-22 summarizes the NUTS release calculations for the CRA-2004 PA. Based on the screening calculations, a total of 1402 release calculations are performed for the CRA-2004 PA. For each vector that is retained (based on the screening calculations), release calculations are performed for a set of intrusion times.

Table PA-22. NUTS Release Calculations in the CRA-2004 PA

NUTS Scenario	Number of vectors (all replicates)	Flow field	Intrusion time (t_1)
S1	1 + 0 + 0 = 1	BRAGFLO S1 scenario	N/A
S2	60 + 64 + 61 = 185	BRAGFLO S2 scenario	E1 intrusion at 100 and 350 years
S3	49 + 55 + 51 = 155	BRAGFLO S3 scenario	E1 intrusion at 1,000, 3,000, 5,000, 7,000 and 9,000 years
S4	13 + 14 + 11 = 38	BRAGFLO S4 scenario	E2 intrusion at 100, 350 years
S5	12 + 13 + 11 = 36	BRAGFLO S5 scenario	E2 intrusion at 1,000, 3,000, 5,000, 7,000 and 9,000 years

Table PA-22 lists five scenarios for release calculations corresponding to the five BRAGFLO scenarios. Each NUTS scenario uses the flow field computed for the corresponding BRAGFLO scenario. The intrusion times for the NUTS scenarios are accommodated by shifting the BRAGFLO flow fields in time so that the NUTS and BRAGFLO intrusions coincide. For example, the NUTS S3 scenario with an intrusion at 3,000 years requires a flow field for the time interval between (3,000 yr, 10,000 yr); this scenario uses the BRAGFLO S3 flow field for the time interval between (1,000 yr, 8,000 yr).

Values for the variables indicating intrusion into excavated area (e_1), penetration of pressurized brine (b_1), plugging pattern (p_1) and drilling location (l_1) are the same as in the corresponding

BRAGFLO scenario. Values for the activity level $\boldsymbol{a}_i$ and for mining time t_{min} are not specified for the NUTS scenarios.

PA-6.7.3 PANEL Calculations

As outlined in Section PA-4.4, the code PANEL is used to estimate releases to the Culebra associated with E1E2 scenarios and to estimate radionuclide concentrations in brine for use in the estimation of direct brine releases. An E1E2 scenario assumes two drilling intrusions into the same waste panel: the first intrusion being an E2 intrusion (Table PA-22) occurring at time t1 and the second intrusion being an E1 intrusion (Table PA-22) occurring at time t_2. PANEL calculations are performed for t_2 = 100, 350, 1,000, 2,000, 4,000, 6,000 and 9,000 years using the flow field produced by the single BRAGFLO calculation for Scenario S6, for a total of 7 × nR × nLHS = 7 × 3 × 100 = 2100 PANEL calculations. The BRAGFLO flow field is shifted forward or backward in time as appropriate so that the time of the second intrusion (t_2) coincides. The shifting of the BRAGFLO flow field results in values for the time (t_1) of the first intrusion (E2) for the PANEL calculations given by

$$t_1 = \max\left\{100\,yr,\ t_2 - 1200\,yr\right\}, \tag{270}$$

where the restriction that t_1 cannot be less than 100 years results from the definition of $\boldsymbol{x}_{st}$, which does not allow negative intrusion times, and from the assumption of 100 years of administrative control during which there is no drilling (i.e., $\lambda_d(t) = 0\ \text{yr}^{-1}$ for $0 \le t \le 100$ yr; see Equation (7)). Under this convention, what is specified in concept by the definition of Scenario S6 for the BRAGFLO calculations differs from what is actually done computationally because t_1 does not always precede t_2 by 1200 yr in the PANEL calculation. Values for the other variables defining the element $\boldsymbol{x}_{st}$ of S_{st} for the PANEL E1E2 scenarios are the same as in the BRAGFLO S6 scenario.

Calculation of radionuclide concentration are not specific to any BRAGFLO scenario. The concentration calculations compute the mobilized activity in two different brines (Castile and Salado) and are performed at 100, 125, 175, 350, 1,000, 3,000, 5,000, 7,500 and 10,000 years for a total of 2 × 9 × nR = 54 calculations.

PA-6.7.4 CUTTINGS_S Calculations

The code CUTTINGS_S computes the volumes of solids removed from the repository by cuttings and cavings (see Section PA-4.5) and spallings (see Section PA-4.6). Table PA-23 lists the CUTTINGS_S calculations performed for the CRA-2004 PA, totaling 78 × nR × nLHS = 78 × 3 × 100 = 23,400 CUTTINGS_S calculations.

Table PA-23. CUTTINGS_S Scenarios in the CRA-2004 PA

Scenario	Description
S1	Intrusion into lower, middle, and upper waste panel in undisturbed (i.e., E0 conditions) repository at 100, 350, 1,000, 3,000, 5,000, and 10,000 years = 18 combinations.
S2	Initial E1 intrusion at 350 years followed by a second intrusion into the same, adjacent, and nonadjacent waste panel at 550, 750, 2,000, 4,000 or 10,000 years = 15 combinations.
S3	Initial E1 intrusion at 1000 years followed by a second intrusion into the same, adjacent, and nonadjacent waste panel at 1200, 1,400, 3,000, 5,000 or 10,000 years = 15 combinations.
S4	Initial E2 intrusion at 350 years followed by a second intrusion into the same, adjacent, and nonadjacent waste panel at 550, 750, 2,000, 4,000 or 10,000 years = 15 combinations.
S5	Initial E2 intrusion at 1000 years followed by a second intrusion into the same, adjacent, and nonadjacent waste panel at 1,200, 1,400, 3,000, 5,000 or 10,000 years = 15 combinations.

The CUTTINGS_S S1 scenario computes volumes of solid material released from the initial intrusion in the repository. Initial conditions for the CUTTINGS_S S1 scenario are taken from the results of the BRAGFLO S1 scenario at the time of the intrusion for areas Waste Panel, South RoR, and North RoR in Figure PA-8, corresponding to the lower, middle, and upper waste panels. In this scenario, the excavated area is penetrated ($e_1 = 1$) and the drilling location (l_1) is defined as one of the nodes (Figure PA-6) in the appropriate panel of Figure PA-20. The actual locations at which the intrusions are assumed to occur correspond to the points in Figure PA-20 designated "Down-dip well," "Middle well," and "Up-Dip Well" for the lower, middle, and upper waste panel, respectively. Values for the variables indicating penetration of pressurized brine (b_1), plugging pattern (p_1), activity level ($\mathbf{a}_1$), and for mining time (t_{min}) are not specified for the CUTTINGS_S S1 scenario.

The other CUTTINGS_S scenarios (Scenario S2, Scenario S3, Scenario S4, and Scenario S5) compute volumes of solids released by a second or subsequent intrusion. Initial conditions are taken from the results of the corresponding BRAGFLO scenario at the time of the second intrusion. As in the BRAGFLO scenarios, the first intrusion occurs in the lower waste panel (area Waste Panel in Figure PA-8) so the drilling location (l_1) is defined as one of the nodes in Panel 5 (Figure PA-6). The second intrusion occurs in the same waste panel as the first intrusion (area Waste Panel in Figure PA-8), an adjacent waste panel (area South RoR in Figure PA-8), or a nonadjacent waste panel (area North RoR in Figure PA-8). Hence the drilling location (l_2) is defined as one of the nodes (Figure PA-6) in the appropriate panel of Figure PA-20.

The activity level for the first intrusion $\mathbf{a}_1$ takes a value that indicates penetration of CH-TRU waste (i.e., $\mathbf{a}_1 = [2, CH_{11}, CH_{12}, CH_{13}]$) but the specific waste streams penetrated (i.e. CH_{11}, CH_{12}, CH_{13}) are not specified. For the second intrusion, the excavated area is penetrated

($e_2 = 1$) and the drilling location (l_2) is defined as one of the nodes (Figure PA-6) in the appropriate panel, as described above. The actual locations at which the intrusions are assumed to occur correspond to the point in Figure PA-20 designated "Down-dip well" for the first intrusion for Category (1) intrusions and "Up-dip well, first or second intrusion" for Category (2) intrusions. As for the first intrusion, the activity level $\boldsymbol{a}_2$ only indicates penetration of CH-TRU waste. Values for the other variables defining the first intrusion (e_1, b_1, and p_1) are the same as in the corresponding BRAGFLO scenario. Values for the other variables defining the second intrusion (b_2 and p_2) and the mining time t_{min} are not specified for the CUTTINGS_S scenarios.

PA-6.7.5 BRAGFLO Calculations for Direct Brine Release Volumes

Volumes of brine released to the surface at the time of an intrusion are calculated using BRAGFLO as described in Section PA-4.7. Calculations of DBR volumes were conducted for the same scenarios as for CUTTINGS_S (Table PA-23). Thus, the elements of S_{st} described in Section PA-6.7.4 also characterize the elements of S_{st} for which DBR volumes are computed; a total of 23,400 BRAGFLO calculations were performed.

PA-6.7.6 MODFLOW Calculations

As described in Section PA-4.8, the MODFLOW calculations produce flow fields in the Culebra for two categories of conditions: partially-mined conditions in the vicinity of the repository and fully-mined conditions in the vicinity of the repository (Figure PA-23). As specified in 40 CFR § 194.32(b), partially-mined conditions are assumed to exist by the end of the period of administrative control (i.e., at 100 years after closure). After the time that mining occurs within the LWB (t_{min}; see Section PA-3.8), fully-mined conditions are assumed for the remainder of the 10,000 regulatory period. The flow fields for partially-mined conditions are calculated by MODFLOW using the t-fields for partially-mined conditions (see Section PA-4.8.2). Additional MODFLOW calculations determine the flow fields for fully-mined conditions and are performed using the t-fields for fully-mined conditions. Thus a total of $2 \times nR \times nLHS = 2 \times 3 \times 100 = 600$ MODFLOW calculations were performed. The element CTRAN of $\boldsymbol{x}_{su}$ (see Table PA-17) specifies the association between the uncertain transmissivity fields and the calculation of flow fields by MODFLOW.

Table PA-24. MODFLOW Scenarios in the CRA-2004 PA

MODFLOW: 600 Flow-Field Calculations
PM: Partially mined conditions in vicinity of repository
FM: Fully mined conditions in vicinity of repository
Total calculations = 2 nR nLHS = 2 × 3 × 100 = 600
Note: Only 100 unique transmissivity fields were constructed with MODFLOW for use in the analysis. The transmissivity fields are an input to the calculation of flow-fields. In each replicate, the transmissivity field used for a particular flow field was assigned using an index value (CTRAN, see Table PA-17) included in the LHS.

PA-6.7.7 SECOTP2D Calculations

The SECOTP2D calculations are performed for the same elements $\mathbf{x}_{st,0}$ and $\mathbf{x}_{st,m}$ of S_{st} defined in Section PA-6.7.6 for the MODFLOW calculations for a total of $2 \times nR \times nLHS = 2 \times 3 \times 100 = 600$ SECOTP2D calculations.

Table PA-25. SECOTP2D Scenarios in the CRA-2004 PA

SECOTP2D: 600 Calculations
PM: Partially mined conditions in vicinity of repository
FM: Fully mined conditions in vicinity of repository
Total calculations = 2 nR nLHS = 2 × 3 × 100 = 600
Note: Each calculation includes a unit release of each of four radionuclides: ^{241}Am, ^{239}Pu, ^{230}Th, ^{234}U.

PA-6.8 Computation of Releases

The mechanistic computations outlined in Section PA-6.7 are used to compute releases for each sampled element $\mathbf{x}_{st}$ of S_{st}. Releases from the repository can be partitioned into three categories: undisturbed releases, which may occur in futures without drilling intrusions; direct releases, which occur at the time of a drilling event; and long-term releases, which occur as a consequence of a history of drilling intrusions. For a given future ($\mathbf{x}_{st}$ of S_{st} in Equation (261)) other than undisturbed conditions ($\mathbf{x}_{st,0}$) the direct and long-term releases are computed by the code CCDFGF (WIPP PA 2003a) from the results of the mechanistic calculations summarized in Section PA-6.7, performed with the models presented in Chapter PA-4.0. Releases from an undisturbed repository are computed from the results of the NUTS S1 scenario (Section PA-6.7.2).

PA-6.8.1 Undisturbed Releases

Releases from the repository for the futures ($\mathbf{x}_{st,0}$) in which no drilling intrusions occur are computed by the NUTS release calculations for E0 conditions (Table PA-22). The NUTS model computes the activity of each radionuclide that reaches the accessible environment during the regulatory period via transport through the MBs and through the Dewey Lake Red Beds. These releases are represented as $f_{MB}\left[\mathbf{x}_{st,0}, f_B\left(\mathbf{x}_{st,0}\right)\right]$ and $f_{DL}\left[\mathbf{x}_{st,0}, f_B\left(\mathbf{x}_{st,0}\right)\right]$ in Equation (24).

PA-6.8.2 Direct Releases

Direct releases include cuttings, cavings, spallings, and DBRs. The model for each component of direct releases computes a volume (solids or liquid) released to directly to the surface for each drilling intrusion. These volumes are combined with an appropriate concentration of activity in the released waste.

PA-6.8.3 Construction of Cuttings and Cavings Releases

Each drilling intrusion encountering waste is assumed to release a volume of solid material as cuttings as described in Section PA-4.5.2. The uncompacted volume of waste removed by cuttings (V_{cut}) is computed by Equation (104). In addition, drilling intrusions that encounter CH-TRU waste may release additional solid material as cavings, as described in Section PA-4.5.2. The uncompacted volume of material removed by cuttings and cavings combined ($\boldsymbol{V = V_{cut} + V_{cav}}$) is computed by Equation (105). For a drilling intrusion that encounter RH-TRU waste, the final eroded diameter D_f in Equation (105) is equal to the bit diameter in Equation (104). In the CRA-2004 PA, all drilling intrusions assume a drill bit diameter of 12.25 in (Attachment PAR, Table PAR-13).

The uncompacted volume of material removed is not composed entirely of waste material; rather, the uncompacted volume includes MgO and any void space initially present around the waste containers. The volume of waste removed (V_w) is determined by multiplying the uncompacted volume by the fraction of excavated volume (FVW) of the repository that is occupied by waste. In the CRA-2004 PA, FVW = 0.386 for CH-TRU waste and FVW = 1.0 for RH-TRU waste (Attachment PAR, Table PAR-45), thus

$$\boldsymbol{V_w = V \times FVW} \ . \tag{271}$$

The activity in the material released by cuttings and cavings is determined by stochastically selecting a subset of the set of all waste streams. The vector ($\boldsymbol{a_i}$) described in Section PA-3.7 determines which type of waste (CH-TRU or RH-TRU) and which waste streams are selected. The activity per m^3 of waste stream volume is computed for each waste stream at a discrete set of times by the code EPAUNI (Fox 2003), the results of the EPAUNI calculations are presented in Attachment PAR, Tables PAR-50 through PAR-61. Activities at other times are determined by linear interpolation. The cuttings and cavings release $\boldsymbol{f_C\left(x_{st}\right)}$ is the product of the average activity per m^3 (C_r, computed as the average activity over the waste streams comprising the selected subset with the assumption that each waste stream contributes an equal volume to the release) and the volume of waste released (Equation (272)).

$$\boldsymbol{f_C\left(x_{st}\right) = V_w \times C_r} \ . \tag{272}$$

PA-6.8.4 Determining Initial Conditions for Direct and Transport Releases

A sequence of intrusions into the repository can change the conditions in and around the repository and hence affect releases from subsequent intrusions. This section describes how panel and repository conditions are determined for a given intrusion.

PA-6.8.4.1 Determining Repository and Panel Conditions

Direct releases by DBR and spallings, and subsequent releases by radionuclide transport require a determination of the conditions in the intruded panel and in the repository at the time of the intrusion. One of three conditions is assigned to the repository:

E0	the repository is undisturbed by drilling,
E1	the repository has at least one E1 intrusion, or
E2	the repository has one or more E2 intrusions but no E1 intrusions.

In addition, each panel is assigned one of four conditions:

E0	the excavated regions of the panel have not been intruded by drilling,
E1	the panel has one previous E1 intrusions (intersects a brine reservoir in the Castile),
E2	the panel has one or more previous E2 intrusions (none intersect brine reservoirs), or
E1E2	the panel has at least two previous intrusions, at least one of which is an E1 intrusion.

Repository conditions are used to determine direct releases for each intrusion by DBRs and spallings. Panel conditions are used to determine releases by transport through the Culebra.

When an intrusion into CH-TRU waste occurs, the stochastic variables in Table PA-20 are used in the algorithm shown in Figure PA-33 to determine the type of the intrusion (E1 or E2). The type of the intrusion is used to update the conditions for the intruded panel and the repository before stepping forward in time to the next intrusion.

PA-6.8.4.2 Determining Distance from Previous Intrusions

Direct releases by DBR and spallings require a determination of the distance between the panel hit by the current intrusion and the panels hit by previous intrusions. In the CRA-2004 PA, the 10 panels are divided into three groups: lower, consisting of only panel 5; middle, including of panels 3, 4, 6, and 9; and upper, including of panels 1, 2, 7, 8, and 10, as shown in Figure PA-21. These divisions are consistent with the representation of the repository in the BRAGFLO model for Salado flow (Section PA-4.2) and for DBRs (Section PA-4.7).

Although the initial intrusion can occur in any of the 10 actual waste panels, direct releases for the initial intrusion are modeled as if the initial intrusion occurred in a lower waste panel (panel 4 or 5; see Figure PA-6), by using initial conditions for direct releases from the waste panel in the BRAGFLO grid (Figure PA-8), which are mapped to the lower panel in Figure PA-21. This treatment is the same as in the CCA PA and is conservative, since the waste panel typically has higher brine saturation than do the panels in the rest of repository areas (see Sections PA-7.1.2 and PA-8.3.2). Initial conditions for direct releases from subsequent intrusions are modeled by one of three cases: lower, middle, and upper, corresponding to the three panel groups shown in Figure PA-21 and listed in Table PA-24. The lower case represents a second intrusion into a previously intruded panel. The middle case represents an intrusion into an undisturbed

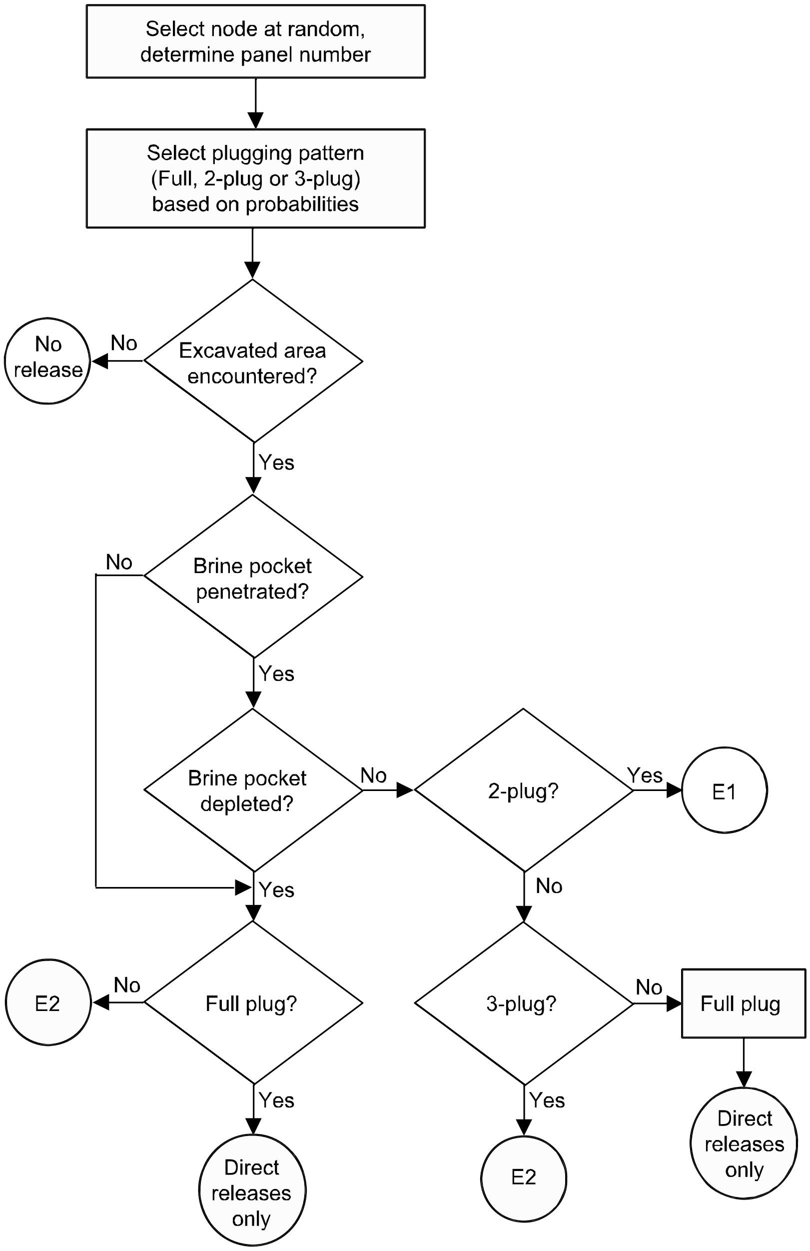

Figure PA-33. The Determination of the Type of Intrusion.

panel that is adjacent to a previously disturbed panel. The upper case represents an intrusion into an undisturbed panel that is not adjacent to a previously disturbed panel. Adjacent panels share one side in common and nonadjacent panels share no sides in common.

Selection of the time and location of the previous intrusion used to determine distance from the current intrusion depends on the repository condition. The repository condition is determined by the intrusion of greatest consequence across all panels prior to the current intrusion. E1 intrusions are assumed to be of the greater consequence than E2 intrusions. The previous intrusion is selected by finding the closest panel (same, adjacent, nonadjacent) whose intrusion condition, excluding the current intrusion, is equal to the repository condition. The time of the previous intrusion is the time of the most recent intrusion having the greatest consequence and closest distance. Likewise, the condition of each panel is equal to the intrusion of greatest consequence into the panel prior to the current intrusion.

PA-6.8.5 Construction of Direct Brine Releases

DBRs (also termed blowout releases) are calculated for all intrusions that encounter CH-TRU waste. DBRs $f_{DBR}\left(\mathbf{x}_{st}\right)$ are constructed from volume of brine released (V_{DBR}) to the surface (Equation (175)) and radionuclide concentrations in brine (C_{bl}, see Equation (85)). Brine volume released to the surface is computed by BRAGFLO (Section PA-4.7.3) for the times listed in Table PA-23; brine volumes released for intrusions at other times are computed by linear interpolation (WIPP PA 2003d).

Calculation of DBR volumes distinguishes between the first intrusion and subsequent intrusions. The release volumes for the initial intrusion (E0 repository conditions) are further distinguished by the panel group (upper, middle, and lower). As shown in Table PA-23, BRAGFLO computes release volumes for the initial intrusion at each of a series of intrusion times; the release volume for the initial intrusion at other times is computed by linear interpolation (WIPP PA 2003a). Release volumes for subsequent intrusions are distinguished by the current state of the repository (E1 or E2) and the relative distance between the panel intruded by the current borehole and the panel of the initial intrusion (same, adjacent, non-adjacent). The algorithms for determining repository conditions and distance between intrusions are described in Section PA-6.8.4.

As indicated in Table PA-23, DBR volumes for a second intrusion are computed by BRAGFLO for a set of combinations of repository condition, distance between intrusions, and time between intrusions. Brine release volumes for other combinations of condition, distance, and time are computed by linear interpolation (WIPP PA 2003a). Brine releases from third and subsequent intrusions are computed as if the current intrusion was the second intrusion into the repository.

Radionuclide concentrations in brine (C_{bl}) are calculated by PANEL (Section PA-6.7.3) for the times listed in Table PA-22; concentrations at other times are computed by linear interpolation (WIPP PA 2003a). The type of intrusion (E1 or E2) determines the brine (Salado or Castile brine) selected for the concentration calculation; for E1 intrusions, Castile brine is used, and Salado brine is used for E2 intrusions.

The direct brine release is computed as the product of the release concentration and the volume, V_{DBR}, i.e.

$$f_{DBR}\left(\mathbf{x}_{st}\right) = V_{DBR} \times C_{bl} \qquad (273)$$

PA-6.8.6 Construction of Spallings Releases

Spallings releases are calculated for all intrusions that encounter CH-TRU waste. The construction of the spallings release $f_{SP}\left(\mathbf{x}_{st}\right)$ is nearly identical to that described in Section PA-6.8.5 for the calculation of DBRs except that volumes of solid material released will be used rather than volumes of brine. These solid releases are calculated with the spallings submodel of the CUTTINGS_S program for the combinations of repository condition, distance from previous intrusions, and time between intrusions listed in Table PA-23. Linear interpolation determines the releases for other combinations of repository condition, distance, and time between intrusions (WIPP PA 2003a).

The concentration of radionuclides in the spallings release volume is computed as the average activity per m^3 in the CH-TRU waste at the time of intrusion. Activities in each waste stream are computed at a discrete set of times by the code EPAUNI (Fox 2003); activities at other times are determined by linear interpolation.

PA-6.8.7 Radionuclide Transport Through the Culebra

One potential path for radionuclide transport from the repository is up through boreholes to the Culebra, then through the Culebra to the LWB (Section 6.4.6). As indicated in Table PA-22, the NUTS and PANEL models are used to estimate radionuclide transport through boreholes to the Culebra $f_{NP}\left(\mathbf{x}_{st}\right)$ for a fixed set of intrusion times; releases to the Culebra for intrusions at other times are determined by linear interpolation (WIPP PA 2003a). NUTS computes the release to the Culebra over time for E1 and E2 boreholes; PANEL computes the release to the Culebra for an E1E2 borehole.

Each borehole may create a pathway for releases to the Culebra. The first E1 or E2 borehole in each panel creates a release path, with the radionuclide release taken from the appropriate NUTS data. Subsequent E2 boreholes into a panel with only E2 boreholes do not cause additional releases; WIPP PA assumes that a subsequent E2 borehole into a panel having only earlier E2 intrusions does not provide a significant source of additional brine, and thus does not release additional radionuclides to the Culebra.

An E1E2 borehole results from the combination of two or more intrusions into the same panel, at least one of which is an E1 intrusion. A subsequent E1 borehole changes the panel's condition to E1E2, as does an E2 borehole into a panel that has an earlier E1 intrusion. Once E1E2 conditions exist in a panel, they persist throughout the regulatory period. However, releases from a panel with E1E2 conditions are restarted for each subsequent E1 intrusion into that panel, since additional E1 intrusions may introduce new volumes of brine to the panel.

Releases to the Culebra are summed across all release pathways to the Culebra to obtain total releases to the Culebra $r_k\left(t\right)$ for the k^{th} radionuclide at each time t. Releases to the Culebra include both dissolved radionuclides and radionuclides sorbed to colloids. The WIPP PA assumes that radionuclides sorbed to humic colloids disassociate and transport as do dissolved radionuclides; other colloid species do not transport in the Culebra (see Attachment SOTERM). The release to the Culebra is partitioned into dissolved and colloid species by multiplying $r_k\left(t\right)$ by radionuclide-specific factors for the fraction dissolved and the fraction on colloids (see Table 4.3.1). Dissolved radionuclides are transported through the Culebra.

Radionuclide transport through the Culebra is computed by the code SECOTP2D (Section PA-4.9) for partially-mined and fully-mined conditions (Section 6.4.6.2.3) as indicated in Table PA-25. These computations assume a 1 kg source of each radionuclide placed in the Culebra between 0 and 50 years, and result in the fraction of each source $f_{m,k}(t)$, where m is the mining condition and k is the index for the radionuclide) reaching the LWB at each subsequent time t. For convenience, the time-ordering of the data from SECOTP2D is reversed so that the fraction $f_{m,k}(t)$ associated with year t = 200, for example, represents the release at the boundary at year 10,000 for a release occurring between 150 and 200 years.

The total release through the Culebra $R_{Cul,k}$ is calculated for the kth radionuclide by

$$R_{Cul,k} = \sum_{t_i \le t_m} r_k(t_i) f_{PM,k}(t_i) + \sum_{t_i > t_m} r_k(t_i) f_{FM,k}(t_i), \tag{274}$$

where $r_k(t_i)$ is the release of the kth radionuclide to the Culebra in kg at time t_i and $f_{PM,k}(t_i)$ and $f_{FM,k}(t_i)$ are the fractions of a unit source placed in the Culebra in the interval (t_{i-1}, t_i) that reaches the LWB by the end of the 10,000-year regulatory period, for partial mined and fully mined conditions within the LWB, respectively. The function $f_{m,k}(t)$ changes when mining is assumed to occur within the LWB; hence the sum in the equation above is evaluated in two parts, where t_{min} is the time that mining occurs. The total releases through the Culebra $f_{ST}(\mathbf{x}_{st})$ is computed by converting the release of each radionuclide $R_{Cul,k}$ from kg to EPA units, then summing over all radionuclides.

PA-6.8.8 CCDF Construction

For each vector $\mathbf{x}_{su,k}$ in the space of subjective uncertainty, the code CCDFGF samples a sequence $\mathbf{x}_{st,i}$, i = 1, 2, …, nS of futures. In the CRA-2004 PA, nS = 10,000; this number of futures is sufficient to generate an adequate estimate of the mean CCDF for total releases for comparison with the boundary line specified in 40 CFR § 191.13, as demonstrated in Section PA-9.1. A release $f(\mathbf{x}_{st,i})$ for each future is then constructed as described in Sections PA-6.8.1 through PA-6.8.7. Once the $f(\mathbf{x}_{st,i})$ are evaluated, the CCDF can be approximated as indicated in Equation (275).

$$prob(Rel > R) = \int_{S_{st}} \delta_R\left[f(\mathbf{x}_{st})\right] d_{st}(\mathbf{x}_{st}) dV_{st} \cong \sum_{i=1}^{nS} \delta_R\left[f(\mathbf{x}_{st,i})\right] / nS \tag{275}$$

A binning technique is used to construct the desired CCDF (i.e., the consequence axis is divided into a sequence of bins and the number of values for $f(\mathbf{x}_{st,i})$ falling in each bin is accumulated). In addition, all values for $f(\mathbf{x}_{st,i})$ are saved and subsequently ordered to provide an alternative method for constructing the CCDFs. In addition to the total CCDF for all releases, it will be possible to obtain CCDFs for individual release modes (e.g., cuttings, spallings, direct brine releases, to Culebra, through MBs, through Culebra). The logic for the production of the CCDFs is diagrammed in Figure PA-34.

The CCDF construction indicated in this section is for a single sample element $\boldsymbol{x}_{su,k}$ of the form indicated in conjunction with Equation (260). Repeated generation of CCDFs for individual sample elements $\boldsymbol{x}_{su,k}$, i.e. for the vectors representing epistemic uncertainty in the model results, will lead to the distribution of complete CCDFs.

PA-6.9 Sensitivity Analysis

Evaluation of one or more of the models discussed in Chapter PA-4.0 with the LHS in Equation (260) creates a mapping

$$\left\{\boldsymbol{x}_{su,k}, \boldsymbol{y}_{su,k}\right\}, \text{ k} = 1, 2, \ldots, \text{nLHS} \tag{276}$$

from analysis inputs (i.e., $\boldsymbol{x}_{su,k}$) to analysis results (i.e., $\boldsymbol{y}\left(\boldsymbol{x}_{su,k}\right)$), where $\boldsymbol{y}_{su,k}$ denotes the results obtained with the model or models under consideration. A vector notation is used for y because, in general, a large number of predicted results are produced by each of the models used in the CRA-2004 PA. In addition, $\boldsymbol{y}\left(\boldsymbol{x}_{su,k}\right)$ could also correspond to a CCDF for normalized release constructed from model results associated with $\boldsymbol{x}_{su,k}$. Sensitivity analysis explores the mapping in Equation (276) to determine how the uncertainty in individual elements of $\boldsymbol{x}_{su}$ affects the uncertainty in individual elements of $\boldsymbol{y}\left(\boldsymbol{x}_{su}\right)$. Understanding how uncertainty in analysis inputs affects analysis results aids in understanding the current PA, and aids in improving the models for future PAs.

The presentation of results from each major model in the WIPP PA is accompanied by sensitivity analyses of the most important output of each major model. Where practical, sensitivity analysis results are based on a pooling of the results obtained for the three replicated LHSs (i.e., R1, R2, R3) discussed in Section PA-6.4. In other cases, the sensitivity analysis is based on the results for the first replicate (i.e., R1), and statistics are compared across the three replicates.

Three principle techniques are used in the sensitivity analysis: scatterplots; regression analyses to determine standardized regression coefficients and partial correlation coefficients; and stepwise regression analyses. Each technique is briefly discussed. A discussion of sensitivity analyses conducted for the CCA PA is provided in Helton et al. (1998).

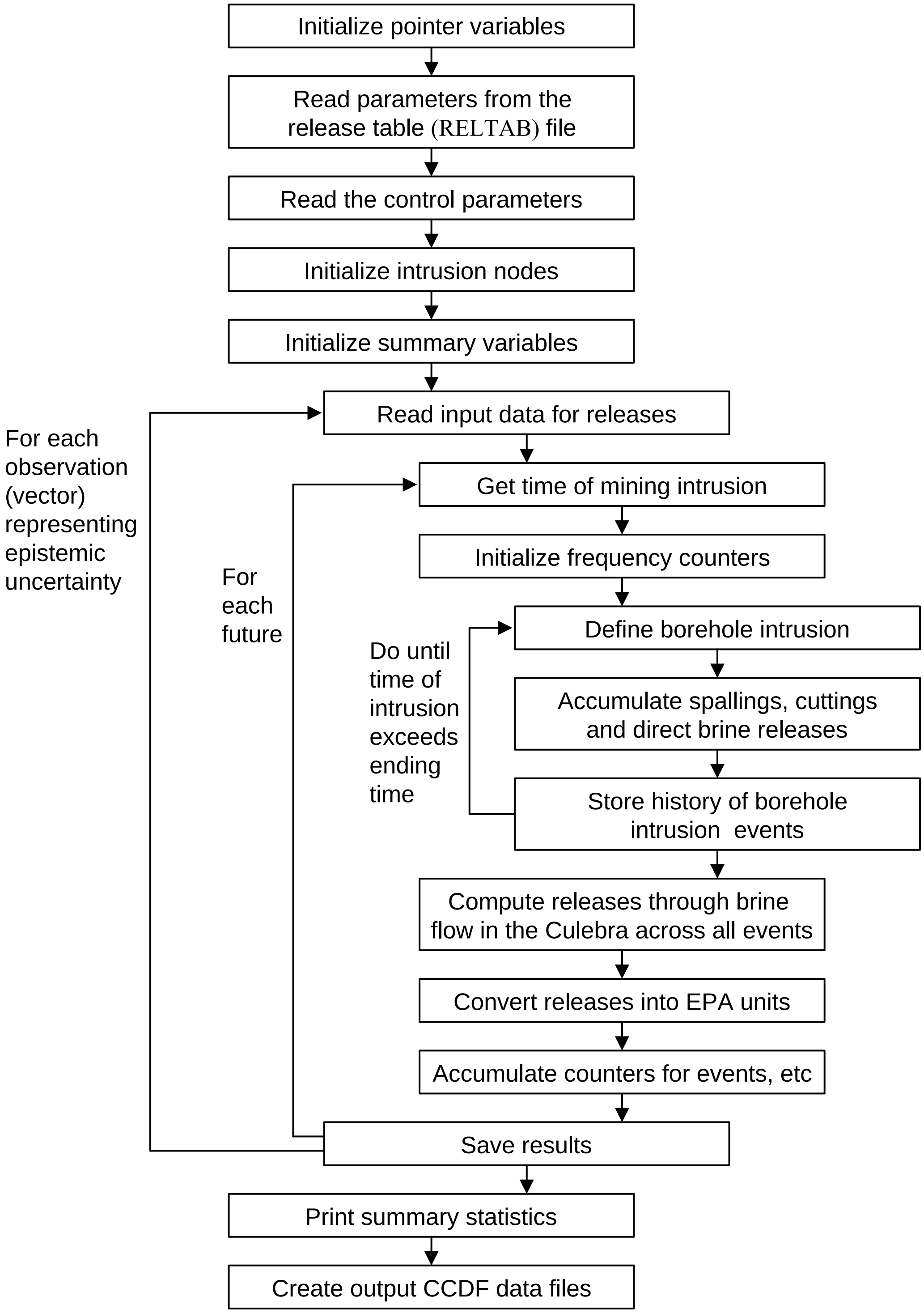

Figure PA-34. Processing of Input Data to Produce CCDFs.

PA-6.9.1 Scatterplots

Scatterplots are the simplest sensitivity analysis technique, performed by plotting the points

$$\left(x_{kj}, y_k\right), \text{ k = 1, 2, …, nLHS} \tag{277}$$

for each element x_j of x. The resulting plots can reveal relationships between y and the elements of x (i.e., the x_j). Scatterplots can be effective at revealing nonlinear relationships or threshold values, and at screening the elements of x for further investigation. The examination of such plots when Latin hypercube sampling is used can be particularly revealing due to the full stratification over the range of each input variable. Iman and Helton (1988) provide an example where the examination of scatterplots revealed a rather complex pattern of variable interactions.

PA-6.9.2 Regression Analysis

A more formal investigation of the mapping in Equation (276) can be based on regression analysis. In this approach, a model of the form

$$y = b_0 + \sum_{j=1}^{n} b_j x_j \tag{278}$$

is developed from the mapping between analysis inputs and analysis results shown in Equation (276), where the x_j are the input variables under consideration and the b_j are coefficients that must be determined. The coefficients b_j and other aspects of the construction of the regression model in Equation (278) can be used to indicate the importance of the individual variables x_j with respect to the uncertainty in y. The CRA-2004 PA employs the method of least squares to determine the coefficients b_j (Myers 1986).

Often the regression in Equation (278) is performed after the input and output variables are normalized to mean zero and standard deviation one. The resulting coefficients b_j are called standardized regression coefficients (SRCs). When the x_j are independent, the absolute value of the SRCs can be used to provide a measure of variable importance. Specifically, the coefficients provide a measure of importance based on the effect of moving each variable away from its expected value by a fixed fraction of its standard deviation while retaining all other variables at their expected values.

Partial correlation coefficients (PCCs) can also provide a measure of the linear relationships between the output variable y and the individual input variables. The PCC between y and an individual variable x_p is obtained from the use of a sequence of regression models. First, the following two regression models are constructed:

$$\hat{y} = b_0 + \sum_{\substack{j=1 \\ j \neq p}}^{n} b_j x_j \text{ and } \hat{x}_p = c_0 + \sum_{\substack{j=1 \\ j \neq p}}^{n} c_j x_j \ , \tag{279}$$

Then, the results of the two preceding regressions are used to define the new variables $y - \hat{y}$ and $x_p - \hat{x}_p$. By definition, the PCC between y and x_p is the correlation coefficient between $y - \hat{y}$

and $x_p - \hat{x}_p$. Thus, the PCC provides a measure of the linear relationship between y and x_p with the linear effects of the other variables removed.

Regression and correlation analyses often perform poorly when the relationships between the input and output variables are nonlinear. This is not surprising since such analyses are based on the assumption of linear relationships between variables. The problems associated with poor linear fits to nonlinear data can be avoided by use of the rank transformation (Iman and Conover 1979). The rank transformation is a simple concept: data are replaced with their corresponding ranks and then the usual regression and correlation procedures are performed on these ranks. Specifically, the smallest value of each variable is assigned the rank 1, the next largest value is assigned the rank 2, and so on up to the largest value, which is assigned the rank m, where m denotes the number of observations. The analysis is then performed with these ranks being used as the values for the input and output variables. A formal development of PCCs and the relationships between PCCs and SRCs is provided by Iman et al. (1985).

*PA-6.9.3 Stepwise Regression Analysi*s

Stepwise regression analysis provides an alternative to constructing a regression model containing all the input variables. With this approach, a sequence of regression models is constructed. The first regression model contains the single input variable that has the largest impact on the uncertainty in the output variable (i.e., the input variable that has the largest correlation with the output variable y). The second regression model contains the two input variables that have the largest impact on the output variable: the input variable from the first step plus whichever of the remaining variables has the largest impact on the uncertainty not accounted for by the first variable (i.e., the input variable that has the largest correlation with the uncertainty in y that cannot be accounted for by the first variable). Additional models in the sequence are defined in the same manner until a point is reached at which further models are unable to meaningfully increase the amount of the uncertainty in the output variable that can be accounted for.

Stepwise regression analysis can provide insights on the importance of the individual variables. First, the order in which the variables are selected in the stepwise procedure provides an indication of their importance, with the most important variable being selected first, the next most important variable being selected second, and so on. Second, the R^2 values at successive steps of the analysis also provide a measure of variable importance by indicating how much of the uncertainty in the dependent variable can be accounted for by all variables selected through each step. When the input variables are uncorrelated, the differences in the R^2 values for the regression models constructed at successive steps equals the fraction of the total uncertainty in the output variable that can be accounted for by the individual input variables being added at each step. Third, the absolute values of the SRCs in the individual regression models provide an indication of variable importance. Further, the sign of an SRC indicates whether the input and output variable tend to increase and decrease together (a positive coefficient) or tend to move in opposite directions (a negative coefficient).

PA-7.0 RESULTS FOR THE UNDISTURBED REPOSITORY

The PA tabulates releases from the repository for undisturbed conditions. Releases to the accessible environment from the undisturbed repository fall under two sets of protection requirements. The first, as set forth 40 CFR § 191.15, protects individuals from radiological exposure; the second, in 40 CFR Part 191, Subpart C, protects groundwater resources from contamination. Chapter 8 describes how WIPP complies with these two requirements. This section supplements Chapter 8 by presenting flow (BRAGFLO) and transport (NUTS) results from modeling the undisturbed repository.

PA-7.1 Salado Flow

Flow in the Salado is computed by BRAGFLO (see Section PA-4.2). This section summarizes the Salado flow calculation results for the undisturbed scenario (S1). Pressure in the repository, brine saturation in the waste, and brine flow out of the repository are presented, along with sensitivity analyses that identify the uncertain parameters to which these results are most sensitive. The analysis package for Salado Flow (Stein and Zelinski 2003b) contains a detailed presentation on the BRAGFLO model, calculation results, and further sensitivity analyses.

PA-7.1.1 Pressure in the Repository

In undisturbed conditions, pressure strongly influences the extent to which contaminated brine might migrate from the repository to the accessible environment. In addition, pressure developed under undisturbed conditions is an initial condition for the models for spallings and DBR (Section PA-4.6 and Section PA-4.7, respectively).

The Salado flow model represents the repository as five regions in the numerical grid: three waste-filled regions (the Waste Panel, South RoR, and North RoR in Figure PA-8) and two excavated regions with no waste (Ops and Exp in Figure PA-8), which are combined in this analysis into the single nonwaste region. Figure PA-35 shows pressure in each region for the 100 realizations in Replicate R1. Pressures within the three waste-filled areas are very similar, because gas generation occurs in each region simultaneously. The pressure in the nonwaste region tends to be lower than in the waste-filled regions due to the intervening panel closures (CONC_PCS in Figure PA-8).

During the first 1,000 years, repository pressure may increase rapidly due to several factors: rapid initial creep closure of rooms (see Attachment PORSURF); initial inflow of brine causes gas generation due to corrosion; and availability of CPR material to produce gas by microbial degradation. Pressure generally approaches a steady-state value after 1,000 years as room closure ceases, brine inflow slows (thereby reducing gas generation by corrosion), and CPR materials are consumed.

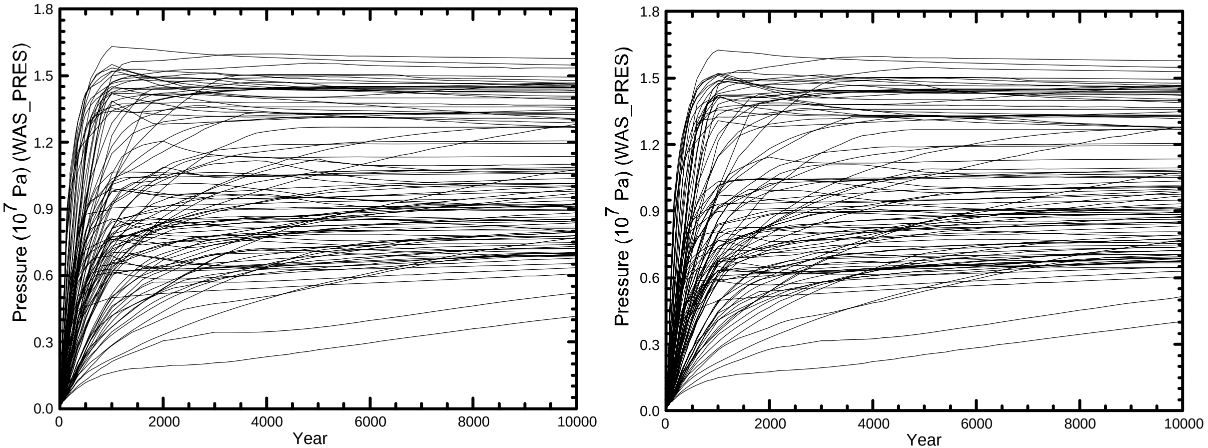

a) Waste Panel

b) South Rest of Repository

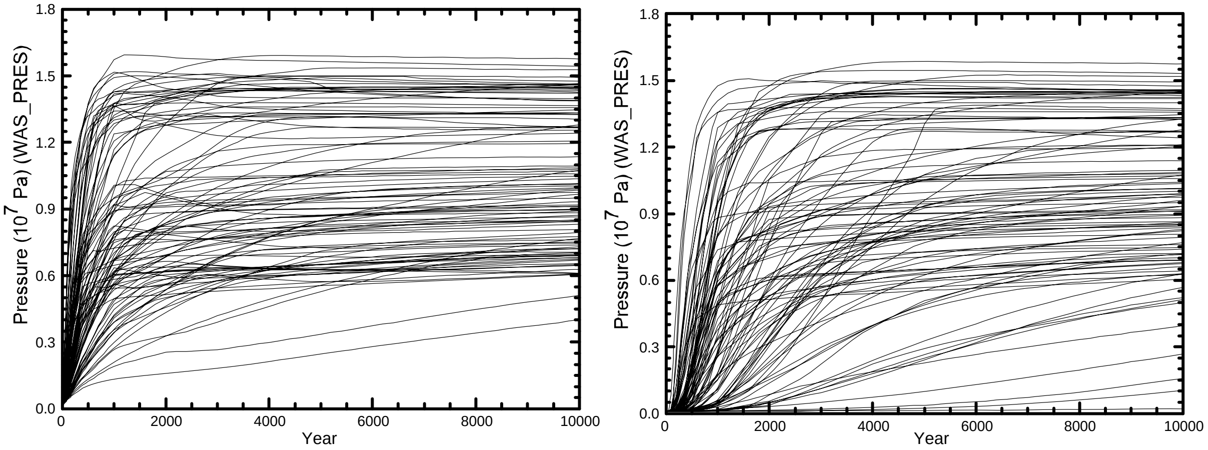

c) North Rest of Repository

d) Non-Waste Areas

Figure PA-35. Pressure in the Excavated Areas, Replicate R1, Scenario S1.

Figure PA-36 shows the mean and 90th percentile values for pressure in each region. There is a consistent pattern of declining pressure from the waste panel through South RoR (SRR_PRES) and North RoR (NRR_PRES) to the nonwaste region (NWA_PRES). The differences in pressure reflect the slow migration of gas from waste-filled regions to the nonwaste regions where no gas is being produced. The 90th percentile pressures level off between 14 and 15 MPa indicating equilibrium between gas generation, which increases pressure, and pressure relief processes (e.g., fracturing, outward migration of fluids, and increased porosity of the excavated areas).

Sensitivity analyses are used to determine the importance of parameter uncertainty to the uncertainty in model results. Figure PA-37 shows partial rank correlation coefficients (PRCCs) resulting from regression between pressure in the waste panel (WAS_PRES) and the uncertain variables in the LHS (Section PA-5.0). The figure shows that uncertainty in the pressure in the waste panel is primarily determined by the sampled input parameter, WMICDFLG, which indicates whether microbial gas generation is active and what materials,

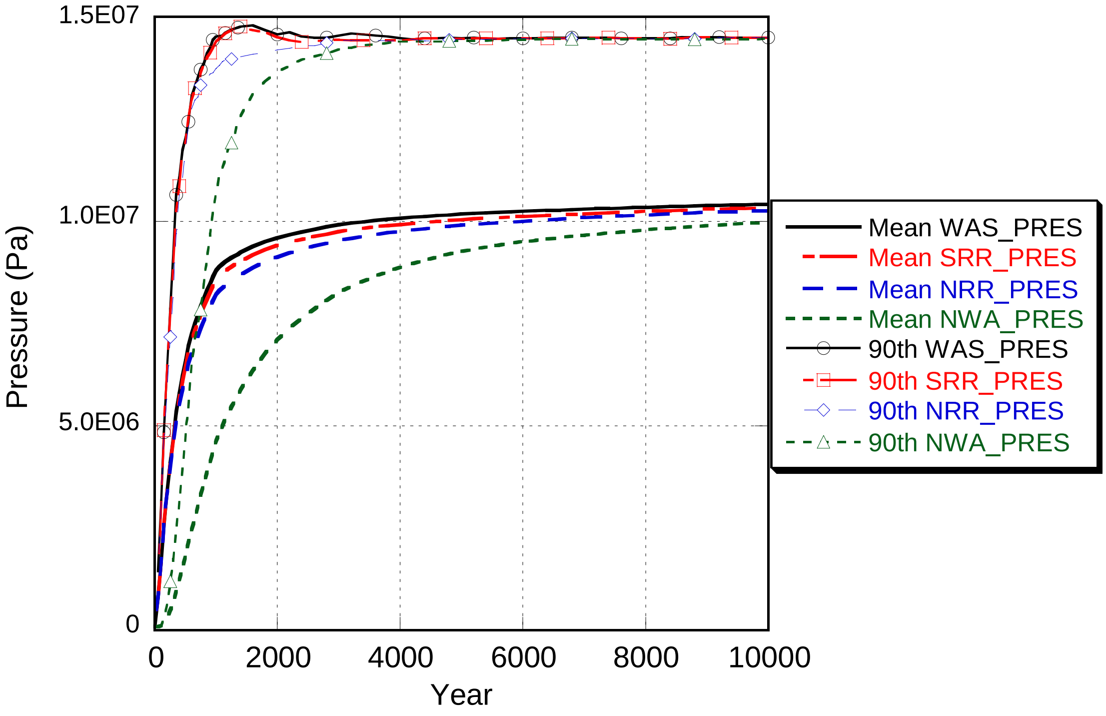

Figure PA-36. Mean and 90th Percentile Values for Pressure in Excavated Areas, Replicate R1, Scenario S1.

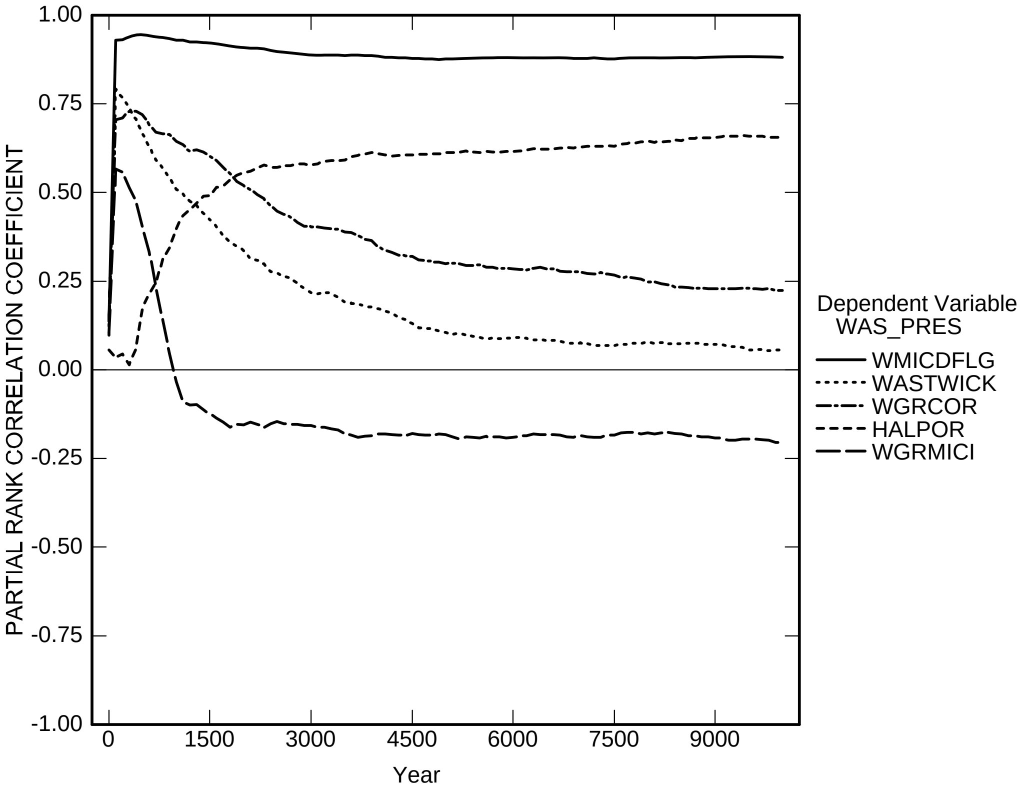

Figure PA-37. Primary Correlations of Pressure in the Waste Panel with Uncertain Parameters, Replicate R1, Scenario S1.

if any, are consumed. The positive correlation indicates that higher pressures result from higher values of WMICDFLG, which represent larger amounts of material available for gas production by microbial activity. The PRCC for WMICDFLG is approximately 0.85 throughout the 10,000-year calculation time, indicating that uncertainty in this parameter explains the variability in the waste panel pressure. Consequently, uncertainties in other parameters are not very significant; the other PRCCs in Figure PA-37 indicate that halite porosity (HALPOR), the inundated microbial gas generation rate (WGRMICI), the corrosion rate for steel (WGRCOR), and the waste wicking parameter (WASTWICK) determine the remaining variability in waste panel pressure.

Figure PA-38 compares statistics for pressure in the waste panel among the three replicates and shows that results for the three replicates are very similar. Mean pressures are nearly coincident; small differences between replicates are observable among the replicates at very high or very low pressures.

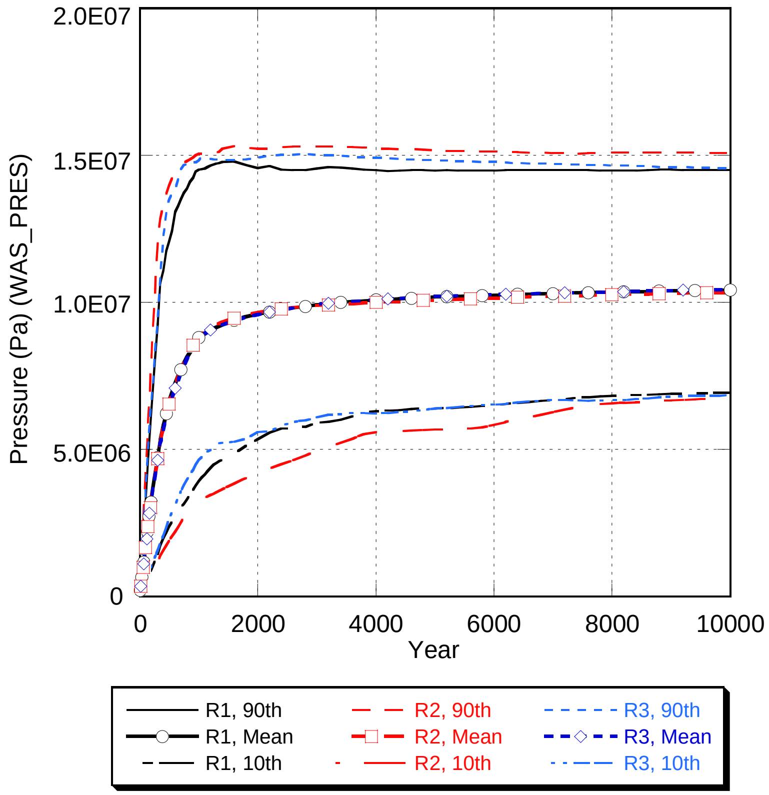

Figure PA-38. Comparison of Pressure in the Waste Panel Between All Replicates, Scenario S1.

PA-7.1.2 Brine Saturation in the Waste

Brine saturation is an important result of the model for Salado Flow, because gas generation processes, which tend to increase pressure, require brine. Brine saturation is also an initial condition in the model for DBR (Section PA-4.7).

Figure PA-39 shows brine saturation in the various excavated areas of the repository for the 100 realizations of Replicate 1. Brine saturation in the waste-filled areas is set initially to 0.015. Saturation increases very rapidly (in the first 100 years) in all excavated areas as brine flows toward the excavations, primarily from the DRZ above the excavation. Initially there is a large pressure differential between the DRZ and the excavated regions, and the relatively high permeability of the DRZ, compared to undisturbed halite, permits the rapid influx of brine. Brine inflow slows as the pressures equalize and as brine saturation in the DRZ decreases. Brine saturation in the waste decreases over time as brine is consumed by corrosion. Brine may also be driven out of the repository by high pressure.

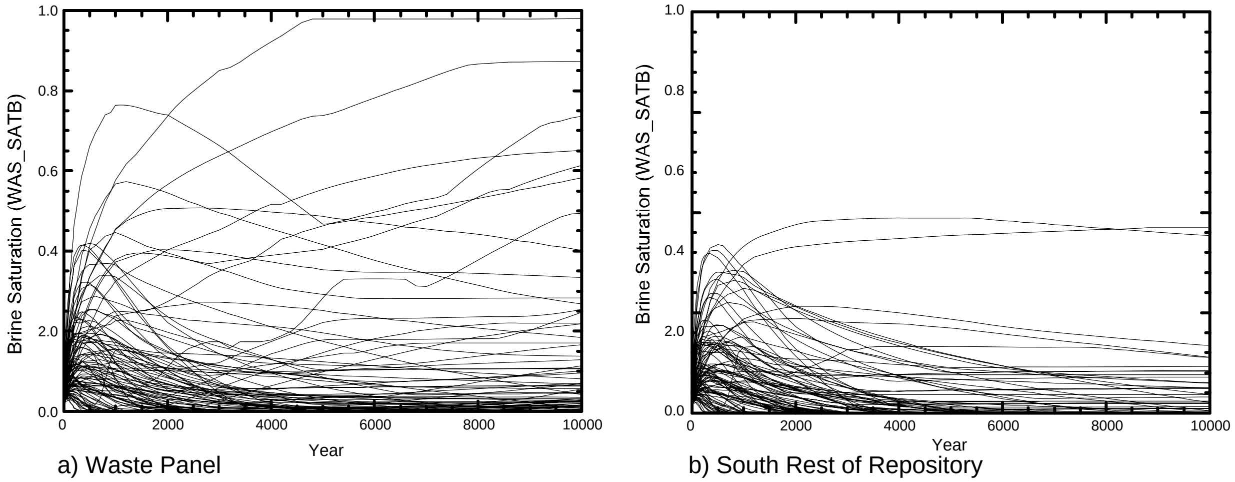

a) Waste Panel

b) South Rest of Repository

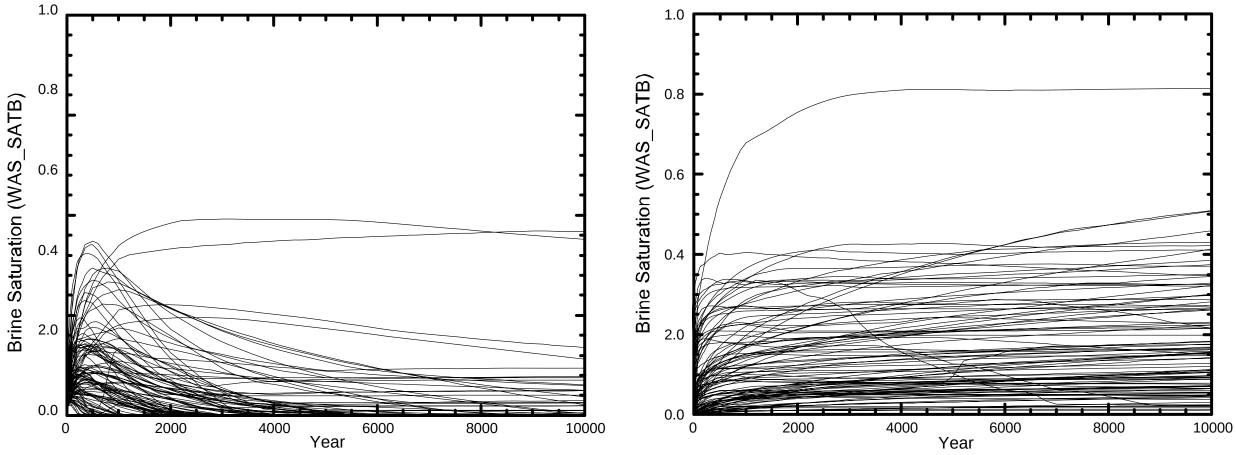

c) North Rest of Repository

d) Non-Waste Areas

Figure PA-39. Brine Saturation in the Excavated Areas, Replicate R1, Scenario S1.

Figure PA-40 compares statistics for brine saturation between the different regions of the repository. Brine saturation in the waste panel (WAS_SATB) tends to be greater than in the rest of repository regions (SRR_SATB and NRR_SATB) due to the artificial two-dimensional modeling of the Salado; in the modeling grid (Figure PA-8), the waste panel has direct contact with the anhydrite MBs while the rest of repository regions do not. Brine saturation in the

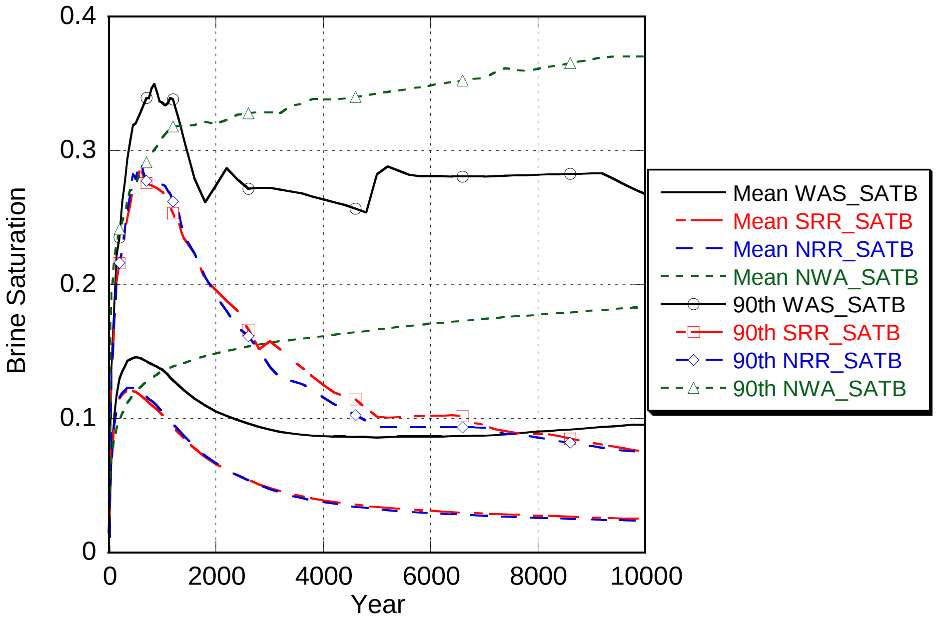

Figure PA-40. Mean and 90th Percentile Values for Brine Saturation in Excavated Areas, Replicate R1, Scenario S1.

non-waste region (NWA_SATB) is higher than in the waste-filled regions due to brine consumption in the waste regions, but also due to the panel closures. Brine that enters the experimental area flows down the stratigraphic gradient into the operations area, then ponds up against the panel closure separating the operations area from the waste filled regions.

Regression between the brine saturation in the waste panel (WAS_SATB) and the uncertain parameters in the LHS identifies a number of parameters that contribute to the uncertainty in brine saturation. The relative importance of these parameters varies over the 10,000-year modeling period, and none of the parameters is clearly dominant. Figure PA-41 shows positive correlations with halite porosity (HALPOR) and DRZ permeability (DRZPRM). Increases in halite porosity increase the volume of brine available in the material overlying the waste; increases in DRZ permeability accelerate drainage into the waste. Negative correlations are found between brine saturation and the corrosion rate (WGRCOR) and the wicking factor (WASTWICK) because increases in these two variables increase the rate at which brine is consumed by corrosion, thus decreasing saturation. The negative correlation between brine saturation and WMICDFLG, which becomes significant near the end of the simulation, indicates that increasing total gas generated (by adding microbial degradation of CPR material) eventually leads to less brine inflow and consequently lower saturation.

Figure PA-42 compares brine saturation statistics for the three replicates. The plots of the mean brine saturation are nearly coincident. Significant differences between replicates are evident at the high end of the saturation scale because there are only a few vectors in each replicate with high saturations.

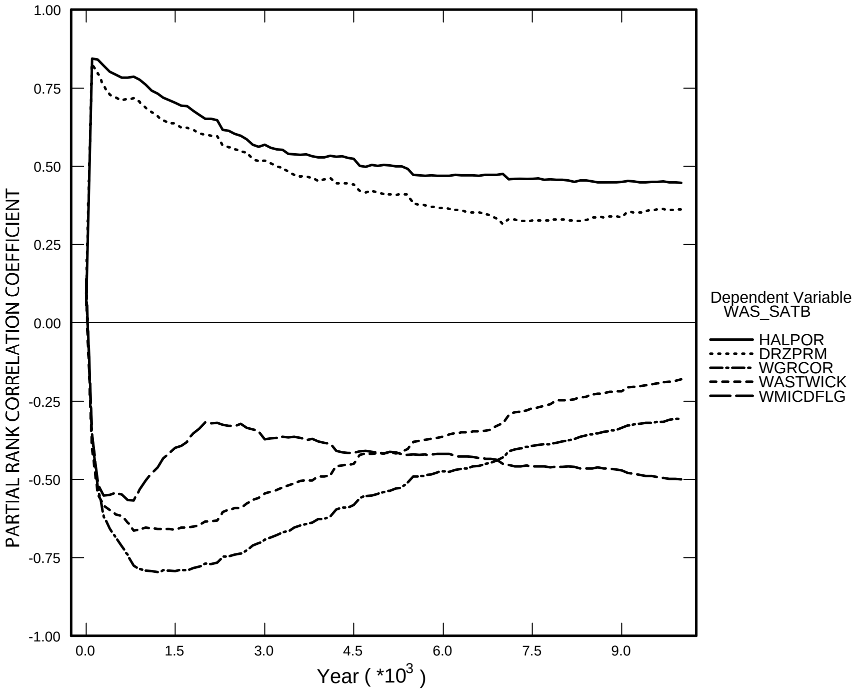

Figure PA-41. Primary Correlations of Brine Saturation in the Waste Panel with Uncertain Parameters, Replicate R1, Scenario S1.

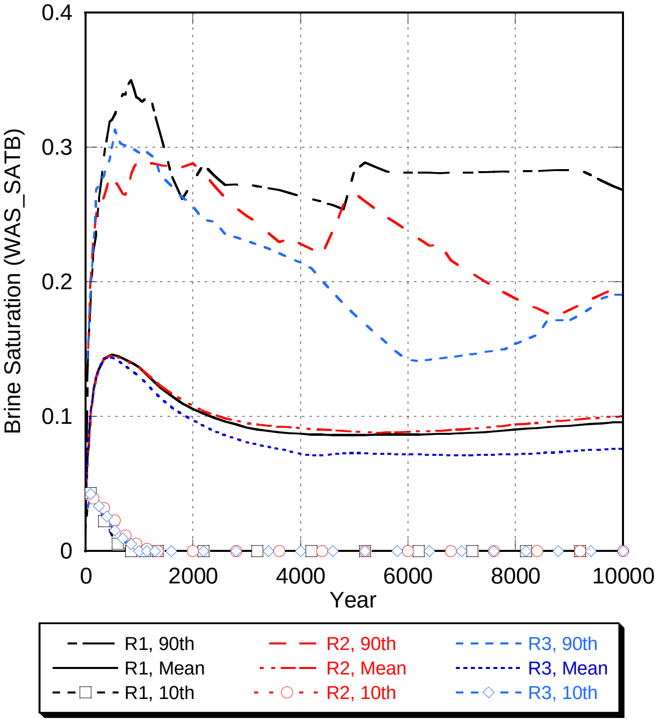

Figure PA-42. Comparison of Brine Saturation in the Waste Panel Between Replicates, Scenario S1.

PA-7.1.3 Brine Flow Out of the Repository

The anhydrite MBs and the shafts provide possible pathways for brine flow away from the repository in the undisturbed scenario (S1). The Salado flow model only tabulates the volume of brine crossing boundaries within the model grid; it does not identify whether the brine contains radionuclides from the waste. Transport is calculated separately from the flow and is discussed in Section PA-7.2.

Figure PA-43 shows cumulative brine outflow from the excavated regions of the repository (BRNREPOC). Brine flow out of the DRZ into the MBs is shown in Figure PA-44, and flow up the shaft to the bottom of the Culebra is shown in Figure PA-45. Comparison of total cumulative brine outflow into all MBs (BRAALOC, Figure PA-44) to total outflow (Figure PA-43) confirms that the primary path for brine outflow is along the MBs.

The distribution of brine flow among the potential pathways varies somewhat between vectors, but typically outflow along MB 139 to the south accounts for most of the total brine outflow. The dominance of MB 139 to the south as the primary conduit for brine outflow is illustrated in Table PA-26, which tabulates maximum brine outflow along each potential pathway for any vector in replicate R1. MB 139 is down the stratigraphic dip, and, being the lowest outflow pathway, it is most frequently saturated.

Figure PA-46 shows the volumes of brine that cross the LWB through the MBs. The largest outflow across the LWB is 433 m^3. Table PA-26 shows that a smaller volume of brine (50 m^3) may reach the Culebra through the shaft. Brine crossing the LWB or moving up the shaft does not necessarily indicate releases from the repository, since the brine may not have been in contact with the waste; the brine may have been present in the MBs at the start of the regulatory period. Section PA-7.2 presents the results of the transport calculations that determine the amount of radionuclides that be released by transport in brine.

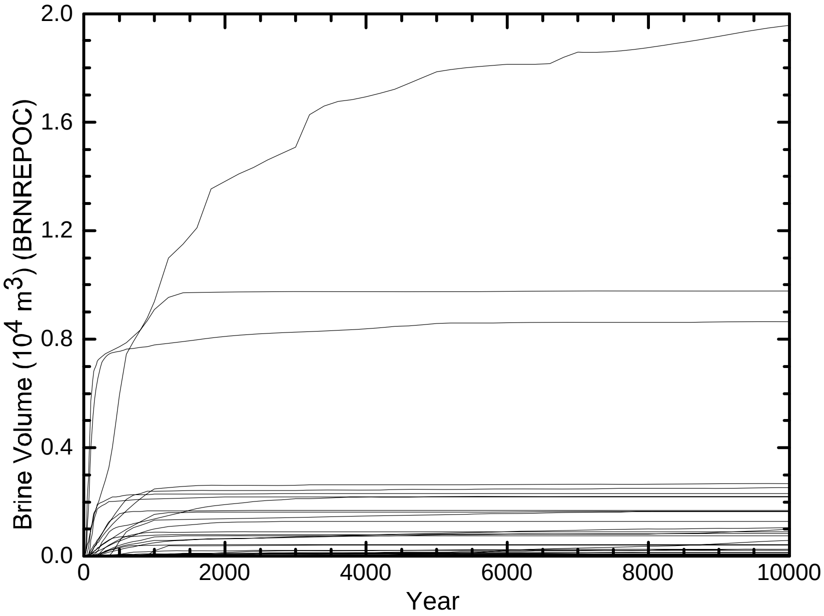

Figure PA-43. Brine Flow Away from the Repository, Replicate R1, Scenario S1.

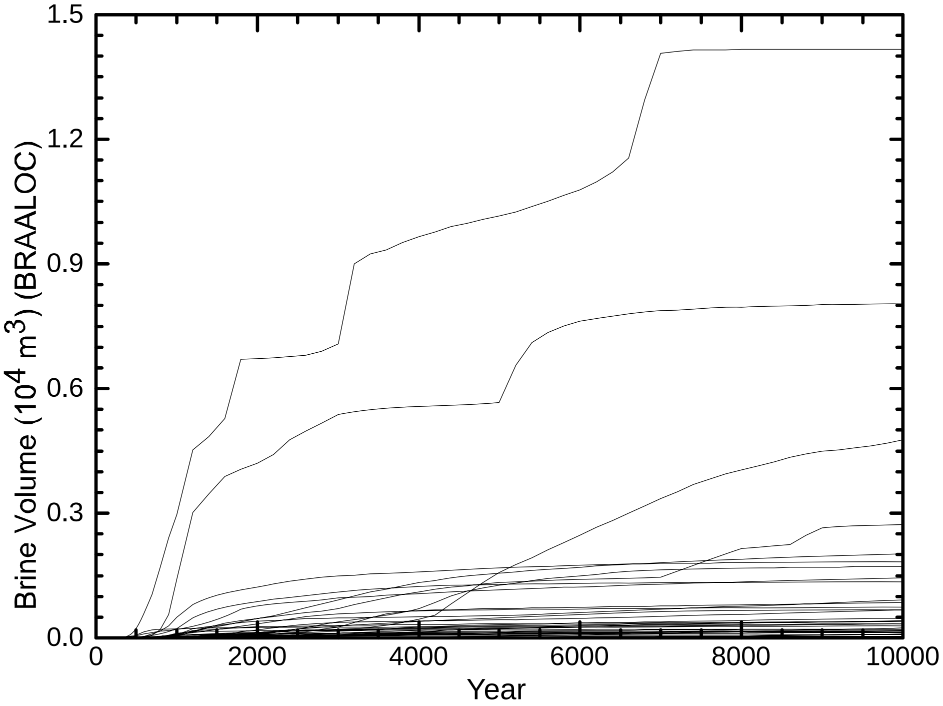

Figure PA-44. Brine Flow Away from the Repository Via All Marker Beds, Replicate R1, Scenario S1.

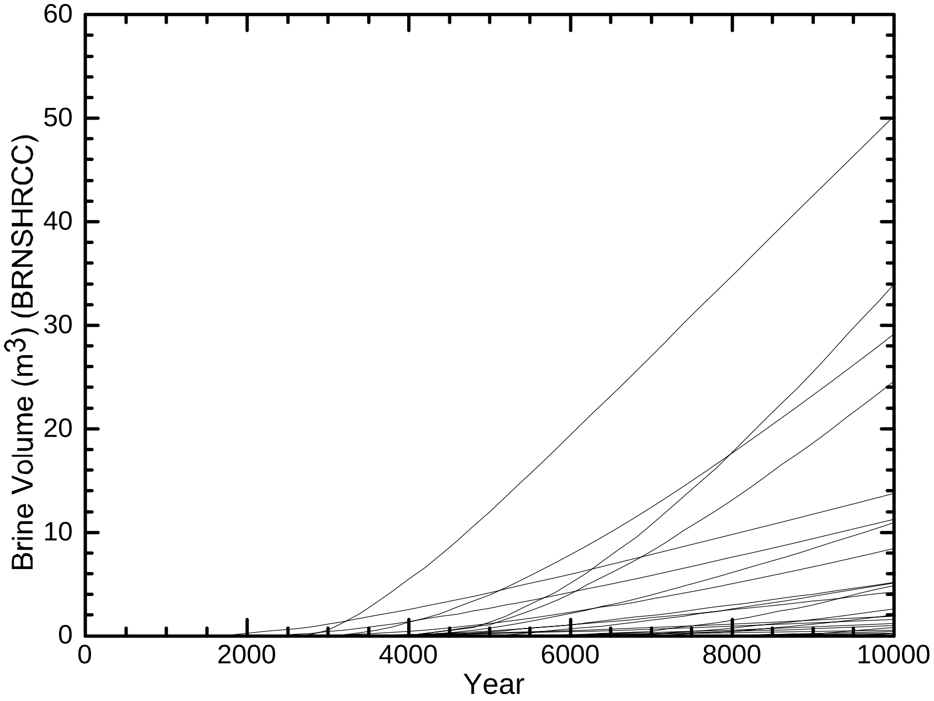

Figure PA-45. Brine Outflow Up the Shaft, Replicate R1, Scenario S1.

Table PA-26. Volume of Brine Outflow by Various Potential Pathways

Pathway for Brine Outflow	Maximum (m^3)
MB 138 North	432
MB 138 South	1,567
Anhydrite AB North	0
Anhydrite AB South	5
MB 139 North	1,832
MB 139 South	12,828
Shaft (to base of Culebra)	50

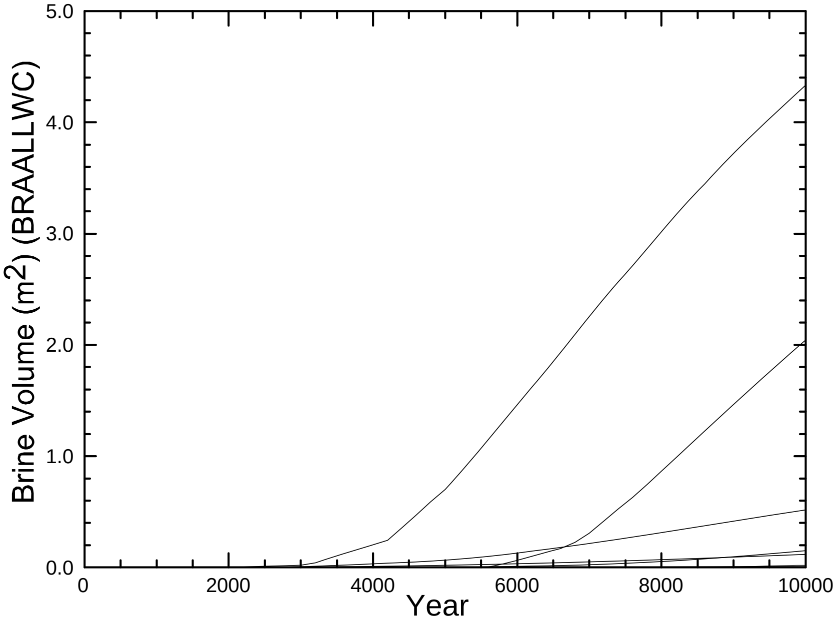

Figure PA-46. Brine Flow Via All MBs Across The LWBs, Replicate R1, Scenario S1.

Regression between total cumulative brine flow into the MBs (BRAALOC) and the uncertain parameters in the LHS (Figure PA-47) shows that uncertainty in brine outflow into the MBs is primarily determined by WMICDFLG, which indicates whether microbial gas generation is modeled and what materials, if any, are consumed. The positive correlation of WMICDFLG with BRAALOC is comparable to the correlation of WMICDFLG with pressure in the waste panel (WAS_PRES) indicating that increasing pressure correlates with increasing brine flow into the marker beds. The PRCC for WMICDFLG is approximately 0.85 throughout the 10,000-year calculation time, indicating that uncertainty in this parameter explains roughly 85% of the variability in BRAALOC. The porosity of halite (HALPOR) accounts for most of the remaining uncertainty. Increasing HALPOR means that more brine is available in the DRZ for inflow into the repository, and brine inflow is a necessary precursor to outflow. The influence of the other three parameters listed in Figure PA-47 is negligible.

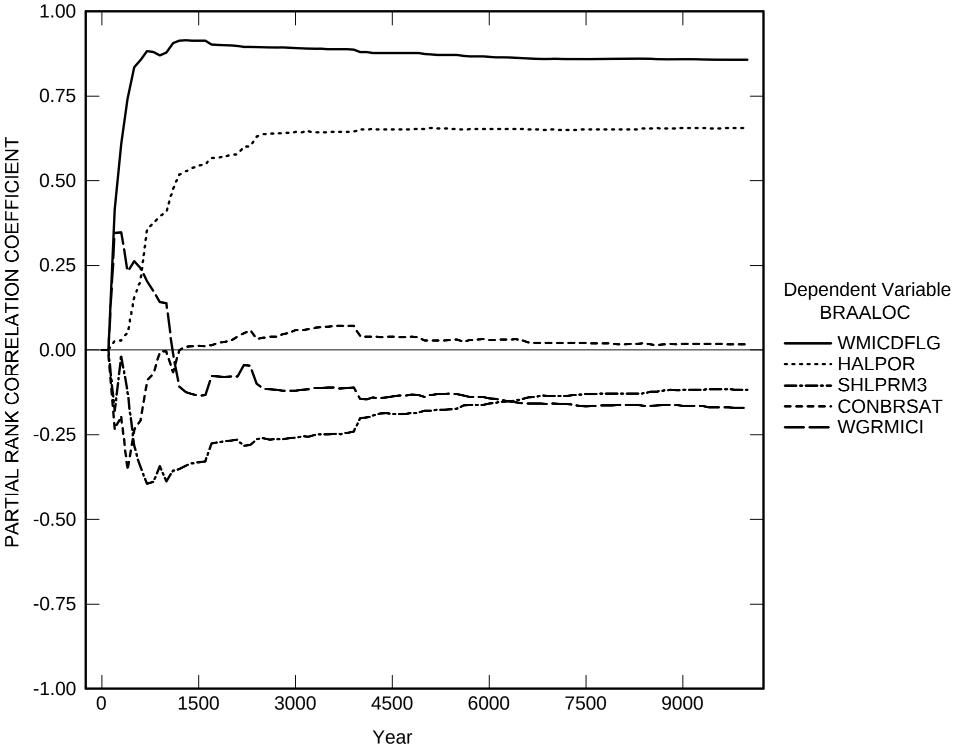

Figure PA-47. Primary Correlations of Total Cumulative Brine Flow Away from the Repository Through All MBs with Uncertain Parameters, Replicate R1, Scenario S1.

Figure PA-48 compares statistics of brine outflow from the repository for the three replicates, and shows that all three replicates produce similar results. The BRNREPOC provides a more valid basis for comparison among the replicates than the other outflow variables, because it has fewer vectors with zero values.

PA-7.2 Radionuclide Transport

Radionuclide transport in the undisturbed scenario is calculated by the code NUTS. Screening runs are used to determine which vectors have the potential to transport radionuclides to the accessible environment (see Section PA-6.7.2). Full transport simulations are run for all vectors that are screened in. This section summarizes the transport results for the undisturbed repository, both up the shaft to the Culebra, and through the Salado to the LWB. Lowry (2003) presents a detailed analysis of NUTS results for the CRA-2004 PA.

PA-7.2.1 Transport to the Culebra

No vectors showed any amount of radionuclide transported to the Culebra through the shafts from the undisturbed repository. Consequently, no radionuclides can transport through the Culebra to the LWB in undisturbed conditions.

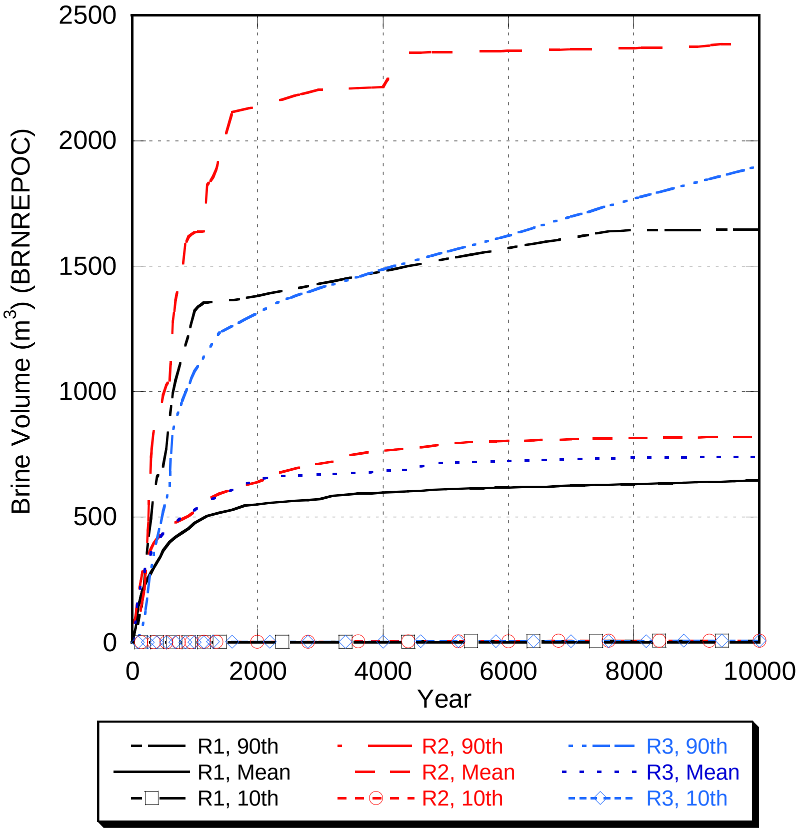

Figure PA-48. Comparison of Brine Flow Away from the Repository between Replicates, Scenario S1.

PA-7.2.2 Transport to the Land Withdrawal Boundary

In all three replicates (300 vectors) of the CRA-2004 PA, only one vector displayed non-zero releases across the LWB from the undisturbed repository. Vector 82 of Replicate R1 released a total of 2.89×10^{-15} EPA units out the southern anhydrite MB 139 over 10,000 years. The release is predominately ^{239}Pu. In this vector, quantities of all of the isotopes move through the MB about 677 m. However, at 984 m from the edge of the repository the concentration of ^{239}Pu decreases to less than 1×10^{-7} EPA units. The total distance from the repository edge to the LWB is 2,400 m. Thus, the non-zero release in this vector is indicative of numerical dispersion resulting from the coarse grid spacing between the repository and the LWB, rather than a probable transport of radionuclides.

The releases from the undisturbed scenario are insignificant when compared to releases from drilling intrusions (see Section PA-9.0). Consequently, releases in the undisturbed scenario are omitted from the calculation of total releases from the repository (see Section PA-9.0) to satisfy the containment requirements of 40 CPR Part 194. Chapter 8.0 demonstrates that WIPP complies with the individual protection requirements of 40 CFR § 191.15 and the groundwater protection requirements of 40 CFR Part 191, Subpart C.

PA-8.0 RESULTS FOR A DISTURBED REPOSITORY

The WIPP repository might be disturbed by exploratory drilling for natural resources during the 10,000-year regulatory period. Drilling could create additional pathways for radionuclide transport, especially in the Culebra, and could release material directly to the surface. In addition, mining for potash within the LWB might alter flow in the overlying geologic units and may accelerate transport through the Culebra. The disturbed scenarios used in PA modeling capture the range of possible releases resulting from drilling and mining.

As outlined in Section PA-6.8, total releases are computed by the code CCDFGF, which evaluates the function f in Equation (24) for each stochastically generated future of the repository. Total releases comprise transport releases and direct releases. Transport releases generally involve movement of radionuclides up an abandoned borehole into the Culebra, then through the Culebra to the LWB. Transport of radionuclides to the Culebra is computed using the codes NUTS and PANEL (see Section PA-4.3 and Section PA-4.4, respectively) using the brine flows computed by BRAGFLO. Transport through the Culebra is computed by the code SECOTP2D (see Section PA-4.9) using flow fields calculated by MODFLOW (see Section PA-4.8).

Direct releases occur at the time of a drilling intrusion and include releases of solids (cuttings, cavings, and spallings) computed using the code CUTTINGS_S (see Section PA-4.5 and Section PA-4.6) and direct releases of brine computed using BRAGFLO (see Section PA-4.7). Pressure and brine saturation within the waste are initial conditions to the models for direct releases. Results from the undisturbed repository (see Section PA-7.0) are used as the initial conditions for the first intrusion. To calculate initial conditions for subsequent intrusions, and to compute the source of radionuclides for transport in the Culebra, a set of drilling scenarios are used to calculate conditions within the repository after an intrusion, using BRAGFLO (Section PA-6.7.1).

This section first summarizes the scenarios used to represent drilling intrusions and the resulting repository conditions calculated by BRAGFLO. Next, transport releases are presented, followed by cuttings and cavings, spallings, and DBRs. Finally, total releases from the repository are summarized.

PA-8.1 Drilling Scenarios

As described in Section PA-3.9, the PA considers two types of drilling intrusions, E1 and E2. The E1 scenario represents the possibility that a borehole connects the repository with a pressurized brine reservoir located within the underlying Castile formation. The E2 scenario represents a borehole that does not connect the repository with an underlying brine reservoir. Repository conditions are calculated for the E1 scenario at 350 and 1,000 years, referred to as the BRAGFLO S2 and S3 scenarios, respectively. The BRAGFLO scenarios S4 and S5 represent E2 drilling events that occur at 350 and 1,000 years, respectively. An additional BRAGFLO scenario, S6, simulates the effects of an E2 intrusion at 800 years followed by an E1 intrusion 1,200 years later into the same panel. For more details on the BRAGFLO scenarios, see Section PA-6.7.1.

PA-8.2 Mining Scenarios

Long-term releases within the Culebra could be influenced by future mining activities that remove all the known potash reserves within the LWB and cause the transmissivity within the overlying Culebra to change. As outlined in Section PA-3.8, full mining of known potash reserves within the LWB in the absence of active and passive controls occurs with a probability specified as a Poisson process with a rate of 10^{-4} yr^{-1}. For any particular future $\boldsymbol{x}_{st}$ in S_{st}, this rate is used to define a time t_{min} at which full mining has occurred. As described in Section PA-6.8.7, flow fields are calculated for the Culebra for two conditions: partial mining, which assumes that all potash as been mined from reserves outside the LWB; and full mining, which assumes all reserves have been mined both inside and outside the LWB. Transport through the Culebra uses the partial mining flow fields prior to t_{min}, and the full mining flow fields after t_{min}.

PA-8.3 Salado Flow

This section summarizes the results of the Salado flow calculations for the disturbed scenarios. Stein and Zelinski (2003b) provide a detailed presentation on the BRAGFLO model, calculation results, and further sensitivity analyses

PA-8.3.1 Pressure in the Repository

Figure PA-49 shows pressure in the waste panel (WAS_PRES for area Waste Panel of Figure PA-8) for the 100 vectors of replicate R1 for each BRAGFLO scenario (Table PA-21). Scenario S1 represents undisturbed repository conditions; the pressure in the waste panel in scenario S1 (Figure PA-49a) is analyzed in Section PA-7.1. Before the drilling intrusions at 350 or 1,000 years, repository pressure increases as described in Section PA-7.1.

After the intrusion, pressure exhibits patterns that vary depending on the type of intrusion and upon sampled input variables related to the intrusion.

Scenarios S2 and S3 represent E1 intrusions at 350 and 1,000 years, respectively (Table PA-21). At the time of the intrusion, brine flow from the Castile brine reservoir leads to an increase in pressure (Figure PA-49b and c). However, pressure drops sharply 200 years after the intrusion when the borehole plugs above the repository fail (Table PA-5) and the permeability of the borehole generally increases. However, in vectors with low borehole permeability after plug failure, pressure does not change noticeably as a result of the borehole plug failure. Twelve hundred years after the drilling intrusion, the permeability of the borehole connecting the repository to the Castile is reduced by an order of magnitude because of creep closure (Table PA-5). This material change reduces pressure slightly in some vectors, but does not appear to have a significant effect on the pressure in most vectors.

Scenarios S4 and S5 represent E2 intrusions at 350 years and 1,000 years, respectively. The borehole plugs effectively prevent any change in repository pressure from the time of the intrusion until the borehole plugs fail (Figure PA-49d and e). As in the scenarios for E1 intrusions, pressure generally drops sharply when the plugs fail, except for vectors with low borehole permeability after plug failure.

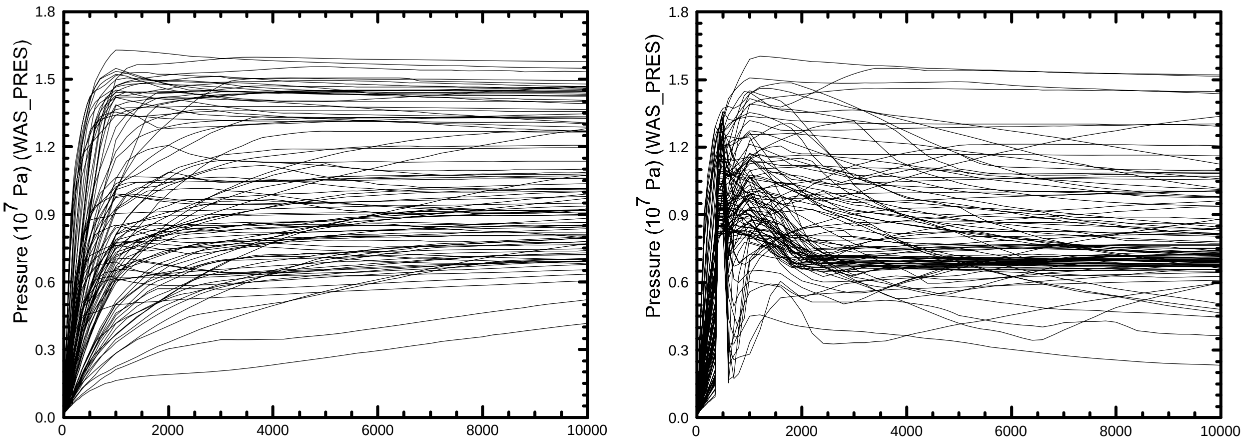

a) Scenario S1

b) Scenario S2

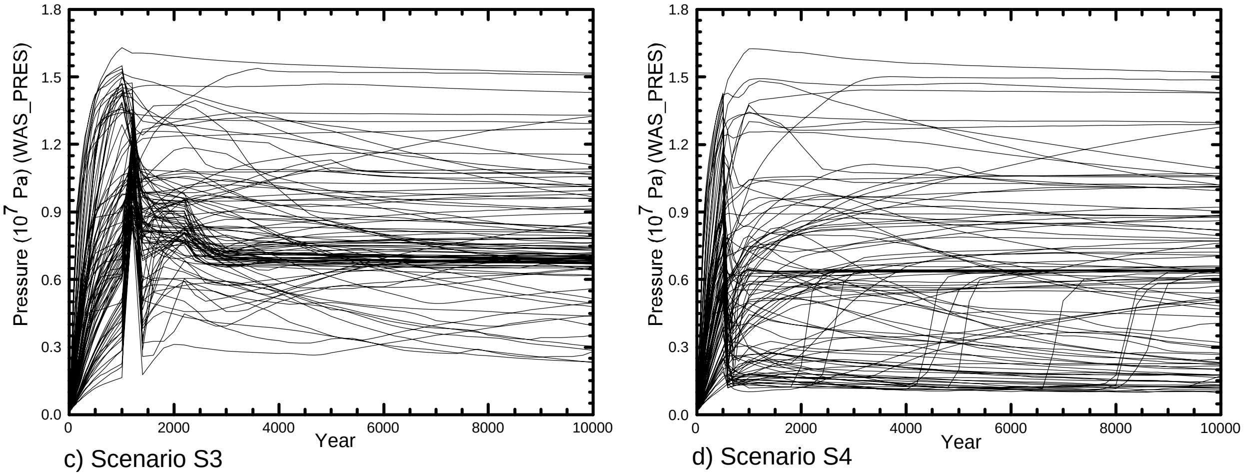

c) Scenario S3

d) Scenario S4

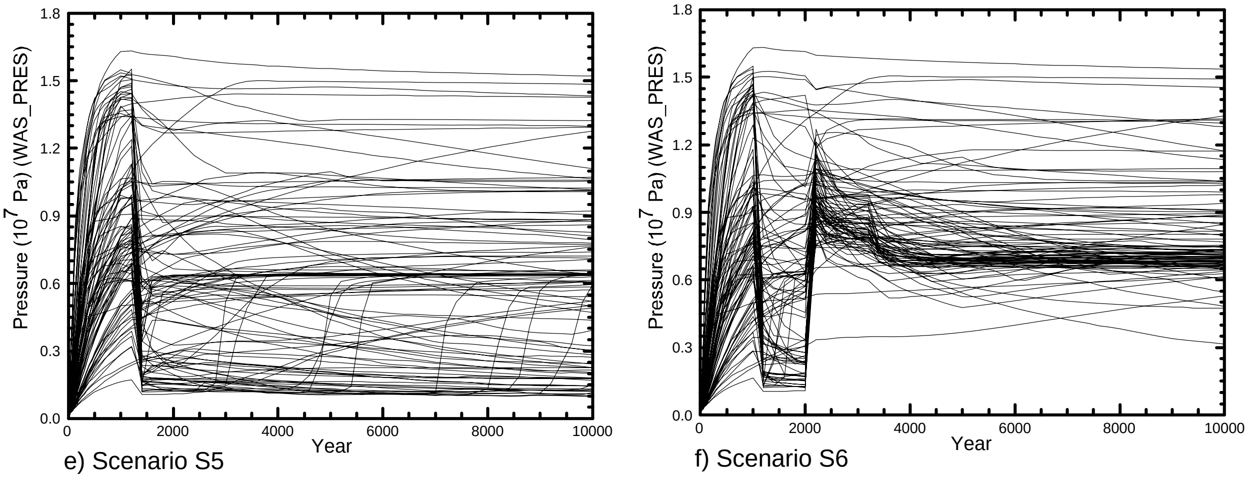

e) Scenario S5

f) Scenario S6

Figure PA-49. Pressure in the Waste Panel for All Scenarios, Replicate R1.

Scenario S6 represents two intrusions into the same panel: an E2 intrusion at 800 years followed by an E1 intrusion at 2000 years. Figure PA-49f shows pressure in the panel for the S6 scenario. The changes in pressure after the first intrusion are nearly identical to that observed in Scenario S5 (Figure PA-49e). In most vectors, the pressure decreases so much that there is a sharp increase in pressure at the time of the second intrusion, which connects the waste panel to the Castile brine reservoir. The changes in pressure after the second intrusion are very similar to those predicted after an E1 intrusion (Scenario S3, Figure PA-49c).

Figure PA-50 shows pressure in the rest of repository areas (SRR_PRES for area South RoR and NRR_PRES for area North RoR in Figure PA-8) and in the nonwaste areas (NWA_PRES averaged over areas Ops and Exp in Figure PA-8) for Scenarios S2 and S5, which represent E1 and E2 drilling intrusions into the waste panel at 350 and 1,000 years, respectively. In general, pressure in the rest of repository and nonwaste areas is not immediately affected by the intrusion. The presence of the Option D panel closures (see Section PA-4.2.8) inhibits flow of gas and brine between the intruded panel and adjoining areas, moderating the effects of the intrusion.

Figure PA-51 compares mean pressure in the waste panel among the scenarios. Pressure in the disturbed scenarios tends to be lower after the intrusion than pressure in the undisturbed scenario due to the borehole connection to the surface. By 2,000 years after the intrusion, the mean pressure after an E1 intrusion (Scenarios S2, S3, and S6) is about 80 percent of the mean pressure in undisturbed conditions (Scenario S1), and the mean pressure after an E2 intrusion (scenarios S4 and S5) is 60 percent of the mean pressure in undisturbed conditions.

Figure PA-52 illustrates the differences in pressure among the various excavated regions after an E1 intrusion at 350 years (Scenario S2). Following the intrusion, mean pressure in the waste panel (WAS_PRES) is temporarily higher than in the other repository regions. About 1,500 years after the intrusion, mean pressure in the South RoR (SRR_PRES) and North RoR (NRR_PRES) is approximately equal to mean pressure in the waste panel. Mean pressure in the nonwaste regions (NWA_PRES) is lower than pressure in the waste-filled regions until about 4,000 years after the intrusion. The delay in pressure equalization between different repository regions is due to the panel closures, which tend to prevent rapid exchange of brine and gas between regions (Hansen et al. 2002) unless pressure exceeds the fracture initiation pressure (approximately 12-14 MPa) after which pressure can rapidly equalize among the regions.

Regression between pressure in the waste panel for an E1 intrusion at 350 years (Scenario S2) and the uncertain parameters in the analysis (Section PA-5.2) shows that the uncertainty in the permeability of the borehole (BHPERM) is largely responsible for the uncertainty in pressure after the borehole plugs fail (Figure PA-53). Before the borehole plugs fail, pressure is most sensitive to variations in the initial pressure in the Castile (BPINTPRS) and the indicator for microbial gas generation (WMICDFLG). Increases in BPINTRS can increase brine flow from the Castile to the repository; larger values of WMICDFLG indicate the potential to generate additional gas as a consequence of the additional brine flowing into the

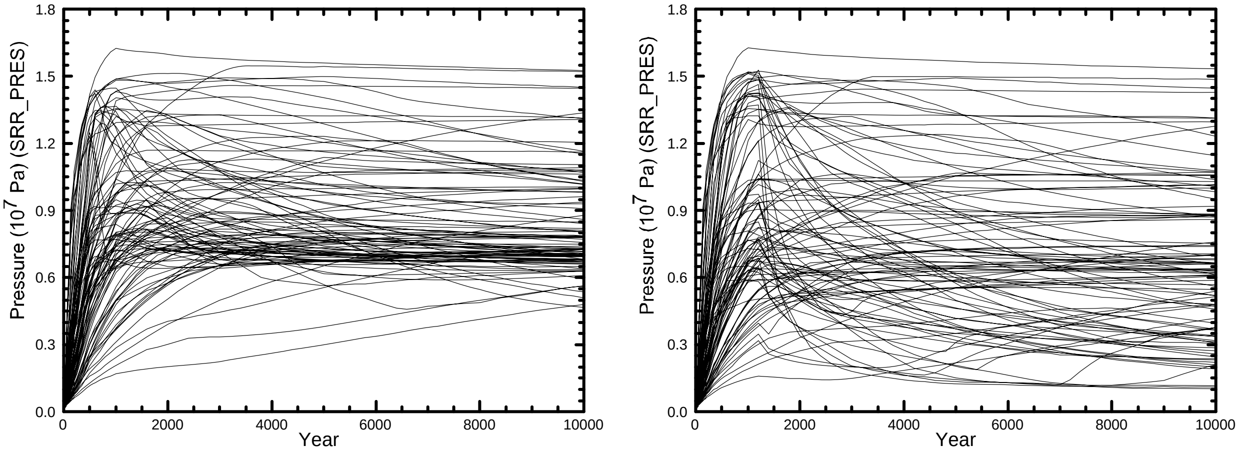

a) Scenario S2 - South Rest of Repository

b) Scenario S5 - South Rest of Repository

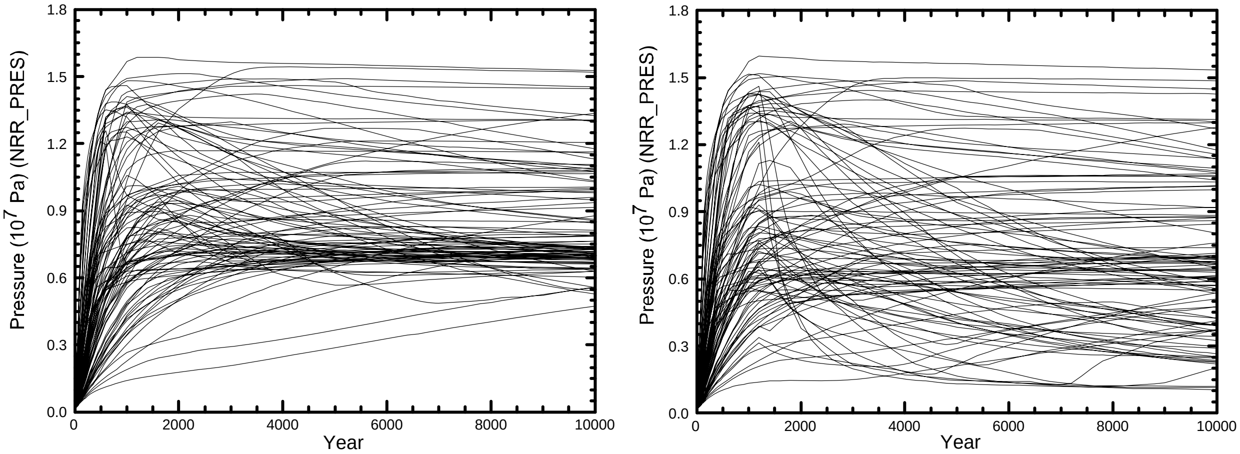

c) Scenario S2 - North Rest of Repository

d) Scenario S5 - North Rest of Repositoiry

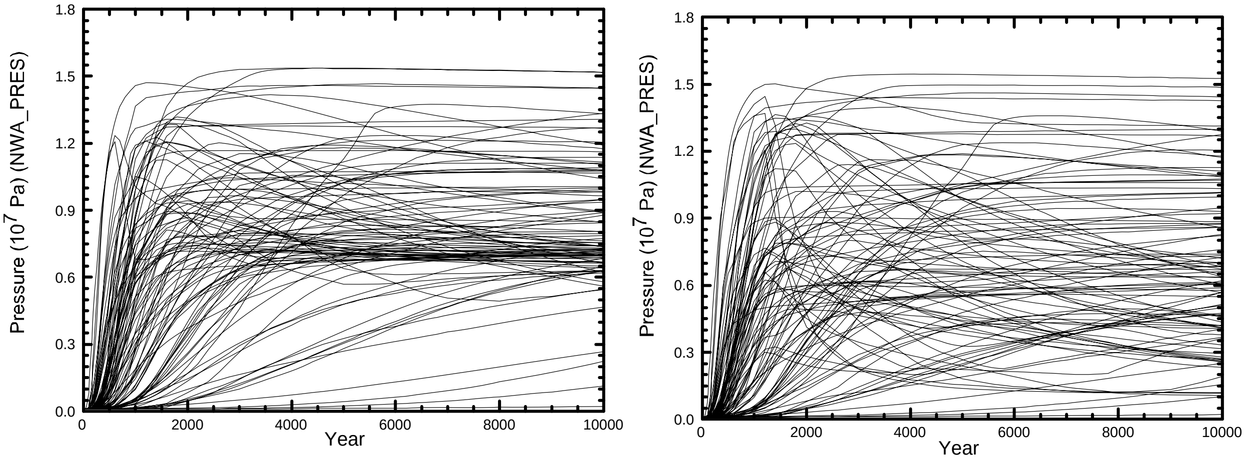

e) Scenario S2 - Non-Waste Areas

f) Scenario S5 - Non-Waste Areas

Figure PA-50. Pressure in Various Regions, Replicate R1, Scenarios S2 And S5.

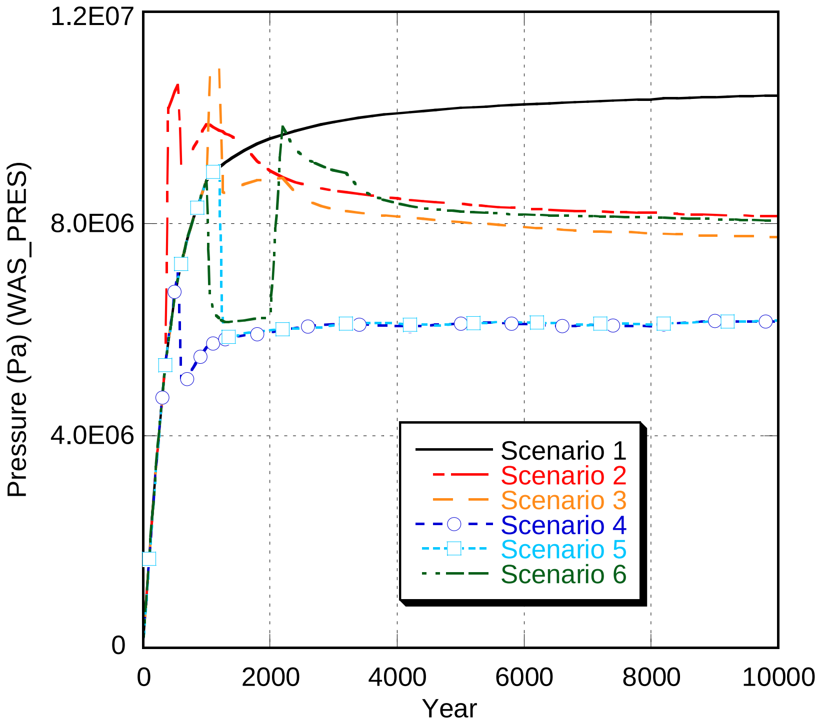

Figure PA-51. Mean Pressure in the Waste Panel for All Scenarios, Replicate R1

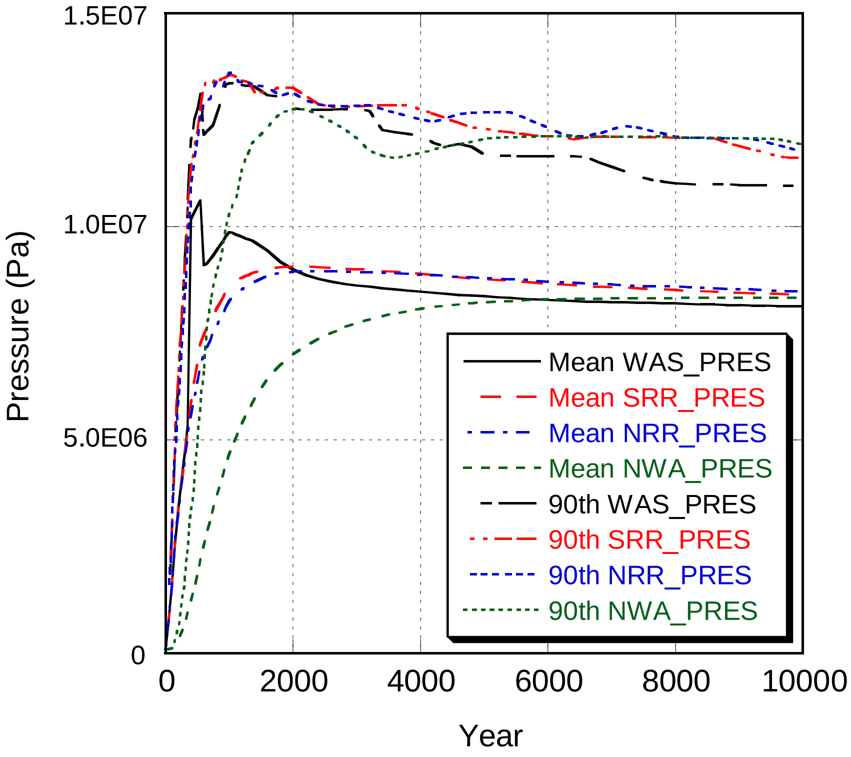

Figure PA-52. Mean And 90th Percentile Values For Pressure In The Excavated Regions Of The Repository, Replicate R1, Scenario S2.

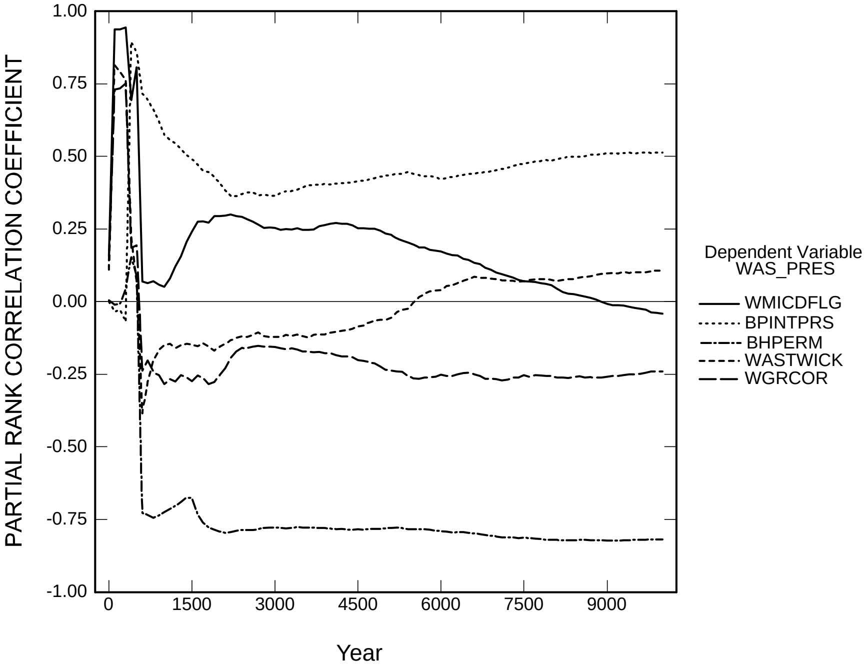

Figure PA-53. Primary Correlations For Pressure In The Waste Panel With Uncertain Parameters, Replicate R1, Scenario S2.

repository. Figure PA-54 shows the regression analysis results for an E2 intrusion at 1,000 years (Scenario S5). As in the analysis of Scenario S2, before the intrusion, the uncertainty in the indicator for microbial gas generation (WMICDFLG) is most important; after the borehole plugs fail, uncertainty in the permeability of borehole fill (BHPERM) is most important. Regression analyses for an E1 intrusion at 1,000 years and for an E2 intrusion at 350 years lead to similar conclusions (Stein and Zelinski, 2003b).

Figure PA-55 compares statistics for pressure in the waste panel for scenario S2 among the three replicates, and show that the three replicates produced statistically similar results.

PA-8.3.2 Brine Saturation

Brine saturation tends to increase after a drilling intrusion. Figure PA-56 shows brine saturation in the waste panel (WAS_SATB for area Waste Panel in Figure PA-8) for replicate R1 of each BRAGFLO scenario. In many vectors, the intruded panel becomes saturated after an E1 intrusion (Scenarios S2, S3, and S6). Depending on the borehole permeability and pressures in the repository and in the brine reservoir, quantities of brine can flow from the reservoir into the intruded panel, possibly filling the panel. In contrast, after an E2 intrusion (Scenarios S4 and S5) saturation increases for only a few vectors. An E2 intrusion tends to reduce the pressure in the intruded panel by releasing fluids (mainly gas) up the borehole (Figure PA-49). The reduced pressure in the waste permits an increase in brine inflow from the DRZ and the MBs. In addition, in some vectors brine can flow down the borehole from the Culebra into the intruded panel, depending on the permeability of the borehole.

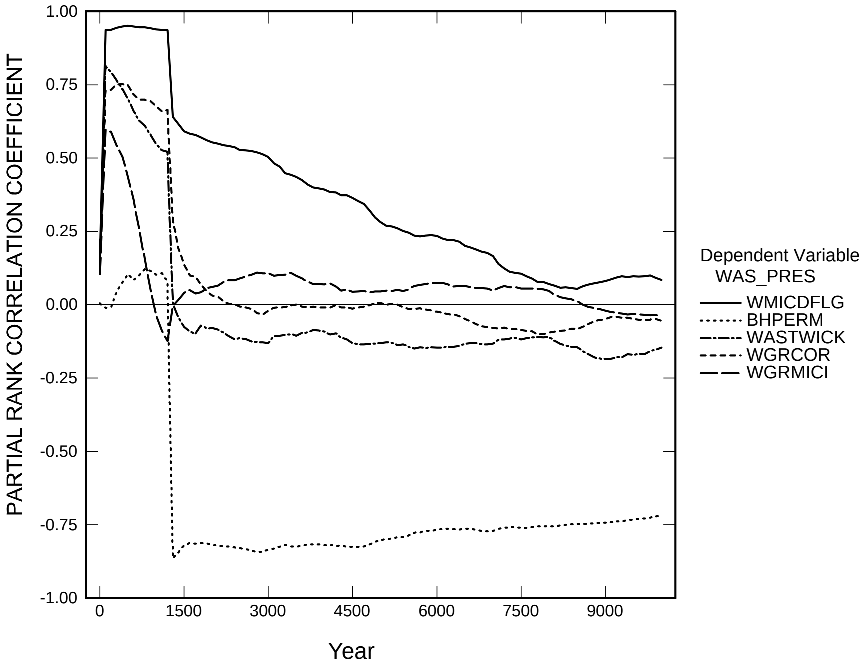

Figure PA-54. Primary Correlations For Pressure In The Waste Panel With Uncertain Parameters, Replicate R1, Scenario S5.

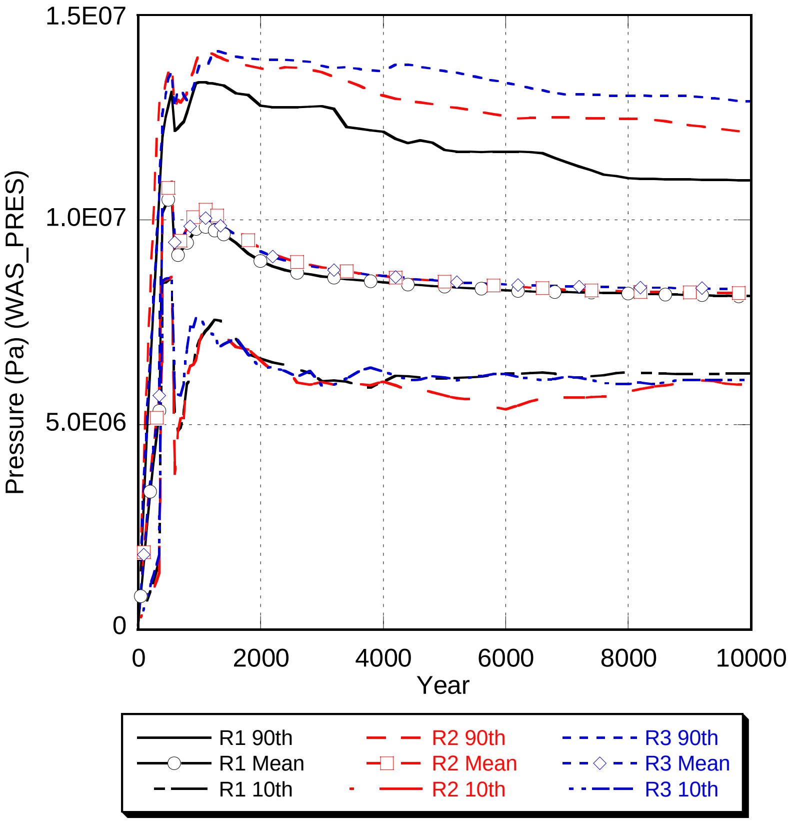

Figure PA-55. Statistics For Pressure in the Waste Panel For All Replicates, Scenario S2.

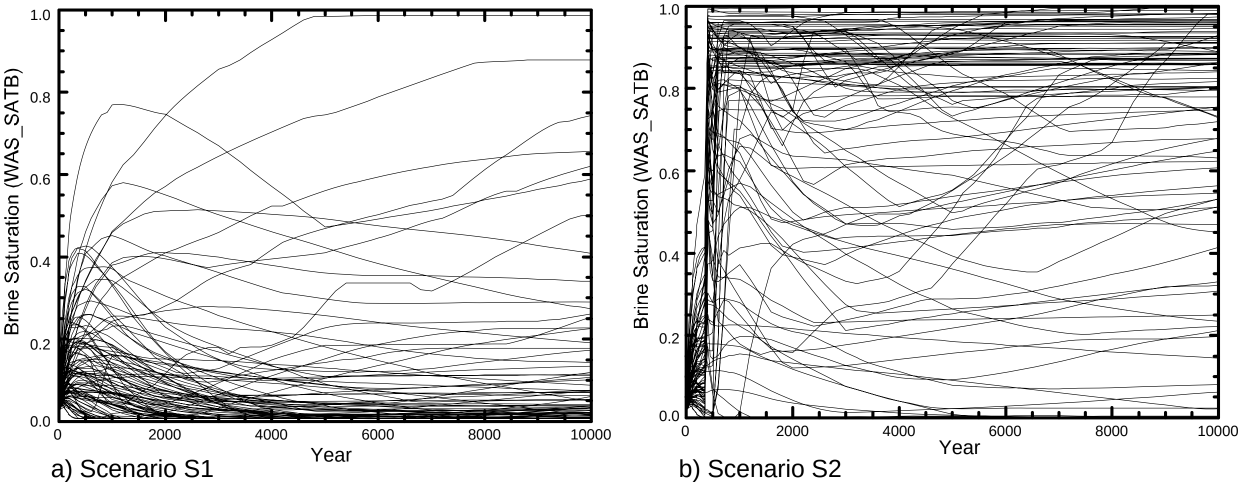

a) Scenario S1 b) Scenario S2

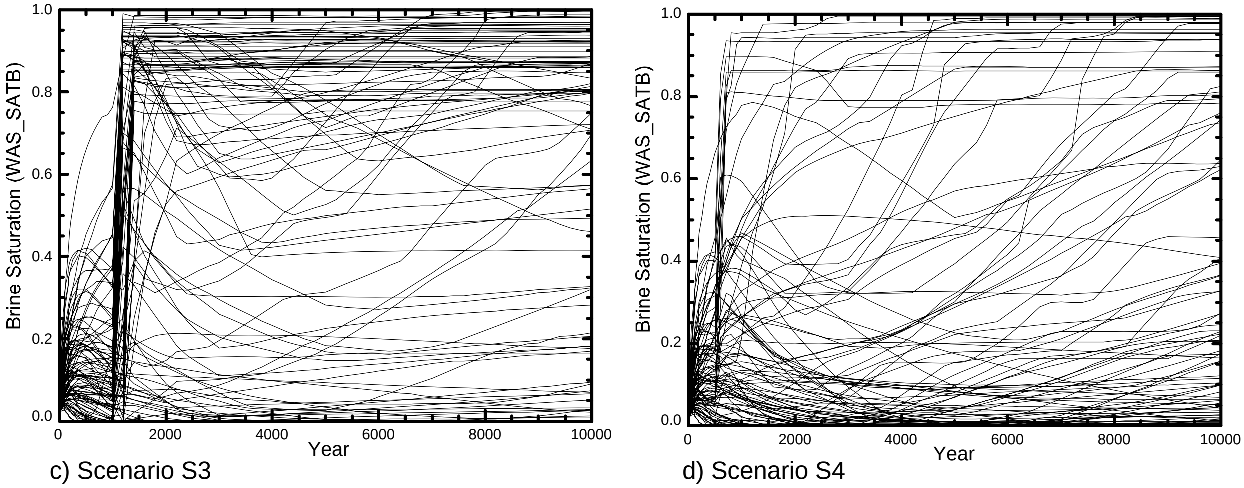

c) Scenario S3 d) Scenario S4

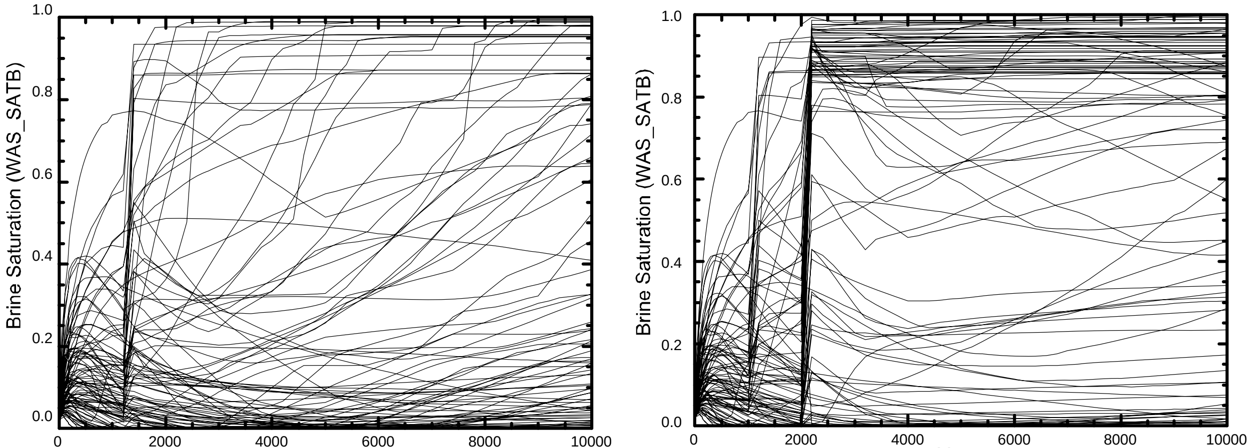

e) Scenario S5 f) Scenario S6

Figure PA-56. Brine Saturation in the Waste Panel for All Scenarios, Replicate R1.

Figure PA-57 compares the mean values for brine saturation in the waste panel (WAS_SATB) for each scenario. Brine saturation is highest after E1 intrusions (Scenarios S2, S3, and S6), but also increases somewhat after an E2 intrusion (Scenarios S4 and S5). However, saturation in other excavated areas is not generally increased. Figure PA-58 shows brine saturation in the rest of repository (SRR_SATB for area South RoR and NRR_SATB for area North RoR in Figure PA-8) and in the nonwaste areas (NWA_SATB averaged over areas Ops and Exp in Figure PA-8) for the Scenarios S2 and S5. Comparison of Figure PA-57 with Figure PA-39, which shows brine saturation in undisturbed conditions, reveals that brine saturation in unintruded regions is generally unaffected by the intrusion. The panel closures separating the intruded panel from these regions effectively prevent brine flow between excavated areas. In addition, the intruded panel is modeled as one of the panels at the southern end of the repository, and hence is down the stratigraphic dip from the other excavated regions.

Figure PA-58 also shows that brine saturation in the nonwaste areas (areas Ops and Exp in Figure PA-8) is somewhat higher than in the rest of repository areas (areas South RoR and North RoR in Figure PA-8). Brine saturation in the nonwaste areas is higher because of the lack of brine consuming corrosion processes in these areas and their position adjacent to the northern marker beds, which supply brine to the excavated area. The rest of repository areas have the lowest saturations because they are not connected to the brine reservoir, corrosion consumes brine in these regions, and their internal position in the two-dimensional grid (Figure PA-8) prevents direct flow of brine from the MBs.

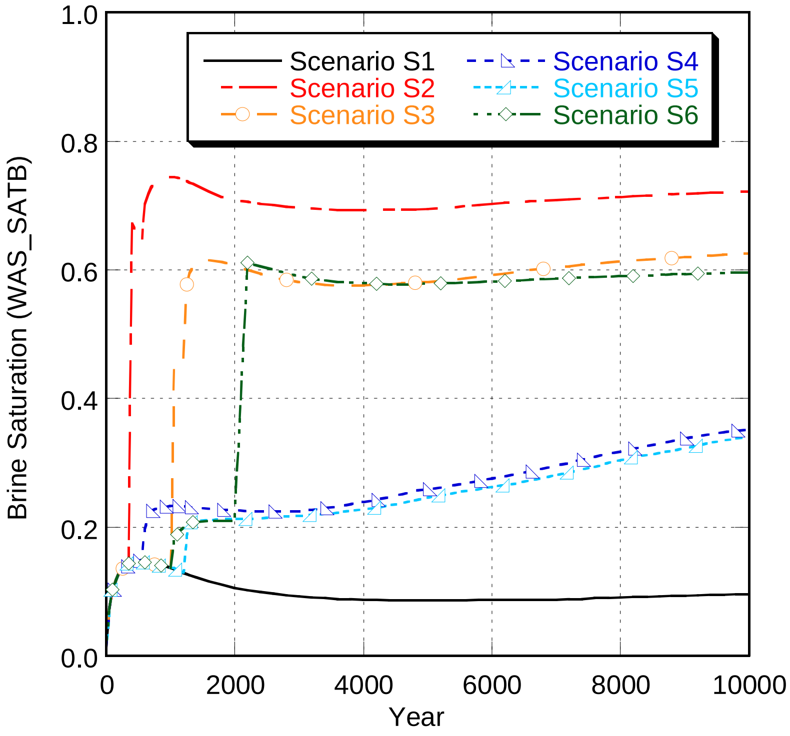

Figure PA-57. Mean Values for Brine Saturation in the Waste Panel for All Scenarios, Replicate R1.

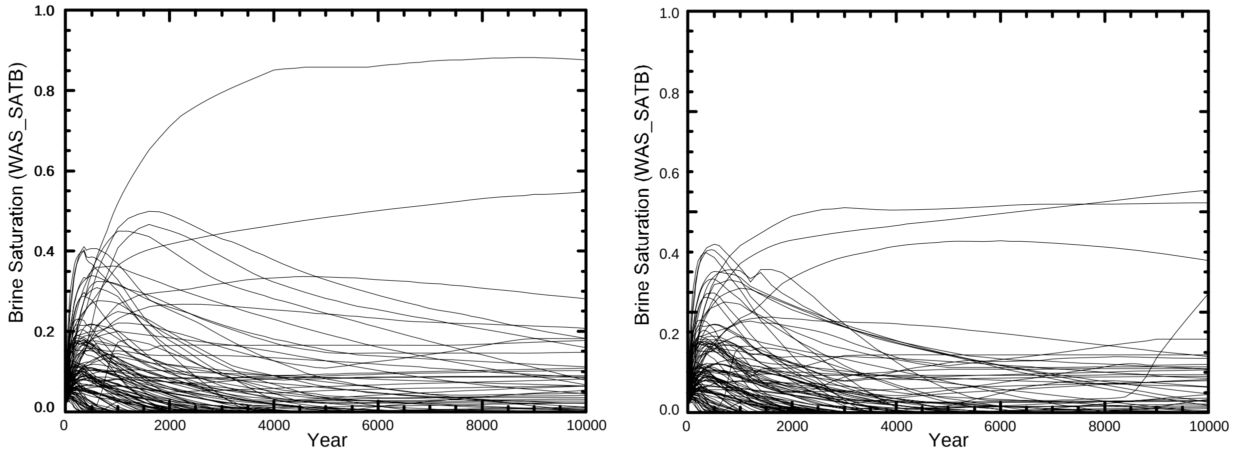

a) Scenario S2 - South Rest of Repository

b) Scenario S5 - South Rest of Repository

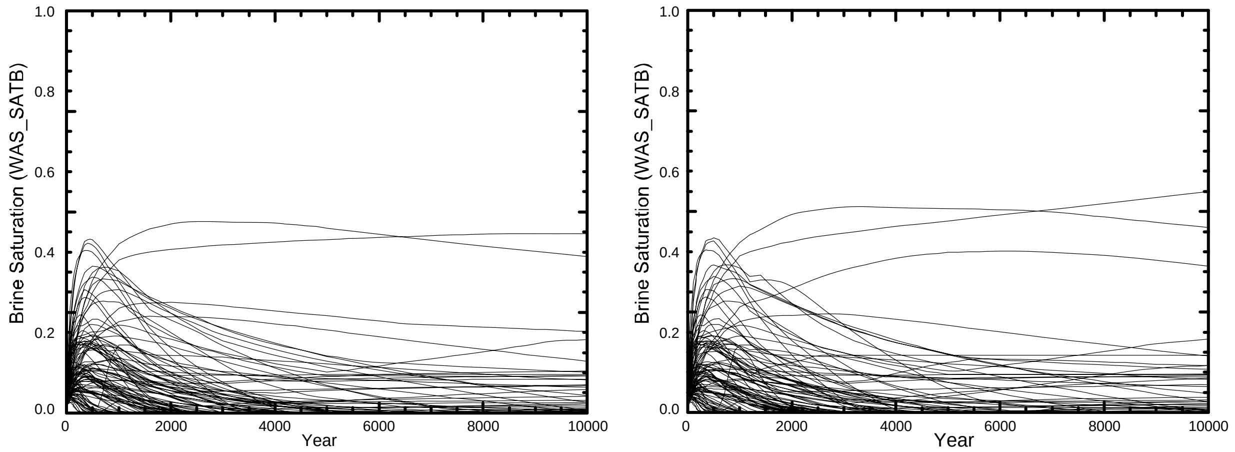

c) Scenario S2 - North Rest of Repository

d) Scenario S5 - North Rest of Repository

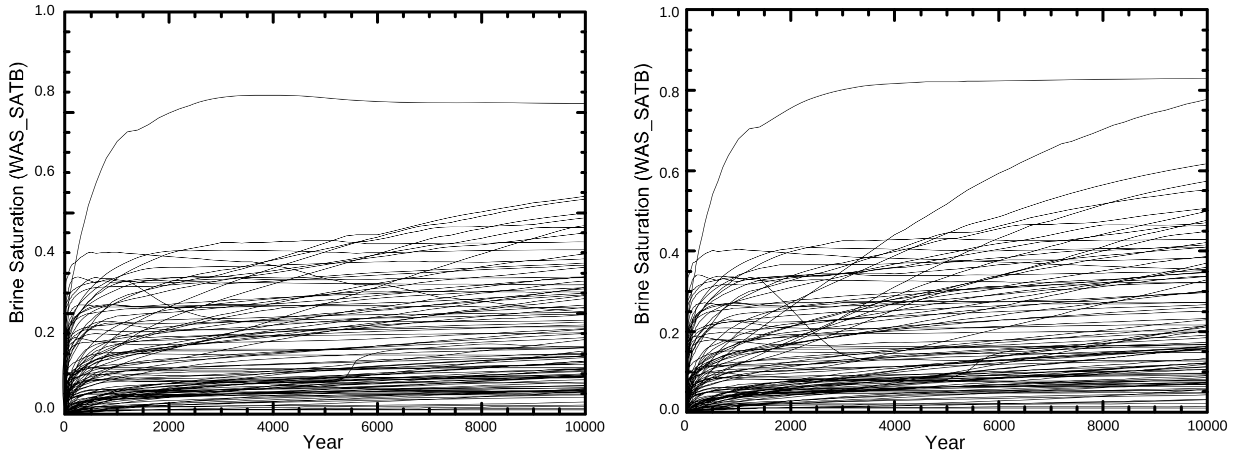

e) Scenario S2 - Non-Waste Areas

f) Scenario S5 - Non-Waste Areas

Figure PA-58. Brine Saturation in Excavated Areas, Replicate R1, Scenarios S2 and S5.

Figure PA-59 compares mean and 90th percentile brine saturations among the excavated areas for an E1 intrusion at 350 years (Scenario S2). Brine saturations in the waste panel are the highest due to the connection with the brine reservoir. Comparison of Figure PA-59 to Figure PA-40, which shows mean pressure for undisturbed conditions, indicates that brine saturation outside of the waste panel is very similar to the undisturbed Scenario S1.

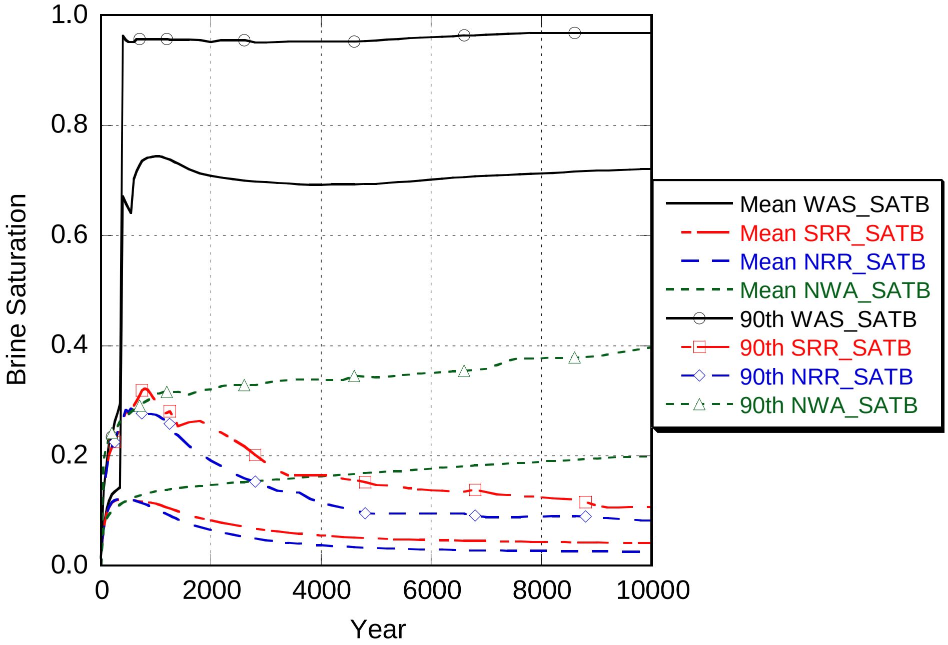

Figure PA-59. Statistics For Brine Saturation in Excavated Areas, Replicate R1, Scenario S2.

Figure PA-60 shows the results of the regression analysis between brine saturation in the waste panel (WAS_SATB) for the S2 scenario and the uncertain parameters in the analysis (Section PA-5.2). For most of the time after the intrusion, uncertainty in borehole permeability (BHPERM) is primarily responsible for the uncertainty in brine saturation, with increases in borehole permeability leading to increases in brine saturation. The indicator for microbial degradation (WMICDFLG), which has a negative correlation with the brine saturation in the waste panel, also has a significant influence throughout the 10,000-year modeling period. Because the S2 scenario models an intrusion at 350 years, much of the CPR material is still present in the waste. Additional brine entering the waste panel would saturate more of the waste and accelerate the degradation of the CPR material, increasing gas pressure, and in turn retarding brine inflow. Thus, the negative correlation between the indicator for microbial degradation and brine saturation is quite strong immediately after the intrusion, but decreases in importance at later times. Uncertainty in the other parameters in Figure PA-60 (HALPOR, DRZPRM, and WGRCOR, defined in Table PA-17), have relatively little influence on brine saturation. Regression analysis of waste saturation for the S3 scenario yields a similar result (Stein and Zelinski 2003b).

Figure PA-61 shows the results of the regression analysis between brine saturation in the waste panel (WAS_SATB) for the S5 scenario and the uncertain parameters in the analysis (Section PA-5.2). As with the S2 scenario, borehole permeability is the primary factor

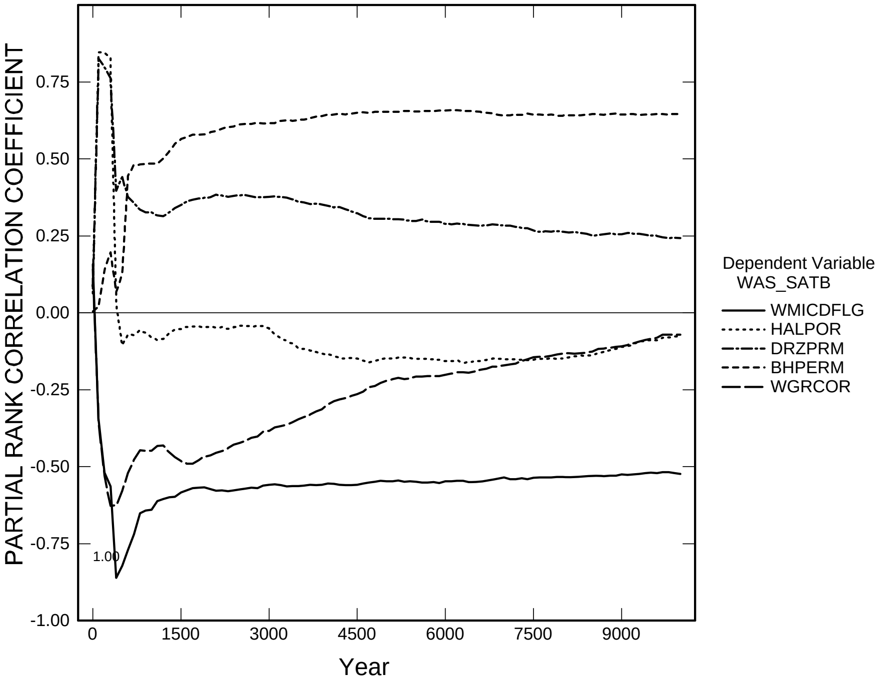

Figure PA-60. Primary Correlations for Brine Saturation in the Waste Panel with Uncertain Parameters, Replicate R1, Scenario S2.

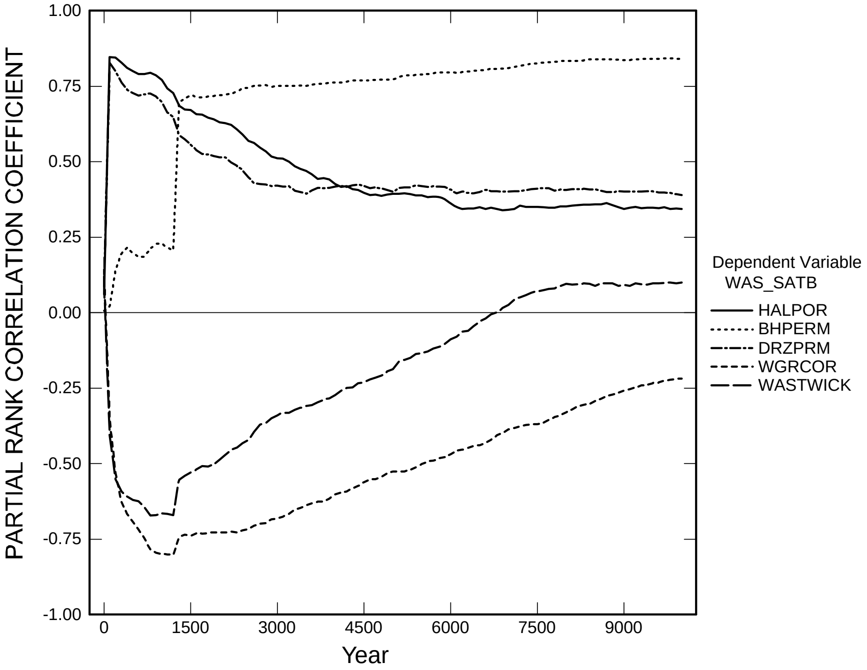

Figure PA-61. Primary Correlations of Brine Saturation in the Waste Panel with Uncertain Parameters, Replicate R1, Scenario S5.

influencing brine saturation in the waste panel (WAS_SATB) after the borehole plugs fail. Regression analysis of waste saturation for the S4 scenario yields a similar result (Stein and Zelinski 2003b).

Figure PA-62 compares statistics for brine saturation for the three replicates of the S2 scenario, and shows that the replicates produced similar results.

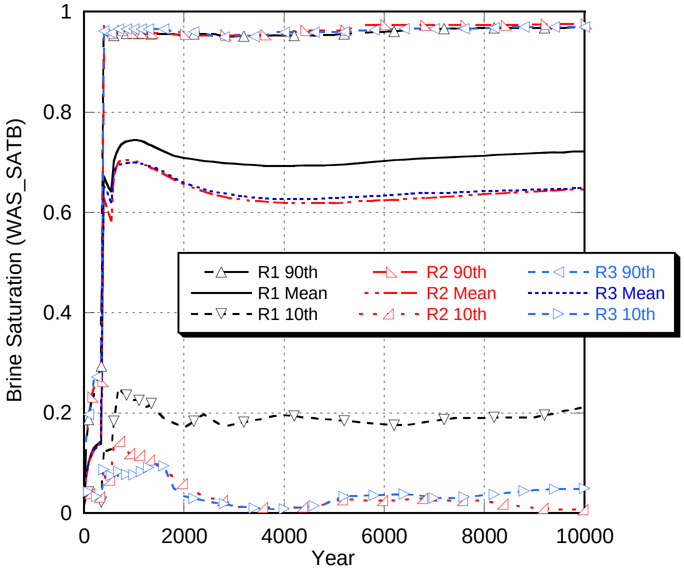

Figure PA-62. Statistics for Brine Saturation in the Waste Panel For All Replicates, Scenario S2.

PA-8.3.3 Brine Flow Out of the Repository

This section describes the flow of brine up a borehole to the Culebra. Brine flow to the Culebra is an important input to the calculations of long-term releases in the Culebra, described in Section PA-8.4.3. Direct brine flow up the borehole to the surface at the time of drilling is modeled separately in the DBR calculations, presented in Section PA-8.5.3.

Figure PA-63 shows cumulative brine flow out of the repository (BRNREPOC) and brine flow up a borehole to the Culebra (BRNBHRCC) for the five BRAGFLO scenarios that model drilling intrusions. The largest volumes of brine flow from the repository after E1 intrusions (Scenarios S2, S3, and S6), which is consistent with the higher brine saturation in the intruded panel (Figures PA-56b, PA-56c, and PA-56f, respectively). The similarity between the plots of BRNREPOC and BRNBHRCC indicate that nearly all the brine leaving the repository after an intrusion flows up the borehole to the Culebra. The few vectors that show brine flow out of the repository before the drilling intrusion generally have either very high pressures or very high DRZ permeability, allowing brine to flow from the repository into the MBs before the intrusion occurs. At 1,200 years after an E1 intrusion, the permeability of the borehole between the repository and the Castile is reduced by an order of magnitude because of creep closure (see Table PA-5), reducing brine flowing into the repository and causing a corresponding decrease in brine out of the repository.

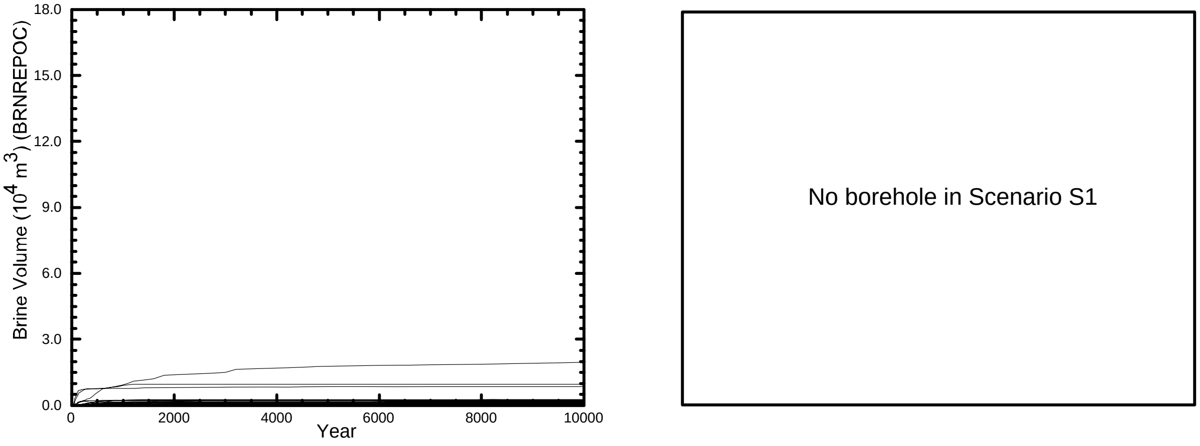

a: Scenario S1 - BRNREPOC

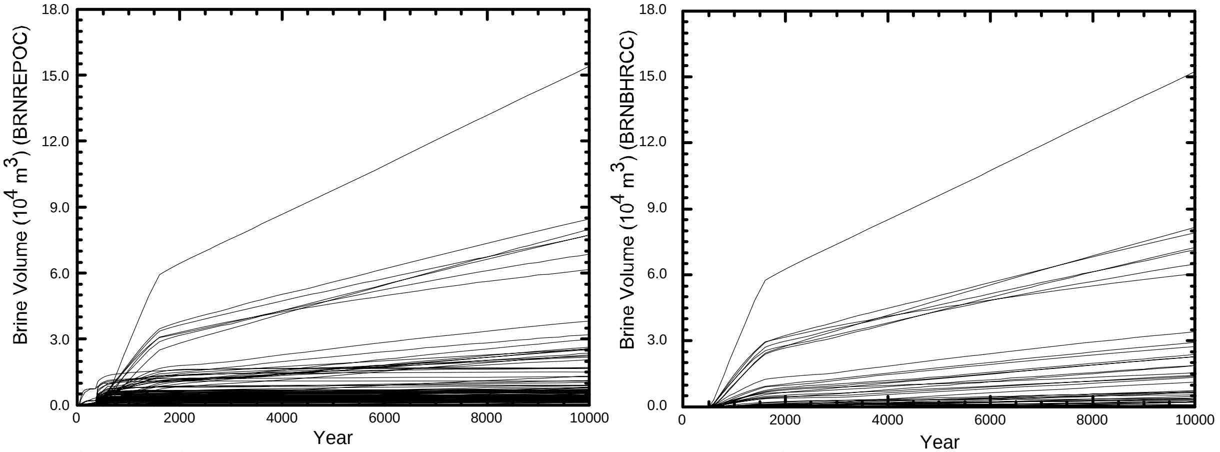

b: Scenario S2 - BRNREPOC c: Scenario S2 - BRNBHRCC

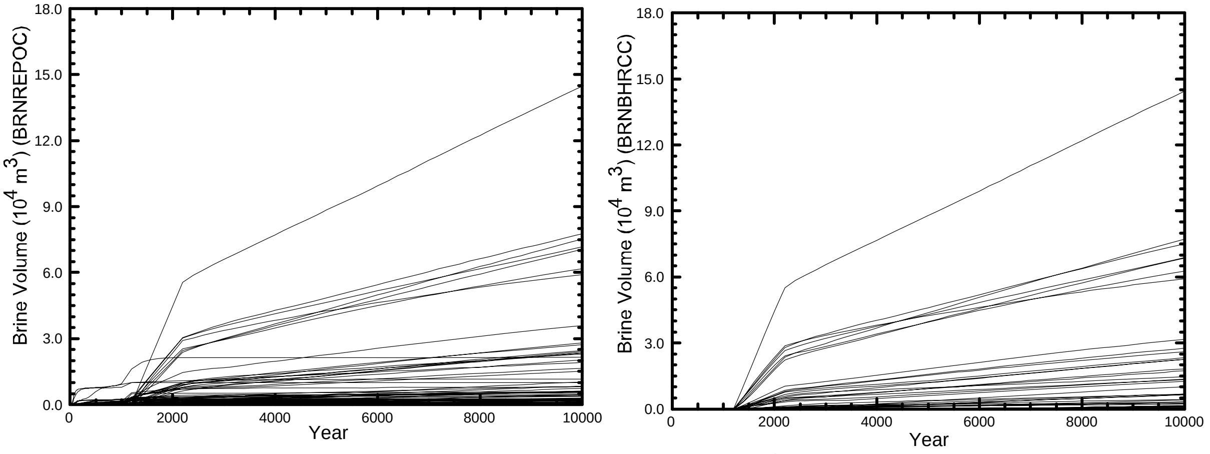

d: Scenario S3 - BRNREPOC e: Scenario S3 - BRNBHRCC

Figure PA-63. Total Cumulative Brine Outflow and Brine Flow Up the Borehole in All Scenarios, Replicate R1.

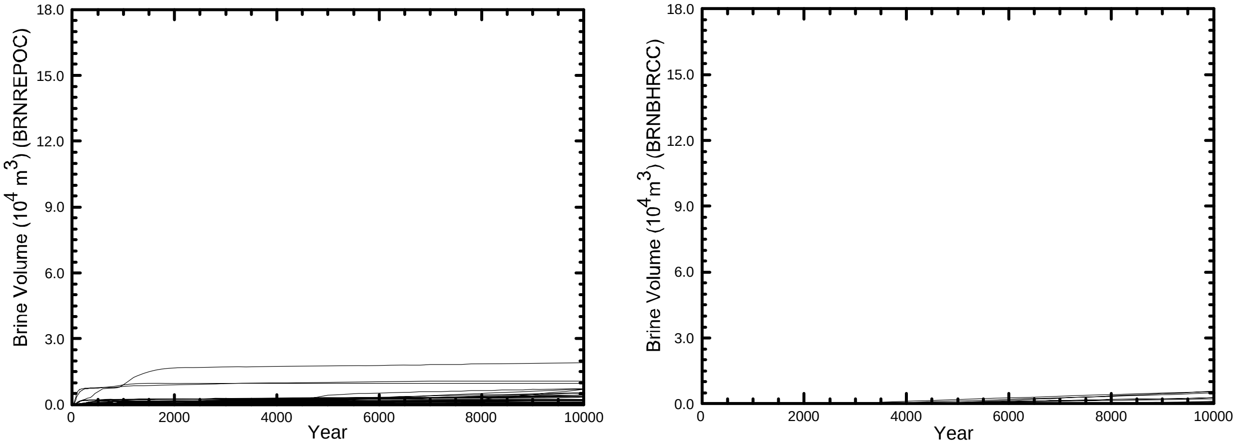

f) Scenario S4 - BRNREPOC

g) Scenario S4 - BRNBHRCC

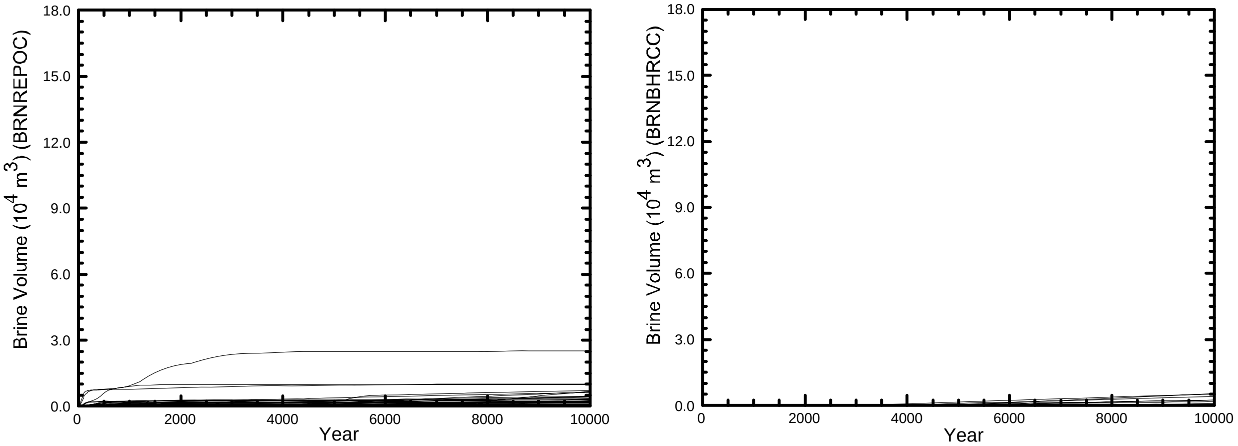

h) Scenario S5 - BRNREPOC

i) Scenario S5 - BRNBHRCC

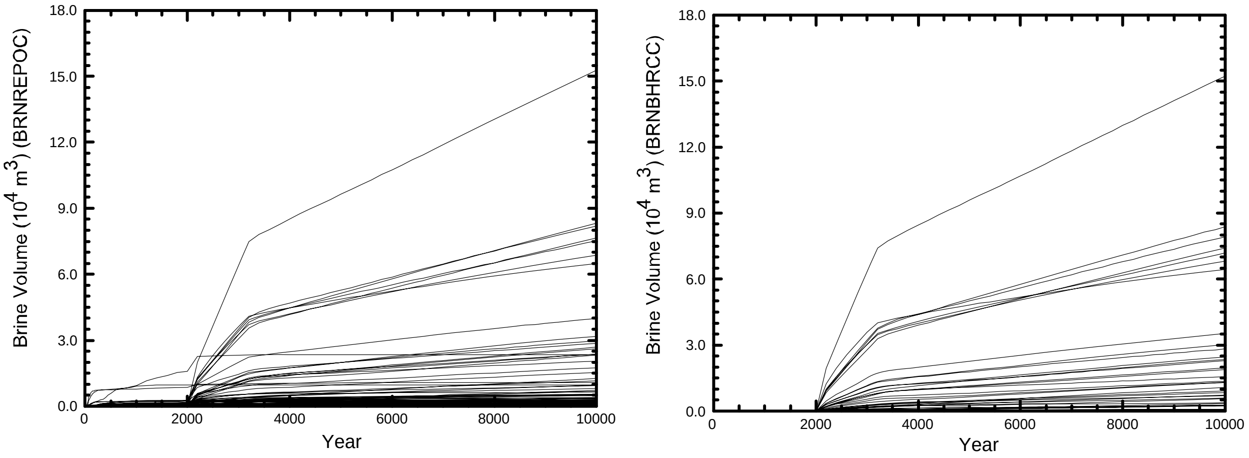

j) Scenario S6 - BRNREPOC

k) Scenario S6 - BRNBHRCC

Figure PA-63(cont). Total Cumulative Brine Outflow and Brine Flow Up the Borehole in All Scenarios, Replicate R1

Figure PA-64 shows the results of regression analysis between the brine flow up the borehole to the Culebra (BRNBHRCC) and the uncertain parameters in the analysis (Section PA-5.2). Before the intrusion, non-zero values of BRNBHRCC result from numerical error in the calculation; these values do not exceed 10^{-18} m^3 and thus the correlation to uncertainty in shaft permeability (SHUPRM) is not meaningful. Immediately after the intrusion, uncertainty in the permeability of the undegraded borehole plugs (PLGPRM) contributes most of the uncertainty in brine flow volumes. After the borehole plugs degrade (200 years after the intrusion), uncertainty in the permeability of the borehole (BHPERM) almost exclusively determines the uncertainty in brine volumes reaching the Culebra. The indicator for microbial degradation (WMICDFLG) is weakly correlated with the small amount of uncertainty that is not explained by the uncertainty in borehole permeability.

Figure PA-65 compares statistics for brine flow out of the repository for the three replicates of Scenario S2. The figure shows that brine flow results are very similar among replicates.

PA-8.4 Radionuclide Transport

In the disturbed scenarios, radionuclide transport in the Salado is calculated by the code NUTS (see Section PA-4.3). Transport from the Salado to the Culebra is calculated by NUTS and PANEL (see Section PA-4.3 and Section PA-4.4). Transport within the Culebra is calculated by SECOTP2D (see Section PA-4.9). For all transport calculations, mobilized concentrations of radionuclides in Salado and Castile brines are computed by the code PANEL (see Section PA-4.4).

This section summarizes the transport results for the disturbed scenarios. Detailed analysis of the NUTS results is presented in Lowry (2003). Garner (2003) provides analysis of the PANEL results; Kanney (2003) presents analysis of the SECOPT2D results.

PA-8.4.1 Radionuclide Source Term

The code PANEL calculates the source term for transport, which is the time-varying concentration of radioactivity mobilized in brine, either as dissolved isotopes or as isotopes sorbed to mobile colloids. Two different brines are considered: the interstitial brine present in the Salado Formation, which is magnesium rich; and the brine in the Castile Formation, which is sodium rich. Radionuclide solubility in the two brines can be considerably different. Before an E1 intrusion, performance assessment assumes that the brine in the repository is Salado brine. After an E1 intrusion, brine in the repository is assumed to be from the Castile.

Figure PA-66 and Figure PA-67 show the source term in Salado and Castile brines, respectively, as a function of time for all vectors in replicate R1. Concentrations are expressed as EPA units/m^3 to combine the radioactivity in different isotopes. Short-lived radionuclides, such as ^{238}Pu, decay rapidly in the first few years. After this initial decay, the source term is dominated by Am (Garner 2003); the concentration of Am is limited by its solubility until all the inventory of Am is in solution. After all Am is in solution, the total radionuclide concentration generally decreases as the Am decays, until the source term becomes dominated by Pu (Garner 2003). The horizontal lines in the figures indicate periods of time when the

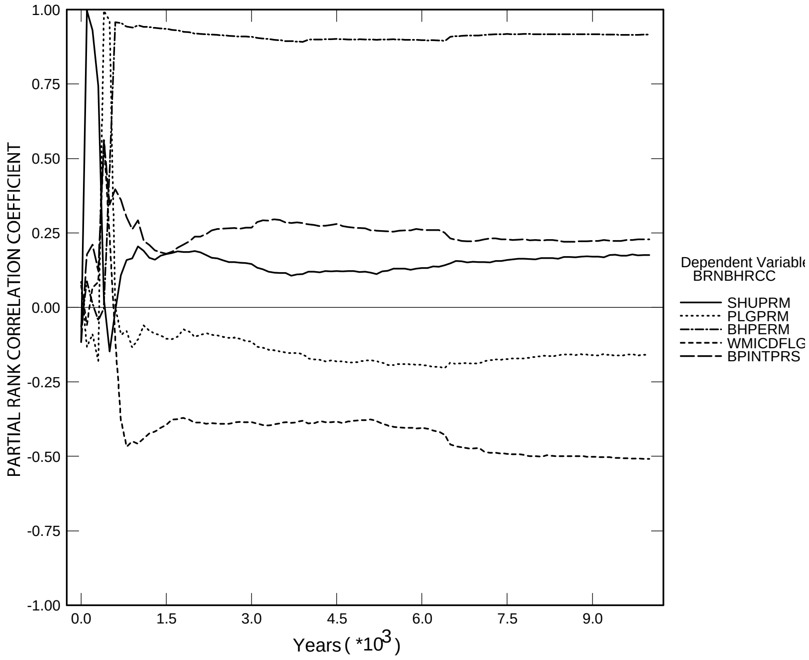

Figure PA-64. Primary Correlations for Cumulative Brine Flow Up the Borehole with Uncertain Parameters, Replicate R1, Scenario S2.

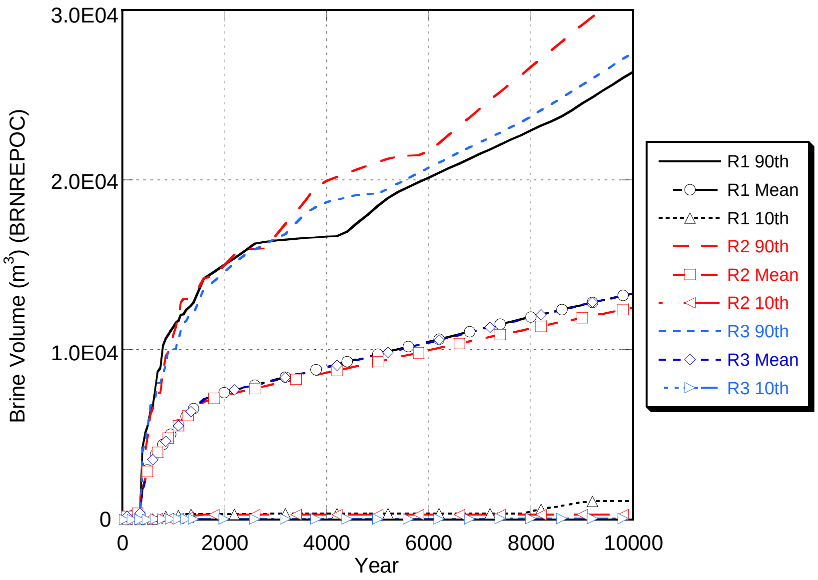

Figure PA-65. Statistics for Cumulative Brine Outflow in All Replicates, Scenario S2.

total radionuclide concentration is limited by the solubility of Am (before about 3,000 years) or Pu (after about 6,000 years). Thus, the uncertainty in total radionuclide concentration is determined by the uncertainty factors used in the calculation of solubilities for Am and Pu (see Table PA-9).

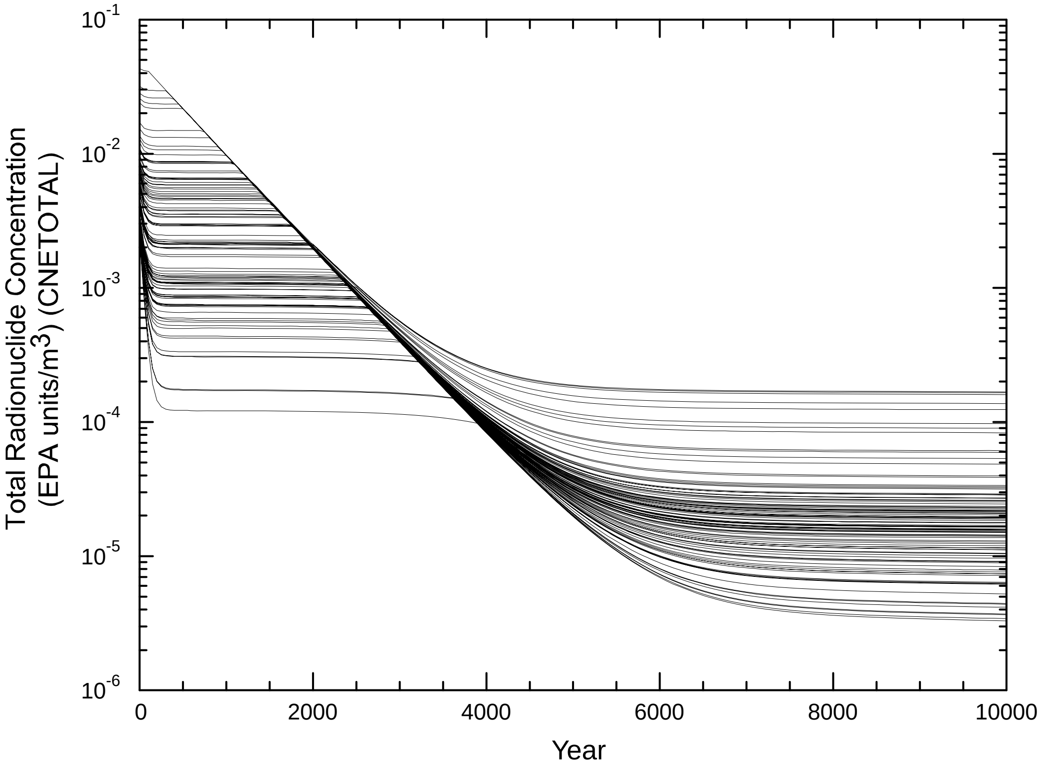

Figure PA-66. Total Mobilized Concentrations in Salado Brine.

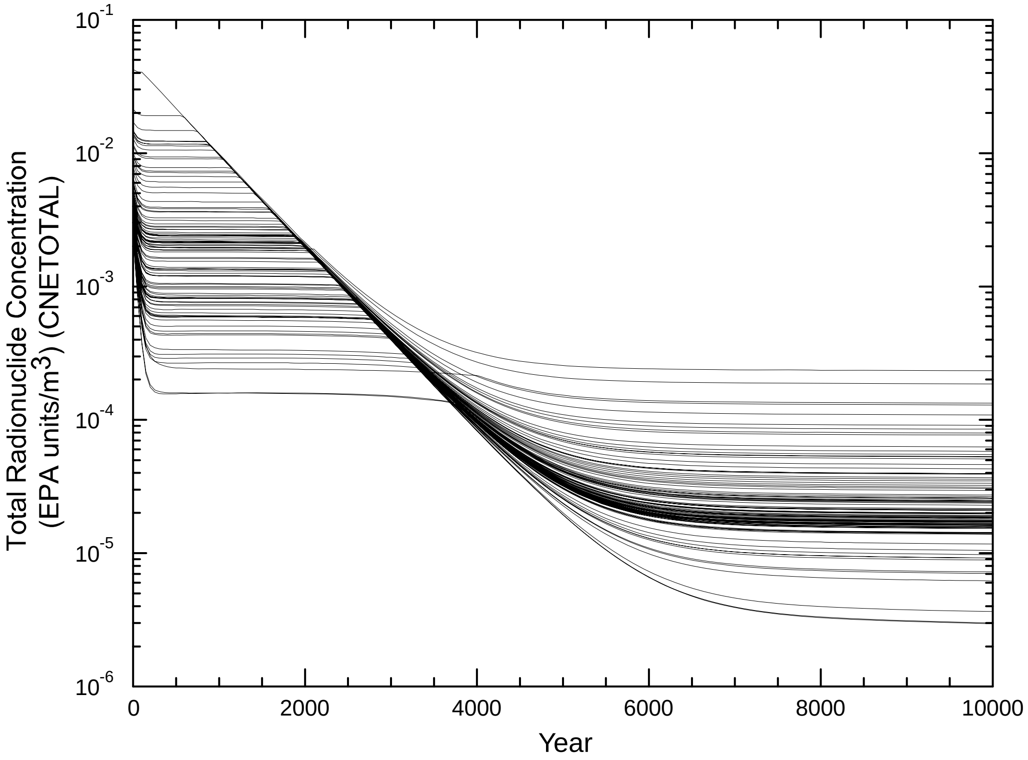

Figure PA-67. Total Mobilized Concentrations in Castile Brine.

PA-8.4.2 Transport through Marker Beds and Shaft

In the disturbed scenarios, none of the 300 realizations resulted in transport of radionuclides through the MBs and across the LWB (Lowry 2003). In addition, no realization showed transport of radionuclides through the shaft to the Culebra.

PA-8.4.3 Transport to the Culebra

In four of the disturbed scenarios (S2, S3, S4, and S5), transport to the Culebra is modeled with the code NUTS. In the multiple intrusion scenario (S6), the code PANEL is used to calculate transport to the Culebra. Figures PA-68 through PA-71 show cumulative radioactivity transported up the borehole to the Culebra. Transport to the Culebra is larger and occurs for more vectors in the S2 and S3 scenarios (E1 intrusions) than in the S4 or S5 scenarios (E2 intrusions). For most vectors that show significant transport, most of the transport occurs over a relatively short period of time, immediately after the borehole plugs fail.

Figure PA-72 shows total EPA units transported to the Culebra via the borehole in the S6 scenario. Almost no radionuclides are released after the E2 intrusion at 800 years; most transport occurs immediately following the E1 intrusion at 2,000 years.

Figure PA-73 and Figure PA-74 compare mean values among all three replicates for cumulative normalized releases up the borehole to the Culebra for scenarios S3 and S6, respectively. These figures show that the results from each replicate are very similar.

Sensitivity analysis of total radionuclides transported to the Culebra identified a strong linear relationship between the uncertainty in the total release to the Culebra and the uncertainty in the brine flow up the borehole (calculated by BRAGFLO; see Section PA-8.3.3). Figure PA-75 shows the relationship between total releases to the Culebra (EPATBHRC, calculated by NUTS; see Section PA-4.3) and brine flow up the borehole (BRNBHRCC, calculated by BRAGFLO; see Section PA-8.3.3) at 10,000 years after an E1 intrusion at 1,000 years (Scenario S3). Figure PA-76 shows the relationship between total releases to the Culebra (LDETOTAL, calculated by PANEL; see Section PA-4.4) and brine flow up the borehole (BRNBHRCC, calculated by BRAGFLO; see Section PA-8.3.3) at 10,000 years after the combination of an E2 intrusion at 800 years followed by an E1 intrusion in the same panel at 2,000 years (Scenario S6).

Sensitivity analysis (Section PA-8.3.3) identified borehole permeability (BHPERM) as the most important parameter contributing to the uncertainty in flow up the borehole (BRNBHRCC). Separate stepwise regression analyses (Lowry 2003; Garner 2003) confirmed the correlation between uncertainty in borehole permeability and releases to the Culebra. These analyses also identified the initial pressure in the brine pocket (BPINTPRS), indicator for microbial action (WMICDFLG), and steel corrosion rate (WGRCOR) as contributing to uncertainty in releases to the Culebra although the importance of these parameters is much less than that of borehole permeability.

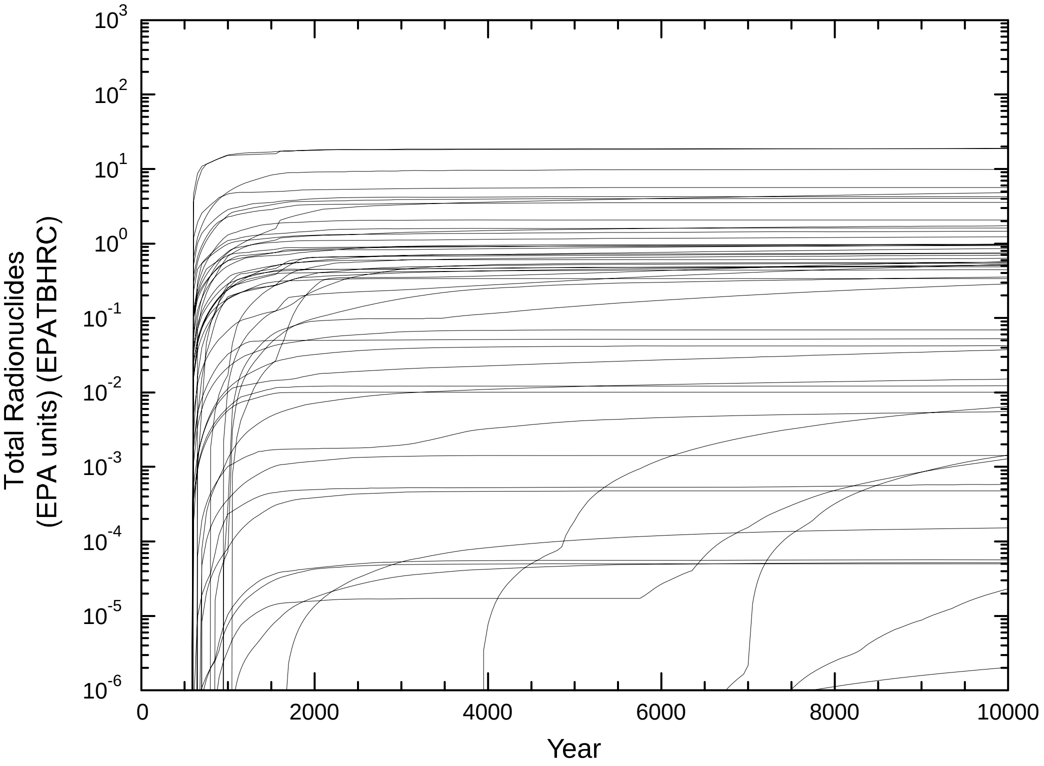

Figure PA-68. Cumulative Normalized Release Up the Borehole, Replicate R1, Scenario S2.

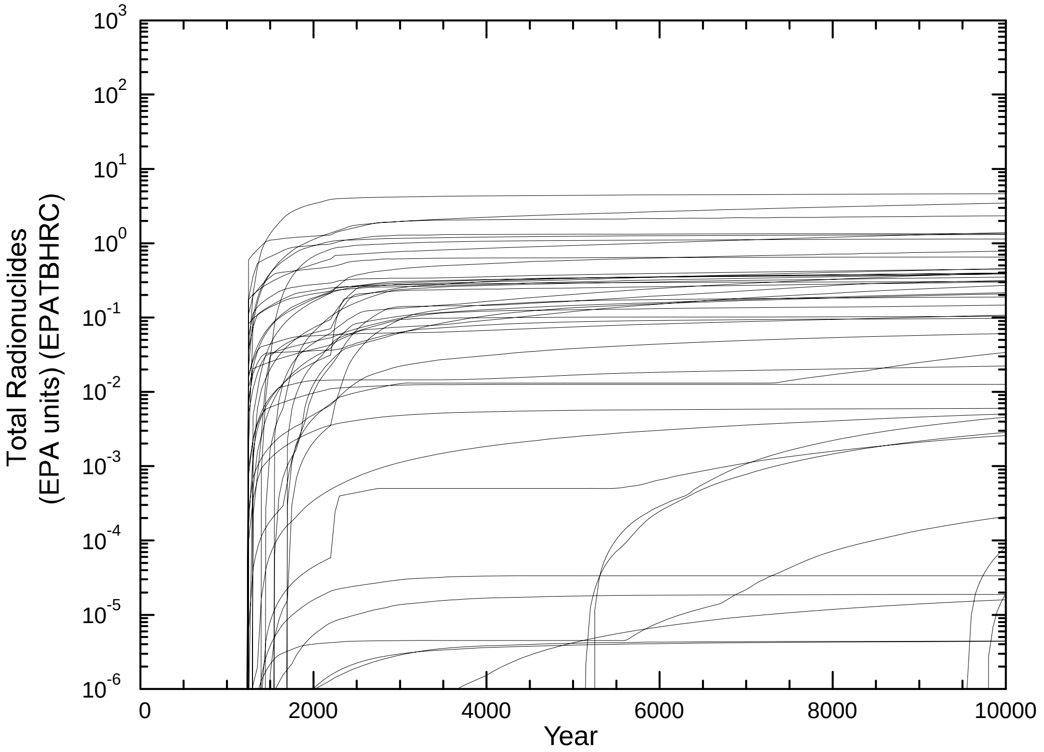

Figure PA-69. Cumulative Normalized Release Up the Borehole, Replicate R1, Scenario S3.

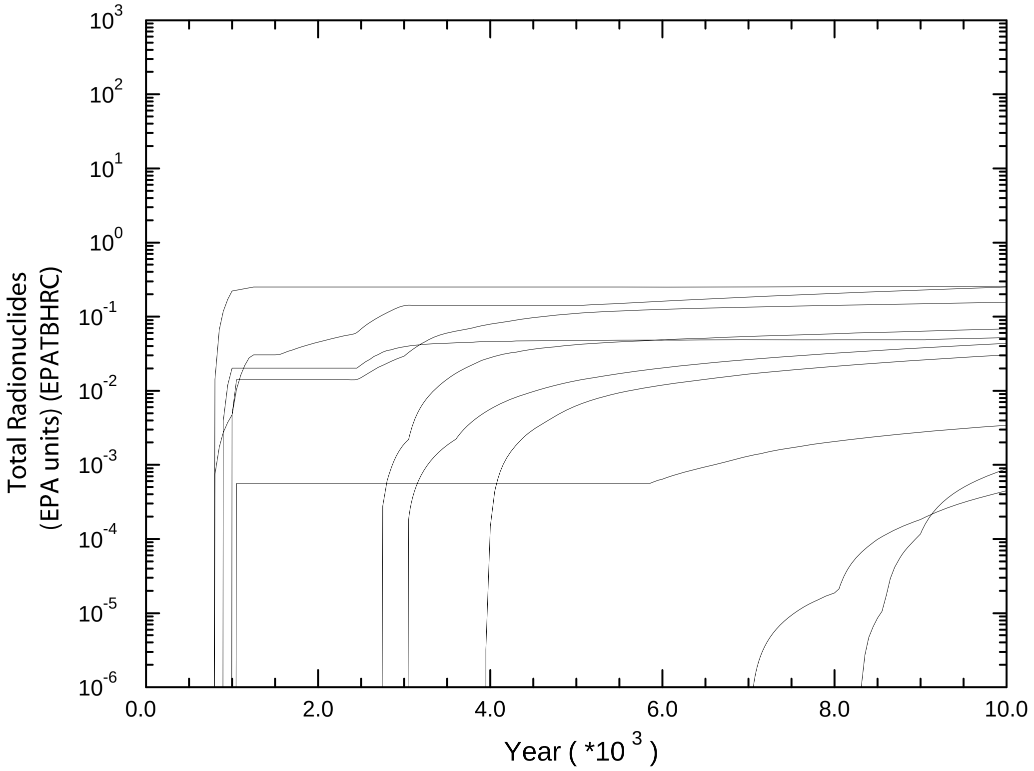

Figure PA-70. Cumulative Normalized Release Up the Borehole, Replicate R1, Scenario S4.

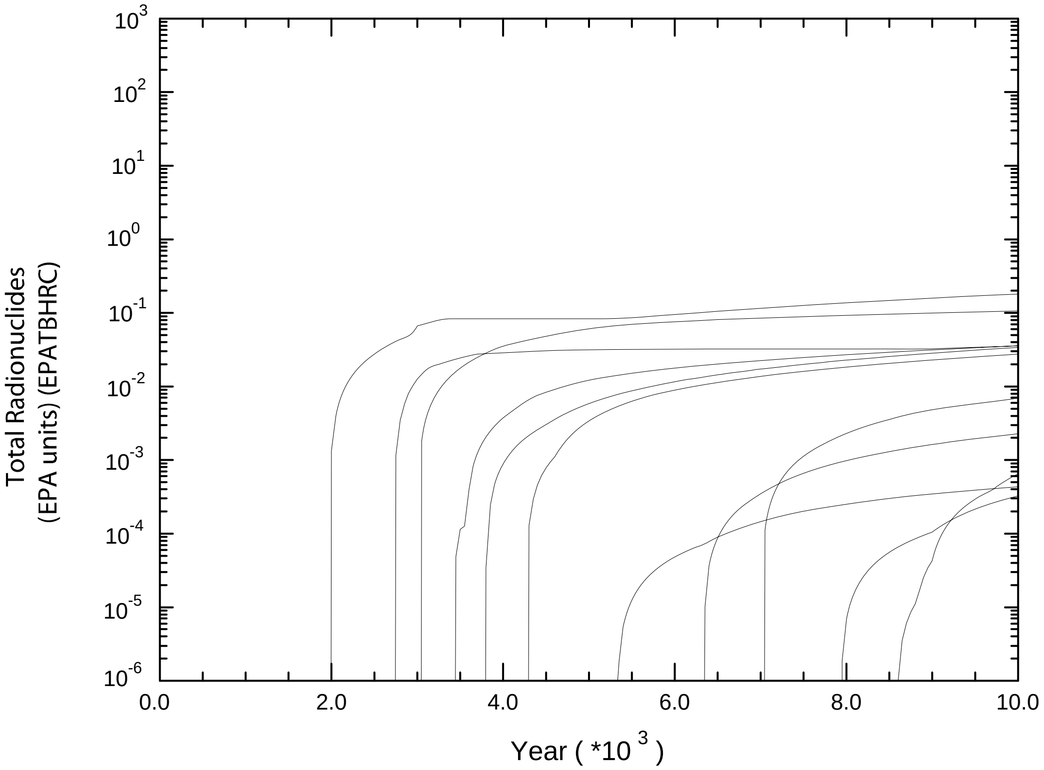

Figure PA-71. Cumulative Normalized Release Up the Borehole, Replicate R1, Scenario S5.

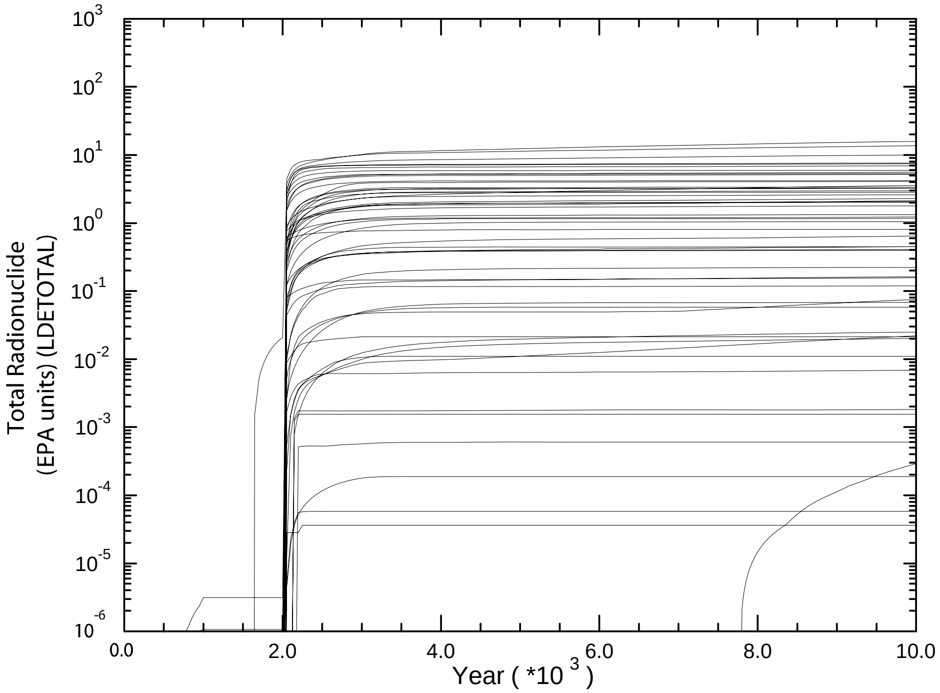

Figure PA-72. Cumulative Normalized Release Up the Borehole, Replicate R1, Scenario S6.

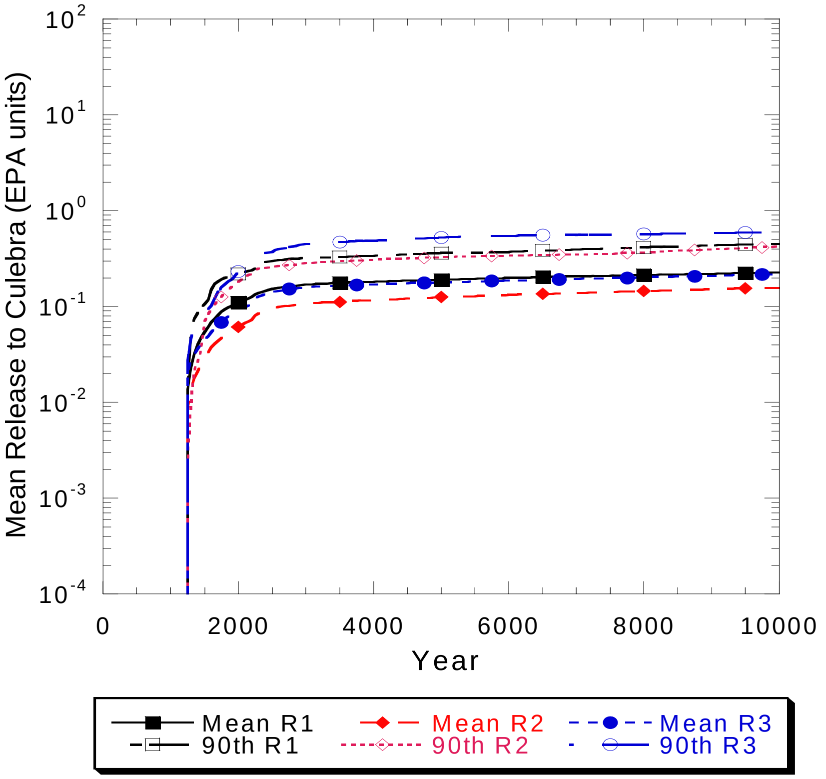

Figure PA-73. Mean Values for Cumulative Normalized Release Up the Borehole for All Replicates, Scenario S3.

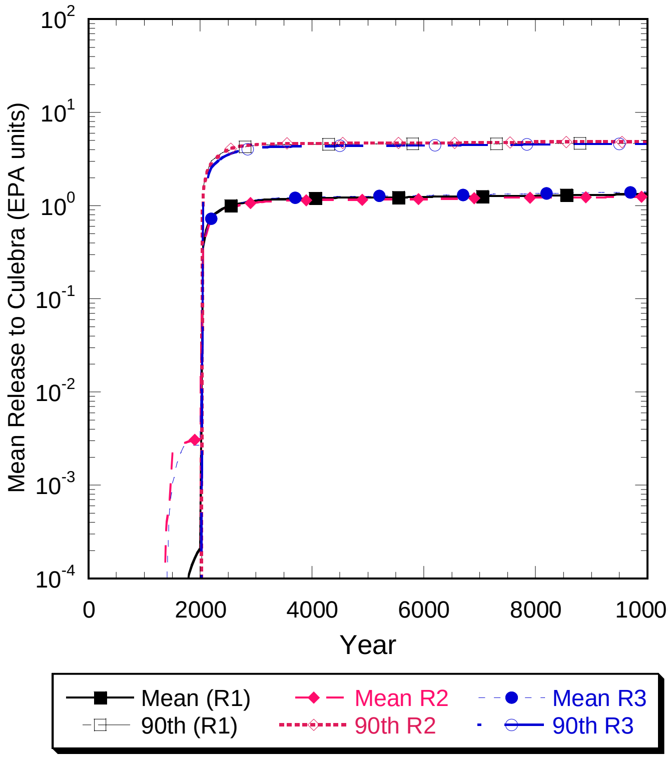

Figure PA-74. Mean Values for Cumulative Normalized Release Up Borehole for All Replicates, Scenario S6.

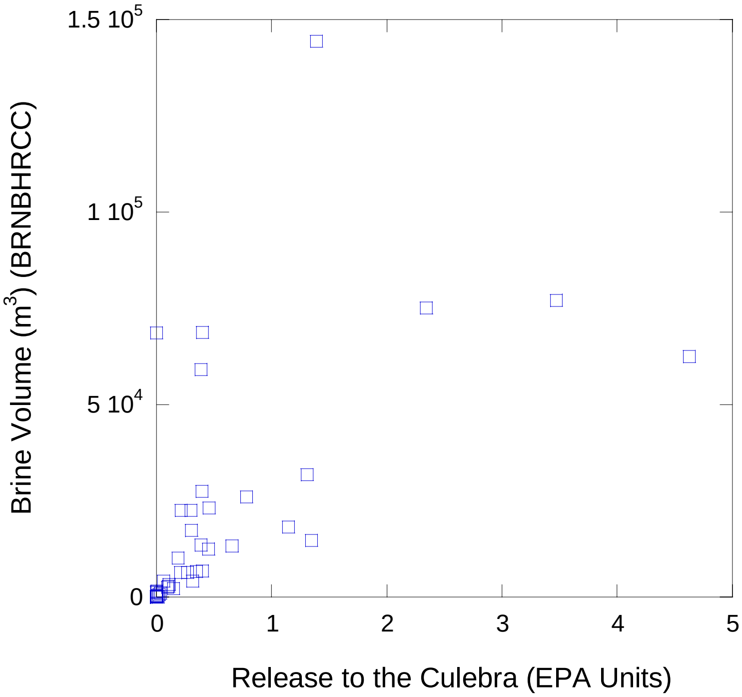

Figure PA-75. Comparison of Total Release to Culebra with Flow Up Borehole, Replicate 1 Scenario S3.

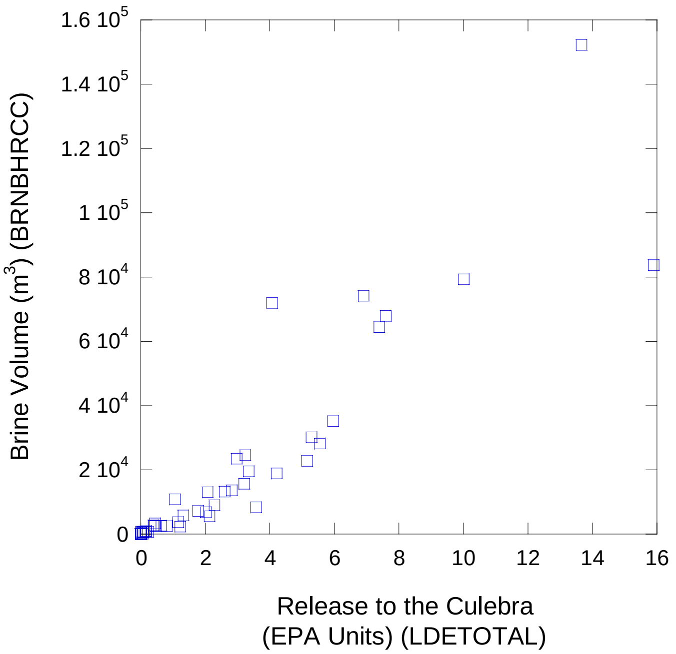

Figure PA-76. Comparison of Total Release to Culebra with Flow Up Borehole, Replicate 1 Scenario S3.

PA-8.4.4 Transport through the Culebra

Releases through the Culebra are calculated with the code SECOTP2D (see Section PA-4.9). As explained in Section PA-6.8.7, transport through the Culebra is calculated for a release of 1 kg of each of four radionuclides (^{241}Am, ^{234}U, ^{230}Th, and ^{239}Pu). Am is present as Am(III) and Th as Th(IV). Uranium may be present as either U(IV) or U(VI); plutonium may be present as Pu(III) or Pu(IV). The oxidation state of uranium and plutonium is an uncertain parameter (see WOXSTAT in Table PA-17). The total release of radionuclides across the LWB at the Culebra is calculated by the code CCDFGF by convoluting the SECOTP2D results with the transport to the Culebra calculated by NUTS and PANEL. This section discusses the SECOTP2D results; releases through the Culebra are presented in Section PA-9.5.

Transport calculations were performed for both partial-mining and full-mining scenarios. The partial-mining scenario assumes the extraction of all potash reserves outside the LWB while full mining assumes that all potash reserves both inside and outside the LWB are exploited. Flow fields in the Culebra are computed separately for each mining scenario by the code MODFLOW (see Section PA-4.8).

All SECOTP2D results, regardless of magnitude, are included in the calculation of releases through the Culebra. In practice, most non-zero releases computed by SECOTP2D are vanishingly small and result from numerical error (Kanney 2003). Consequently, the analysis of SECOTP2D results focused on realizations in which at least one billionth (10^{-9}) of the 1 kg source was transported to the land withdrawal boundary.

PA-8.4.4.1 Partial Mining Results

Under partial-mining conditions, only the ^{234}U species was transported beyond the LWB in any significant amount during the course of the 10,000-year simulation (Kanney 2003). Table PA-27 shows the eight vectors that resulted in releases greater than one billionth of the 1 kg source. Sensitivity analysis indicates that releases of ^{234}U are associated with the (VI) oxidation state. This result is reasonable because the matrix distribution coefficients for uranium in the (IV) state are much lower than for the (VI) state (see Section PA-5.2 and Attachment PAR, Table PAR-35).

Table PA-27. Releases of ^{234}U at LWB in Partial Mining Conditions

Replicate	Vector	^{234}U Release at LWB (fraction of 1 kg source)
3	54	0.479
3	84	0.177
3	38	0.0815
2	10	0.0711
1	58	0.0541
3	23	1.40×10^{-3}
1	8	2.36×10^{-4}
3	71	7.12×10^{-8}

PA-8.4.4.2 Full Mining Results

Under full-mining conditions, only the ^{234}U species was transported beyond the LWB in significant amounts during the course of the 10,000-year simulation. Table PA-28 shows the 18 vectors that resulted in releases greater than one billionth of the source of 1 kg. Sensitivity analysis indicates that releases of ^{234}U in the full mining conditions are also associated with the U(VI) oxidation state.

Two vectors showed releases of ^{239}Pu greater 1×10^{-9} kg. Replicate 2, vector 71 computed a release of 6.15×10^{-6} kg; replicate R1, vector 92 showed a release of 2.03×10^{-9} kg. No releases of ^{230}Th or ^{241}Am exceeded 1×10^{-9} kg.

PA-8.4.4.3 Additional Information

More detailed information on the results of the Culebra transport calculations can be found in the Analysis Package for the Culebra Transport Calculations: Compliance Recertification Application (Kanney 2003).

Table PA-28. Releases of ^{234}U at LWB in Full-Mining Conditions

Replicate	Vector	^{234}U Release at LWB (fraction of 1 kg source)
2	15	0.987
3	38	0.987
1	58	0.889
1	65	0.766
3	54	0.712
2	10	0.209
3	27	0.0269
1	90	0.0127
2	30	0.0123
1	31	6.18×10^{-3}
3	65	4.72×10^{-3}
3	66	1.80×10^{-4}
2	53	1.66×10^{-5}
3	67	1.59×10^{-7}
1	67	1.03×10^{-8}
3	42	4.53×10^{-9}
2	33	1.98×10^{-9}
2	24	1.61×10^{-9}

PA-8.5 Direct Releases

Direct releases occur at the time of a drilling intrusion, and include cuttings and cavings; spallings; and DBRs. This section presents analysis of the volume released by each mechanism.

PA-8.5.1 Cuttings and Cavings Volumes

Cuttings and cavings releases are solid waste material that is removed from the repository by the cutting of the drill bit and additional material that is sheared off the borehole wall by the circulation of the drilling fluid. Figure PA-77 shows the CCDFs for the total volume removed to the surface from cuttings and cavings for replicate R1. Figure PA-78 compares statistics for the CCDFs for cuttings and cavings volume for each replicate, and shows that the three replicates produced very similar results.

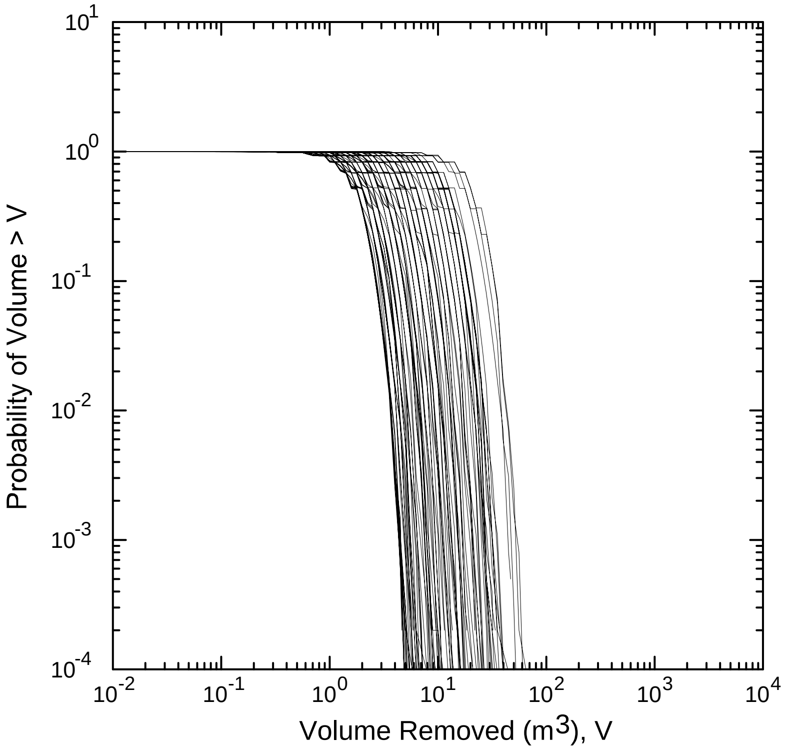

Figure PA-77. Total Volume Removed by Cuttings and Cavings, Replicate R1.

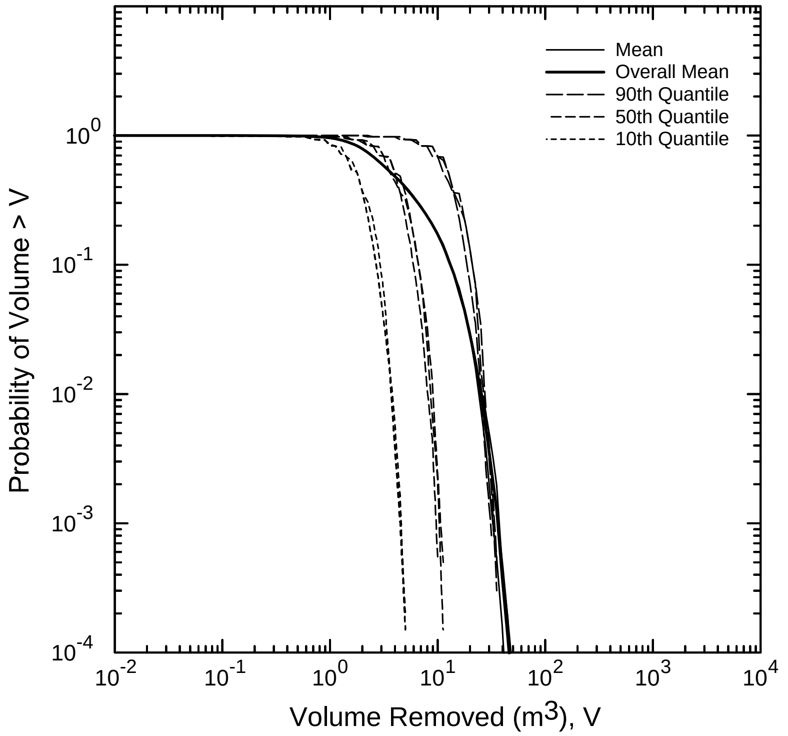

Figure PA-78. Statistics for Volumes Removed by Cuttings and Cavings, All Replicates.

Figure PA-79 shows that the uncertainty in cuttings and cavings volume arises primarily from the uncertainty in the shear strength of the waste (WTAUFAIL, see Table PA-17). The uncertainty in drill string angular velocity (DOMEGA) affects the calculation of cavings volume (Section PA-4.5), but is much less significant (Dunagan 2003a).

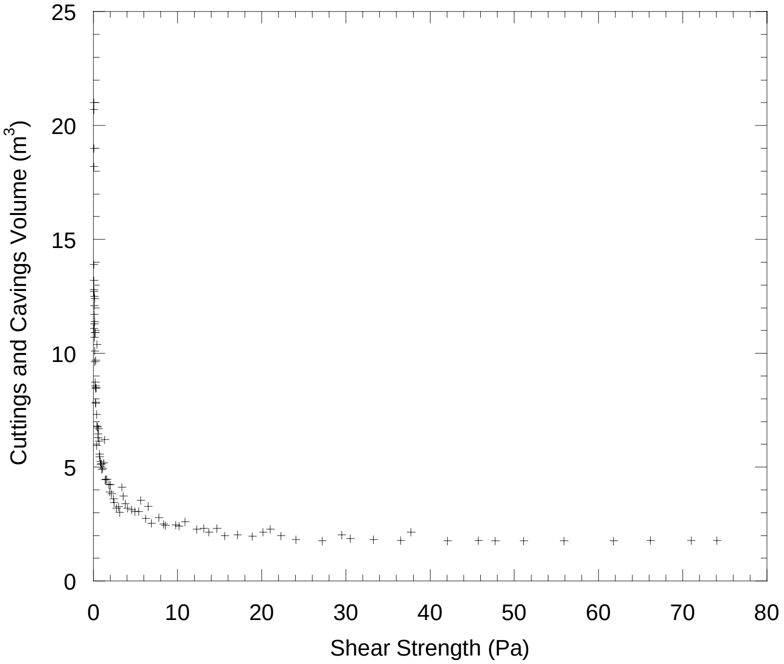

Figure PA-79. Sensitivity of Mean Cuttings and Cavings Volume to Waste Shear Strength.

PA-8.5.2 Spall Volumes

The volume of solid waste material released to the surface due to the spallings mechanism is calculated with the code DRSPALL. As outlined in Section PA-4.6.4, the code was run for each of 50 vectors in an LHS for DRSPALL, and for four values of repository pressure (10, 12, 14, and 14.8 MPa). Figure PA-80 shows the distribution of spall volumes for each value of repository pressure, ordered by increasing spall volume at 14.8 MPa. The maximum volume is 12.062 m^3 occurring at repository pressure of 14.8 MPa. At repository pressure at or below 10 MPa, no spallings occurred.

The distributions presented in Figure PA-80 are the volumes that could be removed by a single intrusion. As outlined in Section PA-4.6.4, the uncertainty in these volumes arises from four variables that are uncertain in the DRSPALL calculations: waste permeability; waste porosity; waste tensile strength; and waste particle diameter. Figure PA-81 and Figure PA-82 show the relationship between the spall volumes (SPALVOL) for the scenario with initial pressure of 14.8 MPa and the particle diameter (PARTDIAM) and the ratio of waste permeability to waste porosity (PERMPOR, from the term k'/ϕ in Equation (145)). Figure PA-81 and Figure PA-82 show that large spall volumes result from combinations of low values of particle diameter and low values for the ratio of waste permeability to waste porosity, and that uncertainty in these two parameters dominates the uncertainty in the spall volume from a single intrusion.

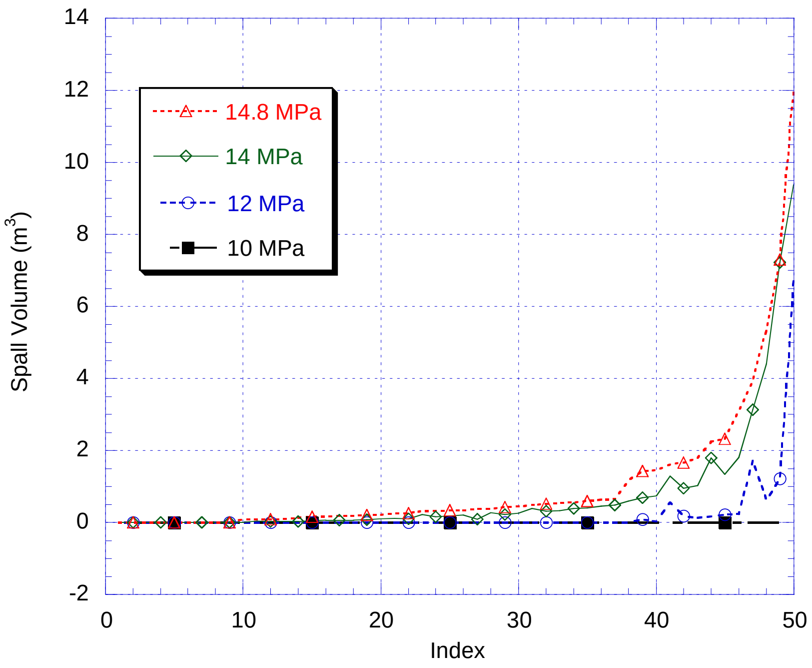

Figure PA-80. Spall Volume for a Single Intrusion (Ranked by Increasing Volume in the 14.8 MPa Scenario).

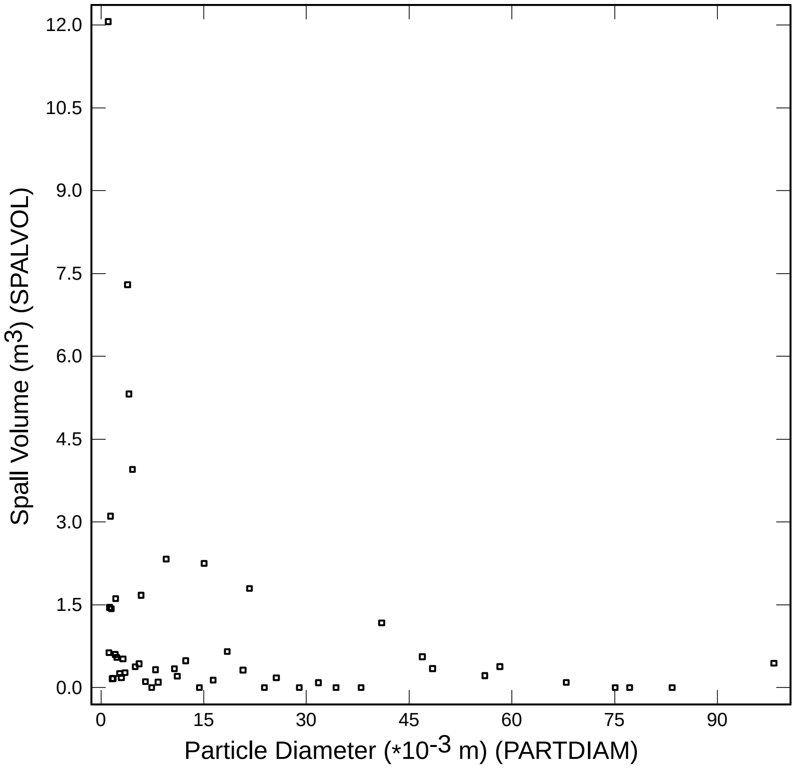

Figure PA-81. Sensitivity of Spall Volume for a Single Intrusion to Particle Diameter, 14.8 MPa Scenario.

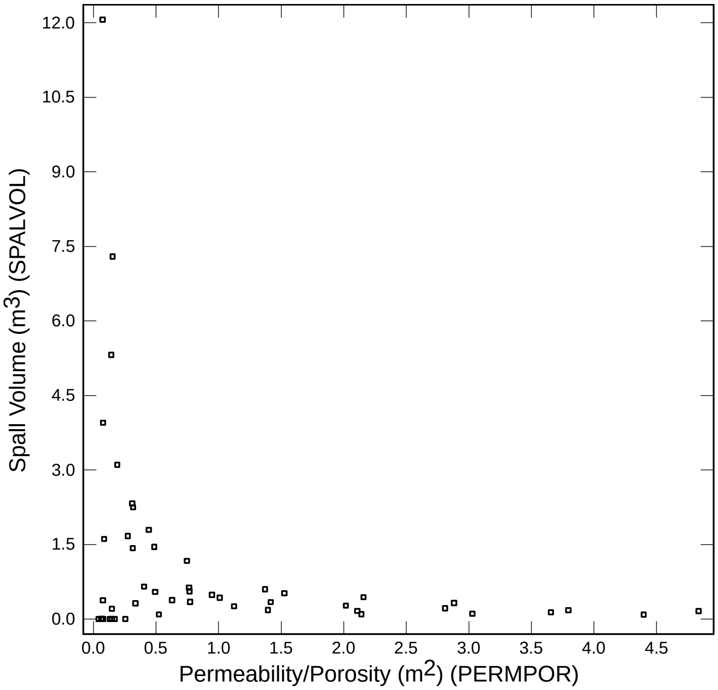

Figure PA-82. Sensitivity of Spall Volume for a Single Intrusion to *Waste Permeability / Waste Porosity* , 14.8 MPa Scenario.

The code CCDFGF stochastically generates futures for the repository and constructs the distribution of total volume removed by spallings for all intrusions (see Section PA-6.5 and Section PA-6.8). Figure PA-83 shows the CCDFs for the volume of material released (m^3) by spallings for replicate R1. Figure PA-84 compares statistics for the distribution of CCDFs for spall volume among the three replicates, and shows that the three replicates produce similar results. The median (50th quantile) and 10th quantile CCDFs do not plot on the scale of Figure PA-84 due to the large number of observations with spall volumes less than 0.01 m^3.

The distribution of spall volumes arises from the uncertain parameters used in the calculation of repository pressure (see Section PA-4.2) and the uncertain volume removed by a single intrusion (Figure PA-80). Section PA-7.1.1 and Section PA-8.3.1 identified three uncertain variables in the space for subjective uncertainty S_{su} that are primarily responsible for the uncertainty in repository pressure: borehole permeability (BHPERM); the indicator for microbial action (WMICDFLG); and the initial pressure in the Castile brine reservoir (BPINTPRS). Thus, these three variables may correlate to uncertainty in the total volume released by spalling.

In addition, the variable RNDSPALL (Table PA-17) in the LHS for the CRA-2004 PA (Equation (254)) assigns vectors from the LHS for DRSPALL (Section PA-4.6.4) to vectors in the LHS for the CRA-2004 PA. The variable RNDSPALL creates a mapping between the uncertain spall volumes in Figure PA-80 and the CCDFs in Figure PA-83. Thus, the spall volume (SPALVOL) for the 14.8 MPa scenario can be included in the sensitivity analysis for total spall volumes.

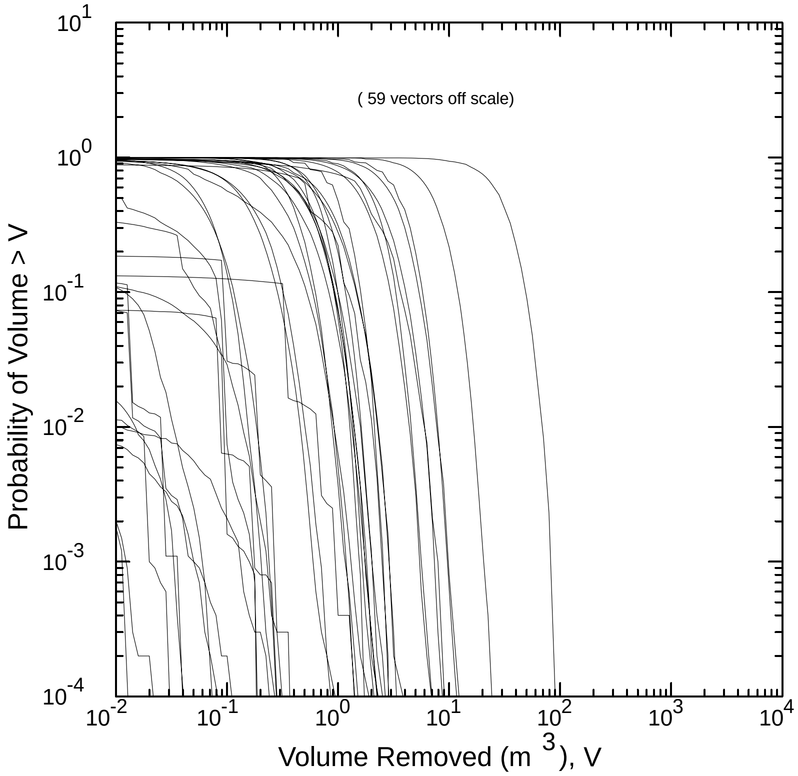

Figure PA-83. Total Volume Removed by Spallings, Replicate R1.

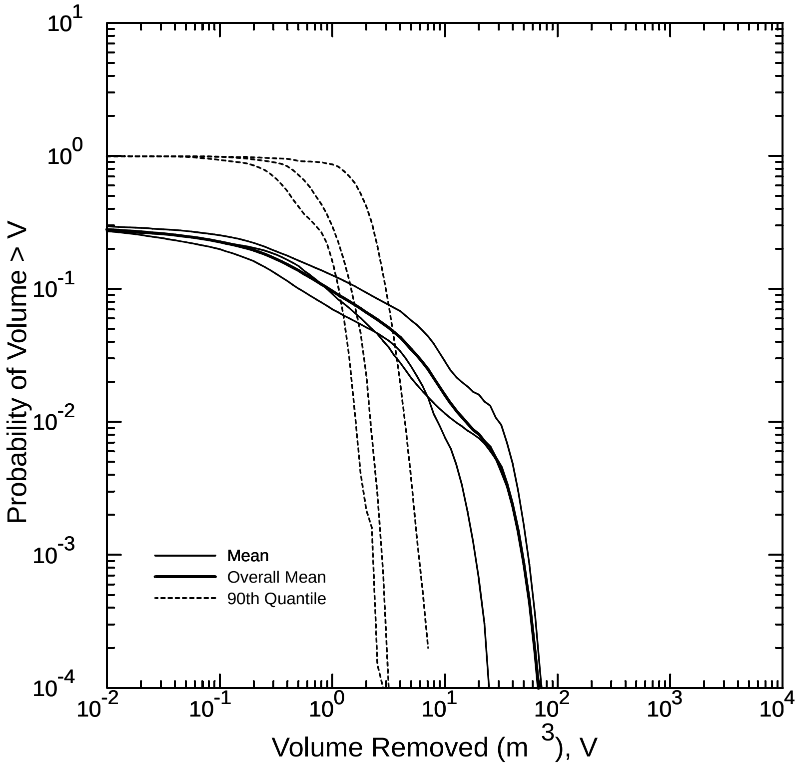

Figure PA-84. Statistics for Total Spall Volume, All Replicates.

Figure PA-85 demonstrates that the uncertainty in mean total spall volume arises primarily from the uncertainty in the indicator for microbial action (WMICDFLG) and the uncertainty in the spall volume from a single intrusion (SPALVOL). The indicator for microbial action (WMICDFLG) partitions the vectors into two sets of equal size: a set of vectors where microbial action occurs (WMICDFLG = 1 or 2) and a set where no microbial action is present (WMICDFLG = 0). Figure PA-80 shows that no spall releases are possible unless pressure exceeds 10 MPa. Figure PA-85 shows that when no microbial action is present, no spallings releases occur even when the spall volume from a single intrusion could be non-zero. Therefore, when no microbial action is present, repository pressure does not exceed the threshold for spall releases. In contrast, when microbial action is present (WMICDFLG = 1 or 2), Figure PA-85 shows that the uncertainty in total mean spall releases arises primarily from the uncertainty in the spall volume from a single release (SPALVOL).

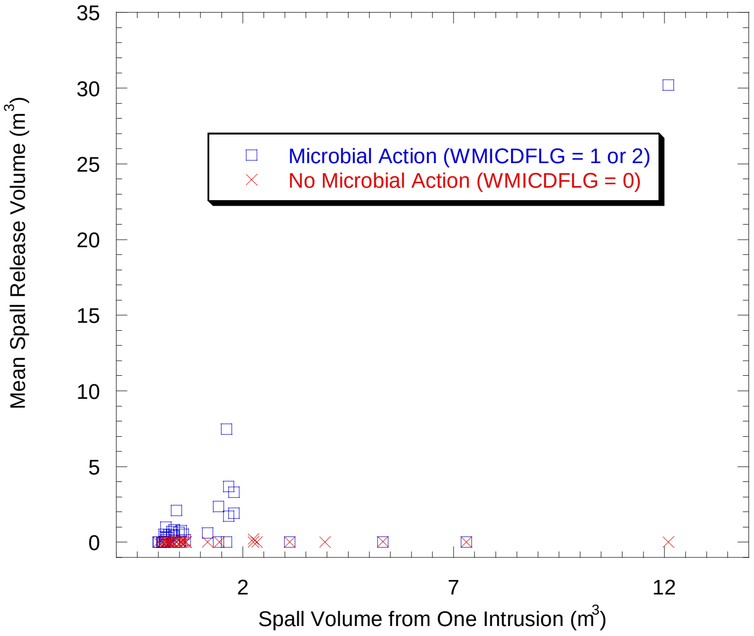

Figure PA-85. Sensitivity of Mean Total Spall Volume, Replicate R1.

PA-8.5.3 Direct Brine Release Volumes

DBRs to the surface can occur during or shortly after a drilling intrusion. For each element of the LHS, the code BRAGFLO (Section PA-4.7) calculates volumes of brine released for a total of 78 combinations of intrusion time, intrusion location, and initial conditions (Section PA-6.7.5) Initial conditions for the DBR calculations are computed by BRAGFLO for five scenarios (S1 through S5; see Section PA-6.7) Results from the S1 scenario represent undisturbed repository conditions; results from the S2 through S5 scenarios represent repository conditions that result after a drilling intrusion.

For replicate R1, only about eight percent of the 7,800 DBR calculations (100 vectors × 78 combinations) resulted in direct brine flow to the surface. The maximum DBR release is approximately 115 m^3. Only intrusions into a lower panel (see Section PA-4.7.1) resulted in significant brine volume releases. In the S1 scenario, the lower panel represents an undisturbed panel at the south end of the repository. In the S2 and S3 scenarios, the lower panel represents any panel that has a previous E1 intrusion; in the S4 and S5 scenarios, the lower panel has a previous E2 intrusion.

Figure PA-86 shows probability plots of DBR volumes for Scenarios S1 through S5, lower intrusion, at the discrete times for which DBR is calculated. A probability plot displays the percentage of the vectors on the x-axis where release volumes are less than the value on the y-axis. Figure PA-86a shows DBR volumes for scenario S1 representing the initial intrusion at various times. Figure PA-86b and Figure PA-86c show DBR volumes for Scenarios S2 and S3, which represent a subsequent intrusion (at various times) into a panel that had an E1 intrusion at 350 years and 1,000 years, respectively. Figure PA-86d and Figure PA-86e show DBR volumes for Scenarios S4 and S5, which represent a subsequent intrusion (at various times) into a panel that had an E2 intrusion at 350 years and 1,000 years, respectively. Release volumes are larger and occur more frequently in the S2 and S3 scenarios, because the lower panel has much higher saturations after an E1 intrusion (Section PA-8.3.2).

Sensitivity analysis determined that DBR volume from a single intrusion is most sensitive to the initial pressure and brine saturation in the intruded panel (Stein 2003). The analysis is illustrated below for scenario S2; similar conclusions follow from analysis of the other scenarios. The initial pressure and brine saturation in the DBRs calculations are transferred from the Salado Flow calculations as described in Section PA-4.7.2. Thus, the uncertain parameters that are most influential to the uncertainty in pressure and brine saturation in the Salado Flow calculations (see Section PA-7.1 and Section PA-8.3) are also most influential in the uncertainty in DBR volumes.

The combination of relatively high pressure and brine saturation in the intruded panel is required for direct brine release to the surface. Figure PA-87 shows a scatter plot of pressure in the waste panel vs. DBR volumes for Scenario S2, lower intrusion with symbols indicating the value of the mobile brine saturation (defined as brine saturation S_b from the solution of Equation (25) minus residual brine saturation S_{br} in the waste (see Table PA-2)). The figure clearly shows that there are no releases until pressures exceed 8 MPa as indicated by the vertical line. Above 8 MPa, a significant number of vectors have zero releases, but these vectors have mobile brine saturations less than zero and thus no brine is available to be released. When mobile brine saturation approaches 1, relative permeability to gas becomes small enough that no gas flows into the well, and in these circumstances DBR releases end after three days (Equation (211)). Thus, in vectors with high mobile brine saturations, DBR releases increase proportionally with increases in pressure, as evidenced by the linear relationship between DBR volume and pressure for mobile brine saturation between 0.8 and 1.0. For vectors with mobile saturations between 0.2 and 0.8, both gas and brine can flow in the well, and the rate of gas flow can be high enough that the ending time of DBR releases may be as long as 11 days. Although brine may be flowing at slower rates in these vectors than in vectors with high mobile saturations, brine flow may continue longer and thus result in larger DBR volumes.

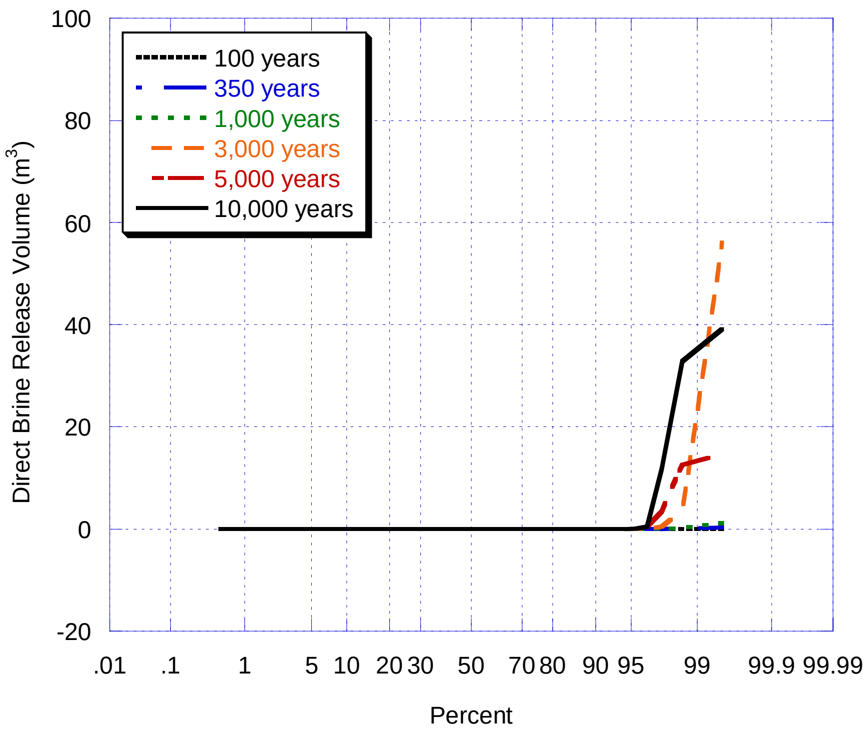

Figure PA-86a. DBRs for Initial Intrusions into Lower Panel (Scenario S1), Replicate R1.

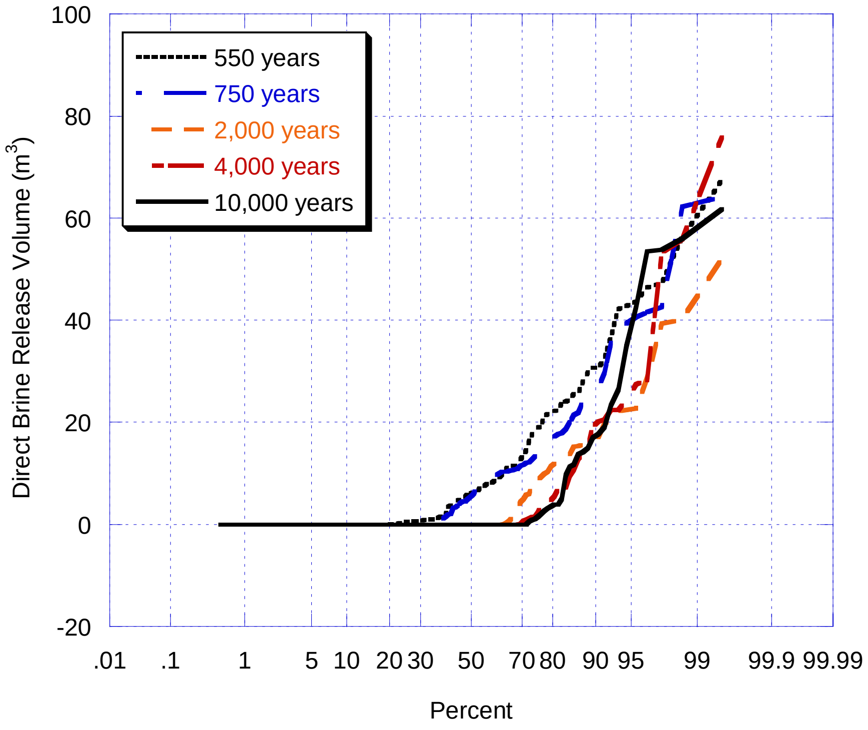

Figure PA-86b. DBRs for Subsequent Intrusions into Lower Panel After an E1 Intrusion at 350 Years (Scenario S2), Replicate R1.

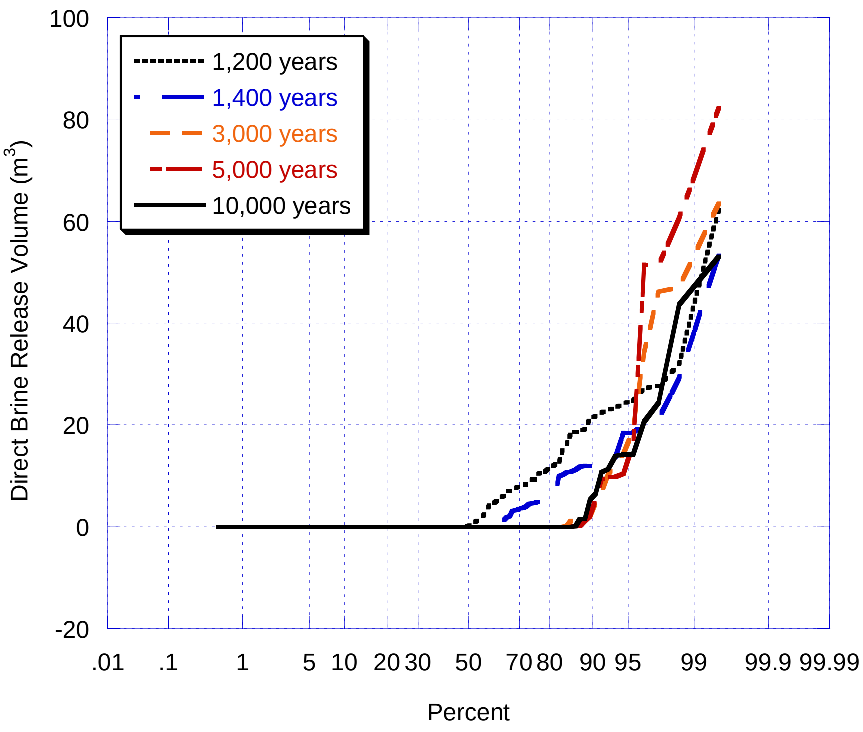

Figure PA-86c. DBRs for Subsequent Intrusions into Lower Panel After an E1 Intrusion at 1,000 Years (Scenario S3), Replicate R1.

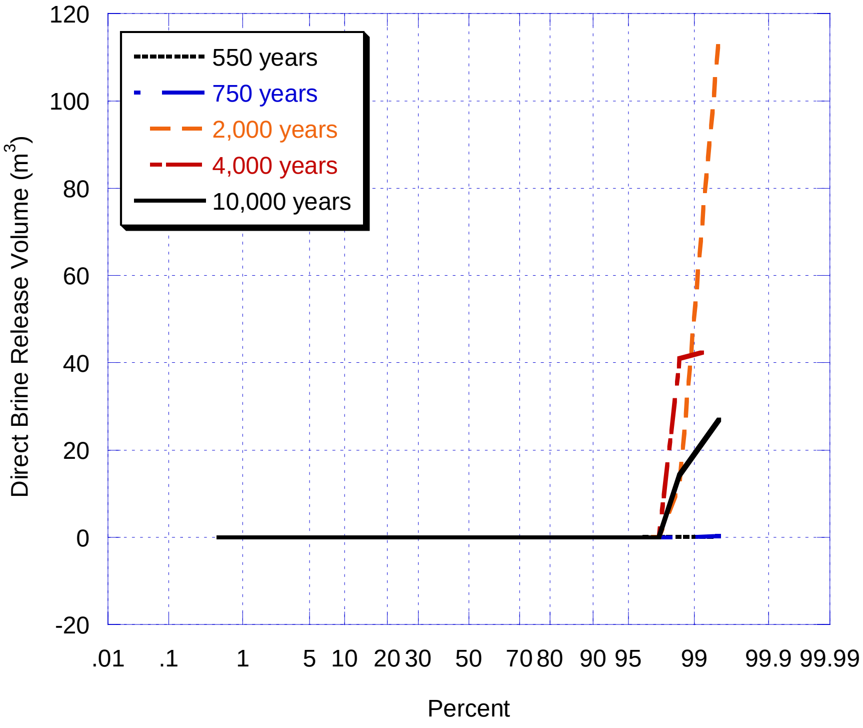

Figure PA-86d. DBRs for Subsequent Intrusions into Lower Panel After an E2 Intrusion at 350 Years (Scenario S4), Replicate R1.

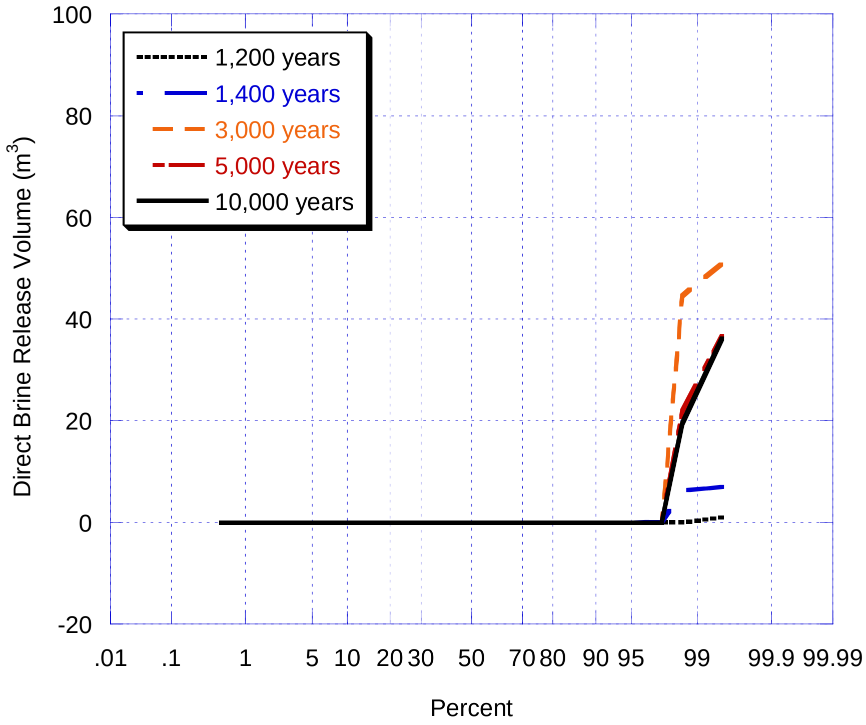

Figure PA-86e. DBRs for Subsequent Intrusions into Lower Panel After an E2 Intrusion at 1,000 Years (Scenario S5), Replicate R1.

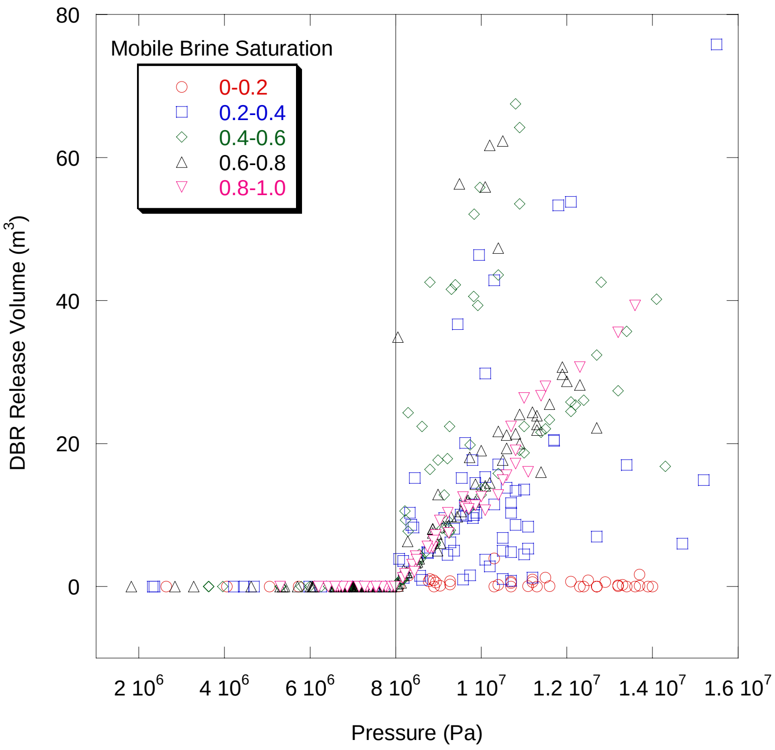

Figure PA-87. Sensitivity of DBR Volumes to Pressure, Replicate R1, Scenario S2, Lower Panel.

Figure PA-88 plots pressure against mobile brine saturation for the S2 scenario for all intrusion times with symbols indicating the range of DBR volumes. It is clear from Figure PA-88 that not all the variability in DBRs can be explained by pressure and saturation alone.

Borehole permeability can also be an important parameter controlling the volume of direct brine released. Borehole permeability is not a direct input to the DBR calculations, but this parameter affects conditions in the repository as modeled in the 10,000-year BRAGFLO calculations, which are used as initial conditions of the DBR model. Figure PA-89 shows a scatter plot of the log of borehole permeability against DBR volume for Scenario S2, lower intrusion with symbols indicating intrusion times. As borehole permeability decreases direct brine releases tend to increase, especially at late intrusion times (4,000 and 10,000 years). Helton et al. (1998) identified this same relationship in analysis of the CCA PA. Low values of borehole permeability tend to result in higher pressures following an E1 intrusion (Figure PA-53), which in turn lead to higher DBRs from subsequent intrusions.

The distributions presented in Figure PA-86 are for volumes of brine that could be released by a single intrusion. The code CCDFGF stochastically generates futures for the repository, specifying drilling times and locations, and constructs the distribution of total brine volume released (see Section PA-6.5 and Section PA-6.8). Figure PA-90 shows the CCDFs for the total brine volume released for replicate R1. Figure PA-91 compares the statistics for the CCDFs for total brine volume released among the three replicates, and shows that the three replicates produced similar results. Due to the number of observations which do not plot on the scale of Figure PA-90, the 10th quantiles do not appear on Figure PA-91.

Table PA-29 summarizes a stepwise regression analysis for mean total DBR volume. The uncertain parameters most important to uncertainty in total DBR volumes are those related to repository pressure (the indicator for microbial action (WMICDFLG) and the rate of steel corrosion (WGRCOR)) and brine saturation (the probability of an intrusion into the Castile brine reservoir (PBRINE), the pressure in the Castile brine reservoir (BPINTPRS), the permeability of the DRZ around the panel closures (DRZPCPRM), and the residual brine saturation in the waste (WRBRNSAT)). The linear regression model is not very effective at explaining the uncertainty in the total DBRs. The lack of resolution is due to the large number of vectors in which no direct brine releases occur; this conclusion was reached after analysis of the CCA PA (Helton et al. 1998).

PA-8.5.4 Additional Information

Dunagan (2003b) provides additional information about the cuttings and cavings releases calculated for the CRA-2004 PA. Additional information about the spallings releases is found in Lord et al. (2003) and Lord and Rudeen (2003). Stein (2003) provides detailed analysis of direct brine releases in the CRA-2004 PA.

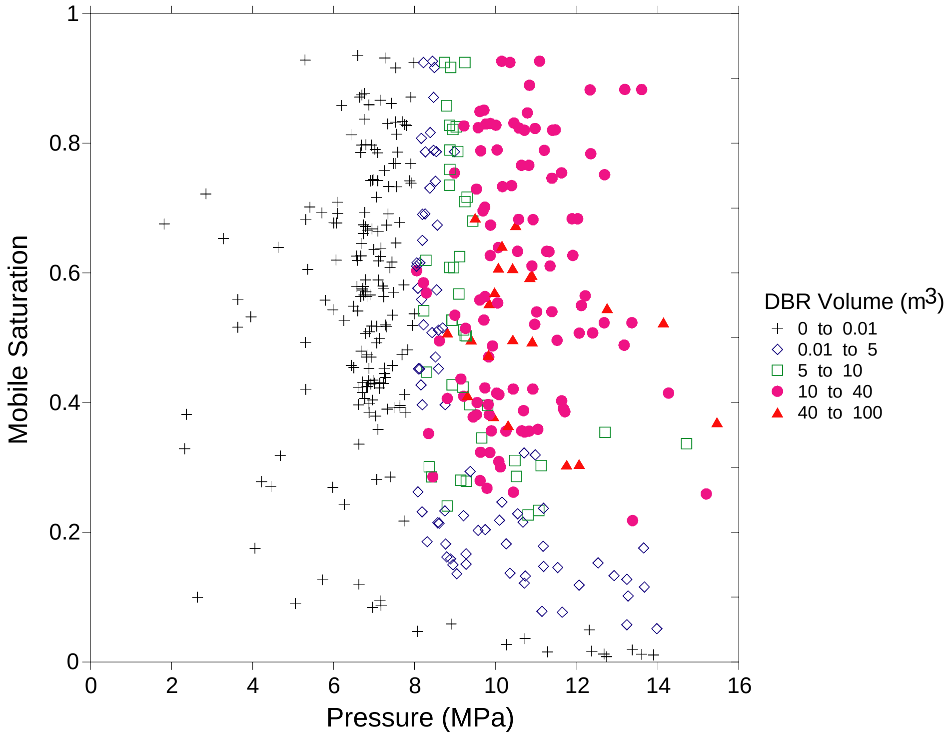

Figure PA-88. Sensitivity of DBR Volumes to Pressure and Mobile Brine Saturation, Replicate R1, Scenario S2, Lower Panel.

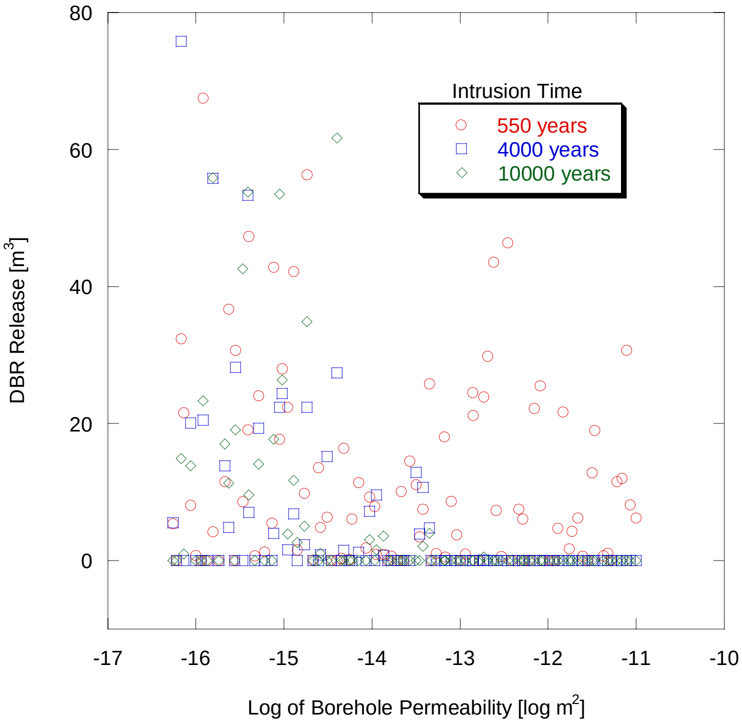

Figure PA-89. Sensitivity of DBR Volumes to Borehole Permeability, Replicate R1, Scenario S2, Lower Panel.

1 **Table PA-29. Stepwise Regression Analysis for Mean Total** DBR **Volume**

Step[1]	Expected Normalized Release		
	Variable[2]	SRRC[3]	R^2 [4]
1	WMICDFLG	–0.583	0.239
2	PBRINE	–0.385	0.378
3	BPINTPRS	0.389	0.515
4	WGRCOR	–0.190	0.553
5	DRZPCPRM	0.176	0.585
6	WRBRNSAT	–0.168	0.613

[1] Steps in stepwise regression analysis

[2] Variables listed in order of selection in regression analysis

[3] Standardized Rank Regression Coefficient in final regression model

[4] Cumulative R^2 value with entry of each variable into regression model

2 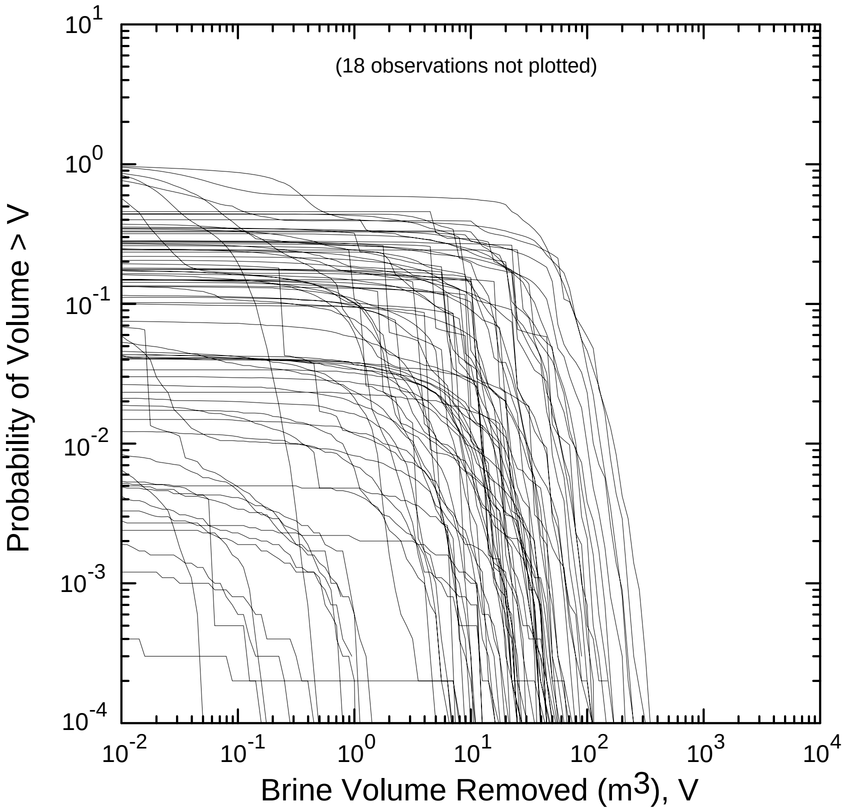

3 **Figure PA-90. Total DBRs Volumes, Replicate R1.**

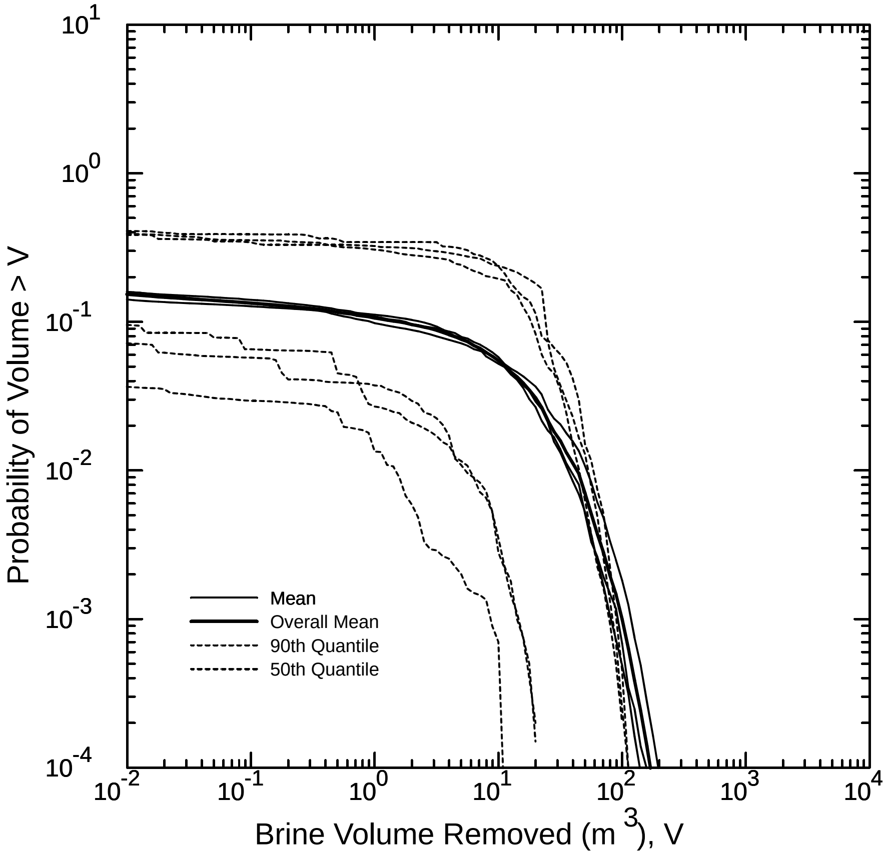

Figure PA-91. Statistics for Total DBR Volumes, All Replicates.

PA-9.0 NORMALIZED RELEASES

This section presents total normalized releases, followed by discussion of each of the four categories of releases that constitute the total release: cuttings and cavings; spallings; DBRs; and transport releases. Finally, this section concludes with a discussion of the sensitivity of total releases to uncertainty in parameter values.

PA-9.1 Total Releases

Figures PA-92, PA-93, and PA-94 show the CCDFs for total releases for replicates R1, R2, and R3 of the CRA-2004 PA. Each CCDF lies below and to the left of the limits specified in 40 CFR § 191.13(a). Thus, the WIPP continues to comply with the containment requirements of 40 CFR Part 191. The consistent increase in total releases at a probability of approximately 0.003 results from unlikely cuttings and cavings releases, as discussed in Section PA-9.6.1.

To compare the distributions of CCDFs among replicates and to demonstrate sufficiency of the sample size, mean and quantile CCDFs are computed. At each value for normalized release R on the abscissa, the CCDFs for a single replicate define 100 values for probability. The arithmetic mean of these 100 probabilities is the mean probability that release exceeds R; the curve defined by the mean probabilities for each value of R is the mean CCDF. The quantile CCDFs are defined analogously.

Figure PA-95 compares the mean, median, 90th and 10th quantiles for each replicate’s distribution of CCDFs for total releases. Figure PA-95 shows that each replicate’s distribution is quite similar, and shows qualitatively that the sample size of 100 in each replicate is sufficient to generate a stable distribution of outcomes.

Each of the mean and quantiles CCDFs in Figure PA-95 is an estimate of the true mean CCDF of the population of CCDFs. The overall mean CCDF is computed as the arithmetic mean of the three mean CCDFs from each replicate, and is an estimate of the true mean CCDF. To quantitatively determine the sufficiency of the sample size, a confidence interval is computed about the overall mean CCDF using Student’s t-distribution. Figure PA-96 shows 95 percent confidence intervals about the overall mean, and provides quantitative confirmation of the sufficiency of the sample size, by displaying the overall mean together with the 0.95 confidence interval of the Student's t-distribution estimated from the individual means of the three independent replicates.

Figure PA-97, Figure PA-98, and Figure PA-99 show the mean CCDFs for each component of total releases, for replicates R1, R2, and R3, respectively. In each replicate, the location of the mean CCDF for total releases is dominated by the cuttings and cavings releases. The mean predicted released from spallings and direct brine are an order of magnitude less than mean releases for cuttings and cavings; therefore, these categories of releases make relatively little contribution to the location of the mean CCDF for total releases. Release by subsurface transport in the Salado or Culebra make essentially no contribution to total releases.

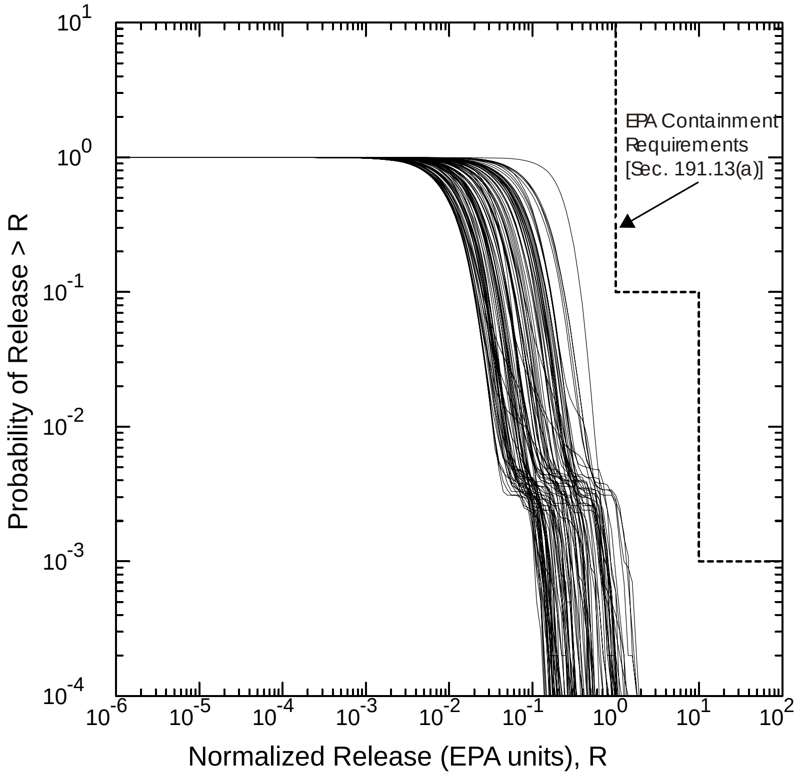

Figure PA-92. Total Normalized Releases, Replicate R1.

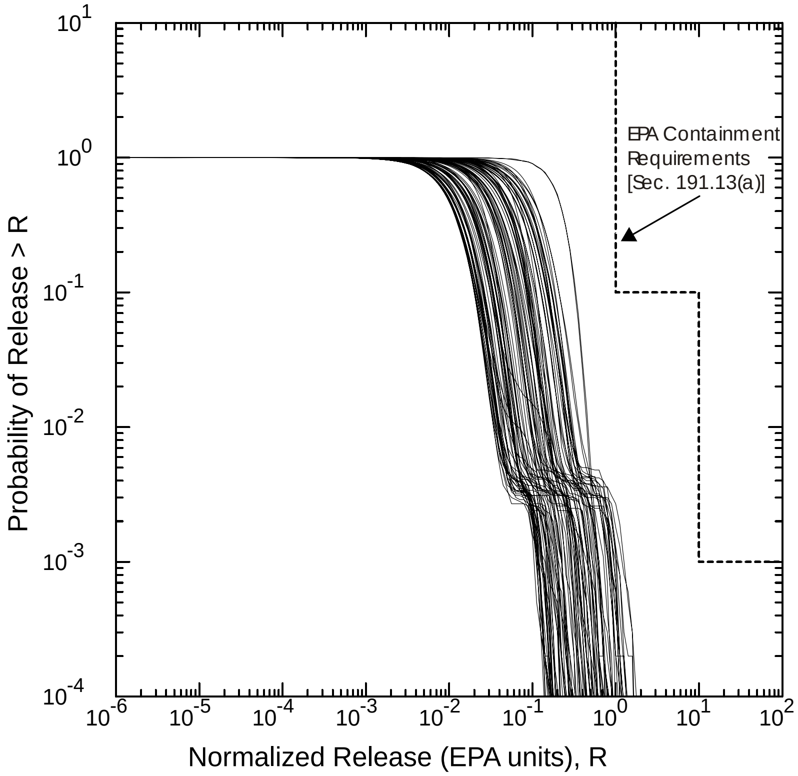

Figure PA-93. Total Normalized Releases, Replicate R2.

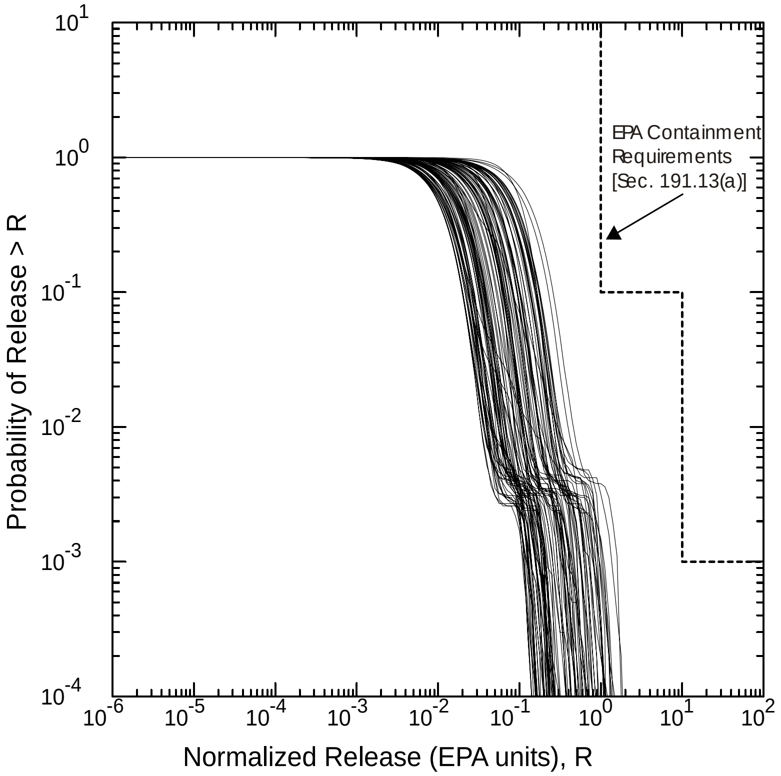

Figure PA-94. Total Normalized Releases, Replicate R3.

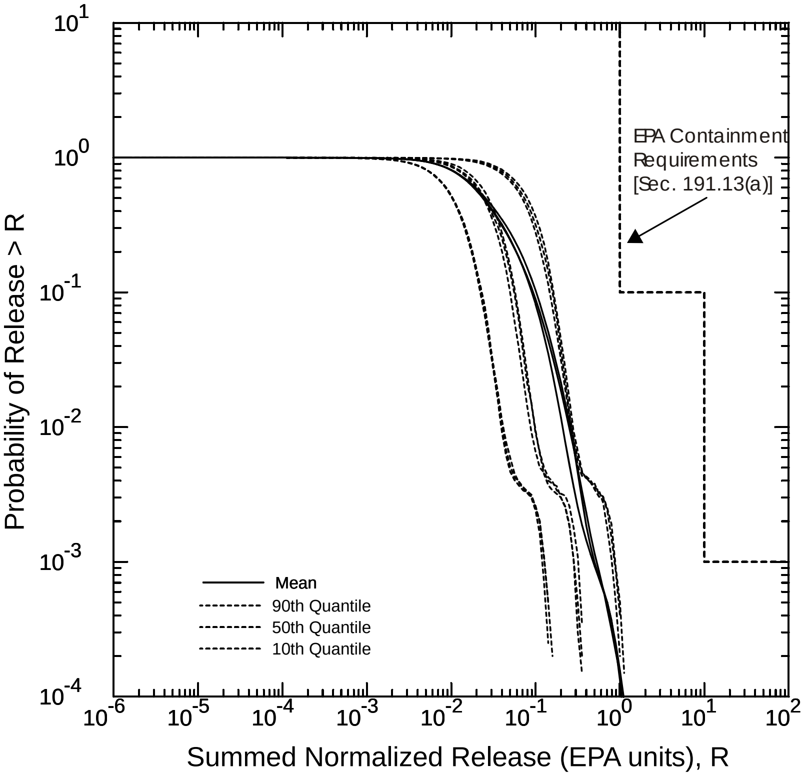

Figure PA-95. Mean and Quantiles CCDFs for Total Normalized Releases, All Replicates.

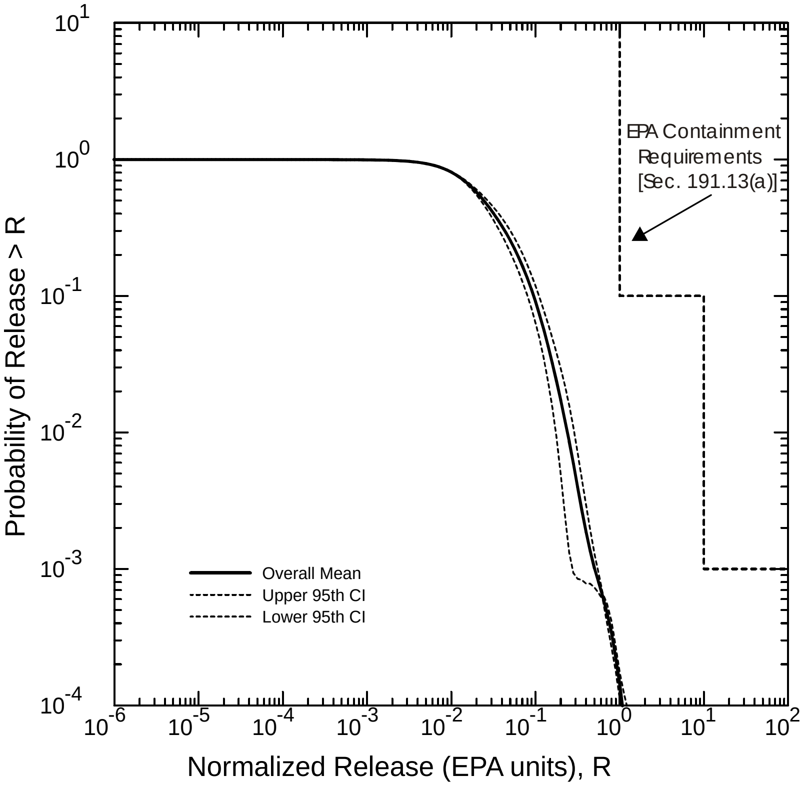

Figure PA-96. Confidence Interval on Overall Mean CCDF for Total Normalized Releases.

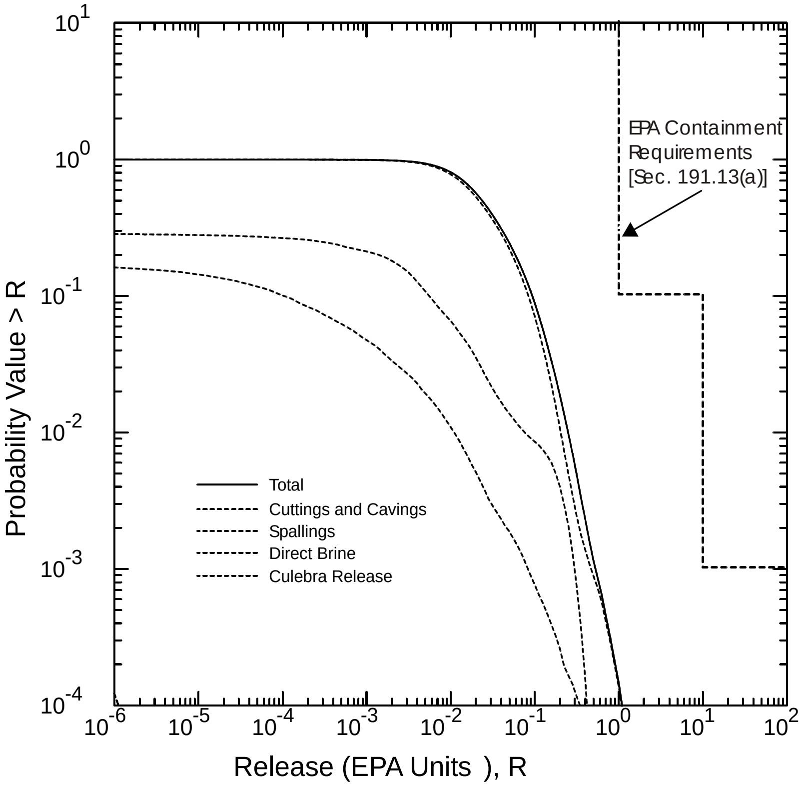

Figure PA-97. Mean CCDFs for Components of Total Normalized Releases, Replicate R1.

1 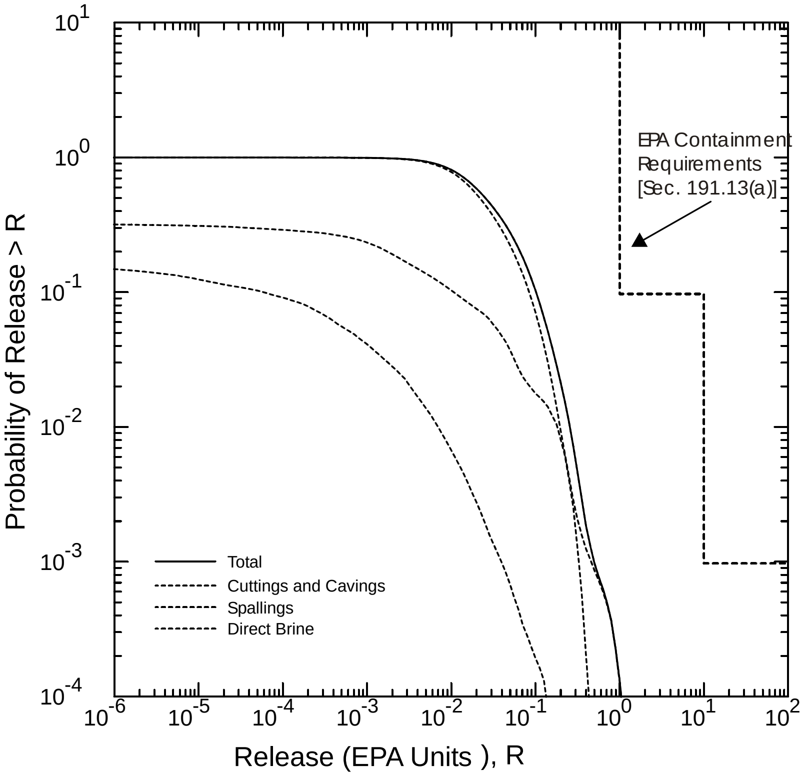

2 **Figure PA-98. Mean CCDFs for Components of Total Normalized Releases, Replicate R2.**

3 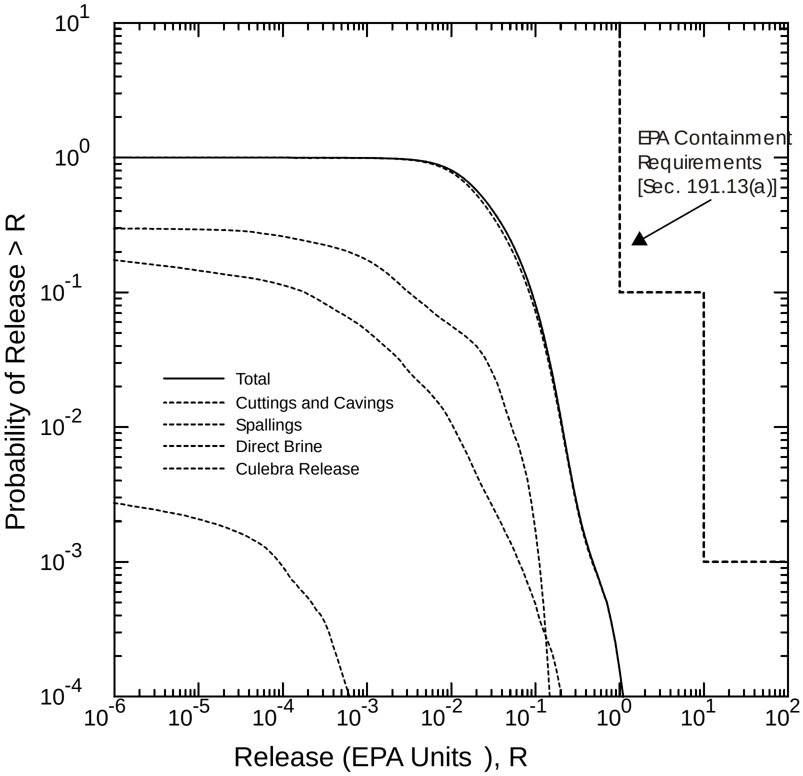

4 **Figure PA-99. Mean CCDFs for Components of Total Normalized Releases, Replicate R3.**

PA-9.2 Cuttings and Cavings Normalized Releases

Figures PA-100, PA-101, and PA-102 show the CCDFs for normalized releases due to cuttings and cavings for replicates R1, R2, and R3. The releases in each replicate are very similar; Figure PA-103 compares the mean and quantile CCDFs for cuttings and cavings releases for each replicate.

The increase in cuttings and cavings releases at a probability of 0.003 in each replicate is due to a few waste streams with very high radioactivity that are present in the updated inventory (Appendix DATA, Attachment F). These waste streams maintain significant radioactivity during the 10,000-year period. For example, a single waste stream (LA-TA-55-48, oil/vermiculate waste from ^{238}Pu heat source fabrication) has a concentration of radioactivity of 4.05 EPA units/m^3 at 100 years after repository closure, decaying to 1.95 EPA units/m^3 by 10,000 years (Fox 2003). This waste stream maintains high radioactivity concentration over time because it contains high quantities of longer-lived radioisotopes, principally ^{239}Pu and ^{240}Pu. The radioactivity concentrations in this waste stream can lead to cuttings and cavings releases exceeding 1 EPA unit for a single intrusion.

The volume of the LA-TA-55-48 waste stream (31 m^3) implies a probability of 31/168,500 = 0.00018 that this waste stream is selected as one of the three waste streams contributing to the cuttings and cavings release for a single intrusion at the probability of 10^2, which is below the EPA containment requirement. However, in any future of the repository, roughly six intrusions are expected (Dunagan 2003b), implying that 18 waste streams are selected for cuttings and cavings releases. The mean probability that the LA-TA-58-48 waste stream is selected at least once for cuttings and cavings releases is estimated to be

$$1-\left(1-0.00018\right)^{18}=0.0033\,;$$

thus, the increase in releases at a probability of about 0.003 in Figure PA-100, Figure PA-101, and Figure PA-102.

Figure PA-103 compares the mean, median, 90th, and 10th quantiles for each replicate's distribution of CCDFs for cuttings and cavings releases. The statistical measures of each replicate's distribution of CCDFs are quite similar, indicating that the sample size of 100 elements in each replicate is sufficient to estimate the distribution of CCDFs. Figure PA-104 shows the 95 percent confidence interval about the overall mean of the CCDFs for cuttings and cavings releases. The upper and lower confidence intervals nearly coincide with the overall mean, showing that the overall mean is estimated quite accurately.

Section PA-8.5.1 presents a sensitivity analysis for cuttings and cavings release volumes, and shows that the uncertainty in total cuttings and cavings volumes arises almost entirely from the uncertainty in waste shear strength (WTAUFAIL; see Table PA-17). Cuttings and cavings releases are computed by multiplying the volume released by the average concentration of radioactivity in the three selected CH-TRU waste streams (see Section PA-3.7). However, the uncertainty in the radioactivity in the cuttings and cavings materials is stochastic uncertainty, and is thus represented by the shape of the individual CCDFs in Figures PA-100, PA-101, and

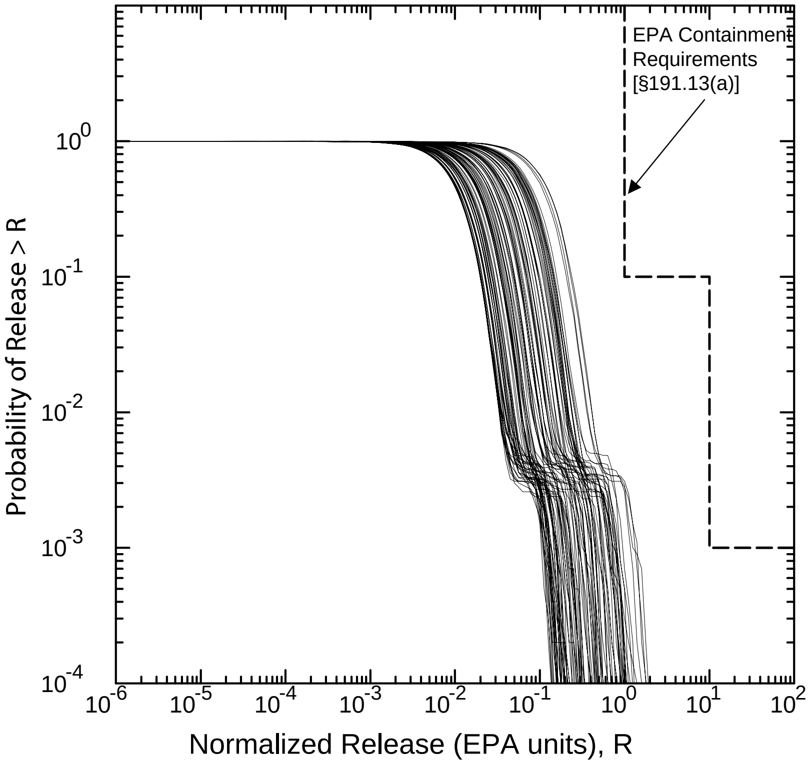

Figure PA-100. Cuttings and Cavings Releases, Replicate R1.

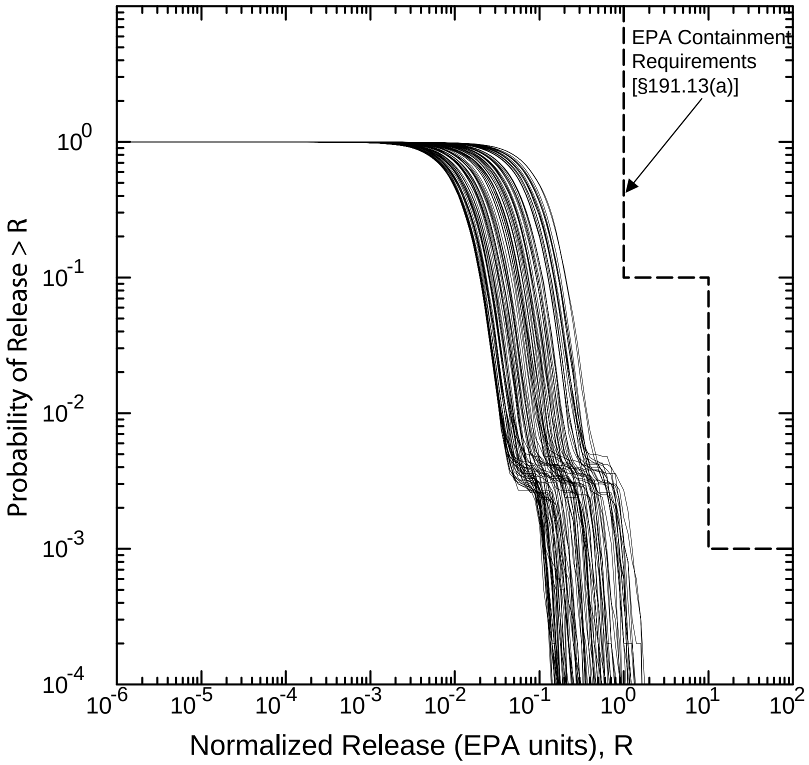

Figure PA-101. Cuttings and Cavings Releases, Replicate R2.

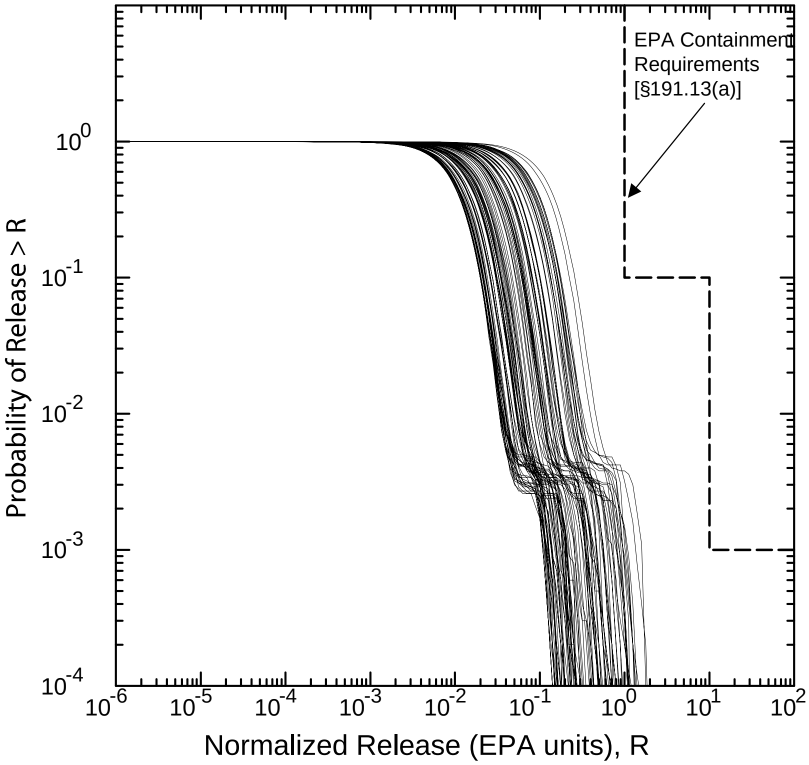

Figure PA-102. Cuttings and Cavings Releases, Replicate R3.

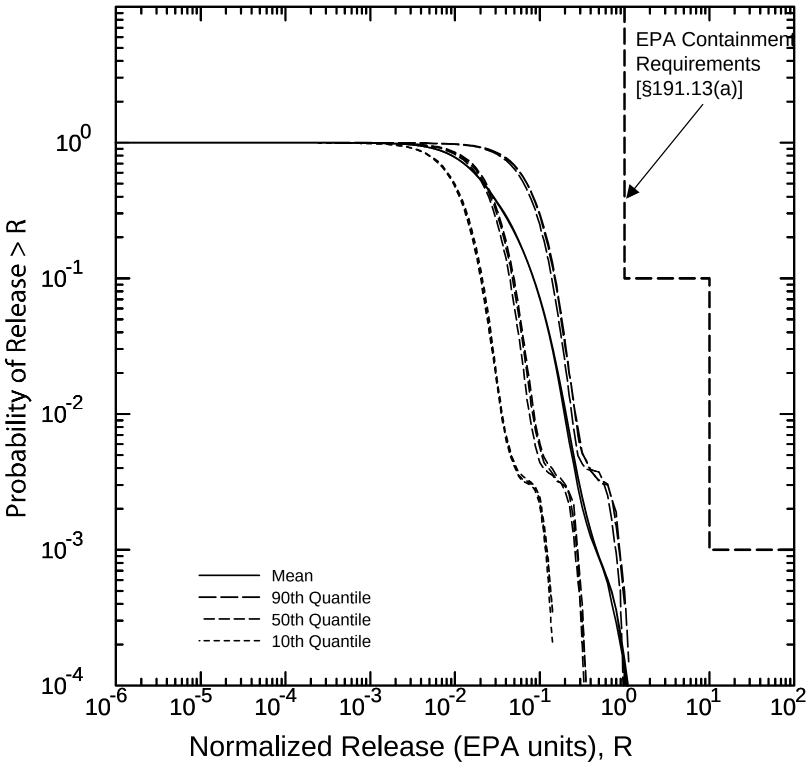

Figure PA-103. Mean and Quantile CCDFs for Cuttings and Cavings Releases, All Replicates.

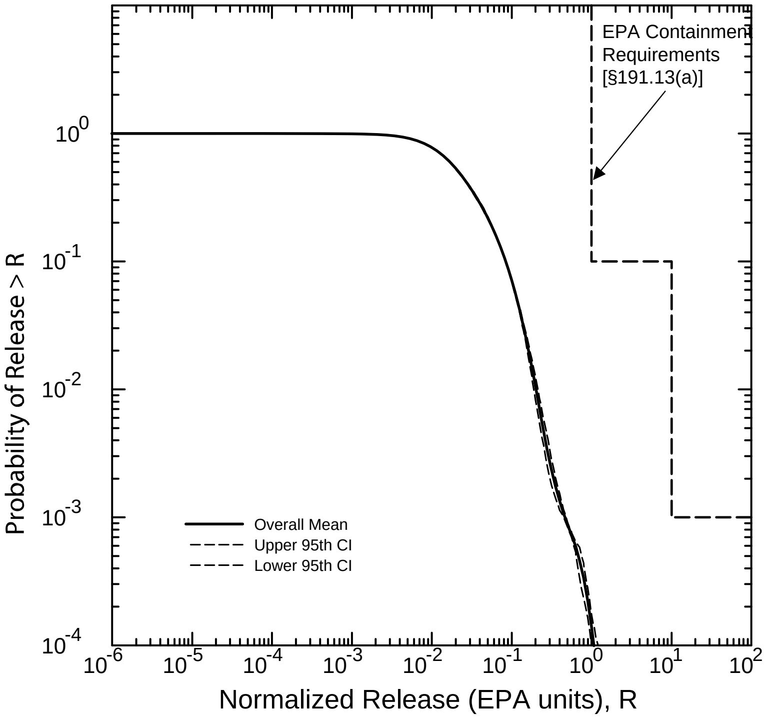

Figure PA-104. Confidence Interval on Overall Mean CCDF for Cuttings and Cavings Releases.

PA-102. Consequently, the uncertainty in mean cuttings and cavings releases is due to the subjective uncertain in the cuttings and cavings volume, as demonstrated in Figure PA-105, which demonstrates the high correlation between mean cuttings and cavings releases and the uncertainty in waste shear strength.

PA-9.3 Spallings Normalized Releases

Figures PA-106, PA-107, and PA-108 show the CCDFs for normalized releases due to spallings for replicates R1, R2, and R3. The releases for each replicate are very similar; Figure PA-109 compares the mean and quantile CCDFs for spallings releases for each replicate and indicates that the distribution of spallings releases are similar in each replicate. Figure PA-110 shows the 95 percent confidence interval about the overall mean of the CCDFs for spallings releases. Although the confidence interval for spallings releases is broader than that shown in Figure PA-104 for cuttings and cavings releases, the overall mean is quite similar to the upper confidence interval, particularly at low probabilities. This result provides confidence that the true mean CCDF for spallings releases does not lie far to the right of the overall mean computed from the three replicates, and thus remains far below the release limits.

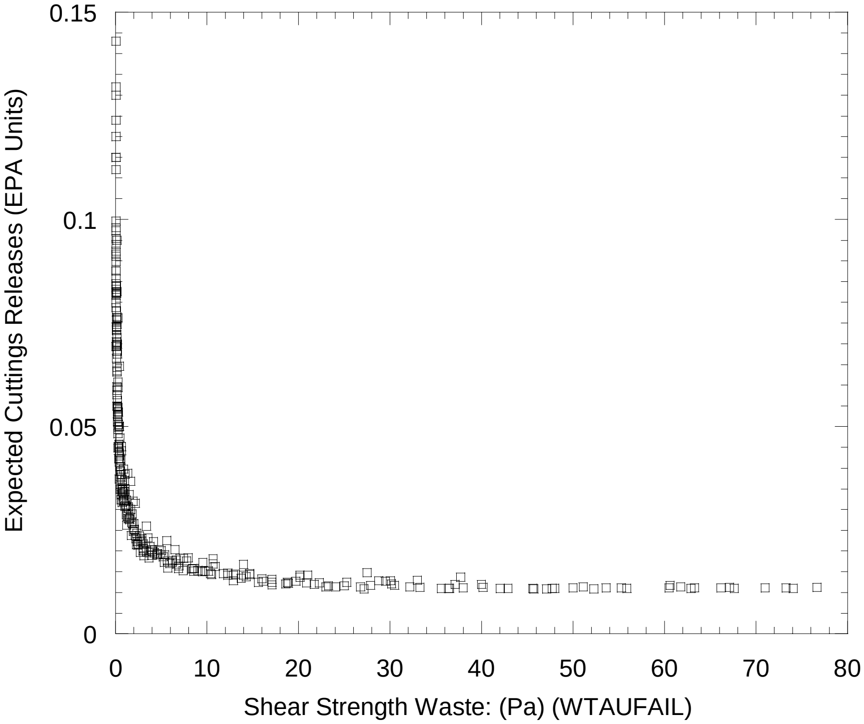

Figure PA-105. Uncertainty in Cuttings and Cavings Releases Due to Waste Shear Strength, All Replicates.

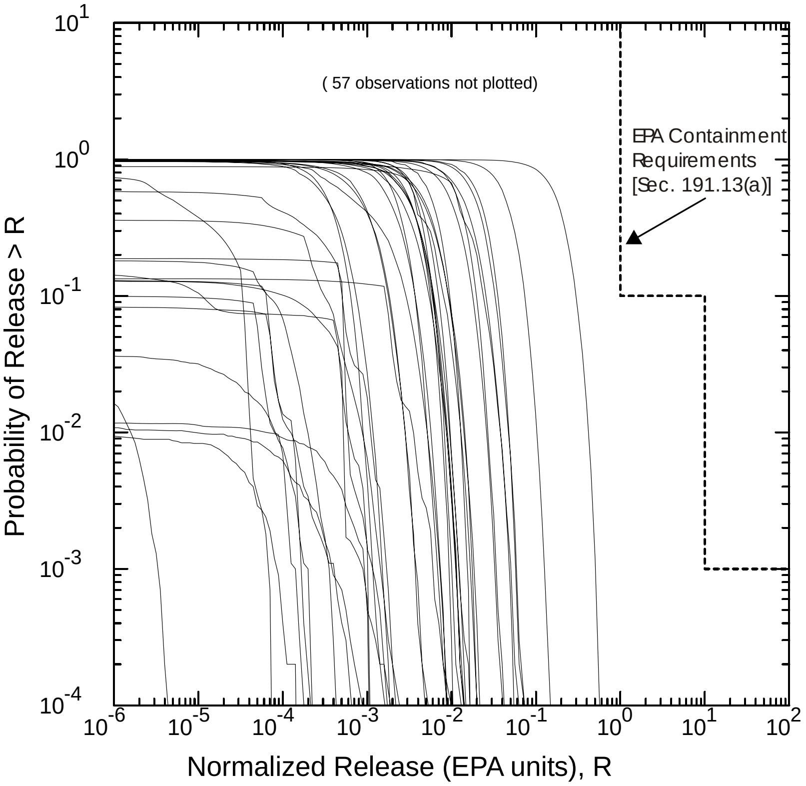

Figure PA-106. Spallings Releases, Replicate R1.

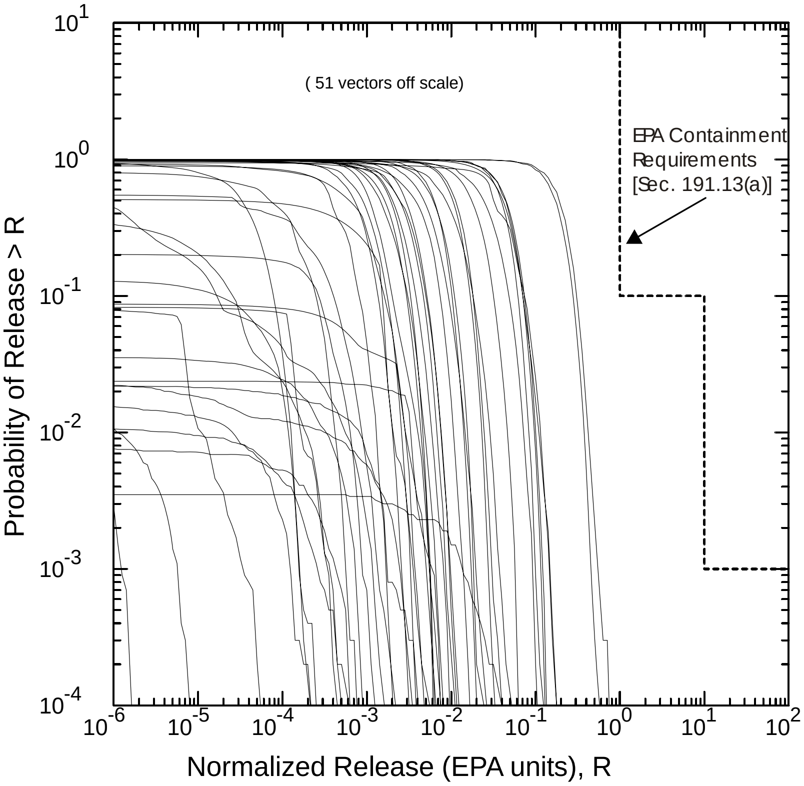

Figure PA-107. Spallings Releases, Replicate R2.

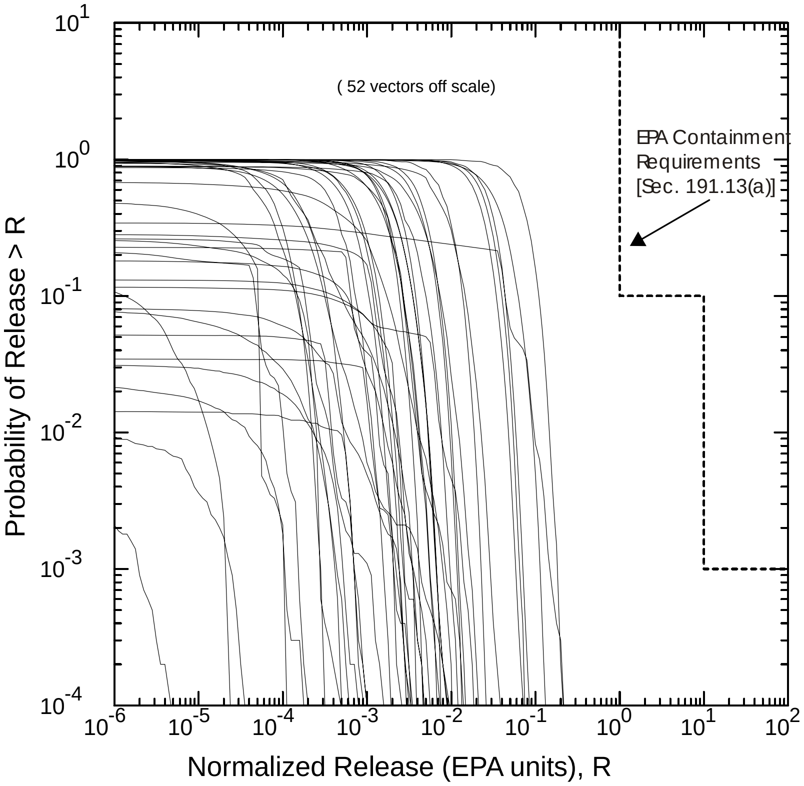

Figure PA-108. Spallings Releases, Replicate R3.

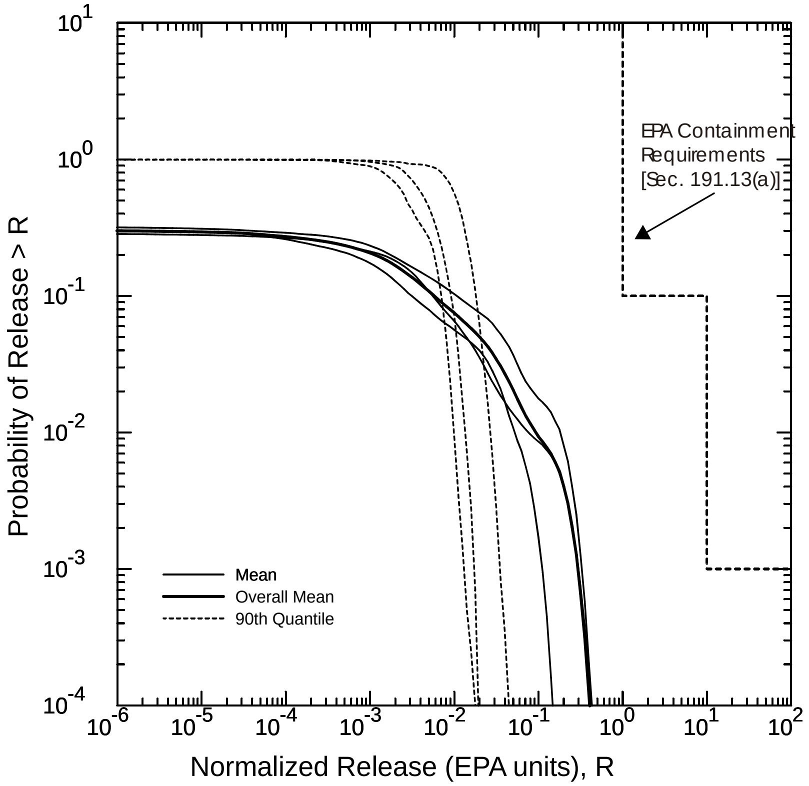

Figure PA-109. Mean and Quantile CCDFs for Spallings Releases, All Replicates.

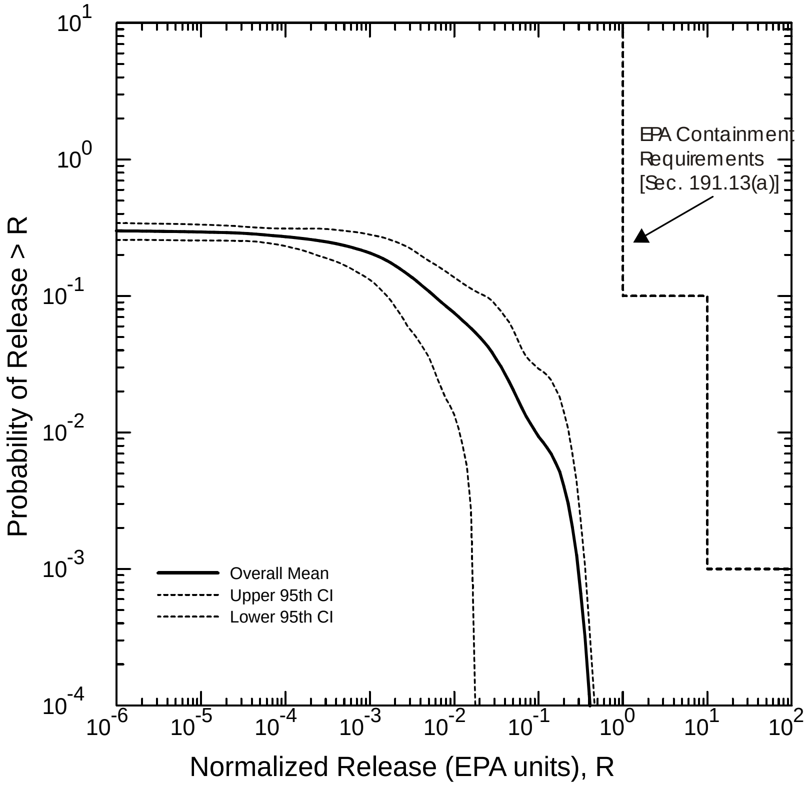

Figure PA-110. Confidence Interval on Overall Mean CCDF for Spallings Releases.

Section PA-8.5.2 presents a sensitivity analysis for spallings release volumes, and shows that the uncertainty in total spall volumes arises from the uncertainty in microbial action (WMICDFLG; see Table PA-17) and the uncertain spall volume from a single intrusion (see RNDSPALL in Table PA-17 and the discussion in Section PA-8.5.2). Since spall releases are computed by multiplying the volume released by the average concentration of radioactivity in the CH-TRU waste at the time of intrusion, the uncertainty in spalling releases is due to the same parameters that contribute to uncertainty in total spall volumes.

PA-9.4 Normalized Direct Brine Releases

Figures PA-111, PA-112, and PA-113 show the CCDFs for normalized direct brine releases for replicates R1, R2, and R3. The releases for each replicate are very similar; Figure PA-114 compares the mean and quantile CCDFs for each replicate; the 10th quantile for normalized DBRs does not plot on the scale of Figure PA-114. Figure PA-115 shows the 95 percent confidence interval about the overall mean of the CCDFs for DBRs, and shows that the overall mean is estimated reasonably well.

Section PA-8.5.3 provides an analysis identifying the sensitivity of the volume of brine released from a single intrusion to the uncertain parameters in the analysis. The sensitivity analysis showed that direct brine release volumes are most sensitive to uncertainty in pressure and brine saturation in the waste, which in turn, are most sensitive to microbial action in the waste (WMICDFLG; see Table PA-17) and borehole permeability (BHPERM).

As described in Section PA-6.8.5, DBRs are computed by multiplying the volume of brine released by the concentration of radionuclides in the brine. A stepwise regression analysis (summarized in Table PA-30) determined that the uncertainty in mean DBR is dominated by the parameters that influence the DBR volumes (WMIDFLG, the indicator for microbial action; BPINTPRS, the pressure in the Castile brine reservoir; PBRINE, the probability of an intrusion hitting the Castile brine reservoir; and WRBRNSAT, the residual brine saturation in the waste). The uncertainty in radionuclide concentration has a lesser influence on mean direct brine release, as only a single related parameter entered the analysis (WSOLAM3C, the uncertainty in the solubility of Am(III) in Castile brine). Figure PA-116 illustrates the sensitivity of mean DBR to DBR volume and to the most influential uncertain parameter, the indicator for microbial action (WMICDFLG). The figure shows that the mean DBRs is roughly proportional to the mean DBR volume among subsets of vectors with or without microbial action.

PA-9.5 Transport Normalized Releases

Figures PA-117 and PA-118 show the CCDFs for normalized releases due to transport through the Culebra for replicates R1 and R3. No transport releases larger than 10^{-6} EPA units occurred in replicate R2. Since the transport releases are small and statistically rare, no confidence intervals or sensitivity analyses are provided.

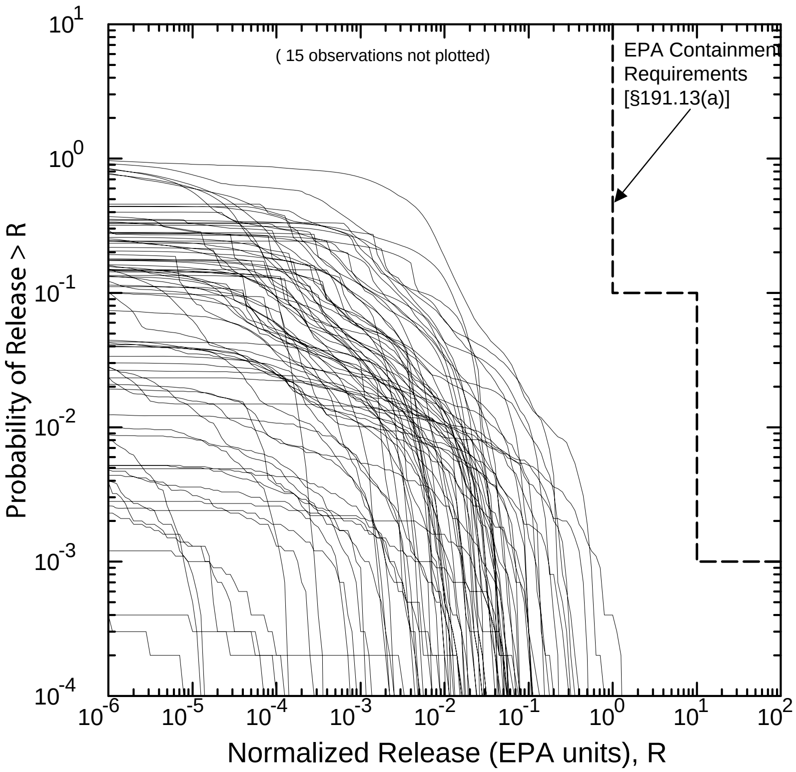

Figure PA-111. DBRs, Replicate R1.

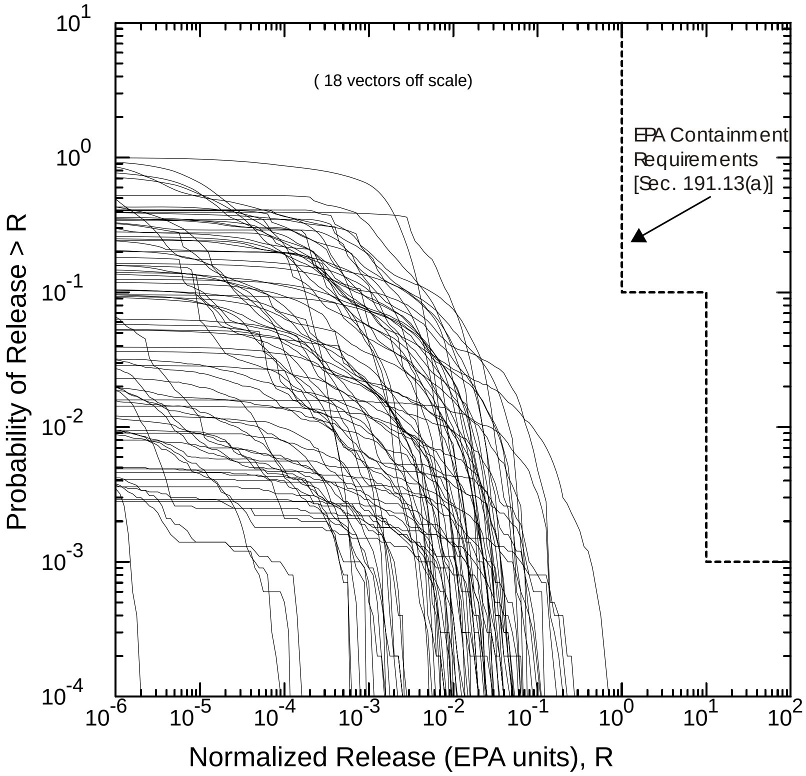

Figure PA-112. DBRs, Replicate R2.

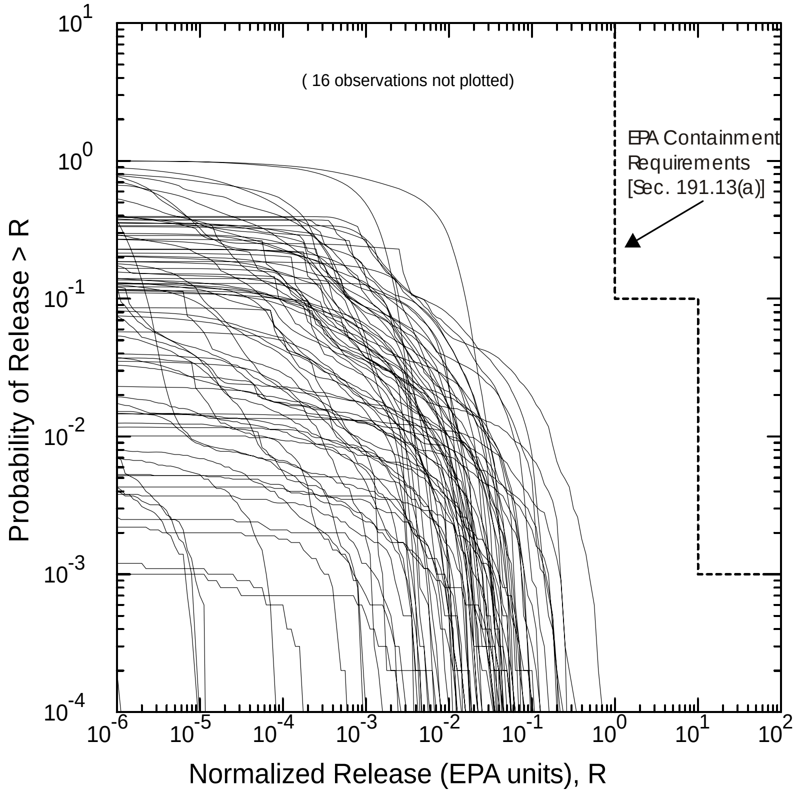

Figure PA-113. DBRs, Replicate R3.

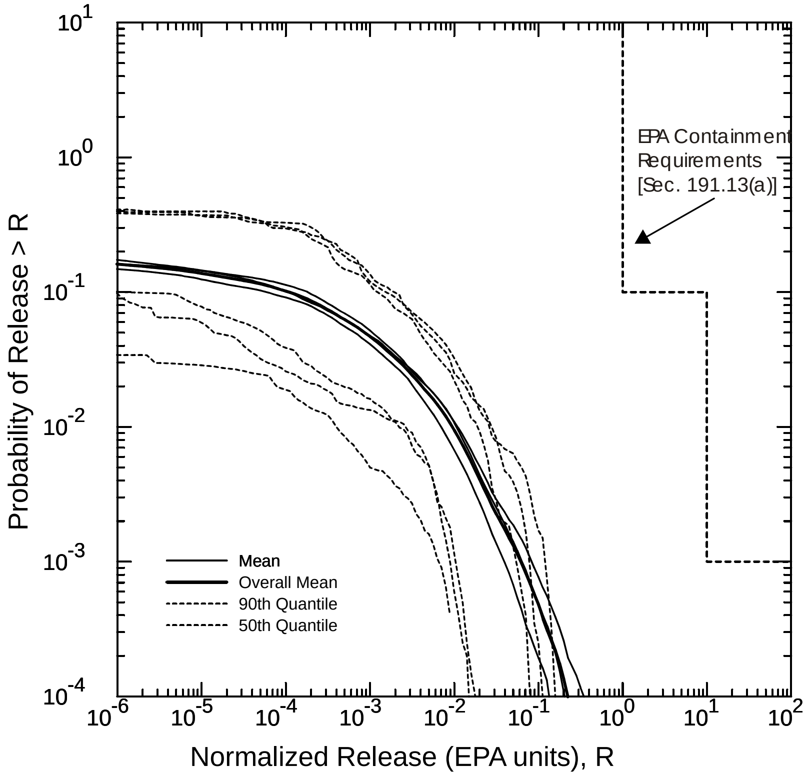

Figure PA-114. Mean and Quantile CCDFs for DBRs, All Replicates.

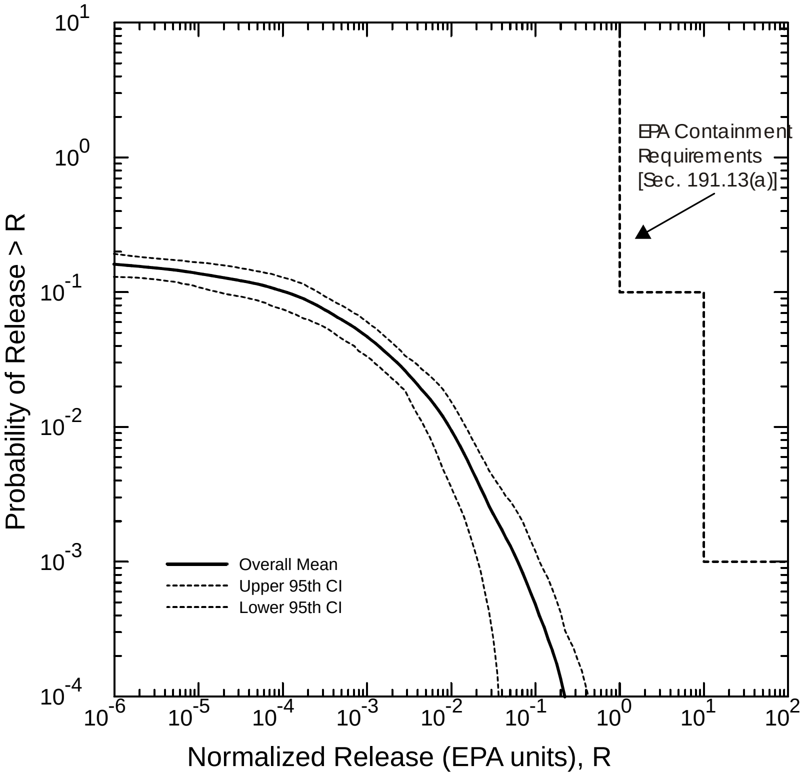

Figure PA-115. Confidence Interval on Overall Mean CCDF for DBRs.

Table PA-30. Stepwise Regression Analysis for Mean Total DBRs

	Expected Normalized Release		
Step[a]	Variable[b]	SRRC[c]	R^2[d]
1	WMICDFLG	-0.46784	0.15776
2	BPINTPRS	0.48223	0.34337
3	PBRINE	0.36000	0.47058
4	WSOLAM3C	0.29070	0.51608
5	WRBRNSAT	-0.15397	0.55481
6	CONGSSAT	-0.22426	0.57556
7	REPIPERM	-0.21496	0.60771
8	WGRCOR	-0.16265	0.63011
9	TENSLSTR	-0.14810	0.64990

[a] Steps in stepwise regression analysis

[b] Variables listed in order of selection in regression analysis

[c] Standardized Rank Regression Coefficient in final regression model

[d] Cumulative R^2 value with entry of each variable into regression model

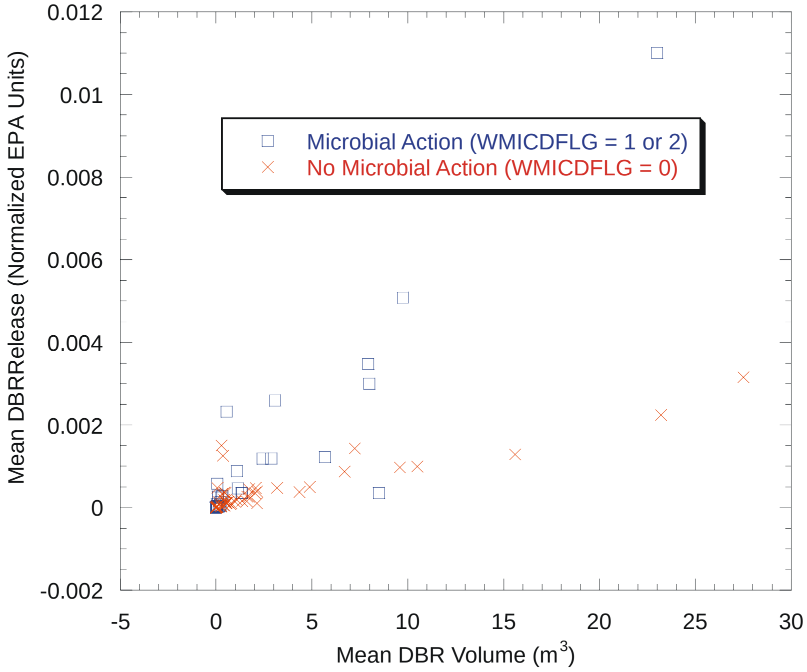

Figure PA-116. Sensitivity of DBRs.

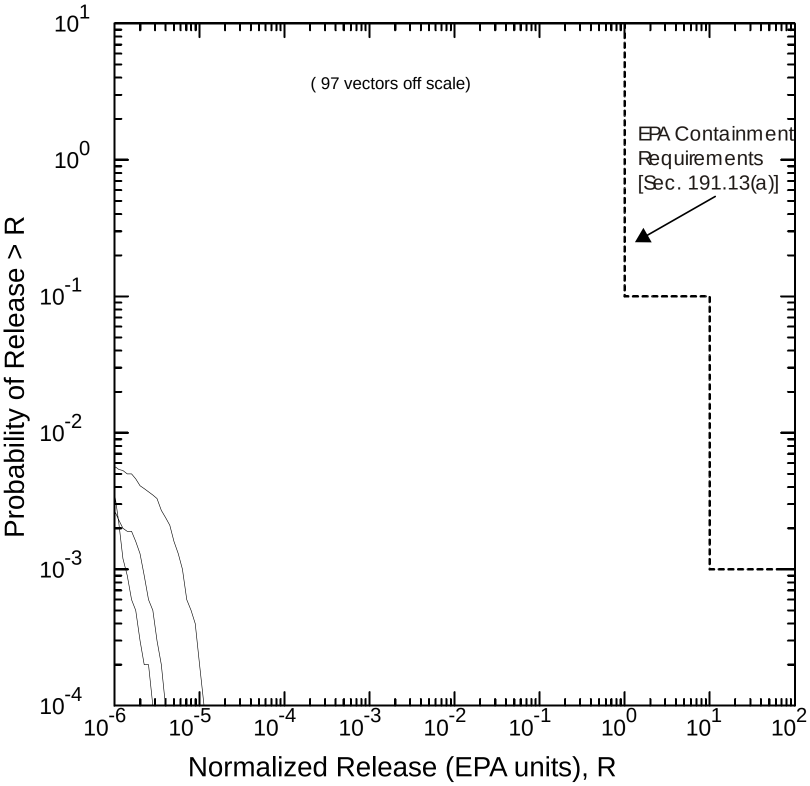

Figure PA-117. Transport Releases Through the Culebra, Replicate R1.

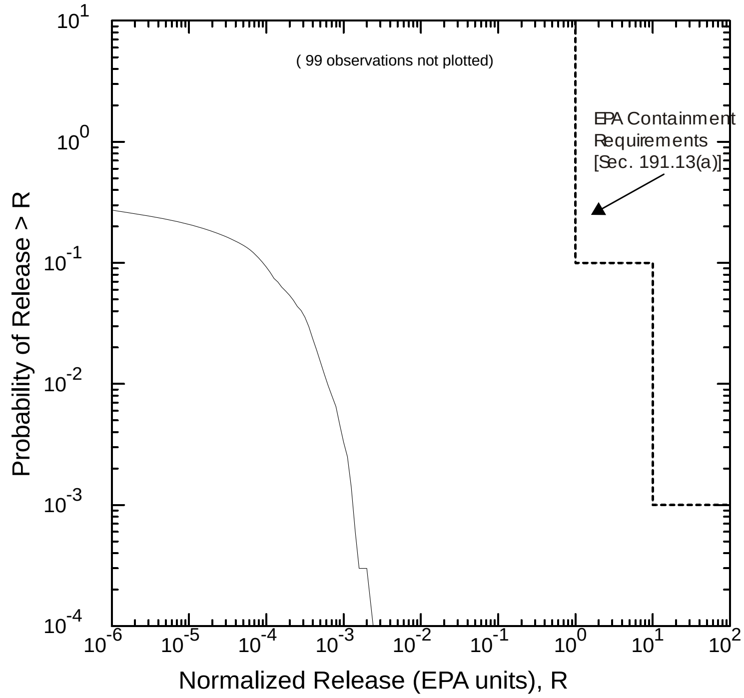

Figure PA-118. Transport Releases Through the Culebra, Replicate R3.

PA-9.6 Sensitivity Analysis for Total Normalized Releases

Uncertainty in total normalized releases is largely due to uncertainty in waste shear strength (WTAUFAIL; see Table PA-17). Table PA-31 lists the results of a stepwise regression between mean total normalized releases and the uncertain parameters in the analysis; waste shear strength (WTAUFAIL) is highly correlated with the uncertainty in mean total normalized releases. Figure PA-119 shows the relationship between the uncertainty in total releases and the uncertainty in WTAUFAIL for all replicates.

Table PA-31. Stepwise Regression Analysis for Mean Total Normalized Releases

	Expected Normalized Release		
Step[a]	Variable[b]	SRRC[c]	R^{2}[d]
1	WTAUFAIL	-0.95137	0.91345
2	WMICDFLG	0.11538	0.92727
3	DOMEGA	0.10735	0.93639
4	SPALLVOL	0.08003	0.94139
5	BPINTPRS	0.06271	0.94475
6	PLGPRM	0.05841	0.94802
7	SHLPRM3	-0.04728	0.95022

[a] Steps in stepwise regression analysis

[b] Variables listed in order of selection in regression analysis

[c] Standardized Rank Regression Coefficient in final regression model

[d] Cumulative R^{2} value with entry of each variable into regression model

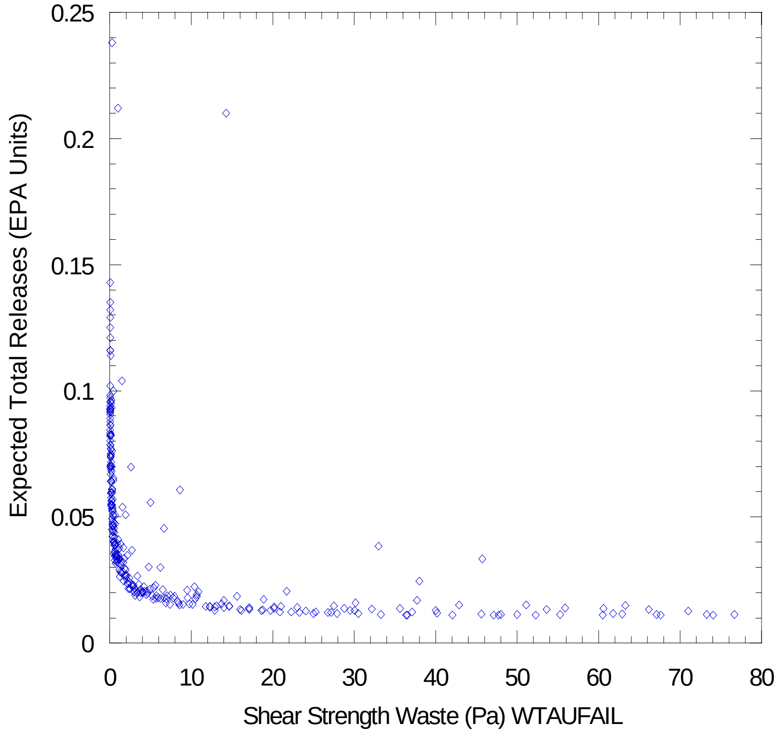

Figure PA-119. Uncertainty in Mean Total Releases Due to Waste Shear Strength, All Replicates.

As shown in Section PA-9.1, cuttings and cavings releases constitute most of the total releases from the repository. As shown in Section PA-8.5.1, most of the uncertainty in cuttings and cavings releases arises from uncertainty in waste shear strength (WTAUFAIL). Thus, uncertainty in WTAUFAIL dominates uncertainty in total releases.

The remaining uncertainty in total releases is primarily due to uncertainty in the spallings releases. Figure PA-120 compares total releases and cuttings and cavings releases for replicate R1, and shows that almost all of the total releases are due to cuttings and cavings. For replicate R1, Figure PA-121 shows the uncertainty in total releases that is not due to uncertainty in cuttings and cavings, and demonstrates that most of the remaining uncertainty arises from uncertainty in spallings releases. This figure shows that spallings releases account for almost all of the variability in the difference between the total releases and cuttings and cavings releases. The small amount of uncertainty in total releases that is not due to cuttings and cavings or spallings arises from uncertainty in the other components of total releases (i.e. DBR and transport releases). Since the three replicates are statistically similar (Figure PA-95), these conclusions hold for all replicates.

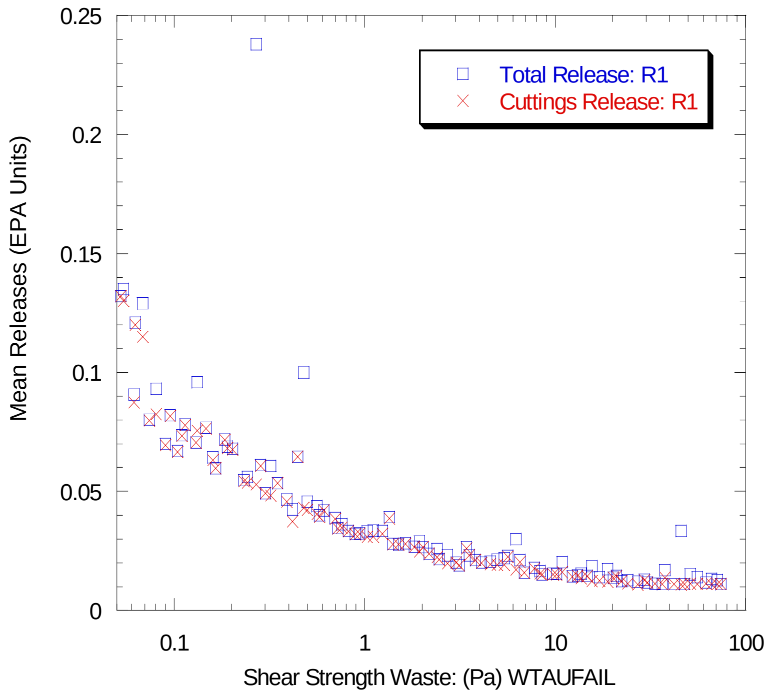

Figure PA-120. Comparison of Mean Total Releases to Mean Cuttings and Cavings Releases, Replicate R1.

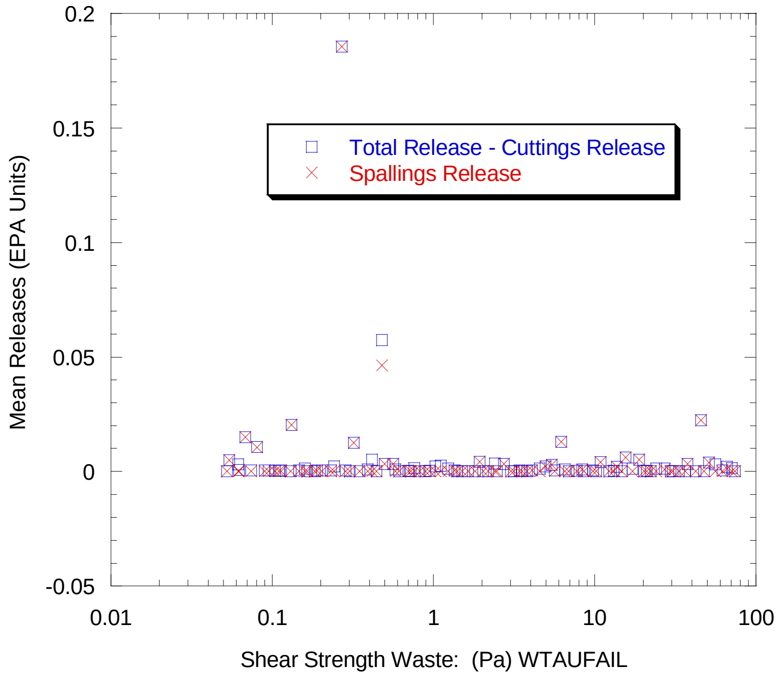

Figure PA-121. Comparison of Mean Total Releases Minus Mean Cuttings Releases to Spall Releases, Replicate R1.

REFERENCES

Abdul Khader, ×M.H., and H.S. Rao. 1974. "Flow Through Annulus with Large Radial Clearance," *American Society of Civil Engineers, Journal of the Hydraulics Division*. Vol. 100, no. HY1, 25-39.

Antoun, T., L. Seanman, D.R. Curran, G.I. Kanel, S.V. Razorenor, A.V. Utkin. 2003. "Spall Fracture." *Springer-Verlag*, New York, NY, USA.

Aronson, D.G. 1986. "The Porous Medium Equation." *Nonlinear Diffusion Problems*. Lecture Notes in Mathematics 1224. Springer-Verlag, New York, NY, USA.

Aziz, K., and A. Settari. 1979. *Petroleum Reservoir Simulation.* London: Applied Science Publishers; New York: Elsevier.

Bateman, H. 1910. "The Solution of a System of Differential Equations Occurring in the Theory of Radio-active Transformations," *Proceedings of the Cambridge Philosophical Society*. Vol. 15, pt. 5, 423-427.

Bean, J.E., M.E. Lord, D.A. McArthur, R.J. MacKinnon, J.D. Miller, and J.D. Schreiber. 1996. "Analysis Package for the Salado Flow Calculations (Task 1) of the Performance Assessment Analysis Supporting the Compliance Certification Application (CCA)." *Analysis Package.* Sandia National Laboratories. Albuquerque, NM. Sandia WIPP Central Files ERMS # 240514.

Barree, R.D., Conway, M.W. 1995 "Experimental and Numerical Modeling of Convective Proppant Transport," *Journal of Petroleum Technology*, March, 216-222.

Bear, J. 1972. D*ynamics of Fluids in Porous Media.* New York, NY: Dover Publications.

Belhaj, H.A., K.R. Agha, A.M. Nouri, S.D. Butt, H.F. Vaziri, and M.R. Islam. 2003. "Numerical Simulation of Non-Darcy Flow Utilizing the New Forchheimer's Diffusivity Equation," SPE 81499, presented at the SPE 13th Middle East Oil Show & Conference, Bahrain, April, 2003.

Berglund, J.W. 1992. *Mechanisms Governing the Direct Removal of Wastes from the Waste Isolation Pilot Plant Repository Caused by Exploratory Drilling*. SAND92-7295. Sandia National Laboratories. Albuquerque, NM.

Berglund, J.W. 1996. "Analysis Package for the Cuttings and Spallings Calculations (Task 5 and 6) of the Performance Assessment Calculation Supporting the Compliance Certification Application (CCA), AP-015 and AP-016." *Analysis package*. Sandia National Laboratories. Albuquerque, NM. Sandia WIPP Central Files ERMS # 240521.

Bilgen, E., R. Boulos, and A.C. Akgungor. 1973. "Leakage and Frictional Characteristics of Turbulent Helical Flow In Fine Clearance," *Journal of Fluids Engineering*. Transactions of the ASME. Series I. Vol. 95, no. 4, 493-497.

Brill, J.P., and H.D. Beggs. 1986. *Two-Phase Flow in Pipes*. 5th ed., first printing. Tulsa, OK: University of Tulsa.

Broc, R., ed. 1982. *Drilling Mud and Cement Slurry Rheology Manual*. Houston, TX: Gulf Publishing Company; Paris: Editions Techni. p.

Brooks, R.H., and A.T. Corey. 1964. “Hydraulic Properties of Porous Media.” *Hydrology Paper No. 3*. Fort Collins, CO: Colorado State University. Sandia WIPP Central Files ERMS # 241117.

Bynum, R.V., C. Stockman, Y. Wang, A. Peterson, J. Krumhansl, J. Nowak, J. Cotton, M.S.Y. Chu, and S.J. Patchett. 1997. “Implementation of Chemical Controls Through a Backfill System for the Waste Isolation Pilot Plant (WIPP),” *Proceedings of the Sixth International Conference on Radioactive Waste Management and Environmental Remediation*, ICEM ‘97, Singapore, October 12-16, 1997. SAND96-2656C. Eds. R. Baker, S. Slate, and G. Benda. New York, NY: American Society of Mechanical Engineers. 357-361.

Caporuscio, F., Gibbons, J., and Oswald, E. 2003. Waste Isolation Pilot Plant: *Salado Flow Conceptual Models Final Peer Review Report*. Report prepared for the U.S. Department of Energy, Carlsbad Area Office, Office of Regulatory Compliance. ERMS # 526879.

Chappelear, J.E., and A.S. Williamson. 1981. “Representing Wells in Numerical Reservoir Simulation—2. Implementation,” *SPEJ Society of Petroleum Engineers Journal*. Vol. 21, no. 3, 339-344.

Cherimisinoff, N.P., Cherimisinoff, P.N., 1984. *Hydrodynamics of Gas-Solids Fluidization*, Gulf Publishing Company, Houston, TX, USA

Christian-Frear, T.L. 1996. “Salado Halite Permeability from Room Q Analysis.” *Records Package*. Sandia National Laboratories. Albuquerque, NM. Sandia WIPP Central Files ERMS # 230721.

Corbet, T.F., and P.M. Knupp. 1996. *The Role of Regional Groundwater Flow in the Hydrogeology of the Culebra Member of the Rustler Formation at the Waste Isolation Pilot Plant (WIPP),* Southeastern New Mexico. SAND96-2133. Albuquerque, NM: Sandia National Laboratories. Albuquerque, NM.

Corbet, T. and P. Swift. 1996a. “Distribution for Non-Salado Parameter for SECOFL2D: Climate Index.” Memo to M.S. Tierney, April 12, 1996. Sandia National Laboratories. Albuquerque, NM. Sandia WIPP Central Files ERMS # 237465, Segment 2.

Corbet, T., and P. Swift. 1996b. “Parameters Required for SECOFL2D: Climate Index.” *Record Package*. Albuquerque, NM: Sandia National Laboratories. Albuquerque, NM. Sandia WIPP Central Files ERMS # 236425.

Darley, H.C.H. 1969. “A Laboratory Investigation of Borehole Stability,” *JPT Journal of Petroleum Technology*. July 1969, 883-892.

Dogherty, J. 2002. *Design Document (DD) for PEST Version 5.5*. Los Alamos National Laboratories. Los Alamos, NM. Sandia WIPP Central Files ERMS #523970.

Dunagan, S.C. 2003a. “Analysis Package for CUTTINGS and CAVINGS: Compliance Recertification Application.” Sandia National Laboratories. Carlsbad, NM. Sandia WIPP Central Files ERMS # 530167.

Dunagan, S.C. 2003b. *Estimated Number of Boreholes Into CH-Waste in 10,000 years. Memorandum to C. Hansen*. Sandia National Laboratories. Carlsbad, NM. Sandia WIPP Central Files ERMS # 532277.

Ely, J.F. and M.L. Huber. 1992. *NIST Thermophysical Properties of Hydrocarbon Mixtures Database (SUPERTRAPP*), Version 1.0, User’s Guide. Gaithersburg, MD: U.S. Department of Commerce, National Institute of Standards and Technology, Standard Reference Data Program. Sandia WIPP Central Files ERMS # 242589.

Ergun, S. 1952. “Fluid Flow Through Packed Columns,” *Chemical Engineering Progress*, 48:89-94.

Feller, W. 1971. *An Introduction to Probability Theory and Its Applications.* 2nd ed. New York, NY: John Wiley & Sons. Vol. 2.

Fletcher, C.A.J. 1988. *Computational Techniques for Fluid Dynamics*. 2nd ed. Berlin; New York: Springer-Verlag. Vols. 1-2.

Fox, B.L. 2003. *Analysis Package for EPA Unit Loading Calculations: Compliance Recertification Application, Revision 1*. Sandia National Laboratories. Carlsbad, NM. Sandia WIPP Central Files ERMS # 531582.

Fox, R.W., McDonald, A.T. 1985. *Introduction to Fluid Mechanics*, 3rd Ed., John Wiley and Sons, New York, USA.

Francis, A.J., J.B. Gillow, and M.R. Giles. 1997. *Microbial Gas Generation Under Expected Waste Isolation Pilot Plant Repository Conditions.* SAND96-2582. Albuquerque, NM: Sandia National Laboratories.

Frigaard, I.A. and N.L. Humphries. 1997. *High Penetration Rates: Hazards and Well Control - A Case Study: Proceedings*, March 1997 Society of Petroleum Engineers/International Association of Drilling Contractors Drilling Conference. SPE paper 37953. Amsterdam, Netherlands: Society of Petroleum Engineers.

Garner, J. 2003. "Analysis Package for PANEL: Compliance Recertification Application." Sandia National Laboratories. Carlsbad, NM. Sandia WIPP Central Files ERMS # 530165.

Gatlin, C. 1960. *Petroleum Engineering: Drilling and Well Completions*. Englewood Cliffs, NJ: Prentice-Hall, Inc.

Graboski, M.S., and T.E. Daubert. 1979. “A Modified Soave Equation of State for Phase Equilibrium Calculations. 3: Systems Containing Hydrogen,” *Industrial and Engineering Chemistry*. Process Design and Development. Vol. 18, 300-306.

Haberman, J.H., and D.J. Frydrych. 1988. "Corrosion Studies of A216 Grade WCA Steel in Hydrothermal Magnesium-Containing Brines," *Scientific Basis for Nuclear Waste Management XI, Materials Research Society Symposium Proceedings*, Boston, MA, November 30 - December 3, 1987. Eds. M.J. Apted and R.E. Westerman. Pittsburgh, PA: Materials Research Society Vol. 112, 761-772.

Hadgu, T., Vaughn, P., Bean, J., Johnson, D., Johnson, J., Aragon, K., and Helton, J. 1999. Modifications to the 96 CCA direct brine release calculations. Memorandum to M. Marietta dated November 2, 1999. Sandia National Laboratories. Carlsbad, NM. Sandia WIPP Central Files ERMS # 511276.

Hansen, C., Leigh, C., Stein, J., and Lord, D. 2002. *"BRAGFLO Results for the Technical Baseline Migration"* Sandia National Laboratories. Carlsbad, NM. Sandia WIPP Central Files ERMS # 523209

Hansen, C. and Leigh, C. 2003. *"A Reconciliation of the CCA and PAVT Parameter Baselines, Rev. 3"* Sandia National Laboratories. Carlsbad, NM. Sandia WIPP Central Files ERMS # 528582

Hansen, F.D., Knowles, M.K., Thompson, T.W., Gross, M., McLennan, J.D., and J.F. Schatz, 1997. *Description and Evaluation of a Mechanistically Based Conceptual Model for Spall,* SAND97-1369, Sandia National Laboratories, Albuquerque, NM.

Hansen, F.D., Pfeifle, T.W., Lord, D.L. 2003. *Parameter Justification Report for DRSPALL.* Sandia National Laboratories. Carlsbad, NM. Sandia WIPP Central Files ERMS # 531057.

Harbaugh, A.W., E.R. Banta, M.C. Hill, and M.G. McDonald. 2000. *MODFLOW-2000: The U.S. Geological Survey Modular Ground-Water Model – User Guide to Modularization Concepts and the Ground-Water Flow Process*. Open File Report 00-92. Reston, VA: U.S. Geological Survey, 121 pp.

Helton, J.C. 1993. "Drilling Intrusion Probabilities for Use in Performance Assessment for Radioactive Waste Disposal," *Reliability Engineering and System Safety*. Vol. 40, no. 3, 259-275.

Helton, J.C. 1996. "Probability, Conditional Probability and Complementary Cumulative Distribution Functions in Performance Assessment for Radioactive Waste Disposal," *Reliability Engineering and System Safety*. Vol. 54, no. 2-3, 145-163.

Helton, J.C. 1997. "Uncertainty and Sensitivity Analysis in the Presence of Stochastic and Subjective Uncertainty," *Journal of Statistical Computation and Simulation*. Vol. 57, no. 1-4, 3-76.

Helton, J.C., and H.J. Iuzzolino. 1993. "Construction of Complementary Cumulative Distribution Functions for Comparison with the EPA Release Limits for Radioactive Waste Disposal," *Reliability Engineering and System Safety*. Vol. 40, no. 3, 277-293.

Helton, J.C., J.D. Johnson, M.D. McKay, A.W. Shiver, and J.L. Sprung. 1995. "Robustness of an Uncertainty and Sensitivity Analysis of Early Exposure Results with the MACCS Reactor Accident Consequence Model," *Reliability Engineering and System Safety*. Vol. 48, no. 2, 129-148.

Helton, J.C., and A.W. Shiver. 1996. "A Monte Carlo Procedure for the Construction of Complementary Cumulative Distribution Functions for Comparison with the EPA Release Limits for Radioactive Waste Disposal," *Risk Analysis*. Vol. 16, no. 1, 43-55.

Helton, J.C., Bean, J.E., Berglund, J.W., Davis, F.J., Economy, K., Garner, J.W., Johnson, J.D., MacKinnon, R.J., Miller, J., O'Brien, D.G., Ramsey, J.L., Schreiber, J.D., Shinta, A., Smith, L.N., Stoelzel, D.M., Stockman, C., and Vaughn, P. 1998. *"Uncertainty and Sensitivity Analysis Results Obtained in the 1996 Performance Assessment for the Waste Isolation Pilot Plant."* Sandia National Laboratories. SAND98-0365.

Helton, J.C. and Davis, F.J. 2003. "Latin Hypercube Sampling and the Propagation of Uncertainty in Analyses of Complex Systems," *Reliability Engineering and System Safety*. Vol 81, no. 1, 23-69.

Hirsch, Charles 1988. "Numerical Computation of Internal and External Flows," *Fundamentals of Numerical Discretization.* Vol. 1. Chichister, UK: John Wiley & Sons.

Howard, B.A. 1996. "Performance Assessment Parameter Input." Memo to M. Marietta, February 23, 1996. Carlsbad, NM: Westinghouse Electric Corporation to Sandia National Laboratories, Albuquerque, NM. Sandia WIPP Central Files ERMS # 247595.

Howarth, S.M., and T. Christian-Frear. 1997. *Porosity, Single-Phase Permeability, and Capillary Pressure Data from Preliminary Laboratory Experiments on Selected Samples from Marker Bed 139 at the Waste Isolation Pilot Plant.* SAND94-0472/1/2/3. Sandia National Laboratories. Albuquerque, NM.

Hunter, R.L. 1985. *A Regional Water Balance for the Waste Isolation Pilot Plant (WIPP) Site and Surrounding Area.* SAND84-2233. Sandia National Laboratories. Albuquerque, NM.

Hurtado, L.D., Knowles, M.K., Kelley, V.A., Jones, T.L., Ogintz, J.B., and Pfeifle, T.W. 1997. *WIPP Shaft Seal System Parameters Recommended to Support Compliance Calculations.* SAND97-1287. Sandia National Laboratories. Albuquerque, NM.

Huyakorn, P.S., B.H. Lester, and J.W. Mercer. 1983. "An Efficient Finite Element Technique for Modelling Transport in Fractured Porous Media: 1. Single Species Transport," *Water Resources Research*. Vol. 19, no. 3, 841-854.

Iman, R.L. 1982. "Statistical Methods for Including Uncertainties Associated with the Geologic Isolation of Radioactive Waste Which Allow for a Comparison with Licensing Criteria," *Proceedings of the Symposium on Uncertainties Associated with the Regulation of the Geologic Disposal of High-Level Radioactive Waste*, March 9-13, 1981. Ed. D.C. Kocher. NUREG/CP-0022, CONF-810372. Washington, DC: U.S. Nuclear Regulatory Commission, Directorate of Technical Information and Document Control. 145-157.

Iman, R.L., M.J. Shortencarier, and J.D. Johnson. 1985. *A FORTRAN 77 Program and User's Guide for the Calculation of Partial Correlation and Standardized Regression Coefficients.* NUREG/CR-4122, SAND85-0044. Sandia National Laboratories. Albuquerque, NM.

Iman, R.L., and W.J. Conover. 1979. "The Use of the Rank Transform in Regression." *Technometrics*. Vol. 21, no. 4, 499-509.

Iman, R.L., and W.J. Conover. 1982. "A Distribution-Free Approach to Inducing Rank Correlation Among Input Variables," *Communications in Statistics: Simulation and Computation.* Vol. B11, no. 3, 311-334.

Iman, R.L., and J.C. Helton. 1988. "An Investigation of Uncertainty and Sensitivity Analysis Techniques for Computer Models," *Risk Analysis.* Vol. 8, no. 1, 71-90.

Iman R.L., and J.C. Helton. 1991. "The Repeatability of Uncertainty and Sensitivity Analyses for Complex Probabilistic Risk Assessments," *Risk Analysis*. Vol. 11, no. 4, 591-606.

James, S.J., and Stein, J. 2002. "Analysis Plan for the Development of a Simplified Shaft Seal Model for the WIPP Performance Assessment." AP-094. Sandia National Laboratories. Carlsbad, NM. Sandia WIPP Central Files ERMS # 524958.

James, S.J., and Stein, J. 2003. *"Analysis Report for the Development of a Simplified Shaft Seal Model for the WIPP Performance Assessment Rev 1."* Sandia National Laboratories. Carlsbad, NM. Sandia WIPP Central Files ERMS # 525203.

Kaufmann, D.W., ed. 1960. *Sodium Chloride, The Production and Properties of Salt and Brine.* ACS Monograph 145. New York, NY: Reinhold Pub. Corp.; Washington, DC: American Chemical Society.

Kanney, J. 2003. "*Analysis Package for the Culebra Transport Calculation: Compliance Recertification Application.*" Sandia National Laboratories. Carlsbad, NM. Sandia WIPP Central Files ERMS # 530168.

Klinkenberg, L.J. 1941. "The Permeability of Porous Media to Liquids and Gases," *API Drilling and Production Practice.* 200-213. Sandia WIPP Central Files ERMS # 208556.

Lee, J. 1982. Well Testing. SPE Textbook Series Vol. 1. New York, NY: Society of Petroleum Engineers of AIME.

Leigh, C., Beauheim, R., Kanney, J. 2003. *"SNL WIPP Analysis Plan AP-100, Revision 0, Analysis Plan for Calculation of Culebra Flow and Transport, Compliance Recertification Application."* Sandia National Laboratories. Carlsbad, NM. Sandia WIPP Central Files ERMS # 530172.

Li, D., Svec, R.K., Engler, T.W. and Grigg, R.B. 2001. "*Modeling and Simulation of the Wafer Non-Darcy Flow Experiments,*" paper SPE 68822, SPE Western Regional Meeting, Bakersfield, CA, March 26-30.

Lide, D.R., ed. 1991. CRC Handbook of Chemistry and Physics. 72nd ed. Boca Raton, FL: CRC Press.

Long, J. 2003. *Execution of the Performance Assessment for the Compliance Recertification Application (CRA1).* Sandia National Laboratories. Carlsbad, NM. Sandia WIPP Central Files ERMS # 530150.

Lord, D.L., Rudeen, D.K., Hansen, C.W. 2003 *Analysis Package for DRSPALL: Compliance Recertification Application Part I – Calculation of Spall Volume.* Sandia National Laboratories. Carlsbad, NM. Sandia WIPP Central Files ERMS # 532766.

Lord, D.L., Rudeen, D.K. 2003. *Sensitivity Analysis Report – Parts I and II, DRSPALL version 1.00, Report for Conceptual Model Peer Review July 7-1*1. Sandia National Laboratories. Carlsbad, NM. Sandia WIPP Central Files ERMS # 524400.

Lowry, T. 2003. *Analysis Package for Salado Transport Calculations: Compliance Recertification Application* . Sandia National Laboratories. Carlsbad, NM. Sandia WIPP Central Files ERMS 530163

Martell, M. 1996a. "Additional Information for the DRZ (Disturbed Rock Zone) Porosity." Memo to C. Lattier, November 14, 1996. Sandia National Laboratories. Albuquerque, NM. Sandia WIPP Central Files ERMS # 242257.

Martell, M. 1996b. "Additional Information for the Culebra Transport Parameter Id: 843, idpram: DNSGRAIN, idmtrl: CULEBRA, WIPP Data Entry Form 464 at WPO # 32689." Memo to C. Lattier, December 10, 1996. Sandia National Laboratories. Albuquerque, NM. Sandia WIPP Central Files ERMS # 232689.

Mattax, C.C., and R.L. Dalton. 1990. *Reservoir Simulation*. SPE Monograph 13. Richardson, TX: Henry L. Doherty Memorial Fund of Society of Petroleum Engineers Inc.

McDonald, M.G., and Harbaugh, A.W. 1988. *A Modular Three-Dimensional Finite-Difference Ground-Water Flow Model: U.S. Geological Survey Techniques of Water-Resources Investigations,* Book 6, Chap. A1. U.S. Government Printing Office.

McKay, M.D., R.J. Beckman, and W.J. Conover. 1979. "A Comparison of Three Methods for Selecting Values of Input Variables in the Analysis of Output from a Computer Code," *Technometrics*. Vol. 21, no. 2, 239-245.

McKenna, S.A. and D. Hart. 2003. *Analysis Report Task 4 of AP-088 Conditioning of Base T-Fields to Transient Heads. Sandia National Laboratories*. Albuquerque, NM. Sandia WIPP Central Files ERMS # 531124.

McTigue, D.F. 1993. *Permeability and Hydraulic Diffusivity of Waste Isolation Pilot Plant Repository Salt Inferred from Small-Scale Brine Inflow Experiments*. SAND92-1911. Sandia National Laboratories. Albuquerque, NM.

Mehl, S.W. and M.C. Hill. 2001. MODFLOW-2000, *The U.S. Geological Survey Modular Ground-Water Model – User Guide to the Link-AMG (LMG) Package for Solving Matrix Equations Using and Algebraic Multigrid Solver*. Open File Report 01-177. Denver, CO: U.S. Geological Survey, 34 pp.

Meigs, L. 1996. “Non-Salado: Diffusive Tortuosity for the Culebra Dolomite (WPO#37226).” Memo to J. Ramsey, May 16, 1996. Sandia National Laboratories. Albuquerque, NM. Sandia WIPP Central Files ERMS # 238940.

Meigs, L., and J. McCord. 1996. *Physical Transport in the Culebra Dolomite.* Sandia National Laboratories. Albuquerque, NM. Sandia WIPP Central Files ERMS # 239167.

Mendenhall, F.T., and W. Gerstle. 1995. “WIPP Anhydrite Fracture Modeling,” *Systems Prioritization Method - Iteration 2 Baseline Position Paper: Disposal Room and Cutting Models.* B.M. Butcher, S.W. Webb, J.W. Berglund, and P.R. Johnson. Sandia National Laboratories. Albuquerque, NM. Sandia WIPP Central Files ERMS # 239830.

Myers, R.H. 1986. *Classical and Modern Regression with Applications*. Boston, MA: Duxbury Press.

Oldroyd, J.G. 1958. “Non-Newtonian Effects in Steady Motion of Some Idealized Elastico-Viscous Liquids,” *Proceedings of the Royal Society of London*. Series A. Mathematical and Physical Sciences. Vol. 245, no. 1241, 278-297. Sandia WIPP Central Files ERMS # 243211.

Podio, A.L. and A.P. Yang, 1986. “Well Control Simulator for IBM Personal Computer,” IADC/SPE 14737. *International Association of Drilling Engineers/Society of Petroleum Engineers paper presented at the IADC/SPE Drilling Conference held in Dallas, TX.* February 10-12.

Poettmann, F.H., and P.G. Carpenter. 1952. “Multiphase Flow of Gas, Oil, and Water Through Vertical Flow Strings with Application to the Design of Gas-lift Installations,” *Drilling and Production Practice.* 257-317.

Prasuhn, A.L. 1980. *Fundamentals of Fluid Mechanics.* Englewood Cliffs, NJ: Prentice-Hall, Inc.

Prausnitz, J.M. 1969. *Molecular Thermodynamics of Fluid - Phase Equilibria.* Englewood Cliffs, NJ: Prentice-Hall, Inc.

Press, W.H., B.P. Flannery, S.A. Teukolsky, and W.T. Vetterling. 1989. *Numerical Recipes in Pascal —The Art of Scientific Computing,* Cambridge University Press, Cambridge England

Rechard, R.P., H. Iuzzolino, and J.S. Sandha. 1990. *Data Used in Preliminary Performance Assessment of the Waste Isolation Pilot Plant (1990).* SAND89-2408. Sandia National Laboratories. Albuquerque, NM.

Roache, P.J. 1972. *Computational Fluid Dynamics*. Rev. printing. Albuquerque, NM: Hermosa Publishers.

Roberts, R. 1996. “Salado: Brine Compressibility.” *Records Package*. Sandia National Laboratories. Albuquerque, NM. Sandia WIPP Central Files ERMS # 231174.

Ross, S.M. 1987. *Introduction to Probability and Statistics for Engineers and Scientists*. New York, NY: John Wiley & Sons.

Ruge, J.K. and K. Stuben. 1987. *Algebraic Multigrid,* in McCormick, S.F. ed., Multigrid Methods: Philadelphia, Society for Industrial and Applied Mathematics, p. 73-130.

Ruth, D. and Ma, H. 1992. “On the Derivation of the Forchheimer Equation by Means of the Averaging Theorem.” *Transport in Porous Media* 7: 255, 264.

Sandia National Laboratories (SNL). 1997. *Summary of Uncertainty and Sensitivity Analysis Results for the EPA-Mandated Performance Assessment Verification Test.* Sandia National Laboratories. Albuquerque, NM. Sandia WIPP Central Files ERMS # 420667.

Savins, J.G., and G.C. Wallick. 1966. “Viscosity Profiles, Discharge Rates, Pressures, and Torques for a Rheologically Complex Fluid in a Helical Flow,” *A.I.Ch.E. Journal.* Vol. 12, no. 2, 357-363.

Stein, J. 2002a. "Methodology behind the TBM BRAGFLO Grid." Memorandum to M.K. Knowles, May 13, 2002. Sandia National Laboratories. Carlsbad, NM. Sandia WIPP Central Files ERMS # 522373.

Stein, J. 2002b. "Errors Identified in Waste Storage Volume Parameters used to Construct BRAGFLO Grid." Memorandum to M. K. Knowles, Sept. 17, 2002. Sandia National Laboratories. Carlsbad, NM. Sandia WIPP Central Files ERMS # 523760.

Stein, J.S. 2003. *Analysis Package for Direct Brine Releases: Compliance Recertification Application REV 1.* Sandia National Laboratories. Carlsbad, NM. Sandia WIPP Central Files ERMS # 532344.

Stein, J., and Zelinski, W. 2003a. *Analysis Report for: Testing of a Proposed BRAGFLO Grid to be used for the Compliance Recertification Application Performance Assessment Calculations. Sandia National Laboratories.* Carlsbad, NM. Sandia WIPP Central Files ERMS # 526868.

Stein, J., and Zelinski, W. 2003b. *Analysis Package for BRAGFLO: Compliance Recertification Application.* Sandia National Laboratories. Carlsbad, NM. Sandia WIPP Central Files ERMS # 530163.

Stoelzel, D.M., and D.G. O’Brien. 1996. “Analysis Package for the BRAGFLO Direct Release Calculations (Task 4) of the Performance Assessment Calculations Supporting the Compliance Certification Application (CCA), AP-029, Brine Release Calculations.” *Analysis Package.* Sandia National Laboratories. Albuquerque, NM. Sandia WIPP Central Files ERMS # 240520.

Stone, C.M. 1997. SANTOS - *A Two-Dimensional Finite Element Program for the Quasistatic, Large Deformation, Inelastic Response of Solids.* SAND90-0543. Sandia National Laboratories. Albuquerque, NM.

Streeter, V.L. 1958. Fluid Mechanics. 2nd ed. New York, NY: McGraw-Hill.

Sweby, P.K. 1984. "High Resolution Schemes Using Flux Limiters for Hyperbolic Conservation Laws." *SIAM Journal on Numerical Analysis*. Vol. 21, no. 5, 995-1011.

Telander, M.R., and R.E. Westerman. 1993. *Hydrogen Generation by Metal Corrosion in Simulated Waste Isolation Pilot Plant Environments: Progress Report for the Period November 1989 Through December 1992.* SAND92-7347. Sandia National Laboratories. Albuquerque, NM:

Telander, M.R., and R.E. Westerman. 1997. *Hydrogen Generation by Metal Corrosion in Simulated Waste Isolation Pilot Plant Environments.* SAND96-2538. Sandia National Laboratories. Albuquerque, NM:

Thompson, T.W., W.E. Coons, J.L. Krumhansl, and F.D. Hansen. 1996. *"Inadvertent Intrusion Borehole Permeability, Final Draft."* May 20, 1996. Sandia National Laboratories. Albuquerque, NM. Sandia WIPP Central Files ERMS # 241131.

Timoshenko, S.P. and J.N. Goodier. 1970. *Theory of Elasticity*, Third Ed. McGraw-Hill: New York, NY.

U.S. Department of Energy (DOE). 1995 *Waste Isolation Plant Sealing System Design Report.* DOE/WIPP-95-3117. Carlsbad, NM: United States Department of Energy, Waste Isolation Pilot Plant, Carlsbad Area Office.

U.S. Department of Energy (DOE). 1996. *Title 40 CFR Part 191 Compliance Certification Application for the Waste Isolation Pilot Plant.* DOE/CAO-1996-2184. Carlsbad, NM: U.S. Department of Energy, Waste Isolation Pilot Plant, Carlsbad Area Office.

U.S. Environmental Protection Agency (EPA). 1985. *"40 CFR 191: Environmental Standards for the Management and Disposal of Spent Nuclear Fuel, High-Level and Transuranic Radioactive Wastes; Final Rule," Federal Register*. Vol. 50, no. 182, 38066-38089.

U.S. Environmental Protection Agency (EPA). 1993. *"40 CFR 191: Environmental Radiation Protection Standards for the Management and Disposal of Spent Nuclear Fuel, High-Level and Transuranic Radioactive Wastes; Final Rule," Federal Register*. Vol. 58, no. 242, 66398-66416.

U.S. Environmental Protection Agency (EPA). 1996. *"40 CFR Part 194: Criteria for the Certification and Re-Certification of the Waste Isolation Pilot Plant's Compliance With the 40 CFR Part 191 Disposal Regulations; Final Rule," Federal Register*. Vol. 61, no. 28, 5224-5245.

U.S. Environmental Protection Agency (EPA). 1998. Technical Support Document for 194.23: Models and Computer Codes, EPA Air Docket A-93-02 V-B-6, Washington DC.

van Genuchten, R. 1978. *Calculating the Unsaturated Hydraulic Conductivity with a New Closed-Form Analytical Model.* Report 78-WR-08. Princeton, NJ: Princeton University, Department of Civil Engineering, Water Resources Program. Sandia WIPP Central Files ERMS # 249486.

Vargaftik, N.B. 1975. *Tables on the Thermophysical Properties of Liquids and Gases in Normal and Dissociated States.* 2nd ed. Washington, DC: Hemisphere Pub. Corp.; New York, NY: Distributed by Halsted Press.

Vaughn, P. 1996. “WAS_AREA and REPOSIT SAT_RBRN Distribution.” Memo with attachments to M. Tierney, February 13, 1996. Sandia National Laboratories. Albuquerque, NM. Sandia WIPP Central Files ERMS # 234902.

Walas, S.M. 1985. *Phase Equilibria in Chemical Engineering.* Boston, MA: Butterworth Publishers.

Walker, R.E. 1976. “Hydraulic Limits are Set by Flow Restrictions,” *Oil and Gas Journal*. Vol. 74, no. 40, 86-90.

Walker, R.E., and W.E. Holman. 1971. “Computer Program Predicting Drilling-Fluid Performance,” *Oil and Gas Journal.* Vol. 69, no. 13, 80-90.

Wang, Y., and L. Brush. 1996a. “Estimates of Gas-Generation Parameters for the Long-Term WIPP Performance Assessment.” Memo to M. Tierney, January 26, 1996. Sandia National Laboratories. Albuquerque, NM. Sandia WIPP Central Files ERMS # 231943.

Wang, Y., and L. Brush. 1996b. “Modify the Stoichiometric Factor y in BRAGFLO to Include the Effect of MgO Added to WIPP Repository as Backfill.” Memo to M. Tierney, February 23, 1996. Sandia National Laboratories. Albuquerque, NM. Sandia WIPP Central Files ERMS # 232286.

Weast, R.C., ed. 1969. *Handbook of Chemistry and Physics.* 50th ed. Cleveland, OH: Chemical Rubber Pub. Co.

Webb, S.W. 1992. “Appendix A: Uncertainty Estimates for Two-Phase Characteristic Curves for 1992 40 CFR 191 Calculations,” *Preliminary Performance Assessment for the Waste Isolation Pilot Plant, December 1992.* Volume 3: Model Parameters. Sandia WIPP Project. SAND92-0700/3. Sandia National Laboratories. Albuquerque, NM. A-147 through A-155.

Welchon, J.K., A.F. Bertuzzi, and F.H. Poettmann. 1962. “Chapter 31 Wellbore Hydraulics,” *Petroleum Production Handbook*. Eds. T.C. Frick and R.W. Taylor. Dallas, TX: Society of Petroleum Engineers of AIME. 31-1 to 31-36.

Whittaker, A., ed. 1985. *Theory and Application of Drilling Fluid Hydraulics.* Boston, MA: International Human Resources Development Corporation.

Whitaker, S. 1996. “The Forchheimer Equation: A Theoretical Development.” *Transport in Porous Media* 25: 27-61.

Williamson, A.S., and J.E. Chappelear. 1981. "Representing Wells in Numerical Reservoir Simulation: Part 1 - Theory," "Representing Wells in Numerical Reservoir Simulation: Part 2 - Implementation." *Society of Petroleum Engineers Journal*. Vol. 21, no. 3, 323-338.

WIPP Performance Assessment. 1991-1992. *Preliminary Comparison with 40 CFR Part 191, Subpart B for the Waste Isolation Pilot Plant, December 1991*. SAND91-0893/1-4. Sandia National Laboratories. Albuquerque, NM. Vols. 1-4.

WIPP Performance Assessment. 1992-1993. *Preliminary Performance Assessment for the Waste Isolation Pilot Plant,* December 1992. SAND92-0700/1-5. Sandia National Laboratories. Albuquerque, NM. Vols. 1-5.

WIPP Performance Assessment. 1996a. *"User's Manual for LHS, Version 2.41."* Sandia National Laboratories. Albuquerque, NM. Sandia WIPP Central Files ERMS # 230732.

WIPP Performance Assessment. 1997a. *"User's Manual for NUTS, Version 2.05."* Sandia National Laboratories. Albuquerque, NM. Sandia WIPP Central Files ERMS # 246002.

WIPP Performance Assessment. 1997b. *"User's Manual for SECOTP2D, Version 1.41."* Sandia National Laboratories. Albuquerque, NM. Sandia WIPP Central Files ERMS # 245734.

WIPP Performance Assessment. 1998a. *"User's Manual for FMT (Version 2.40)"* Sandia National Laboratories. Carlsbad, NM. Sandia WIPP Central Files ERMS # 243037.

WIPP Performance Assessment. 1998b. *"Design Document for PANEL Version 4.00."* Sandia National Laboratories. Carlsbad, NM. Sandia WIPP Central Files ERMS # 52169.

WIPP Performance Assessment. 2003a. *"Design Document/User's Manual for CCDFGF Version 5.00."* Sandia National Laboratories. Carlsbad, NM. Sandia WIPP Central Files ERMS # 530471.

WIPP Performance Assessment. 2003b. *"Design Document for BRAGFLO Version 5.00."* Sandia National Laboratories. Carlsbad, NM. Sandia WIPP Central Files ERMS # 525700.

WIPP Performance Assessment. 2003c. *"User's Manual for BRAGFLO Version 5.00."* Sandia National Laboratories. Carlsbad, NM. Sandia WIPP Central Files ERMS # 525702.

WIPP Performance Assessment. 2003d. *"User's Manual for PANEL Version 4.02."* Sandia National Laboratories. Carlsbad, NM. Sandia WIPP Central Files ERMS # 526652.

WIPP Performance Assessment. 2003e. *"User's Manual for CUTTINGS_S, Version 5.10"* Albuquerque, NM: Sandia National Laboratories. Carlsbad, NM. Sandia WIPP Central Files ERMS # 532340.

WIPP Performance Assessment. 2003f. "*Verification and Validation Plan and Validation Document for DRSPALL Version 1.00."* Sandia National Laboratories. Carlsbad, NM. Sandia WIPP Central Files ERMS # 524782.

WIPP Performance Assessment. 2003g. *"Design Document for DRSPALL Version 1.00."* Sandia National Laboratories. Carlsbad, NM. Sandia WIPP Central Files ERMS # 529878.

WIPP Performance Assessment. 2003h. *"User's Manual for DRSPALL Version 1.00."* Sandia National Laboratories. Carlsbad, NM. Sandia WIPP Central Files ERMS # 524780.

WIPP Performance Assessment. 2003i**.** "Design Document for CUTTINGS Version 5.10." Sandia National Laboratories. Carlsbad, NM. Sandia WIPP Central Files ERMS # 532336.